

INFLUENCE OF SPECIMEN GEOMETRY AND GRADING CURVE ON THE PERFORMANCE OF AN UNBOUND GRANULAR MATERIAL

by

Eben Barnard van Zyl

*Thesis presented in fulfilment of the requirements for the degree
of Master of Science in the Faculty of Engineering at
Stellenbosch University*



Supervisor:

Professor Kim Jonathan Jenkins
SANRAL Chair in Pavement Engineering
Department of Civil Engineering

Co-supervisor:

Mrs Chantal Rudman
Department of Civil Engineering

March 2015

DECLARATION

By submitting this thesis electronically, I declare that the entirety of the work contained therein is my own, original work, that I am the sole author thereof (save to the extent explicitly otherwise stated), that reproduction and publication thereof by Stellenbosch University will not infringe any third party rights and that I have not previously in its entirety or in part submitted it for obtaining any qualification.

Signature:

Date: 06-02-2015.....

Copyright © 2015 Stellenbosch University
All rights reserved

SUMMARY

This research study investigates the influence of specimen geometry and grading curve, on the performance of a typical South African unbound granular material. The experimental design incorporates three grading curves to evaluate the influence of grading. In addition, to evaluate the influence of specimen geometry, two specimen sizes were included into the experimental design. Laboratory testing consisted of monotonic tri-axial tests to evaluate the shear performance (Cohesion and Friction Angle) and more complex short duration dynamic tri-axial tests to evaluate the load spreading ability/stiffness (Resilient Modulus) of the selected materials.

In order to achieve the objectives of this study, a large tri-axial apparatus was needed that could accommodate specimens as large as 300mm ϕ * 600mm high. This would allow a full grading of large aggregate (up to 50mm particle size) to be accurately evaluated. Further development and commissioning of such a large tri-axial apparatus therefore formed part of this study.

The representative parent material selected for testing consisted of a G2 graded crushed Hornfels stone. The material was dried and sieved into fractions where after it was carefully reconstituted to allow for accurate control of specimen grading during specimen preparation. The three grading curves consisted of two adjusted grading curves (referred to as *S19* and *G19C*), adjusted from the full G2 grading, and the full G2 grading itself (referred to as the *Full* grading curve).

Material property tests, Sieve Analysis, Bulk Relative Density (BRD) and Optimum Moisture Content (OMC) tests were performed to gain an understanding of the material characteristics. Moisture-Density relationship curves were developed to identify a common Moisture Content that, for all three grading curves, would yield a common Dry Density. A Moisture Content of 4.7% was identified that would yield a Dry Density of 2340 kg/m³ for all three grading curves. This density could be achieved for both sizes of specimen preparation apparatuses without damaging material particles. Specimens were compacted using the representative vibratory hammer compaction method, sealed and left for 24 hours to allow redistribution of moisture and initial development of Cohesion.

The shear parameters (Cohesion and Friction Angle) were investigated through

monotonic tri-axial testing. It was found that Cohesion and Friction Angle are influenced by both grading curve and specimen geometry. Cohesion was found to reduce as the coarseness of the material grading increased (i.e. finer *S19* grading yielded higher Cohesion than its coarser *G19C* counterpart) and the Friction Angle was found to increase with increase coarseness (i.e. finer *S19* grading yielded lower Friction Angles when compared to the *G19C* grading).

The influence of specimen geometry was also investigated. It was observed that Cohesion decreased with an increase in specimen size. Friction Angle on the other hand was found to increase with increased specimen size.

From dynamic tri-axial test results, it was observed that the Resilient Modulus is influenced by both specimen geometry and grading curve. The influence of specimen geometry however is complex and no constant trend throughout the grading curves tested could be identified. Grading curve however was found to increase the Resilient Modulus for coarser gradings (i.e. coarser *G19C* vs finer *S19*). Increased large particle-to-particle contact area yields higher friction within the material specimen, resulting in lower strains induced by higher stresses, i.e. higher Resilient Modulus.

It was shown, for both monotonic and dynamic tri-axial tests, that the coarser *G19C* grading curve yields more representative results to that of the *Full* grading curve when compared to the finer *S19* grading. This was observed for shear and resilient performance properties. Additionally, a simple design case study yields similar trends.

In conclusion, material characterisation plays an important role in the design of unbound granular materials (UGM's). Current laboratory characterisation techniques however used adjusted gradings to limit the effects stemming from the ratio between specimen diameter and maximum particle size. This research has shown that some of the current practices do not best represent the true in-situ grading. It has been shown that both grading curve and specimen geometry influence the performance of UGM's which, in turn, influences the design of a pavement structure. Therefore, accurate modelling of the true in-situ grading, through testing apparatuses capable of accommodating in-situ gradings, is required.

OPSOMMING

Hierdie navorsingsstudie evalueer die invloed van proefstukgeometrie en gradering, op die gedragseienskappe van 'n tipiese Suid Afrikaanse ongebinde granulêre aggragaat. Om die invloed van gradering te evalueer, is 'n eksperimentele ontwerp ontwikkel wat drie materiaal graderings insluit. Verder, om die invloed van proefstukgeometrie te evalueer, is twee proefstukgroottes toegevoeg tot die eksperimentele ontwerp. Monotoniese drie-assige toetse is uitgevoer om die skuifsterkte (Kohesie en Wrywingshoek) van die materiaal te ondersoek. Addisioneel is die styfheid (Veerkragmodulus) van die materiaal ondersoek deur dinamiese drie-assige toetse.

Om die doelwitte van hierdie studie te bereik was 'n groot skaalse drie-assige toets apparaat benodig wat groot, 300mm ϕ * 600mm hoogte, proefstukke kan akkommodeer. So 'n apparaat laat toe dat die volle gradering van aggragaat (tot en met 50mm korrels) akkuraat geëvalueer kan word. Daarom vorm die ontwikkeling en opstelling van so 'n apparaat deel van hierdie studie.

Die tipiese Hornfels gebreekte klip, met 'n G2 gradering, wat ondersoek is, was gedroog en in verskeie fraksies gesif om die akkuraatheid van proefstuk voorbereiding te beheer. Die drie graderings bestaan uit twee aangepaste graderings (S19 en G19C gradering skale), aangepas vanaf die volle G2 gradering, en die vol G2 gradering homself (verwys na as die "Full" gradering skaal).

Materiaal gedragstoetse, Sif Analises, Nat Gekompakteerde Relatiewe Digtheid (BRD) en Optimum Vog Inhoud (OVI) toetse, was uitgevoer om die materiaal eienskappe te ondersoek. Om 'n gemeenskaplike Vog Inhoud en Droë Digtheid, wat vir al drie graderings geld, te vind, is Vog-Digtheid verhoudingskurwes ontwikkel. Vanaf die kurwes is identifiseer dat 'n Vog Inhoud van 4.7% 'n Droë Digtheid van 2340 kg/m³ vir al drie graderings sal lewer. Vibrasie kompaksie is toegepas om albei skale van proefstukke te kompakteer waarna die proefstukke vir 24 uur geseel is om vogverspreiding en ontwikkeling van Kohesie toe te laat.

Monotoniese drie-assige toetse is uitgevoer om die skuifsterkte parameters (Kohesie en Wrywingshoek) te ondersoek. Die resultate het gewys dat beide gradering en proefstukgeometrie die Kohesie en Wrywingshoek beïnvloed. Daar was gevind dat Kohesie verlaag indien die grofheid van die gradering verhoog (m.a.w. die fyner S19

gradering lewer hoër Kohesie waardes i.v.m. die growwer *G19C* gradering). Die Wrywingshoek is gevind om te verhoog soos die grofheid van die gradering verhoog (m.a.w. die fyner *S19* gradering het laer Wrywingshoeke gelewer i.v.m. die growwer *G19C* gradering).

Resultate het verder gewys dat groter proefstukke laer Kohesie en hoër Wrywingshoeke lewer. Daar kan wel gedebateer word dat variasie in materiaal die verandering van die skuifsterkte parameters gee, maar die proefstukvariasie is beperk om sodoende die invloed daarvan onopmerkbaar te maak.. Verder is die verlaging in Kohesie en verhoging in Wrywingshoek, a.g.v. 'n vergroting in proefstuk grootte, vir albei aangepaste graderings geobserveer. Dit is 'n moontlike aanduiding dat die verandering nie materiaal afhanklik is nie maar eerder beïnvloed word deur die grens toestande tydens kompaksie.

Dinamiese drie-assige toets resultate het gewys dat die Veerkragsmodulus beïnvloed word deur beide proefstuk geometrie en gradering. Daar is gevind dat die invloed van proefstukgeometrie kompleks is, en geen konstante verhouding, wat vir alle toets graderings geld, kon identifiseer word nie. Vir die invloed van gradering is daar gewys dat die Veerkragsmodulus hoër is vir die growwer gradering (m.a.w. *G19C* gradering lewer hoër styfheid as *S19* gradering). 'n Verhoging in korrel-tot-korrel kontak area lewer hoër interne wrywing in die proefstuk wat bydrae tot laer vervorming by hoër spannings, m.a.w. hoër Veerkragsmodulus.

Baie interessant, vir beide monotoniese en dinamiese drie-assige toetse is gevind dat die growwer *G19C* gradering, i.v.m. die fyner *S19* gradering, die ware *G2 (Full)* gradering beter verteenwoordig. Hierdie observasie is geldig vir beide die skuifsterkte parameters en weerstands eienskappe.

Aggregaat karakterisering is 'n belangrike deel in die ontwerp van 'n ongebinde granulêre materiaal laag. Huidige karakterisering metodes gebruik aangepaste graderings sodat resultate nie beïnvloed word deur die verhouding tussen proefstuk diameter en maksimum klipgrootte nie. Hierdie ondersoek het gevind dat van die huidige aanpassings nie die ware gradering verteenwoordig nie. Die resultate wys dat beide gradering en proefstuk geometrie die gedrag van die ongebinde granulêre materiaal beïnvloed, so ook die ontwerp van 'n padstruktuur. Daar is dus 'n behoefte om die ware gradering te ondersoek wat slegs moontlik is met groot skaalse toets apparaat, wat groot klip korrels kan toets. Verder, indien daar 'n verstandhouding

tussen huidige (klein skaalse) toets apparaat en groot skaalse apparaat ontwikkel kan word, kan resultate aangepas word, vanaf die klein skaalse resultate, om die ware materiaal gedrag meer te verteenwoordig.

ACKNOWLEDGEMENTS

Support, as a verb, is:

To bear all or part of the weight of

and/or

To give assistance to

With the above definitions in mind, I want to show my sincere gratitude and appreciation to all parties involved, for bearing part of the weight and assisting me, in my work toward obtaining my master's degree.

I acknowledge:

- My Heavenly Father for His strength, support and the talents invested in me.
- Most of all my parents, Willie and Ina van Zyl, for their love, support (mentally and financially), inspiration and sacrifices made throughout my studies.
- My brother and sisters, Willie, Annemie and Julene, for their love and support.
- My fiancé, Jo-Rene Engelbrecht, for her love, understanding and motivation.
- My promoter and supervisor, Professor Kim Jenkins, for his friendship, endless support, sharing of knowledge, guidance and assistance in completing this research.
- Mrs Chantal Rudman, for her friendship, assistance and motivation during the darker days and her endless help with the commissioning of the large-size tri-axial.
- My fellow MScEng students; Achille, Fabrice and Romei for all the jokes and discussions, assistance and sharing of knowledge.
- Laboratory assistants, Colin, Eric and Gavin for their assistance with material sieving and specimen preparation.
- All my Stellenbosch friends, of whom I cannot mention all the names, for all the fun and joy that you have brought to my life over the years.

I would like to send a special note of appreciation to the South African National Road Agency Limited (SANRAL) for their funding towards the development of the large tri-axial apparatus.

TABLE OF CONTENT

DECLARATION	i
SUMMARY	ii
OPSOMMING	iv
ACKNOWLEDGEMENTS	vii
TABLE OF CONTENT	viii
LIST OF TABLES AND FIGURES	xii
LIST OF SYMBOLS AND ABBREVIATIONS	xvii
CHAPTER 1: INTRODUCTION	1
1.1 Background and Problem Statement	1
1.2 Objectives	2
1.3 Scope of Study	2
1.4 Limitations	3
1.5 Outline of This Dissertation	3
CHAPTER 2: LITERATURE REVIEW	5
2.1 Introduction	5
2.2 Pavement Structures	5
2.2.1 History of Roads	5
2.2.2 South African Approach	7
2.2.3 Pavement Loading	9
2.3 Review of Unbound Granular Material Behaviour	10
2.3.1 Mechanical Behaviour	11
2.3.2 Factors Influencing the Mechanical Behaviour of UGM's	27
2.3.3 Laboratory Characterisation of UGM's	40
2.4 Unbound Granular Layer Construction	51
2.4.1 Classification and Specifications	51

2.4.2	Field Compaction Methods	53
2.5	Conclusion.....	54
CHAPTER 3: RESEARCH DESIGN AND METHODOLOGY		57
3.1	Introduction.....	57
3.2	Experimental Design	57
3.3	Material Procurement and Testing	60
3.3.1	Sieving	60
3.3.2	Grading	60
3.3.3	Moisture-Density Relation	63
3.4	Testing Methodology	72
3.4.1	Material Preparation.....	72
3.4.2	Mixing	73
3.4.3	Compaction.....	75
3.4.4	Curing	80
3.4.5	Testing and Data Processing.....	81
3.5	Trouble Shooting	103
3.5.1	Preliminary Testing	104
3.5.2	Dynamic Tri-axial Testing	105
3.6	Summary	107
CHAPTER 4: ANALYSIS AND DISCUSSION OF RESULTS.....		109
4.1	Introduction.....	109
4.2	Quality Control.....	109
4.2.1	Small-size Specimens.....	109
4.2.2	Large-size Specimens	113
4.3	Monotonic Tri-axial Testing	115
4.3.1	Presentation of Initial Test Results.....	116
4.3.2	Influence of Specimen Geometry.....	119
4.3.3	Influence of Grading Curve	121

4.3.4	Comparison.....	123
4.3.5	Additional Testing	126
4.4	Dynamic Tri-axial Testing	127
4.4.1	Presentation of Initial M_r Test Results.....	128
4.4.2	Modelling of Resilient Behaviour.....	130
4.4.3	Comparison.....	140
4.4.4	Additional Testing	143
CHAPTER 5: DESIGN CONSIDERATION.....		150
5.1	Pavement Structure and Loading	150
5.2	Unbound Basecourse M_r Iteration	152
5.3	Design Life Calculations	155
5.3.1	Unbound Granular Base Layer	155
5.3.2	Cement Stabilised Subbase Layer.....	158
5.3.3	Comparison of Design Life.....	159
CHAPTER 6: CONCLUSIONS AND RECOMMENDATIONS.....		161
6.1	Conclusions.....	161
6.1.1	General Conclusions.....	161
6.1.2	Influence of Specimen Geometry.....	163
6.1.3	Influence of Grading Curve	164
6.1.4	Comparison of Grading Curves.....	165
6.2	Recommendations.....	166
6.2.1	Future Research	166
6.2.2	Testing Protocols	167
6.2.3	Testing Apparatus.....	168
REFERENCES.....		169
APPENDICES		175
Appendix A: Material Densities Based on Vibratory Compaction.....		176
Appendix B: Monotonic Tri-axial Test Results.....		178

Appendix C: Dynamic Tri-axial Test Results	182
Appendix D: Modelling of Mr- Θ Model	188
Appendix E: Modelling of Mr- Θ - σ_d/σ_{df} Model.....	190
Appendix F: 0.1 – 0.9 Loading Rate.....	192
Appendix G: 0.05 – 0.95 Loading Rate	197
Appendix H: Comparison of Models and Influence of Deviator Stress Ratio.....	199
Appendix I: Influence of Increased Density on Resilient Modulus during Dynamic Testing	201
Appendix J: Iterative Design Calculations of Resilient Modulus.....	203

LIST OF TABLES AND FIGURES

Table 2- 1: Summary of Different Resilient Modulus Test Protocol Properties (Anochie-Boateng et al., 2009).....	48
Table 2- 2: Guidelines for Compaction Specifications of Granular Base Layers (COLTO, 1998)	52
Table 3- 1: Sieve Sizes	60
Table 3- 2: Breakdown of Material Fraction Combinations for Each Grading and Sample Size	73
Table 3- 3: Layer Thickness and Mass Data	76
Table 3- 4: Comparison between Small- and Large-Size Tri-axial Testing Devices	83
Table 3- 5: Loading Regime for Short Duration Dynamic Tri-axial Test	98
Table 3- 6: Summary of Loading Schedule used for Short Duration Dynamic Tri-axial Test	100
Table 4- 1: Summary of Standard Deviations	114
Table 4- 2: Summary of Moisture Content during Compaction and After Testing	115
Table 4- 3: Summary of Cohesion and Friction Angle for Various Grading and Specimen Sizes	118
Table 4- 4: Summary of Material Coefficients and Correlation Coefficients for Calibrated Models	133
Table 5- 1: Iterative Design Method to Compute Resilient Modulus (Small-Size S19 Specimens) .	153
Table 5- 2: Summary of Final M_r Values	153
Table 5- 3: Summary of Design Life Calculation for Unbound Granular Basecourse Layer	157
Table 5- 4: Summary of Design Life Calculations for Stabilised Subbase Layer	159
Figure 2- 1: Load Transfer through the Pavement Structure (SAPEM, 2013)	6
Figure 2- 2: Typical Roman Pavement Structure (SAPEM, 2013)	7
Figure 2- 3: Stresses Condition Beneath Moving Wheel Load: (a) Stresses on Pavement Element; (b) Variation of Stresses Over Time as Wheel Passes; (c) Principal Stresses on Pavement Element – Element Rotates; (d) No Rotation – Shear Stress Reversal (Brown, 1996).....	10
Figure 2- 4: (a) Monotonic Loading to Failure, (b) Strain in UGM’s caused by a Single Load Cycle (Araya, 2011).....	12
Figure 2- 5: Illustration of Poisson’s Ratio in three Dimensions (PavementInteractive, 2007)	12
Figure 2- 6: Mohr-Coulomb Representation of Monotonic Tri-axial Test (Jenkins, 2010)	15
Figure 2- 7: Mohr-Coulomb representation of two cases with Equal Stress Ratios (Theyse, 2007) .	17
Figure 2- 8: Stiffness or Elastic Modulus as a Function of Stress and Strain (SAPEM, 2013)	17
Figure 2- 9: Unbound Granular Material Behaviour under Repeated Loading (Thom, 1988)	18

Figure 2- 10: Schematic Illustration of the Cyclic Axial Deviator Stress Principal (Jenkins, 2000)	19
Figure 2- 11: M_r - θ Model of Resilient Modulus (Jenkins, 2010)	20
Figure 2- 12: Representation of M_r - θ Model Data in Relation to “mild” Regime Tested Data (van Niekerk, 2002).....	21
Figure 2- 13: Representation of M_r - θ Model Data in Relation to “severe” Regime Tested Data (van Niekerk, 2002).....	22
Figure 2- 14: Representation of the M_r - θ Model’s fit on Test Data (van Niekerk, 2002).....	25
Figure 2- 15: Representation of the M_r - θ - σ_d Model’s fit on Test Data (van Niekerk, 2002)	25
Figure 2- 16: Poisson’s Ratio in Relation to Deviator Stress Ratio for Both Models (van Niekerk, 2002)	27
Figure 2- 17: Effective Stress in a Partially Saturated Granular Material (Theyse, 2010)	28
Figure 2- 18: Typical Soil-Water Characteristic Curve for the Wetting and Drying of a Material (Vanapalli et al. 1996).....	29
Figure 2- 19: Cohesion and Friction Angle values as a Function of Moisture Content and Degree of Compaction, for a Weathered Basalt Material (Araya, 2011)	30
Figure 2- 20: Cohesion and Friction Angle values as a Function of Moisture Content, for a Mix Recycled Granulate Material (van Niekerk, 2002)	30
Figure 2- 21: M_r - θ relation for Porphyry Material, for Fine Grading (a) and Coarse Grading (b) for both Wet and Dry Specimen Conditions (Sweere, 1990)	32
Figure 2- 22: Influence of Compaction and Grading Parameter on the Principal Stress Ratio at Failure (Thom, 1988)	33
Figure 2- 23: Cohesion in Relation to DOC for Six Research Sands (van Niekerk, 2002)	34
Figure 2- 24: Friction Angle in Relation to DOC for Six Research Sands (van Niekerk, 2002)	35
Figure 2- 25: M_r - θ Relations as a Function of DOC for a Mix Recycled Granulate Material after 4 days curing (van Niekerk, 2002)	36
Figure 2- 26: Three Physical States of Soil-Aggregate Mixtures (Molenaar, 2010).....	38
Figure 2- 27: Six commonly used Characterisation Tests for UGM’s (Thom et al. 2005)	41
Figure 2- 28: Stress-Strain Relation for a Granular Material under Repeated CBR loading (van Niekerk, 2002).....	42
Figure 2- 29: Principal of Tri-axial Test (Anochie-Boateng et al., 2009).....	43
Figure 2- 30: Schematic representation of monotonic tri-axial tests results for two specimens tested at low and high confining pressure respectively (Jenkins, 2010)	44
Figure 2- 31: Schematic Representation of a Typical Tri-axial Test Set-up, (a) Detailed Cell with Measuring Equipment and (b) Broader Representation of Tri-axial Test Set-up (IDOT, 2009 and Molenaar, 2010 respectively).....	45
Figure 2- 32: Moisture-Density Relation Curve for Different Compactive Effort (Craig, 2004)	50

Figure 2- 33: Primary Roller Selection Guide (Wirtgen, 2004)	54
Figure 3- 1: Flow Chart of the Experimental Design.....	59
Figure 3- 2: Vibratory Sieve	60
Figure 3- 3: S19 Grading Curve	61
Figure 3- 4: G19C Grading Curve.....	62
Figure 3- 5: Full Grading Curve	63
Figure 3- 6: Typical Density-Moisture Relationship Curve.....	64
Figure 3- 7: Small-scale Vibratory Hammer Setup with Bosch Hammer.....	65
Figure 3- 8: Initial Density-Moisture Relationship Curve for Small-scale Vibratory Hammer	67
Figure 3- 9: Material Slush Forced from Mould at Excessively High Moisture Contents	68
Figure 3- 10: Final Density-Moisture Relationship Curve for Small-scale Vibratory Hammer.....	68
Figure 3- 11: Large-scale Vibratory Hammer	69
Figure 3- 12: Final Density-Moisture Relationship Curve for Large-scale Vibratory Hammer.....	70
Figure 3- 13: Combined Density-Moisture Relationship Curves	71
Figure 3- 14: Pan Mixer used to Mix Material	74
Figure 3- 15: Tape Measure Placed on Vibratory Hammer to Control Layer Thickness/Density.....	76
Figure 3- 16: a) Small-Size Split Mould and b) Large-Size Split Mould.....	77
Figure 3- 17: Marking off of Zero Line (Kelfkens, 2008)	78
Figure 3- 18: Indicating the Target Dry Density Line (adjusted from Kelfkens, 2008)	78
Figure 3- 19: Scarifying Tools used to Loosen Top of Compacted Layers.....	79
Figure 3- 20: Dry Density Mark for Layer 2 (adjusted from Kelfkens, 2008)	79
Figure 3- 21: MTS Flextest 40 Controller used for both Small- and Large-size Testing	82
Figure 3- 22: Small-size (Left) and Large-size (Right) Tri-axial Testing Device.....	82
Figure 3- 23: Equipment used for the Manufacturing of small Latex Membranes.....	84
Figure 3- 24: First Layer of Large-size Membrane after Drying	85
Figure 3- 25: Small-size Tri-axial Specimen Assembled for Monotonic Testing	86
Figure 3- 26: Large-size Tri-axial Specimen Compacted On Top of Baseplate.....	87
Figure 3- 27: Large-size Tri-axial Specimen Placed on Baseplate	88
Figure 3- 28: Large-size Tri-axial Cell Connected to Portable Crane	89
Figure 3- 29: Trolley Designed and Built to Assist Moving of Tri-axial Cell	89
Figure 3- 30: Large-size Tri-axial Cell On Top of Trolley.....	90
Figure 3- 31: Large-size Tri-axial Cell being Lifted by the Actuator	90
Figure 3- 32: Large-size Tri-axial Cell Lowered into Position using Vertical Actuator	91
Figure 3- 33: Small-size Specimen Assembled for Dynamic Tri-axial Test	96
Figure 3- 34: A Single Load Cycle for the Short Duration Dynamic Tri-axial Test	97

Figure 3- 35: Resilient Modulus Definition and Calculation (Theyse, 2012)	101
Figure 3- 36: Layout of Large-size Tri-axial Testing Apparatus.....	104
Figure 3- 37: Spacer Blocks used to Level Tri-axial Platform	106
Figure 3- 38: Drilling of Holes through Platform and Support Beams	106
Figure 3- 39: Fixing of Platform to Support Beams to Increase Rigidity	107
Figure 4- 1: Small-size Specimen Quality Control Summary	110
Figure 4- 2: Small-size Specimen Moisture Variation after Testing.....	112
Figure 4- 3: Moisture Adhering to Plastic Surface during Curing	112
Figure 4- 4: Moisture Extruded from Specimen during Dynamic Loading	113
Figure 4- 5: Large-size Specimen Quality Control Summary	114
Figure 4- 6: Stress-Strain Relationship Curve for Small-size S19 Specimens.....	116
Figure 4- 7: Mohr-Coulomb Representation of Small-size S19 Monotonic Test Results.....	117
Figure 4- 8: Percentage Change in Shear Parameters when Changing the Confinement Pressure Range for Small-size Tri-axial	119
Figure 4- 9: Influence of Specimen Geometry on Cohesion.....	120
Figure 4- 10: Influence of Specimen Geometry on Internal Friction Angle.....	121
Figure 4- 11: Influence of Grading Curve on Cohesion	122
Figure 4- 12: Influence of Grading Curve on the Friction Angle	123
Figure 4- 13: Normalised Monotonic Tri-axial Test Results	124
Figure 4- 14: Three Physical States of Aggregate Particle Distribution (Molenaar, 2010)	125
Figure 4- 15: Comparison of Small-size Shear Parameters Prior and Post Dynamic Loading	126
Figure 4- 16: Change in Soil Structure due to Increased Compaction/Density (Multiquip, 2011) ...	127
Figure 4- 17: Typical Resilient Modulus Values for Small-size S19 Specimen 1.....	128
Figure 4- 18: Resilient Modulus – Bulk Stress Relationship, Small-size S19, Specimen 1.....	129
Figure 4- 19: M_r - θ Model Calibrated to Fit Small-size S19 Resilient Modulus Results	131
Figure 4- 20: M_r - θ - σ_d/σ_{df} Model Calibrated to Fit Small-size S19 Resilient Modulus Results ...	132
Figure 4- 21: Comparison of Models at $SR_d = 10, 50$ and 90% for Small-size S19 Specimens	134
Figure 4- 22: Estimated Resilient Modulus Values for the Mr - θ Model.....	135
Figure 4- 23: Estimated Resilient Modulus for the M_r - θ - σ_d/σ_{df} Model with $SR_d = 10\%$	136
Figure 4- 24: Estimated Resilient Modulus for the M_r - θ - σ_d/σ_{df} Model with $SR_d = 50\%$	136
Figure 4- 25: Estimated Resilient Modulus for the M_r - θ - σ_d/σ_{df} Model with $SR_d = 90\%$	137
Figure 4- 26: Estimated Resilient Modulus Values for the Mr - θ Model.....	138
Figure 4- 27: Estimated Resilient Modulus for the M_r - θ - σ_d/σ_{df} Model with $SR_d = 10\%$	139
Figure 4- 28: Estimated Resilient Modulus for the M_r - θ - σ_d/σ_{df} Model with $SR_d = 50\%$	139
Figure 4- 29: Estimated Resilient Modulus for the M_r - θ - σ_d/σ_{df} Model with $SR_d = 90\%$	140

Figure 4- 30: Normalised Resilient Modulus Values for $M_r-\theta$ Model.....	141
Figure 4- 31: Normalised Resilient Modulus Values for $SR_d = 10\%$, $M_r-\theta-\sigma d/\sigma df$ Model.....	142
Figure 4- 32: Normalised Resilient Modulus Values for $SR_d = 50\%$, $M_r-\theta-\sigma d/\sigma df$ Model.....	142
Figure 4- 33: Normalised Resilient Modulus Values for $SR_d = 90\%$, $M_r-\theta-\sigma d/\sigma df$ Model.....	143
Figure 4- 34: Last 55% SR Conditioning Cycle, S-S19	144
Figure 4- 35: Last 55% SR 200 kPa Load Cycle, S-S19.....	145
Figure 4- 36: Last 55% SR 25 kPa Load Cycle, S-S19	145
Figure 4- 37: Last 55% SR 200 kPa Load Cycle, L-S19.....	146
Figure 4- 38: Last Rapid 55% SR 200 kPa Load Cycle, S-S19	147
Figure 4- 39: Resilient Modulus vs Bulk Stress, Small-size S19, 0.1/0.9 Load Cycle.....	148
Figure 4- 40: Resilient Modulus vs Bulk Stress, Small-size S19, 0.05/0.95 Load Cycle.....	148
Figure 4- 41: Influence of Increased Density on Resilient Modulus of Large-size S19 Specimen.....	149
Figure 5- 1: Pavement Structure and Load Layout used in Stress-Strain Analysis.....	150
Figure 5- 2: Normalised Resilient Modulus Values after Iterative Design	154
Figure 5- 3: Horizontal Stress Development in Pavement Structure	155
Figure 5- 4: Vertical Stress Development in Pavement Structure due to Loading.....	156
Figure 5- 5: Progression of DSR in Relation to Pavement Depth.....	158
Figure 5- 6: Comparison of Estimated Design Life Values	159

LIST OF SYMBOLS AND ABBREVIATIONS

Θ : Bulk Stress

C: Cohesion

Φ : Friction Angle

ν : Poisson's Ratio

M_r : Resilient Modulus

AASHTO: American Association of Highway and Transportation Officials

ARD: Apparent Relative Density

BRD: Bulk Relative Density

BSM's: Bitumen Stabilized Materials

CBR: California Bearing Ratio

CCP: Constant Confinement Pressure

COLTO: Committee of Land Transport Officials

DOC: Degree of Compaction

ESA: Equivalent Standard E80 Axles

HCA: Hollow Cylinder Apparatus

LVDT: Linear Variable Displacement Transducer

MST: Multi Stage Failure Test

MTS: Material Testing and Simulation

OMC: Optimum Moisture Content

PTR: Pneumatic Tyre Roller

SAPeM:	South African Pavement Engineering Manual
SF:	Safety Factor
S.R.:	Stress Ratio
SR _d :	Deviator Stress Ratio
TG2:	Technical Guideline: Bitumen stabilized Materials. TG2 second Edition, May 2009
TMH:	Technical Methods for Highways
TRH:	Technical Recommendations for Highways
UGM:	Unbound Granular Material
VCP:	Variable Confinement Pressure

CHAPTER 1: INTRODUCTION

This chapter serves as an introduction to this dissertation.

1.1 Background and Problem Statement

A principal component included in the design of unbound granular base and subbase layers, is the characterisation of the material performance properties. In past times, unbound granular materials (UGM's) were characterised based on physical properties such as gradation, plasticity, hardness, durability, and static shear strength tests (Austin, 2009). These tests however, could not accurately simulate in field conditions or dynamic loading. Therefore, improved tests, better simulating in field conditions and dynamic loading, had to be developed.

Although current laboratory characterisation techniques accurately simulate dynamic loading, drawbacks still exist. Most laboratory test set-ups, used in the characterisation process, cannot incorporate large aggregate particles (usually particles greater than 19mm) due to the influence of ratio between particle size and specimen size. Therefore, laboratories use “scaled” down gradings and, for ease of testing, scaled specimens. As a result, the initial grading (typically 0 to 37.5mm, for crushed stone materials) is modified to a grading suitable for the geometry of the associated test set-up. Thus, the true in-situ grading is not tested.

Several studies have shown grading to have a significant influence on the performance of unbound granular materials. Filler content (particles passing 0.075mm) and grading itself has a significant influence on shear strength characteristics and resilient response. Limited literature however exists on the influence that large aggregate particles (especially 26.5 and 37.5mm) have on the performance properties of unbound granular materials. Within the literature that exists, no certain behaviour can be established that is consistent with all material types. Therefore, it is necessary to research the influence of large aggregate particles on common South African pavement materials, in order to establish an understanding of the influence of grading (particularly maximum aggregate size) on the performance of UGM's.

Furthermore, as mentioned, laboratories use scaled down test specimens for ease of testing and due to the high cost associated with large-scale testing apparatuses. Due

to limited large-scale testing equipment, especially in South Africa, little research, establishing the influence of specimen geometry on performance properties, exists. As the need for testing true in-situ grading curves (only possible with expensive large-scale equipment), that contain large size particles, increase, the need for understanding the effect of specimen geometry becomes more important. Therefore, it is necessary to research the influence of specimen geometry on the performance of unbound granular materials.

In summary, a need for understanding the influence of large aggregate particle, on the performance of South African unbound granular materials, exist. Furthermore, linked to the need for understanding the influence of large aggregate size, a need for understanding the influence of specimen geometry also exists. Therefore, this study will attempt to establish the influence of maximum aggregate size, and specimen geometry, on the performance properties (shear strength and resilient response) of a typical South African crushed stone material.

1.2 Objectives

It is important to note that the secondary objectives of this research study could only be fulfilled by achieving the primary objective, which is the further development and commissioning of an existing large-scale tri-axial apparatus, at Stellenbosch University. A large section of this research project therefore entails work not mentioned in this report. Furthermore, once commissioned, the large apparatus together with the small-size tri-axial was utilised to achieve the objectives mentioned.

The first of the secondary objectives is to evaluate the influence of specimen geometry on the performance properties (shear strength and resilient response) of an unbound granular material. Thereafter the research aims to establish the influence of using adjusted grading curves to evaluate the performance of an unbound granular material through small-size tri-axial testing.

1.3 Scope of Study

To achieve the aforementioned objectives, an experimental testing program was developed that incorporates three methods of grading modification: parallel-scalping method, scalp-add-back method, and no modification method. The experimental testing program, on each of the modification methods, included physical properties tests as well as monotonic and dynamic tri-axial testing.

Physical property tests include: material grading, BRD's (bulk relative densities), and optimum moisture content and maximum dry density calculation based on vibratory hammer compaction.

Tri-axial testing include both monotonic and dynamic (resilient response) tri-axial tests on both small (150mm Φ * 300mm H) and large-size (300mm Φ * 600mm H) specimens. In order to establish an understanding of the influence of confinement, both monotonic and Resilient Modulus tests incorporated a range of confining pressures (25, 50, 100 and 200 kPa). For Resilient Modulus tests, a range of mild Stress Ratios were tested (10, 20, 30, 40 and 55%) which could give an indication of the influence of applied stress.

1.4 Limitations

The limitations of this research study include:

- Material testing is limited to one parent material and experimental testing is limited to monotonic and dynamic tri-axial tests.
- Investigation of the influence of specimen geometry is based on two specimen sizes only.
- Analysis of the *Full* grading curve is limited to large-size tri-axial tests.
- All specimens are prepared using one moisture content and compacted to one target density.
- Large-size monotonic tri-axial testing is limited to the use of three specimens only.
- To ensure specimens do not fail during testing, dynamic tri-axial tests were limited to moderate stress regimes, which only include 10, 20, 30, 40 and 55% applied Stress Ratios.

1.5 Outline of This Dissertation

The dissertation of this research study is divided into five chapters of which a short summary of each is presented below.

Chapter 1: Introduction – This chapter introduces the reader to the dissertation. Firstly, a background into current laboratory characterisation methods, used to evaluate the performance of unbound granular materials, is presented. Secondly, through a problem statement, drawbacks in the current characterisation methods are identified where after the objectives and limitations of the study are set. Presented by

the final sections of this chapter, is the scope of the study followed by an outline of the dissertation.

Chapter 2: Literature Review – A review of previous literature follows in this chapter. Firstly, literature on current pavement structures and the South African approach thereto is provided where after pavement loading is discussed. Finally, unbound granular material performance (mechanical behaviour, influencing factors and laboratory characterisation) and layer construction methods are discussed.

Chapter 3: Research Design and Methodology – This chapter presents a discussion on the experimental design developed and the testing methodology used to achieve the objectives of this research study. Furthermore, material procurement and preliminary testing thereof is discussed. In addition, a section that focusses on all trouble shooting during the research period is presented.

Chapter 4: Analysis and Discussion of Results – This chapter is dedicated to present all test results. Tables present individual test results while the use of graphs allows for a more explanatory presentation of the results. Furthermore, interpretations and discussions are presented to give the reader some indication of the findings.

Chapter 5: Design Consideration – In this chapter, a design life analysis is presented to show the influence of the grading curve on the design life of the pavement structure. The design method presented by the South African Mechanistic Design Method (SAMDM) is used to evaluate the design life of a typical South African class B pavement structure.

Chapter 6: Conclusions and Recommendations – This chapter, the last of this dissertation, presents a synthesis on the findings. Emphasis is placed on the influence of grading curve and specimen geometry, on the laboratory performance characterisation of the tested material. Finally, based on the test results, recommendations are made for further development and improvement to the testing equipment used and for further investigation into this research topic. In addition, recommendations are made on the use of grading modification methods and the loading cycle used during dynamic tri-axial testing.

CHAPTER 2: LITERATURE REVIEW

2.1 Introduction

This Chapter of the report is dedicated to set a detailed technical background for this research project and focuses on the deformation behaviour (shear, resilient and volumetric) of unbound granular materials with the emphasis on the influence of maximum particle size and specimen geometry.

Presented is a review of pavement structures wherein the discussions focus on the historical development of pavement structures, the South African approach to pavement structures, and on pavement loading.

Section 2.3 presents a review on the behaviour of unbound granular materials, followed by a discussion of unbound granular layer construction in Section 2.4. The review, on the behaviour of UGM's include discussions on mechanical behaviour of UGM's, factors influencing the mechanical behaviour of UGM's and laboratory characterisation techniques for UGM's whereas Section 2.4 discusses general specifications and methods of unbound granular layer construction.

This Chapter concludes with a synthesis of the reviewed literature.

2.2 Pavement Structures

2.2.1 History of Roads

Roads, in some sort, have existed since ancient times. Mainly used for trade, in general, they were no more than frequently followed paths such as the tracks made by the movement of foraging and migrating animals. Humans, on the more important routes, maintained and improved their paths at river crossings, swamps and other difficult stretches (Roman roads, 2001). The removal of obstacles such as boulders, trimming back thorn bushes and, in some cases, the laying of branches and logs on the ground to ease human movement all formed part of maintenance routines.

As communities in certain areas grew, their social structures and networks demanded more permanent and improved contact. Roads thus appeared around 3500 B.C. when communities started to interact with each other by travelling, doing business, fighting, and socializing (SAPEM, 2013). During this time the introduction of chariots and wagons to roads, a consequence of the development of the wheel,

highlighted that the existing road materials were inadequate and that the roads required improvement. Therefore, different cultures made their own unique contributions to improving their existing road structures (Roman Roads, 2001): the Egyptians were master surveyors, the Greeks excelled in masonry; the Etruscans developed cement making and together with the Cretans were skilled at paving. The Romans incorporated drainage systems into their roads and recognised the developments of others. By incorporating all of the above-mentioned technological innovations, and adding their own innovation, the Romans constructed a system of roads that remained unmatched for centuries.

As mentioned above, the introduction of chariots and wagons highlighted the need for better quality pavement materials. The existing soil or subgrade, damaged by wheel loads, required some sort of protection from the high stresses at the wheel-road contact area. A pavement structure (layers of better quality material constructed over the subgrade) allowed the spreading of stresses from the surface throughout the pavement structure to the existing subgrade, thereby reducing the stress on the subgrade (Wirtgen, 2004). Figure 2-1 illustrates the reduction of stress through the pavement structure.

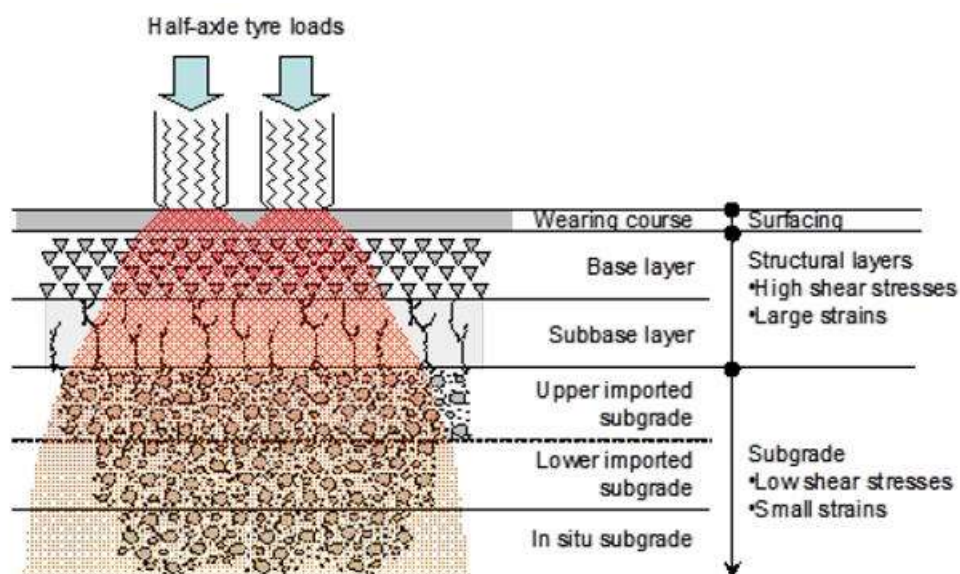


Figure 2- 1: Load Transfer through the Pavement Structure (SAPEM, 2013)

Although the Roman roads were unmatched at the time, they were not the first to incorporate paved roads into their road network. The earliest records of paved roads date back to about 2200 B.C. in Babylonia (modern Iraq), whereas the first Roman road, the Via Appia (the Appian Way), was constructed 334 B.C. (SAPEM, 2013;

Roman Roads, 2001). The Roman roads however were superior in comparison to others. They incorporated a layered system of large stones, with layers of smaller stones, gravel, concrete and large paving stones spread on top (Roman Roads, 2001). To better the performance of their roads, the Roman incorporated drainage ditches on the side of the roads and cambered the surface to shed water. In addition, the pavement structure was constrained between large stone kerbs as illustrated by the schematic of a typical Roman road, Figure 2-2 below. Note the layer system of different materials.

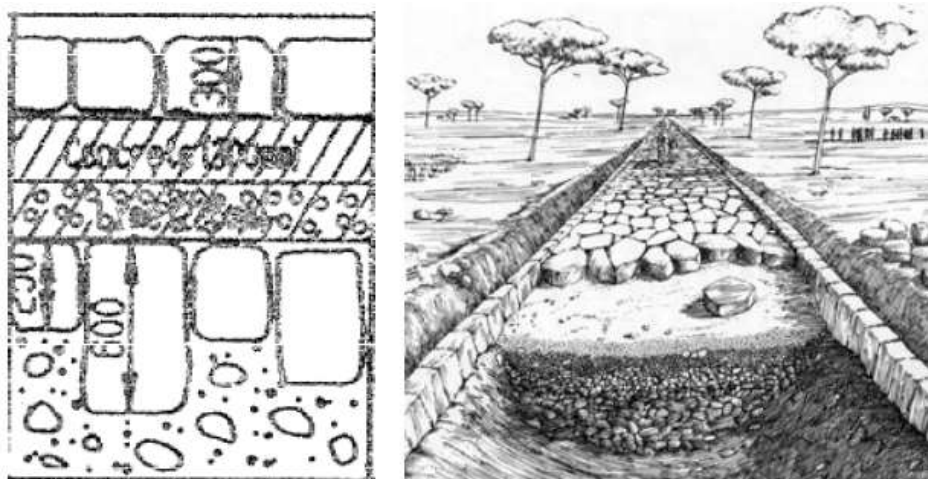


Figure 2- 2: Typical Roman Pavement Structure (SAPEM, 2013)

Some Roman roads lasted for more than a millennium and their basic pavement structure principles still used within modern pavements. Modern pavement structures incorporate a basic structure (three or four layer systems) similar to that developed by the Romans however with some variation in material type and particle size.

2.2.2 South African Approach

The South African approach to pavement structures is similar to that of ancient Rome although it has been refined to suite the South African environment. Layers of different materials, used to spread the load induced by the wheel, results in less stress on the existing, low quality, subgrade (see Figure 2-1).

The pavement foundation and structural layers of South African road pavements mostly consist of UGM's. Other countries also, such as Australia and New Zealand, together with some states in USA, incorporate the use of unbound granular structural pavement layers in combination with a thin wearing course (Theyse, 2007). Figure 2-1 above, shows a typical South African pavement structure as explained above. Note

that, Figure 2-1 also shows the load spreading and the reduction of stresses throughout the pavement structure.

The purpose of each of the structural layers shown in Figure 2-1 is described below (SAPEM, 2013).

- **Wearing Course:** This is a functional layer that provides waterproofing, skid resistance, noise-damping, visibility, drainage and durability against the elements. For surfaced pavements, the surfacing layer consists of spray seals, asphalt or concrete. Note that the wearing course for paved roads is bound.
- **Base:** This is a load spreading layer and the most important layer of the structural layers. The layer must provide support for the surfacing layer and spread the high tyre pressures and wheel loads uniformly over the underlying subbase.
- **Subbase:** This layer provides support for the base during traffic loading and provides a sound platform for the construction of a structural base layer of high integrity. Furthermore, it also protects the underlying unbound layer.
- **Imported Subgrade:** These layers, upper and lower, are primarily capping for the subgrade to provide a workable platform to construct the subbase. These layers also provide depth of cover for the subgrade and further reduce the stresses on the subgrade.
- **Subgrade:** This is the existing material supporting the pavement structure. The existing material can be modified with stabilisers to reduce plasticity, ripped and recompacted to achieve uniform support, or undercut and replaced, depending on its quality.

Typically, the structural layers will consist of two unbound granular layer with the base supported by the subbase layer (Theyse, 2007). The South African approach however is to incorporate a pavement structure known as an inverted or upside-down structure. The inverted structure incorporates a lightly cemented subbase layer as support for the unbound granular base layer.

As mentioned the South African approach incorporates a thin surfacing layer that has little load spreading capabilities. With little load spreading by the wearing course (see Figure 2-1), the unbound base layer is subjected to high stresses approaching that of

the tyre-pavement contact stress. Furthermore, if the surfacing layer does not function as a waterproofing layer, variation in moisture content within the base might occur. The combination of high stresses and moisture within the unbound base layer are most likely to contribute significantly to the deterioration of the pavement structure as a whole (Theyse, 2007).

Pavement design engineers therefore need to understand the effect of high stresses and variable moisture contents on the performance of different granular materials. By researching different materials and developing design models accordingly, the behaviour of unbound granular materials will become clear. Only once pavement design engineers understand the behaviour of UGM's, can confident and accurate decision regarding the use of a specific material be made.

2.2.3 Pavement Loading

Subsection 2.2.2 highlighted the importance of understanding the behaviour of unbound granular materials under loading. Just as important is the loading itself therefore an understanding of the loading mechanism within pavement structures is required.

A pavement structure in field undergoes traffic induced wheel loads that cause stress patterns within the pavement structure (Lekarp et al., 2000). The stress patterns changes as the wheel load passes and are complex. Figures 2-3 (a) and (b) show that a material element within a pavement structure is, subjected to stress pulses caused by moving traffic.

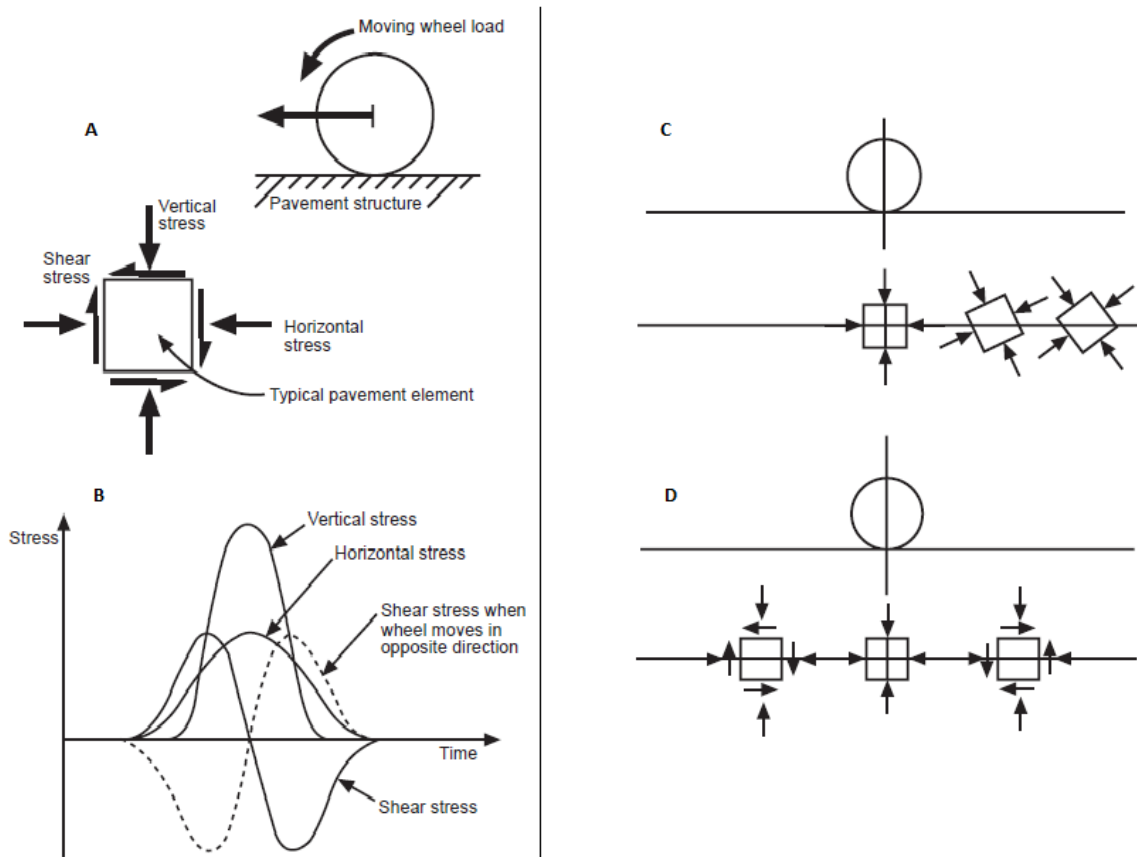


Figure 2- 3: Stresses Condition Beneath Moving Wheel Load: (a) Stresses on Pavement Element; (b) Variation of Stresses Over Time as Wheel Passes; (c) Principal Stresses on Pavement Element – Element Rotates; (d) No Rotation – Shear Stress Reversal (Brown, 1996)

Pulses induce horizontal, vertical and shear stresses on the element. For unbound materials, the horizontal and vertical stresses are both positive, increasing as the load approaches the element. The maximum stress within the material element, both horizontal and vertical, occurs at the point where the wheel load is directly above the element. At this point the principal stresses (stress state without shear stress), will be equal to the horizontal and vertical stresses. As the load moves over and away from the element, the horizontal and vertical stresses will reduce.

In addition, Figures 2-3 (c) and (d) show that a reversal of the shear stresses, commonly referred to as principal stress rotation (Austin, 2009), occur as the load moves over the element.

2.3 Review of Unbound Granular Material Behaviour

Unbound granular materials form the backbone of flexible pavement structures and provide load spreading through the base and subbase layer. Failure within an unbound granular layer is entirely associated to shear and a materials resistance of

shear is a function of the aggregate skeleton i.e. friction caused by aggregate interlocking. With the emphasis on pavement structure performance, the need for better understanding the performance properties of the materials used within these structures become essential. Therefore, this section will review the mechanical behaviour of UGM's and their response to traffic loading in order to gain an understanding of the performance properties. Furthermore, this section will also present discussions on the factors influencing the behaviour of UGM's and the laboratory characterisation techniques of UGM's.

2.3.1 Mechanical Behaviour

The use of materials within pavement layers requires prior knowledge (being empirical or fundamental) of the behaviour of these materials. A true understanding of material behaviour can be determined from fundamental information generated by pure research at research institutes (Thom et.al, 2005). A discussion of the equipment used within this thesis, to obtain fundamental information and to gain an understanding of the behaviour of the tested materials, follows in Subsection 2.3.3.

In this thesis, the phrase “mechanical behaviour” refers to the failure behaviour (shear strength), resilient deformation behaviour (Resilient Modulus and Poisson's ratio) and permanent deformation behaviour. Although this thesis will not focus on permanent deformation, it is important to note that the permanent deformation of UGM's forms part of failure mechanism.

Mechanical behaviour of UGM's under traffic loading has been one of the focus areas of research within pavement engineering. Research has shown that UGM's placed under loads exceeding the materials load bearing capacity will undergo shear failure. Figure 2-4 (a) shows the results from a typical monotonic failure test, on UGM, through a typical stress-strain relationship. Note that an increase in strain is associated with an increase in stress only up to the point of failure. After failure, no further stress is required for an increase in strain.

Furthermore, Figure 2-4 (b) shows that, for a single cycle of repeated loading (simulation of traffic) well below that of the failure stress, UGM's will undergo deformation. Each cycle of loading will result in permanent (irrecoverable) and resilient (recoverable) strain.

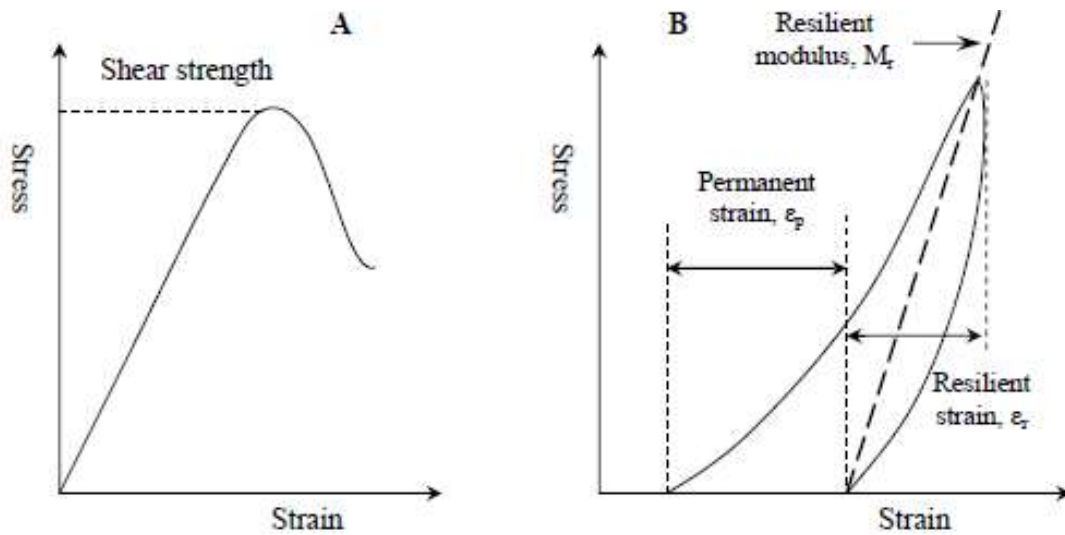


Figure 2- 4: (a) Monotonic Loading to Failure (b) Strain in UGM's caused by a Single Load Cycle (Araya, 2011)

Figure 2-4 a) and b) both show strain in the direction parallel to the applied stress. The reality in a pavement however is more complex, with stress distributed in three dimensions (Jenkins, 2010). In order to understand three dimensional stress strain distributions, the Poisson's Ratio ν of the material under loading is required. Material Poisson's Ratios are calculated as the ratio of the strain perpendicular to the applied stress (transverse strain ϵ_t) in relation to the strain parallel to the applied stress (axial strain ϵ_a). Figure 2-5 and Equations 2-1, 2-2 and 2-3 illustrates the calculation of Poisson's Ratio for a cylindrical specimen.

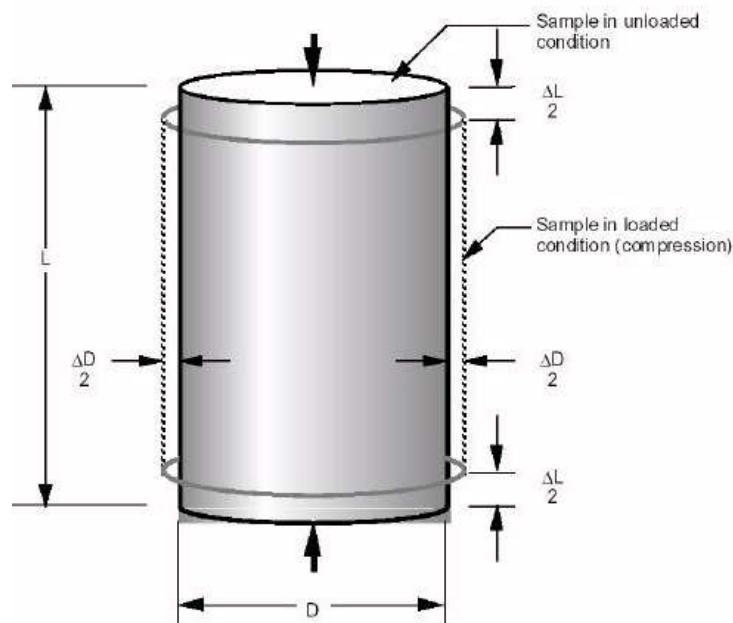


Figure 2- 5: Illustration of Poisson's Ratio in three Dimensions (PavementInteractive, 2007)

$$\nu = \frac{\epsilon_D}{\epsilon_L} \quad 2-1$$

$$\epsilon_D = \frac{\Delta D}{D} \quad 2-2$$

$$\epsilon_L = \frac{\Delta L}{L} \quad 2-3$$

Where:

- ν = Poisson's Ratio [-]
- ϵ_D = transverse strain [-]
- ϵ_L = axial strain [-]
- ΔD = change in diameter [mm]
- D = initial diameter [mm]
- ΔL = change in length [mm]
- L = initial length [mm]

It should be noted that although the theory of elastic behaviour does not allow for an increase in volume, some researchers e.g., Sweere (1990) and van Niekerk (2002) have found that UGM's sometimes exhibit Poisson's Ratios greater than 0.5. The material thus exhibits resilient dilatation, i.e. a volume increase when subjected to shear loads. Larger shear loads result in larger Poisson's Ratios.

2.3.1.1 Shear Strength Behaviour

The SAMDM (South African Mechanistic Design Manual) is one of few mechanistic-empirical (M-E) pavement design manuals that incorporate a methodology for evaluating the bearing capacity of coarse unbound granular materials (Araya, 2011). Under repeated loading, UGM's exhibits deformation due to densification and gradual shear, therefore, understanding the deformation behaviour caused by shear stresses, in order to improve the M-E design method, has been the focus of many research projects.

Several researchers have related the permanent deformation of UGM's to the shear stresses within the material (Maree, 1979, Huurman and van Niekerk, 1995 and 1998, Huurman, 1997, Theyse, 1998 and 2000 and van Niekerk et al. 2000). Maree (1979), in his research of UGM's, developed the concept of a "Safety Factor" (SF) against shear failure which is represented by Equation 2-4 as the ratio between the material shear strength τ_f and the applied shear stress τ_a or equally, by the ratio between the material deviator stress at failure σ_d^f and the applied deviator stress σ_a .

$$\begin{aligned}
 SF &= \frac{\tau_f}{\tau_a} \text{ or } \frac{\sigma_d^f}{\sigma_d^a} \\
 &= \frac{\sigma_1^f - \sigma_3}{\sigma_1^a - \sigma_3} \\
 &= \frac{\sigma_3 \left(K \tan^2 \left(45^\circ + \frac{\phi}{2} \right) - 1 \right) + 2K C \tan \left(45^\circ + \frac{\phi}{2} \right)}{\sigma_1^a - \sigma_3}
 \end{aligned}
 \tag{2-4}$$

Where:

- τ_f = failure shear stress [kPa]
- τ_a = applied shear stress [kPa]
- σ_d^f = deviator stress at failure [kPa]
- σ_d^a = applied deviator stress [kPa]
- σ_1^f = major principal failure stress [kPa]
- σ_1^a = applied major principal stress [kPa]
- σ_3 = minor principal stress (confining pressure of tri-axial test) [kPa]
- ϕ = Friction Angle [°]
- C = Cohesion [kPa]
- K = constant relating to the level of saturation

The constant K depends on the level of saturation. Maree (1979) suggested values for highly (0.6), and normal to dry (0.95) saturation levels however, these constants were subsequently refined by Theyse, et.al. (1996) for saturated (0.65), moderate moisture (0.8) and normal moisture (0.95) conditions

Safety factors are typically calculated in the middle of the granular layer, and at locations along, and between the wheel paths (Jooste, 2004). Safety factors smaller than 1 imply that the applied shear stress exceeds that of the material bearing strength and that rapid deformation will occur for static loads. However, under real life dynamic loading, a shear stress greater, if ever, than the shear strength, will only last for a very short duration. As a result, shear failure will not occur during one load application but rather deformation will accumulate rapidly under repeated loading. On the other hand, however, for safety factors exceeding one, the accumulation of deformation will gradually occur under repeated loading. Note that the failure mechanism however, will be the deformation of the UGM and that the rate of failure is a function of the enormity of the safety factor.

Within the equation developed by Maree (1979), two parameters exist that define a

materials shear strength properties, the Friction Angle ϕ and the Cohesion C . Both these parameters can be determined from a Mohr-Coulomb representation of monotonic tri-axial tests as illustrated by Figure 2-6.

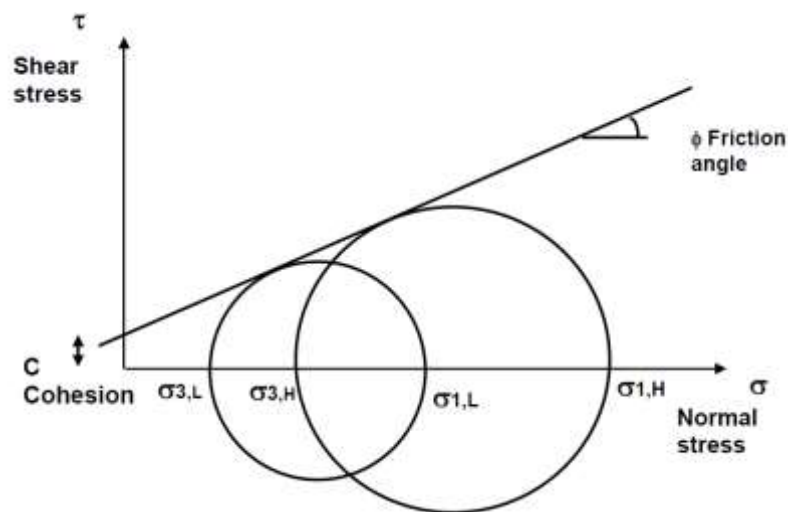


Figure 2- 6: Mohr-Coulomb Representation of Monotonic Tri-axial Test (Jenkins, 2010)

According to the Mohr-Coulomb representation shown, the failure stress σ_1 in Figure 2-6 is a function of the confining stress applied during a monotonic tri-axial test, therefore, at least two tri-axial tests are required to formulate a failure envelope (a tangent line to the Mohr-Coulomb circles).

Showing the results from two monotonic tri-axial tests through a Mohr-Coulomb representation thereof and adding the line tangent to the circles results in an estimation of the materials failure envelope. By assuming a linear failure envelope, the Friction Angle ϕ [in degrees] and the Cohesion C [in kPa] can be determined. Note that the Friction Angle is determined from the slope of the tangent line whereas the intercept of the envelope and the y-axis gives the Cohesion.

In addition, Huurman and van Niekerk (1995), similar to the Safety Factor principal developed by Maree (1979), relates the ratio between the applied major stress σ_1^a and the failure stress σ_1^f to the permanent deformation behaviour of UGM's. Theyse however, through his research of UGM's (Theyse, 1996, 2000), furthered Maree's work and used the inverse of Maree's Safety Factor, called the "Stress Ratio", as the critical parameter controlling the permanent deformation of UGM's.

It should be noted that all of the methods motioned above (Maree, 1979, Huurman and van Niekerk, 1995, and Theyse, 2000), for relating permanent deformation to

shear behaviour, relies on the failure strength σ_1^f to be known. Equation 2-5 provides the formulations of the ratio used by Huurman and van Niekerk (1995) whereas Equation 2-6 provides the formulation of the Stress Ratio (inverse of Maree's Safety Factor). Both equations are first represented in terms of the failure strength σ_1^f and secondly in terms of the shear parameters C and ϕ .

$$\begin{aligned}
 SR &= \frac{\sigma_1^a}{\sigma_1^f} \\
 &= \frac{\sigma_1^a}{\sigma_3 \left(\tan^2 \left(45^\circ + \frac{\phi}{2} \right) \right) + 2C \tan \left(45^\circ + \frac{\phi}{2} \right)}
 \end{aligned} \tag{2-5}$$

$$\begin{aligned}
 SR &= \frac{\sigma_1^a - \sigma_3}{\sigma_1^f - \sigma_3} \\
 &= \frac{\sigma_1^a - \sigma_3}{\sigma_3 \left(\tan^2 \left(45^\circ + \frac{\phi}{2} \right) - 1 \right) + 2C \tan \left(45^\circ + \frac{\phi}{2} \right)}
 \end{aligned} \tag{2-6}$$

Where:

- ϕ = Friction Angle [$^\circ$]
- C = Cohesion [kPa]
- σ_1^f = failure strength [kPa]
- σ_1^a = applied major principal stress [kPa]
- σ_3 = minor principal stress (confining pressure of tri-axial test) [kPa]

Theyse (2007) states that the advantage of using the Stress Ratio is that it normalise the stresses, for equal Stress Ratios, at various applied stress as. Figure 2-7 gives a schematic representation of the normalised stresses. Note that the representation of the Mohr-Coulomb circles shown in Figure 2-7, show that an equal Stress Ratio can be achieved for different applied stresses. Furthermore, rather than to show the behaviour under a single stress state, the Stress Ratio allows comparison between material behaviour under various stress states with equal Stress Ratios.

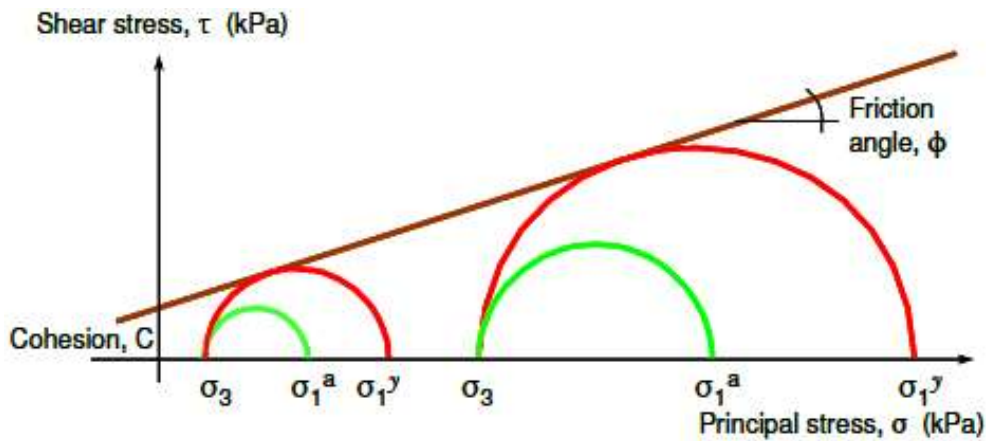


Figure 2- 7: Mohr-Coulomb representation of two cases with Equal Stress Ratios (Theyse, 2007)

It should be noted that all of the above focuses on the failure mechanism of UGM's however, as mentioned in Section 2.2, the purpose of UGM layers are to spread the load incused by traffic throughout the pavement structure. The load spreading ability of granular layers is a function of layer stiffness (Jenkins, 2010) therefore the stiffness of UGM's need to be considered.

2.3.1.2 Resilient Deformation Behaviour

Traditionally, the theory of elasticity defines the elastic properties (Elastic Modulus E and Poisson's Ratio ν) of a material. The stiffness or Elastic Modulus of a material can be characterised by Hooke's Law. This law states that a simple stress strain relation exists, for linear elastic behaviour. In addition, the slope of the relationship reflects the stiffness or Elastic Modulus (also known as Young's Modulus). Figure 2-8 presents a schematic representation of Hooke's law.

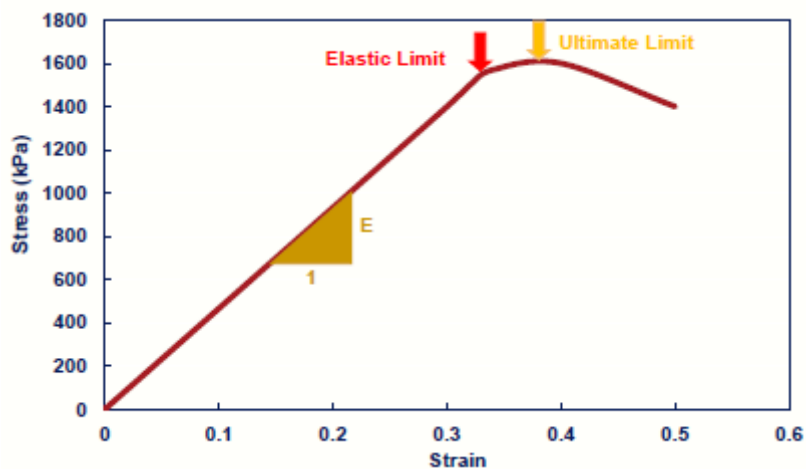


Figure 2- 8: Stiffness or Elastic Modulus as a Function of Stress and Strain (SAPEM, 2013)

By definition, linear elastic behaviour implies that the stress strain relation be linear. Dealing with UGM's however, due to the stress-dependent elastic (recoverable) nature of the material under repeated loading, the Elastic Modulus is replaced by the Resilient Modulus M_r . In addition, the deformation behaviour of UGM's is non-linear elastic, rather, UGM's show elasto-plastic behaviour.

As mentioned in the introduction of Section 2.3.1, researchers have characterised the deformation behaviour, of UGM's, subjected to repeated loading, by an elastic or recoverable (resilient) and non-recoverable (permanent) deformation. Both the resilient and permanent deformation however, is not constant. Figure 2-9 illustrates that, as repeated loading takes place, both the increments of permanent and resilient deformation reduce.

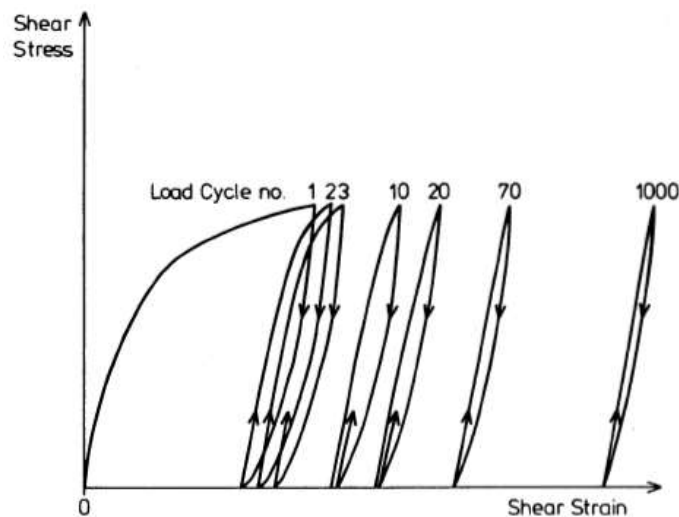


Figure 2- 9: Unbound Granular Material Behaviour under Repeated Loading (Thom, 1988)

The stress strain relation defines the Resilient Modulus of UGM's, similar to the Elastic Modulus, however, within Equation 2-7, the stress used is the cyclic axial deviator stress σ_d and the strain is the recoverable (resilient) strain ϵ_r . Note that Subsection 2.3.1 gives an explanation on the principal of recoverable strain ϵ_r .

$$M_r = \frac{\sigma_d}{\epsilon_r} \quad 2-7$$

Where:

- M_r = Resilient Modulus [MPa]
- σ_d = applied deviator stress ($\sigma_1 - \sigma_3$) [kPa]
- ϵ_r = recoverable or resilient strain [-]

The cyclic axial deviator stress σ_d within Equation 2-7 defines the difference between

the applied major principal stress σ_1 and the sum of the applied minor principal stress σ_3 and the seating stress σ_p , as illustrated by Figure 2-10.

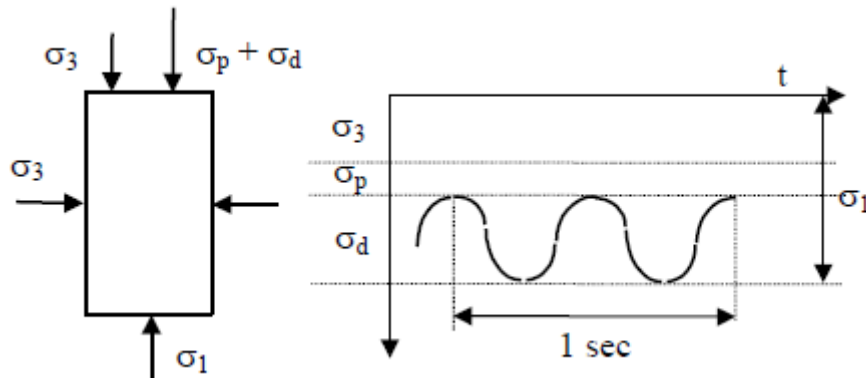


Figure 2- 10: Schematic Illustration of the Cyclic Axial Deviator Stress Principal (Jenkins, 2000)

Figures 2-4 b), 2-9 and 2-10 show that the deformation behaviour of UGM's is far from linear. Sophisticated testing apparatus, capable of applying cyclic loads, is therefore required to test for the Resilient Modulus. For many years has the tri-axial apparatus, capable of applying constant or cyclic stresses in the principal directions, been used to test the Resilient Modulus of UGM's. Paragraph 2.3.3.3 presents a review on the tri-axial test apparatus.

Through the findings of an extensive literature review on the structural response on UGM's, Lekarp et al. (2000) presented a "State of the Art" on the resilient and permanent deformation of these materials. The review showed that several factors influenced the resilient response, each with varying degrees of importance. In this review however, Subsection 2.3.2 presents a discussion on the influence of some of these factors with the emphasis placed on the influence of maximum aggregate size and sample geometry.

In the past, and currently, many research projects aim to develop models that accurately describe and predict the resilient behaviour of UGM's. These models however are, formulated under unique conditions therefore, an understanding of the models formulation and shortcomings are required. In this study three of the many available models for predicting Resilient Modulus and two for predicting Poisson's Ratio, are discussed. Note that although more models, for both Resilient Modulus and Poisson's Ratio exist, the primary focus of this thesis is not model related. Some models are therefore only reviewed to give the reader background information on the formulation and shortcomings of some existing models and the models used within

this thesis.

M_r - Θ Model

The M_r - Θ model, due to its simplicity, is one of the most widely used models for predicting the Resilient Modulus of non-linear elastic materials. The model, first described by Seed et al. (1962, cited Uthus, 2007) is a non-linear, stress dependent power function. Sweere (1990) however states that Brown and Pell (1967), through pulse load tests on an instrumented pavement built in a test pit, obtained stiffness values for UGM's. By plotting the obtained values on a double-logarithmic scale, in relation to the applied Bulk Stress Θ (sum of the principal stresses), a straight-line relationship was found. This method of representing the stiffness-stress relation of UGM's has now become a standard used within pavement engineering. Figure 2-11 shows a schematic representation of the M_r - Θ model, Equation 2-8.

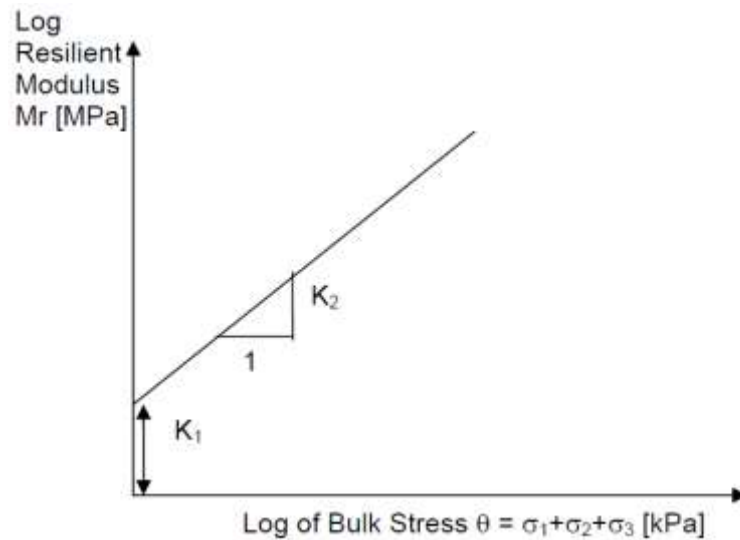


Figure 2- 11: M_r - Θ Model of Resilient Modulus (Jenkins, 2010)

$$M_r = k_1 \left(\frac{\theta}{\sigma_0} \right)^{k_2} \quad 2-8$$

Where:

- M_r = Resilient Modulus [MPa]
- Θ = Bulk Stress ($\sigma_1 + \sigma_2 + \sigma_3$) [kPa]
- σ_0 = reference stress (1) [kPa]
- k_1 = material regression coefficient [MPa]
- k_2 = material regression coefficient [-]

It is important to note that many researchers use a similar M_r - Θ model (Equation 2-9) which, mathematically, is incorrect.

$$M_r = k_1 \theta^{k_2}$$

2-9

Where: M_r = Resilient Modulus [MPa]
 θ = Bulk Stress ($\sigma_1 + \sigma_2 + \sigma_3$) [kPa]
 k_1, k_2 = material regression coefficients [-]

The dimensions of Equation 2-9 cannot be matches.

Although the M_r - θ model fairly accurately fits the tested data, it is not without drawbacks. Literature (Uzan, 1985, van Niekerk, 2002, Jenkins, 2002, Uthas, 2007 and Araya, 2011), states that the M_r - θ model does not account for the individual influence that the confining stress σ_3 and the applied deviator stress σ_d have on the Resilient Modulus. As a result, all combinations of principal stresses, resulting in equal Bulk Stress, will yield equal Resilient Modulus values.

In addition, van Niekerk (2002) showed that the M_r - θ model does not account for the reduction in stiffness as the applied stress approaches the failure stress. The M_r - θ model is less accurate ($r^2 = 0.945$ versus $r^2 = 0.992$) under “severe” stress regimes when compared to “mild” stress regimes. Figure 2-13 illustrates, that for different confining stresses, the Resilient Modulus reduces as high deviator stresses (“severe” regime) are applied. Note that the M_r - θ model does not account for the influence of “severe” stresses therefore resulting in a lower r^2 value compared to the “mild” regime (Figure 2-12).

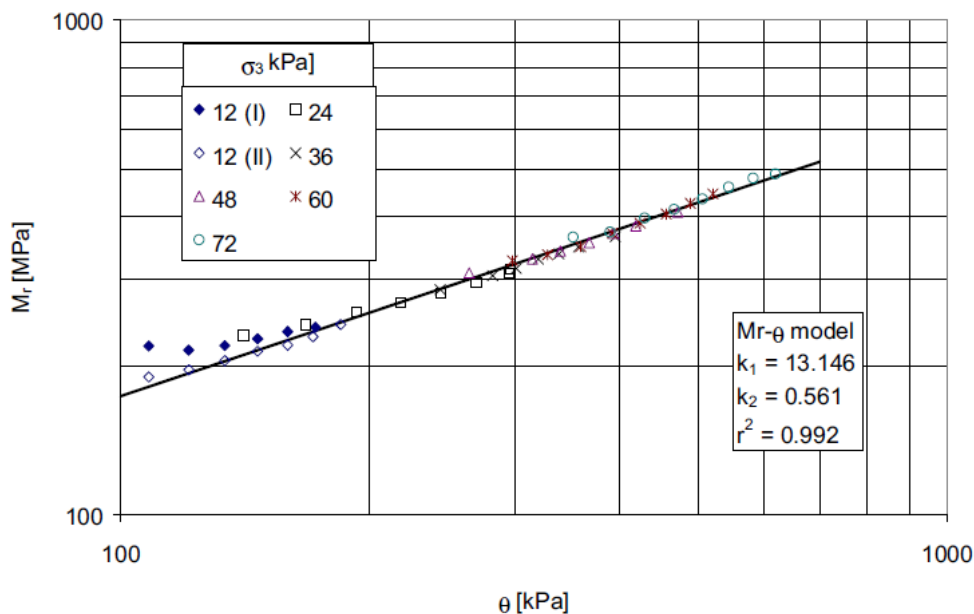


Figure 2- 12: Representation of M_r - θ Model Data in Relation to “mild” Regime Tested Data (van Niekerk, 2002)

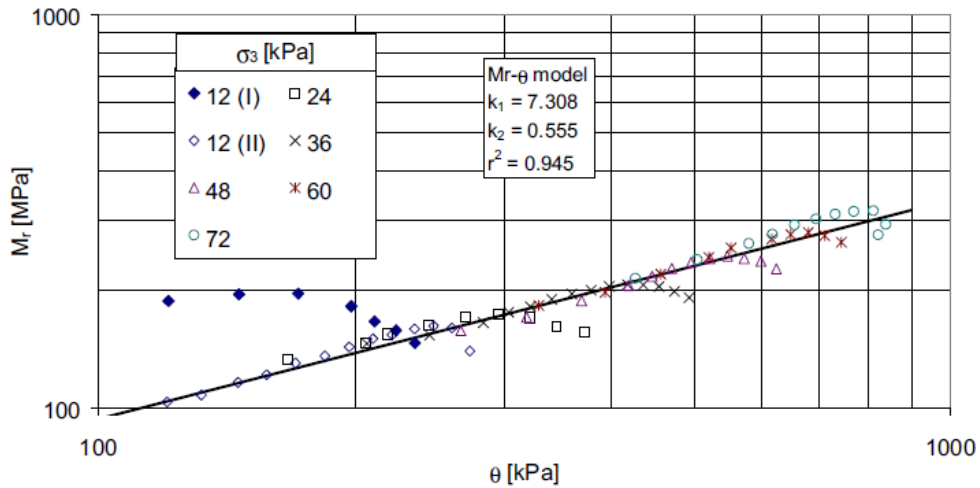


Figure 2- 13: Representation of M_r - Θ Model Data in Relation to “severe” Regime Tested Data (van Niekerk, 2002)

Although not accurate, many researchers often use the M_r - Θ model with a constant Poisson’s Ratio to calculate the transverse strain of a specimen (van Niekerk, 2002 and Araya, 2011). As mentioned the resilient response of UGM’s is stress dependent; therefore, Poisson’s Ratio does not stay constant but rather varies in relation to the applied stress.

Uzan Model

Uzan (1985), in an attempt to account for the shortcomings of the M_r - Θ model, developed a new non-linear model, based on the M_r - Θ model but incorporated the effect of deviator stress.

Uzan (1985) through Equation 2-10 below first presented the model.

$$M_r = k_3 \left(\frac{\theta}{\sigma_0} \right)^{k_4} \left(\frac{\sigma_d}{\sigma_0} \right)^{k_5} \quad 2-10$$

Where:

- M_r = Resilient Modulus [MPa]
- Θ = Bulk Stress ($\sigma_1 + \sigma_2 + \sigma_3$) [kPa]
- σ_d = deviator stress [kPa]
- σ_0 = reference stress (1) [kPa]
- k_3 = material regression coefficient [MPa]
- k_4, k_5 = material regression coefficients [-]

The model has also been further developed by Witczak and Uzan (1988, cited Araya, 2011) for the three-dimensional case where the deviator stress σ_d is replaced with

the octahedral shear stress, as illustrated by Equation 2-11.

$$M_r = k_6 \left(\frac{\theta}{\sigma_0} \right)^{k_7} \left(\frac{\tau_{oct}}{\sigma_0} \right)^{k_8} \quad 2-11$$

Where: M_r = Resilient Modulus [MPa]
 Θ = Bulk Stress ($\sigma_1 + \sigma_2 + \sigma_3$) [kPa]
 τ_{oct} = octahedral shear stress [kPa]
 σ_0 = reference stress (1) [kPa]
 k_6 = material regression coefficient [MPa]
 k_7, k_8 = material regression coefficients [-]

TU-Delft Model

During their research of unbound road building materials, van Niekerk and Huurman (1995) and Huurman (1997), derived a model based on the M_r - Θ model. This model accounted for the influence of confinement and deviator stress separately, as illustrated by Equation 2-12.

$$M_r = k_9 \left(\frac{\sigma_3}{\sigma_0} \right)^{k_{10}} \left(1 - k_{11} \left(\frac{\sigma_1}{\sigma_1^f} \right)^{k_{12}} \right) \quad 2-12$$

Where: M_r = Resilient Modulus [MPa]
 σ_3 = minor principal stress [kPa]
 σ_1 = major principal stress [kPa]
 σ_1^f = major principal stress at failure [kPa]
 σ_0 = reference stress (1) [kPa]
 k_9 = material regression coefficient [MPa]
 k_{10}, k_{11}, k_{12} = material regression coefficients [-]

It should be noted that the first absolute term, $k_9 \left(\frac{\sigma_3}{\sigma_0} \right)^{k_{10}}$, in this model describes the increase of the Resilient Modulus associated with increasing the confining stress σ_3 . The second term, $1 - k_{11} \left(\frac{\sigma_1}{\sigma_1^f} \right)^{k_{12}}$, describes the decrease in the Resilient Modulus as the major principal stress (σ_1) approach the principal failure stress σ_1^f .

Although this model accurately describes the resilient behaviour of granular materials, at “severe” stress levels, it also is not without limitations. The model cannot describe an increment of the Resilient Modulus for granular materials characterised

with an increasing deviator stress, far from failure (Araya, 2011). Therefore, additional models have been developed based on the TU Delft Model. Equation 2-13 shows that, in addition to the TU Delft Model, the $M_r-\Theta-\frac{\sigma_1}{\sigma_1^f}$ Model expresses the Resilient Modulus as a function of the Bulk Stress on a granular material. In addition to the $M_r-\Theta-\frac{\sigma_1}{\sigma_1^f}$ Model, Equation 2-14, $M_r-\Theta-\frac{\sigma_d}{\sigma_d^f}$ Model, first used by Jenkins (2000) in his research of Bitumen Stabilised Materials (BSM's), incorporates the Deviator Stress Ratio $\frac{\sigma_d}{\sigma_d^f}$ rather than $\frac{\sigma_1}{\sigma_1^f}$, to show the behaviour of the Resilient Modulus as the Stress Ratio increases.

$$M_r = k_{13} \left(\frac{\theta}{\sigma_0} \right)^{k_{14}} \left(1 - k_{15} \left(\frac{\sigma_1}{\sigma_1^f} \right)^{k_{16}} \right) \quad 2-13$$

$$M_r = k_{13} \left(\frac{\theta}{\sigma_0} \right)^{k_{14}} \left(1 - k_{15} \left(\frac{\sigma_d}{\sigma_d^f} \right)^{k_{16}} \right) \quad 2-14$$

Where:	M_r	= Resilient Modulus [MPa]
	Θ	= Bulk Stress ($\sigma_1 + \sigma_2 + \sigma_3$) [kPa]
	σ_1	= major principal stress [kPa]
	σ_1^f	= major principal stress at failure [kPa]
	σ_d	= deviator stress [kPa]
	σ_d^f	= deviator stress at failure [kPa]
	σ_0	= reference stress (1) [kPa]
	k_{13}	= material regression coefficient [MPa]
	k_{14}, k_{15}, k_{16}	= material regression coefficients [-]

To show the importance of accurate models, representations of van Niekerk's (2002) results, under "severe" stresses, are shown by Figures 2-14 and 2-15. Figure 2-14 shows that the $M_r-\Theta$ Model cannot accurately describe the behaviour of the material under "severe" stress conditions, whereas Figure 2-15, the $M_r-\Theta-\frac{\sigma_d}{\sigma_d^f}$ Model, better shows the material behaviour at "severe" conditions.

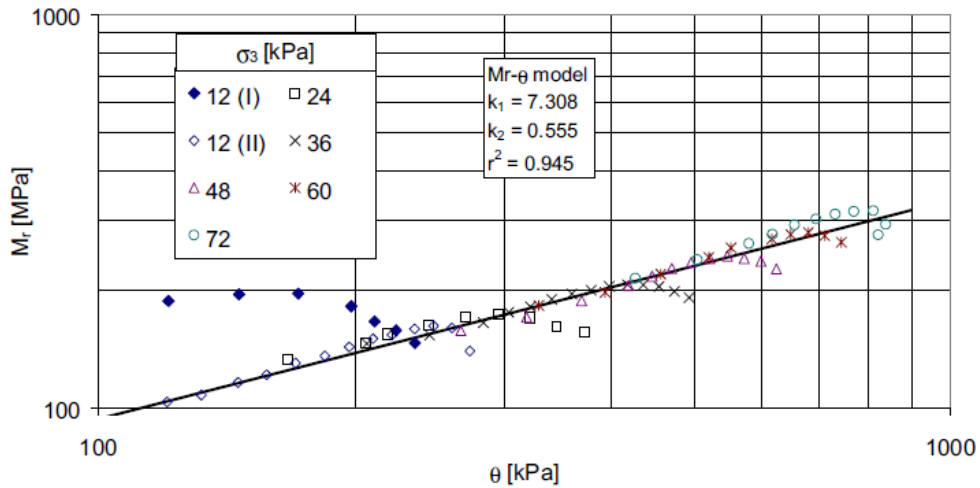


Figure 2- 14: Representation of the M_r - Θ Model's fit on Test Data (van Niekerk, 2002)

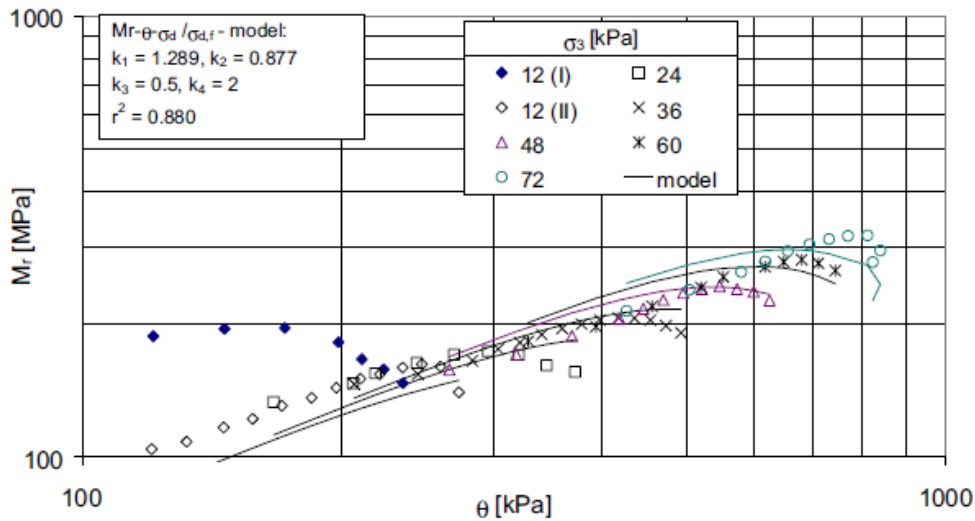


Figure 2- 15: Representation of the M_r - Θ - $\frac{\sigma_d}{\sigma_d-f}$ Model's fit on Test Data (van Niekerk, 2002)

From the figures shown it is clear that, when comparing the M_r - Θ and the M_r - Θ - $\frac{\sigma_d}{\sigma_d-f}$ models, the M_r - Θ Model more accurately (higher r^2 value) fits the test data, however, the latter better shows the material behaviour as the deviator Stress Ratio increases. It is important to note that material behaviour models should not be calibrated to yield the best possible fit rather, to best describe the material behaviour under the associated conditions.

Poisson's Ratio

As mentioned in Section 2.3, to simplify lateral strain calculations, researchers often use Poisson's Ratio ν as a constant within pavement engineering. Consequently, few

models, predicting the change in Poisson's Ratio with variation in stress condition, exist. However, Huurman, through his Doctoral dissertation (Huurman, 1997) developed a model that showed that Poisson's Ratio, similar to the resilient response of UGM's, is also influenced by the applied stress (i.e. Poisson's Ratio is stress dependent).

In a more recent study, van Niekerk (2002) shows models for the prediction of Poisson's Ratio for granular materials, which are also stress dependent. Two of the models suitable for modelling of granular materials, the $\frac{\sigma_d}{\sigma_d^f}$ Model and the $\frac{\sigma_d}{\sigma_d^f}-\sigma_3$ Model are shown by Equation 2-15 and 2-16 respectively.

$$v = n_1 \left(\frac{\sigma_d}{\sigma_d^f} \right)^{n_2} \quad 2-15$$

$$v = n_3 \left(\frac{\sigma_d}{\sigma_d^f} \right)^{n_4} \left(\frac{\sigma_3}{\sigma_0} \right)^{n_5} \quad 2-16$$

Where:

v	= Poisson's Ratio [-]
σ_d	= deviator stress [kPa]
σ_d^f	= deviator stress at failure [kPa]
σ_3	= minor principal stress [kPa]
σ_0	= reference stress (1) [kPa]
n_1 to n_5	= material regression coefficients [-]

Both models relate Poisson's Ratio to the deviator Stress Ratio $\left(\frac{\sigma_d}{\sigma_d^f}\right)$ however, van Niekerk et al. (2000) states that equally well fitting models can be obtained by relating Poisson's Ratio to the $\frac{\sigma_d}{\sigma_3}$ -ratio.

Similar to the $M_r-\Theta$ Model, the $\frac{\sigma_d}{\sigma_d^f}$ Model does not account for the individual influence of the minor principal stress σ_3 rather it only accounts for the increase in Poisson's Ratio as the shear load (higher Stress Ratio) is increased. For UGM's however, the confining stress σ_3 plays an important role in the transverse strain development. Under higher confining stress σ_3 , more friction is generated which results in a resistance to transverse rearrangement of particles, thereby decreasing the Poisson's Ratio.

In contrast to the $\frac{\sigma_d}{\sigma_f}$ Model, the $\frac{\sigma_d}{\sigma_f}\sigma_3$ Model accounts for the influence of confinement by incorporating an additional term $\left(\frac{\sigma_3}{\sigma_0}\right)^{n_5}$, as illustrated by Figure 2-16 below.

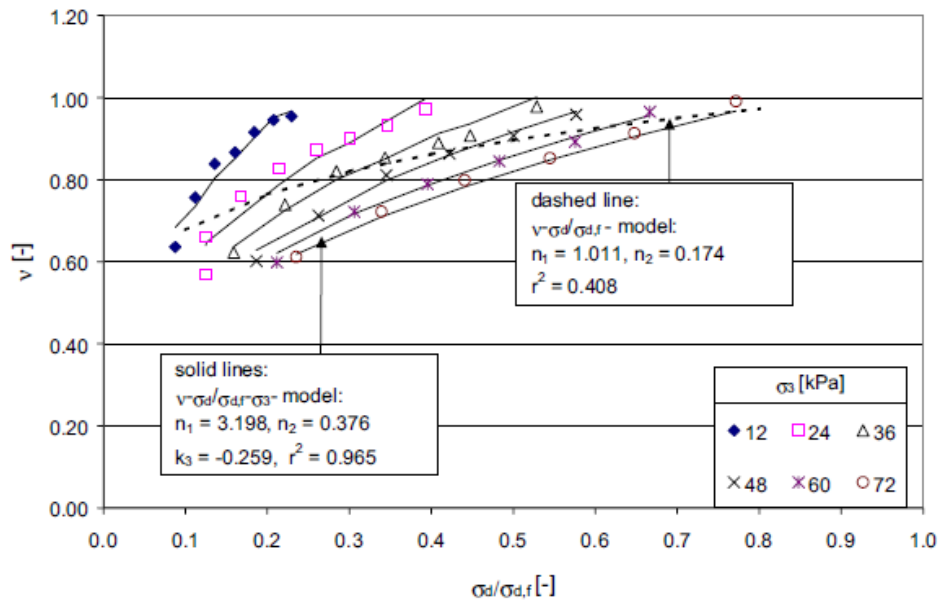


Figure 2- 16: Poisson’s Ratio in Relation to Deviator Stress Ratio for Both Models (van Niekerk, 2002)

Note that the $\frac{\sigma_d}{\sigma_f}\sigma_3$ Model better fits the test data for the various confining stresses.

2.3.2 Factors Influencing the Mechanical Behaviour of UGM’s

In their “*State of the Art*” on the resilient response of unbound aggregates Lekarp et al. (2000) states that, the resilient response of unbound aggregates is affected by several factors with varying degree of importance. Therefore, this section is dedicated to review the influence of factor such as moisture content, degree of compaction and applied stress, on the mechanical behaviour of UGM’s. The emphasis however will be on the influence of grading (particularly maximum aggregate size) and specimen geometry.

The influence of various factors on the shear strength of UGM’s, is best described by the change in shear properties C and ϕ and the effective stress of the material associated with the specific influencing factor whereas, the resilient deformation behaviour is best described by the change in Resilient Modulus and Poisson Ratio.

The effects of influencing factors are best shown graphically by charts in which shear properties, M_r - θ relations, and Poisson Ratio relations are grouped for the various

influence factors under consideration. Therefore, this method of showing the influence of factors will be used within this review.

2.3.2.1 Influence of Moisture Content

Moisture in a pavement structure has its origin from many sources; groundwater, surface water migrating through the shoulder, ditches or through cracks in the surface of the road (Uthus, 2007 and Araya, 2011). Due to excessive pore water pressure, caused by too much trapped water in combination with cyclic traffic loading, the effective stress of an unbound material within a pavement structure may reduce. Consequently the bearing capacity of the unbound base or subbase layer reduces which ultimately results in complete pavement failure. Figure 2-17 illustrates that soil suction or suction pressure contributes to the effective stress of a material.

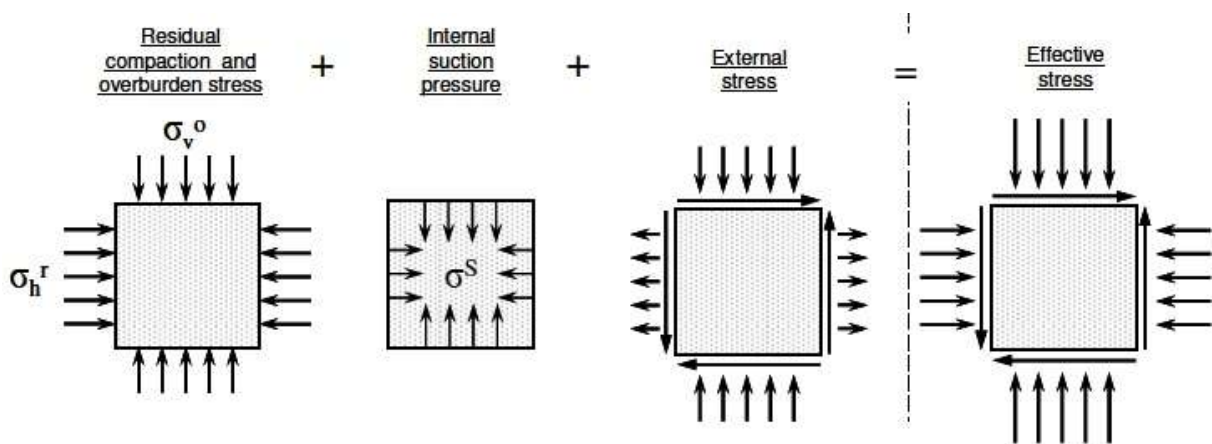


Figure 2- 17: Effective Stress in a Partially Saturated Granular Material (Theyse, 2010)

The suction in a material can be seen as a stress holding the unbound granular particles together. Note that higher suction pressures increase the materials effective stress, whereas a decrease in suction will lower the effective stress of the material. In addition, Vanapalli et al. (1996), through a soil-water characteristic curve (Figure 2-18) have shown that the suction pressure induced within a material is a function of the degree of saturation.

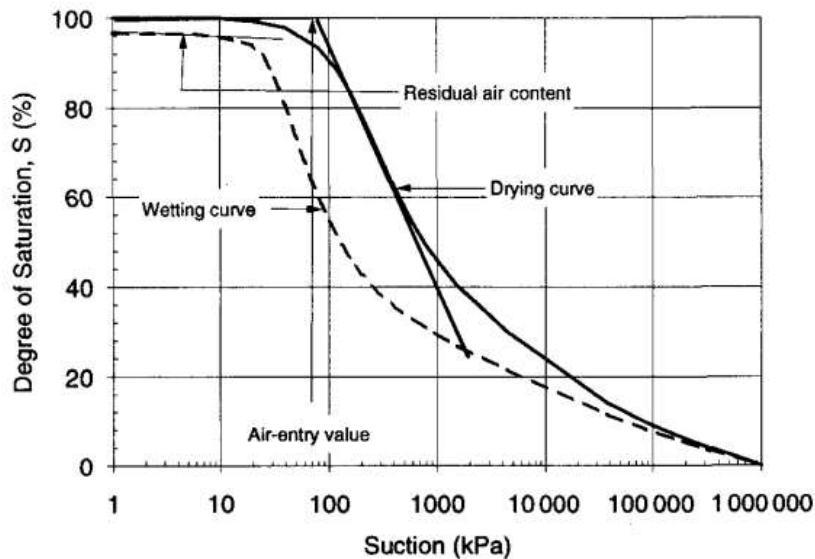


Figure 2- 18: Typical Soil-Water Characteristic Curve for the Wetting and Drying of a Material (Vanapalli et al. 1996)

The figures show that an increase in saturation (wetting curve, Figure 2-18) results in a reduction of the suction stress. The effect of reduced suction, as mentioned, is reduced effective stress (Figure 2-17) and reduced shear strength.

Werkmeister (2003) and Werkmeister et al. (2003) considered the influence of climate conditions (Spring-thaw period) on the deformation behaviour of a granular layer in two pavement structures. For both structures she found that a slight 1% change in moisture content had a significant influence on the deformation behaviour of the UGM layers.

Research by van Niekerk (2002), into mix recycled granulates, and Araya (2011), into granular materials, have shown that Cohesion C is largely influence by moisture. Araya through his study of ferricrete and weathered basalt found that an increase in moisture content (dry to moderate) generally resulted in an increase in both the materials Cohesion. However, a further increase in moisture content (moderate to wet) resulted in a significant decrease in Cohesion (lower than that of the dry moisture condition) in both materials. Figure 2-19 shows the results obtained by Araya for the weathered basalt. Note that, for equal degrees of compaction (98%) the Cohesion increases from 127 kPa to 171 kPa and then reduced to 88.5 kPa for an incremented moisture increase of 2% starting at 5%. Araya conclude that Cohesion of granular material will increase with increasing moisture content only up to the optimum moisture content (OMC). Above the OMC the Cohesion will decrease

significantly. Furthermore, since the densities of the tested material are similar, 98% DOC, the change in Cohesion cannot be attributed to the effect that moisture has on compaction, but rather to the suction stresses explained earlier.

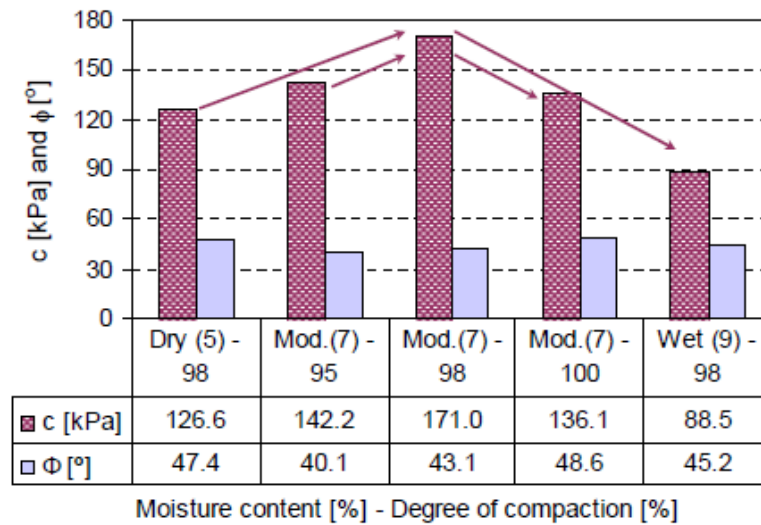


Figure 2- 19: Cohesion and Friction Angle values as a Function of Moisture Content and Degree of Compaction, for a Weathered Basalt Material (Araya, 2011)

Van Niekerk (2002) tested the failure strength in relation to moisture content of mix recycled granulate material, on specimens previously used for Resilient Modulus testing, using a multi stage (MST) failure test. The MST allows for one 300mm Φ * 600mm H specimen to be tested at three confining pressures. This allows the shear performance to be evaluated by means of one specimen instead of three. The results showed an increase in Cohesion with increased moisture content as shown in Figure 2-20.

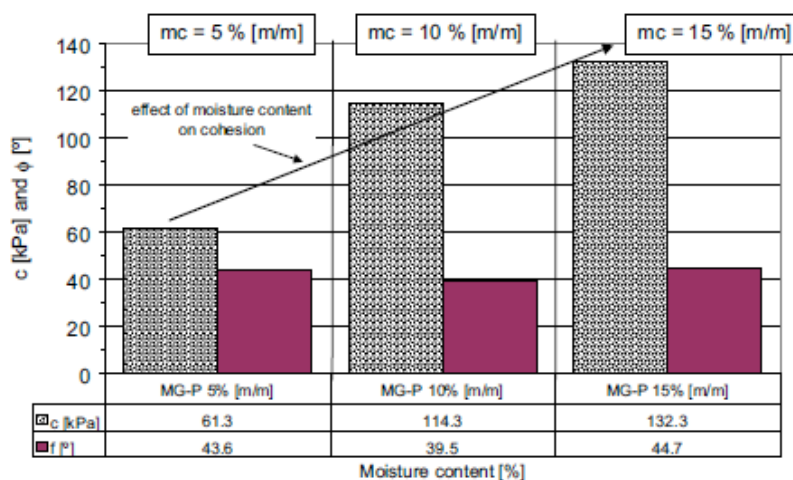


Figure 2- 20: Cohesion and Friction Angle values as a Function of Moisture Content, for a Mix Recycled Granulate Material (van Niekerk, 2002)

Note that, other than Araya's results which showed a decrease in Cohesion at moisture contents greater than the OMC, van Niekerk's results shows a consistent increase. However, as mentioned, the samples used in the failure tests have also been used for Resilient Modulus testing. Furthermore the method of applying confinement to the 300mm Φ * 600mm H tri-axial testing apparatus used is based on a vacuum. As a result, moisture is extracted from the specimen during Resilient Modulus testing resulting in reduced moisture contents when the failure test commences. The moisture contents shown in Figure 2-20, 5%, 10% and 15% are merely the target moisture contents during the sample preparation phase. The true moisture contents however, of the specimens during failure testing can only be calculated once the tests are complete. Moisture content calculation, after Resilient Modulus and MST testing, showed, in fact, that the true moisture contents were 5.2%, 10.5% and 11.0% respectively. It can thus be argued that a true moisture content of around 15%, or anything above OMC, could result in less Cohesion.

In terms of the influence of moisture content on Friction Angle, both Figures 2-19 and 2-20 show no significant change in the Friction Angle. Araya however did notice a small decrease in Friction Angle, for the ferricrete material, with an increase in moisture content.

In their "*State of the Art*", on the resilient deformation behaviour of unbound aggregates, Lekarp et al (2000) states that it is generally agreed that the resilient response of dry to most partially saturated granular materials is similar, but as complete saturation is approached, the behaviour may be affected significantly. From their extensive literature review, Lekarp et al. concluded that an increase in moisture content, particularly at high degrees of saturation, has been shown to result in a marked reduction of the Resilient Modulus as well as Poisson's Ratio.

Sweere (1990), through his study of the influence of moisture on the response behaviour of granular base course materials, also found that moisture has a significant influence on the resilient behaviour of granular materials. Sweere showed, for laterites, that the degree of moisture dependent resilient behaviour was influenced by the amount of fines within the laterites. Laterites with a grading close to the Fuller Curve were shown to be far less moisture dependent than that of laterites containing excess fines. In addition, Sweere also found, when comparing fine and coarse graded porphyry material, that the Resilient Modulus of the fine graded material was

more influenced by moisture than that of its coarse graded counterpart, as shown by Figure 2-21 below.

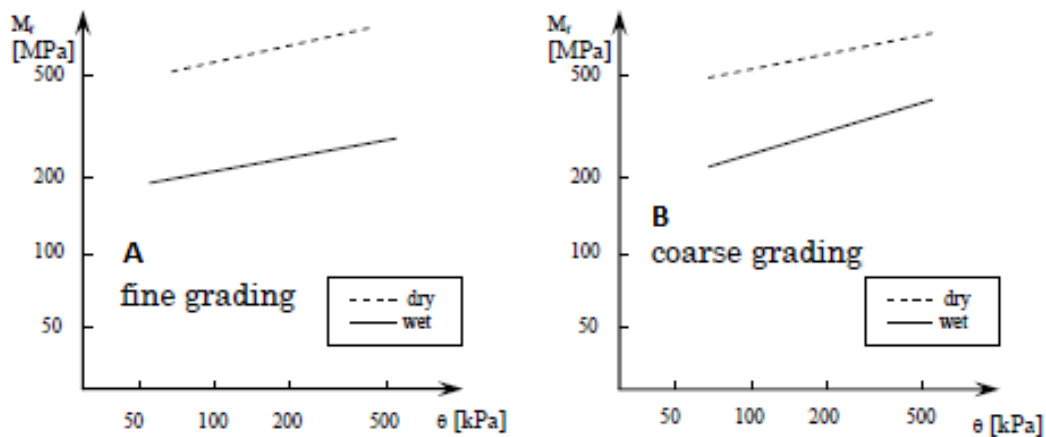


Figure 2- 21: M_r - θ relation for Porphyry Material, for Fine Grading (a) and Coarse Grading (b) for both Wet and Dry Specimen Conditions (Sweere, 1990)

Note that the dry and wet material conditions shown in Figure 2-21 represent the saturation levels of 150 mm diameter tri-axial specimens. The specimens were compacted at optimum moisture content and tested for resilient properties under wet conditions. Once the wet condition tests were completed, specimens were dried, by flushing air through them for 1 week, and tested again under the dry condition. For the fine graded material shown in Figure 2-21 (a) a degree of saturation of 13% and 42% represent the dry and wet material condition respectively, whereas, for the coarse graded material shown by Figure 2-21 (b) a degree of saturation of 7% and 18% represent the dry and wet material condition respectively.

Sweere (1990) concluded that, although moisture content does influence the performance of unbound materials, the influence is significantly related to the fines content.

2.3.2.2 Influence of Compaction or Density

Compaction, of unbound material, is defined as the mechanical alteration of material particles in order to reduce the volume obtained by the mass of material, i.e. increasing the mass to volume ratio or better known as the density (Chilukwa, 2013).

It has been known, for many years, that density has a significant influence on the performance of granular materials (Lekarp et al., 2000).

Thom (1988) studied the influence of density on the mechanical behaviour of crushed

dolomitic limestone. Three different magnitudes of compaction, uncompacted, light compaction, and heavy compaction, for several grading curves, were tested in a 75 mm diameter tri-axial testing apparatus. Light compaction consisted of 150 light blows whereas heavy compaction consisted of 150 heavy blows per layer, both over five layers per sample. It should be noted that compaction was manual, giving rise to the possibility of inconsistency in applied effort. Furthermore, due to apparatus size, a maximum particle size of 10 mm was used for all specimens. In addition, the proportions on particle smaller than 75 microns were kept constant for all the gradings. Thom showed that an increase in density had no significant influence on the resilient behaviour, but concluded that density was a dominant factor in reducing permanent deformation and increasing shear strength. The dominant influence of compaction was shown by plotting the principal Stress Ratio at failure $\frac{\sigma_v}{\sigma_h}$, an indicator of the shear strength, for the three different levels of compaction in relation to the various grading parameters n as shown in Figure 2-22. Note that the principal Stress Ratios for the heavy compaction, for all grading curves, are greater than that of the lightly compacted material.

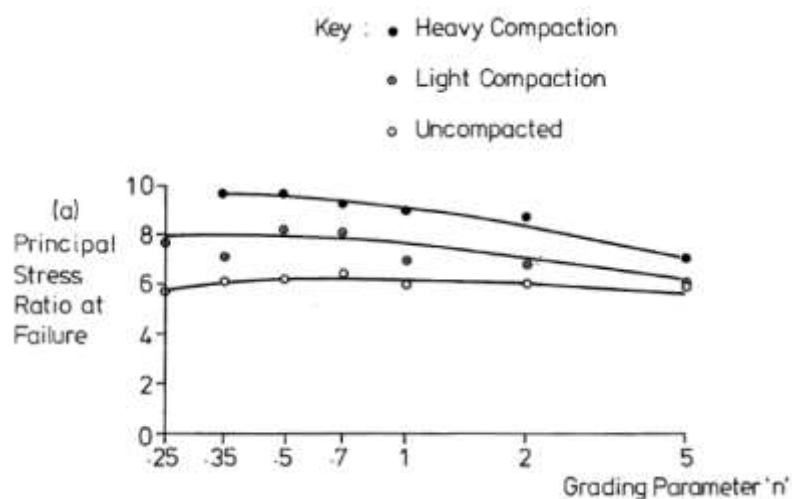


Figure 2- 22: Influence of Compaction and Grading Parameter on the Principal Stress Ratio at Failure (Thom, 1988)

Van Niekerk (2002) and Araya (2011) also investigated the influence of degree of compaction (DOC) on the performance of recycled mix granulates and granular materials respectively. Both van Niekerk and Araya expressed DOC as a percent of maximum standard Proctor dry density and found that an increase in DOC resulted in a gain in Cohesion for all the materials tested. Van Niekerk, through MST testing on samples produced from the three grading limits of mix recycled granulate materials,

cured for 28 days and used for Resilient Modulus testing, noted an increase in Cohesion of 67%, 51% and 126% for the upper, average and lower grading limit respectively. This increase in Cohesion was caused by an increase in the DOC from 97% to 105%. In addition, van Niekerk also tested the mechanical behaviour of six sands and again found that an increase in DOC resulted in increased Cohesion, as illustrated by Figure 2-23.

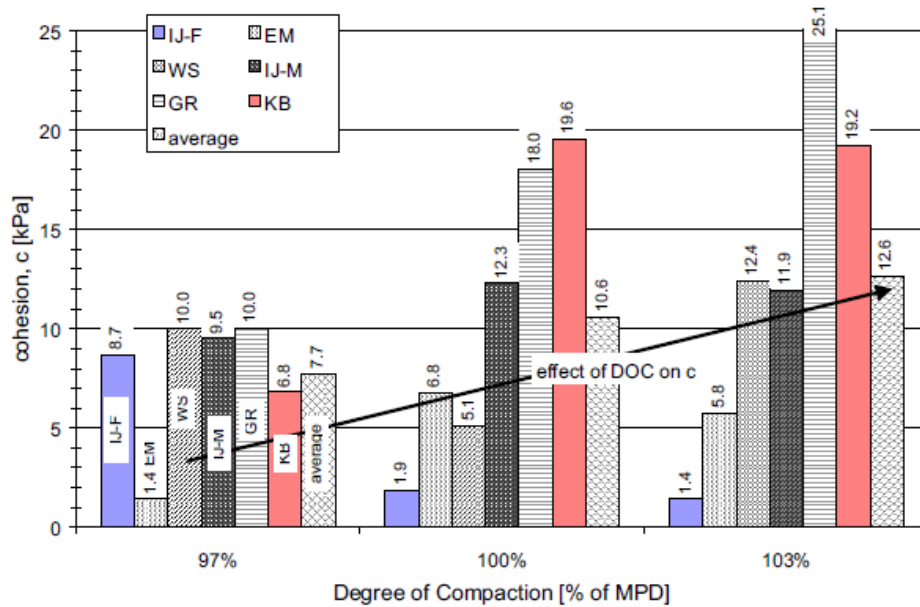


Figure 2- 23: Cohesion in Relation to DOC for Six Research Sands (van Niekerk, 2002)

In terms of Friction Angle, neither van Niekerk nor Araya could find a consistent trend in the change of Friction Angle when related to an increased DOC for their material. Araya found that an increase in DOC from 95% to 100% resulted in an increase of Friction Angle for weathered basalt at 7% moisture content. For ferricrete however, at 7.5% moisture content, a slight decrease was noted whereas tests on South African G1 material showed comparative results to that of the weathered basalt. An increase in DOC from 98% to 105% resulted in an increase in Friction Angle from 52° to 60°.

Tests by van Niekerk on untreated sands however showed a clear trend in the relation between Friction Angle and DOC. Figure 2-24 shows that higher DOC's results in higher Friction Angles obtained for all of the six tested sands.

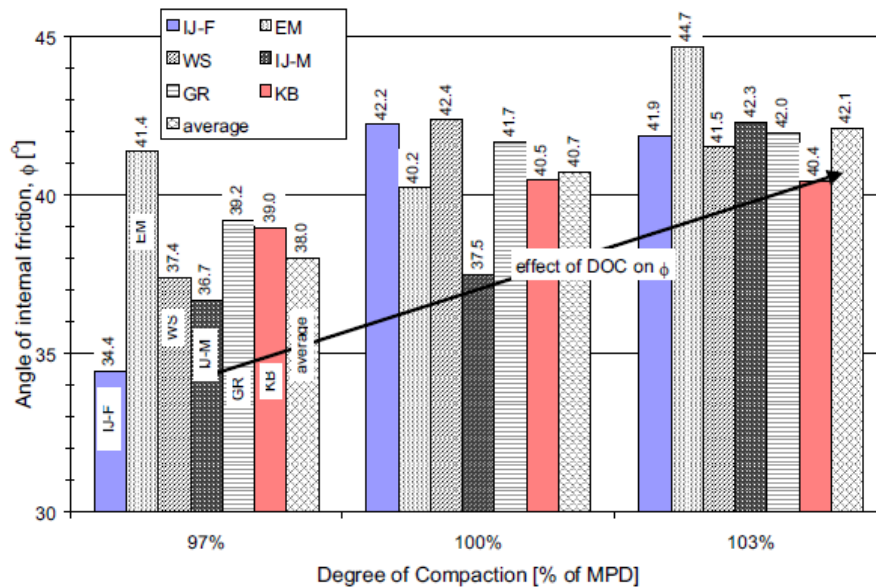


Figure 2- 24: Friction Angle in Relation to DOC for Six Research Sands (van Niekerk, 2002)

In their “*State of the Art*” on the resilient response of granular materials, Lekarp et al. (2000) reviewed literature from as early as 1962 to more recent, 1997, and concluded that the literature is somewhat ambiguous regarding the influence of density on the resilient response of granular materials. Several reviewed studies showed a general increase in Resilient Modulus with increasing density whereas some literature stated that the effect of density, or the state of compaction, is relatively insignificant. Furthermore, the reviewed literature generally showed a slight decrease in Poisson’s Ratio with increasing density.

Van Niekerk (2002), in his research of mix recycled granulates, found that an increase in DOC results in an increase in the Resilient Modulus and a reduction in Poisson’s Ratio. This phenomenon, the increase in stiffness and reduction of Poisson’s Ratio with increasing density, was evident for all material types and grading curves tested, however, the rate of change was related to the material grading used. Figure 2-25 represents the influence of increased DOC on the Resilient Modulus of a mix recycled granulate material as reported by van Niekerk.

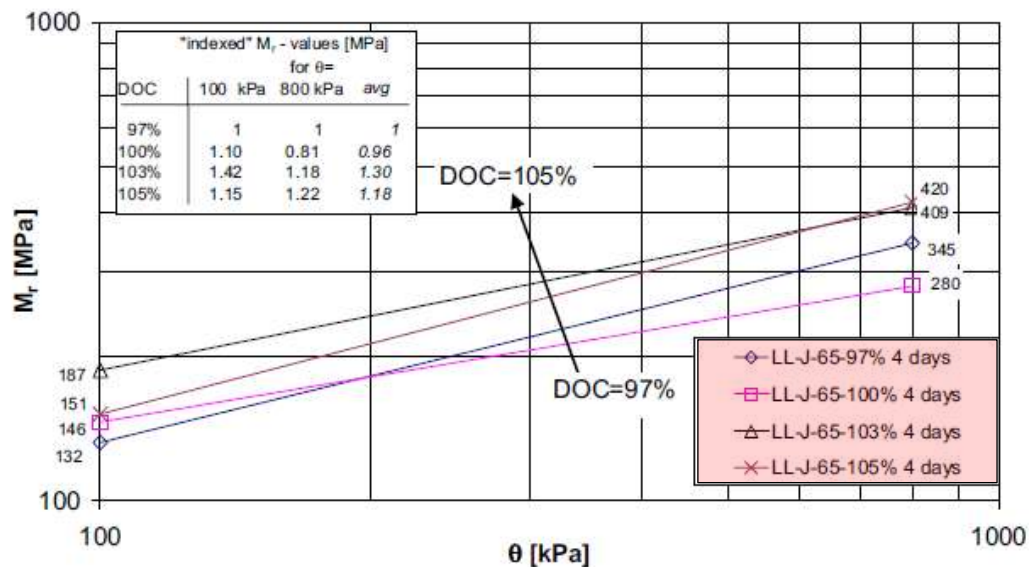


Figure 2- 25: M_r - θ Relations as a Function of DOC for a Mix Recycled Granulate Material after 4 days curing (van Niekerk, 2002)

In addition to van Niekerk, Araya (2011) tested the influence of DOC on the resilient behaviour of a typical South African G1 type material. Araya also found, except for the 100% DOC which was slightly lower than the 98% DOC, the stiffness of the crushed stone to increase with increasing DOC.

2.3.2.3 Influence of Applied Stress

Due to its stress dependent nature, the performance properties of UGM's under static loads are influenced significantly by the effect of stress. By supporting the material (adding confinement), the shear strength increases significantly. This increase in strength is best illustrated by the Mohr-Coulomb representations shown in Subsection 2.3.1.1. In addition, the increase in shear strength due to an increase in confinement can further be explained by placing dry sand in a bucket. Whilst a heap of dry sand will undergo massive deformation, or even collapse, when a person stands on it, the same sand however, placed in a bucket, will be capable of carrying the mass of a person without excessive deformation.

The behaviour of UGM's under cyclic traffic loading is, as mentioned in Section 2.3, stress dependent. Lekarp et al. (2000) states that literature has, without exception, shown the applied stress level to have the most significant influence on the resilient behaviour of unbound materials. In addition, the reviewed literature showed Poisson's Ratio to reduce with increased confinement and increase with increased deviator stress.

Uzan (1985) and Sweere (1990) have both shown that the minor principal stress (confining pressure in a tri-axial cell) and the applied major principal stress both have a significant influence on the Resilient Modulus of unbound granular materials. They found that the Resilient Modulus increased with increasing confinement and with increasing major principal stress.

Uthus (2007) also found that his results followed the trends set by earlier research adding that the influence of confining pressure is far more dominant, 3 to 5 times more, than the influence of applied deviator stress.

Van Niekerk (2002) however showed slight contradictions to the trends set out above. In his research he established two loading regimes, “mild” and “severe”, and noticed that the resilient deformation behaviour of the mix recycled granulate material only followed the above mentioned trends for the lower stress state or “mild” stress state. At high or more “severe” stress states, closer to the failure stress of the material, the resilient deformation behaviour changed and a reduction in Resilient Modulus was noted. This phenomenon of a reduction in Resilient Modulus under “severe” loading is illustrated by Figures 2-12 and 2-13 as shown in Paragraph 2.3.1.2

Furthermore, it should be noted that, due to limitations in testing equipment, all of the above research was based on a constant confining pressure being applied over the duration of the tests. This however does not accurately simulate the in situ stress paths caused by traffic in a pavement (see Figure 2.3). Rondòn et al. (2009) states that in an ideal laboratory test setup should be capable of simulating the rotation of the principal stress direction as explained in Subsection 2.2.3. Lekarp et al. (2000) states that some literature, to compare constant confining pressure (CCP) with variable confining pressure (VCP) tri-axial test, exists. The literature shows that VCP tests yielded somewhat lower Resilient Modulus values than that of CCP, however, the magnitude of the difference was inconsistent and dependent on the applied stress level.

2.3.2.4 Influence of Grading

The grading of UGM's used within pavement structures is critical to the performance of the pavement. It is therefore important to understand the influence of grading.

In laboratories the performance of UGM's is studied through extensive testing

however, due to the high cost and practicality of large-scale testing equipment, scaled down test equipment and samples are used for material characterisation. To achieve realistic results, not influenced by individual large aggregate particles, scaled down gradings need to be incorporated. This is achieved by manipulating the original grading therefore no true field performance can be measured within laboratories rather an approximation thereof. Although grading curve and specimen geometry is closely related, the influence of test apparatus scale and sample geometry will be discussed in Paragraph 2.3.2.5. This paragraph however will focus on the influence of grading and maximum particle size on the mechanical behaviour of UGM's.

Lekarp et al. (2000), through an extensive literature review, found that the stiffness of UGM's is, in some degree, influenced by grading (particle distribution) and particle size. General trends show that the Resilient Modulus decreases when the amount of fines (passing 75 micron) is increased. This can be as a result of reduced large-grain-to-grain contact area. The presence of a large amount of fines, larger than the spaces between the large particles (Figure 2-26 (c)), destroys large-grain-to-grain contact area which results in reduced stiffness.

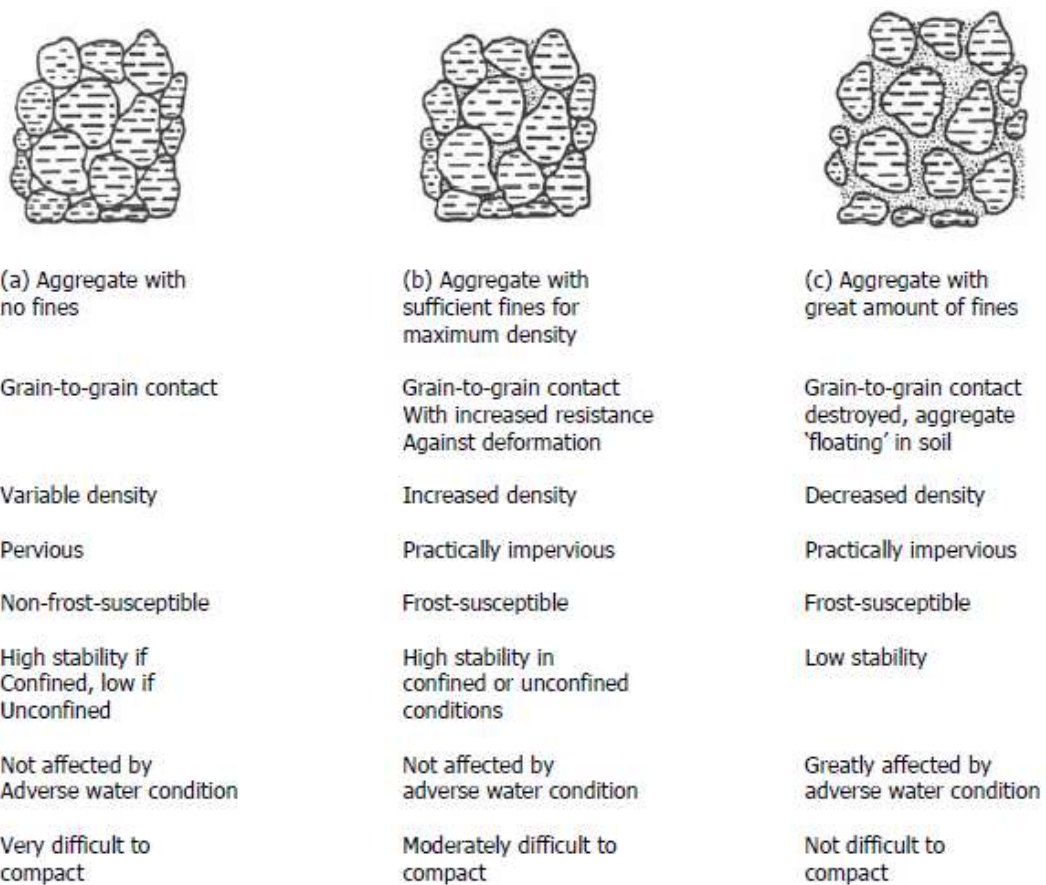


Figure 2- 26: Three Physical States of Soil-Aggregate Mixtures (Molenaar, 2010)

Thom (1988), through his study of crushed dry dolomitic limestone at 4 grading curves, each with a 10 mm maximum aggregate size and a fixed proportion of aggregate smaller than 75 microns, showed that grading has a slight influence on the resilient response but a more dominant influence on the shear strength. Uniformly graded materials, as shown by Figure 2-26 (a), yielded slightly higher stiffness values in comparison to well-graded materials, as shown by Figure 2-26 (b), whereas the more well-graded material yielded higher shear strength values. In addition, Thom studied the influence of particle size by testing four different materials, namely granite, dolomitic limestone, crushed concrete and steel slag with the expectation that any trends common to all four are likely to apply equally to other materials. Tests were again carried out on 75 mm diameter tri-axial specimens created from dry material which was manually compacted using nominally equal compactive effort. To gain an understanding of the influence of aggregate size three or four size fractions were tested for each material type, ranging from 75 microns to 14 mm. From the results, Thom concluded that both the stiffness and shear strength of UGM's decreases with decreasing particle size. Typically, this appears to be about a 25% stiffness reduction and 15% shear strength reduction for a tenfold size decrease.

Sweere (1990) studied the influence of grading curve through a series of resilient tri-axial tests using two specimen sizes, 400mm Φ * 800mm H and 150mm Φ * 300mm H. The results also showed that the Resilient Modulus of granular materials is influenced by grading. For material with the same maximum particle size, those with a coarse grading were shown to be more stress dependent than those with a fine grading.

In a more recent research project however, van Niekerk (2002) investigated the performance behaviour of sands and mix recycled granulates. The results showed that higher stiffness values were achieved for the well-graded materials when compared to that of the uniformly graded materials. This however contradicts the conclusion made by Thom (1988), as mentioned above, and might not have held if more fines were added as the influence of the fines would then become the dominate factor. Van Niekerk however argues that, due to the larger grain-to-grain contact area of a well-graded material (Figure 2-26 (b)) higher friction is induced thereby allowing a well-graded material to take up a large deviator stress for equal deformation (higher stiffness).

For further reading on the influence of moisture, compaction, applied stress, grading and maximum aggregate size, and other factors, on the mechanical behaviour of UGM's, the reader is referred to a "State of the Art" on the resilient response of unbound aggregates, *Lekarp et al. (2000)*.

2.3.2.5 Influence of Specimen Geometry

As mentioned in Paragraph 2.3.2.4, most laboratory characterisation of UGM's, through tri-axial testing, is carried out on adjusted gradings. Research has shown that, an unbalance in maximum aggregate size, in relation to specimen geometry, can influence test results (*Lekarp and Isacsson, 2001*). Further research, establishing a ratio between specimen diameter and maximum aggregate size ($d_{specimen}/d_{max-particle}$), recommend a minimum $d_{specimen}/d_{max-particle}$ ratio of 6-7 to prevent effects stemming from particle size to influence test results (*Sweere, 1990 and van Niekerk et al. 2000*).

In an investigation of specimen geometry, *Thom (1988)* conducted tri-axial tests on four different grading curves using three specimen sizes. *Thom* concluded that, the Resilient Modulus is uninfluenced by the ratio of specimen diameter to maximum aggregate size and that the only effect noticed, as the ratio reduced, was the scatter in the stiffness results. The results however showed that shear strength was significantly influence by the ratio, increasing as the ratio reduced.

Furthermore, *Sweere (1990)* also investigated the influence of specimen diameter in relation to maximum aggregate size, through a series of resilient tri-axial test. The tests results, from testing two specimen sizes (400mm Φ * 800mm H and 150mm Φ * 300mm H) at the original 0/40 grading, for crushed masonry and crushed concrete at equal values of moisture content and dry density, showed inconsistencies with regard to the influence of specimen size. For the smaller specimen the crushed masonry showed higher stiffness values whereas the influence on crushed concrete was negligible. *Sweere*, based on the results obtained, concluded that specimen geometry, in relation to maximum aggregate size, does influence the resilient behaviour of UGM's during tri-axial testing however, the influence is complex and cannot be determined with certainty.

2.3.3 Laboratory Characterisation of UGM's

As mentioned earlier, in Subsection 2.3.1, materials are characterised by generating fundamental information on the material, at research institutes. Several

characterisation techniques exist. The purpose of this Subsection is to give the reader a brief background to some of the most commonly used characterisation methods (see Figure 2-27 below) and to explain the characterisation method used in this research. If further reading on other characterisation techniques is required, refer to Thom et al. (2005).

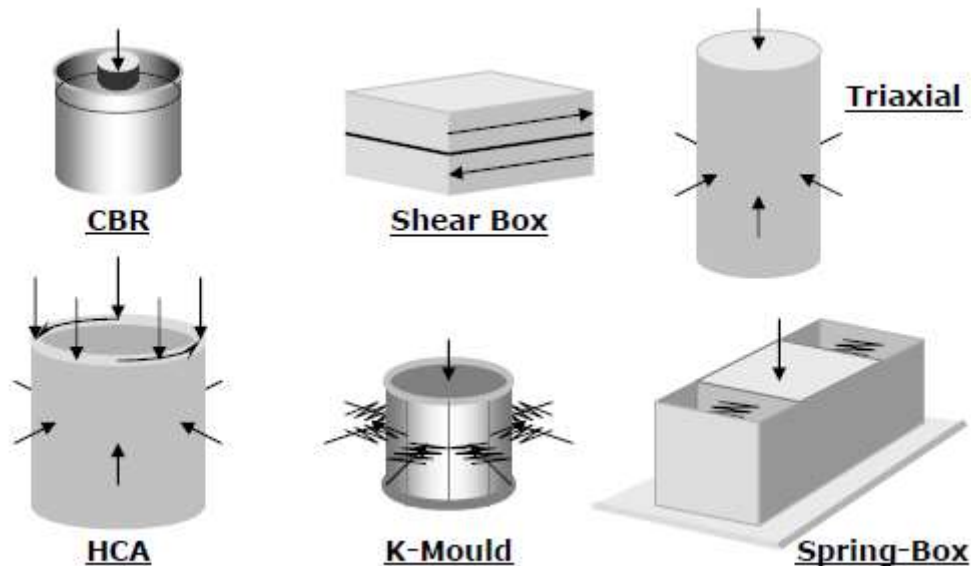


Figure 2- 27: Six commonly used Characterisation Tests for UGM's (Thom et al. 2005)

2.3.3.1 California Bearing Ratio (CBR)

The California Bearing Ratio (CBR) gives an indication of material bearing capacity (Standard CBR) as well as some indication of the resilient behaviour (Repeated Loading CBR). The standard test is a penetration test and applies a displacement-controlled rate (0.8% strain per minute) to a 50.8 mm diameter plate, placed on a 152.4 mm diameter specimen (Thom et al. 2005). The repeated loading CBR however, loads a specimen at a constant rate of 1.24 mm/min until the penetration reaches 2.54 mm, whereat, the force required to achieve the penetration is noted. The specimen is unloaded, where after it is again loaded to the determined force, and again unloaded. This load, unload cycle is repeated 55 times during which displacement and force measurement are recorded. From the data, a stress-strain relation, shown in Figure 2-28, is established. It is this stress-strain relation that is used to estimate the Elastic Modulus of the tested material, as explained in Subsection 2.3.1.

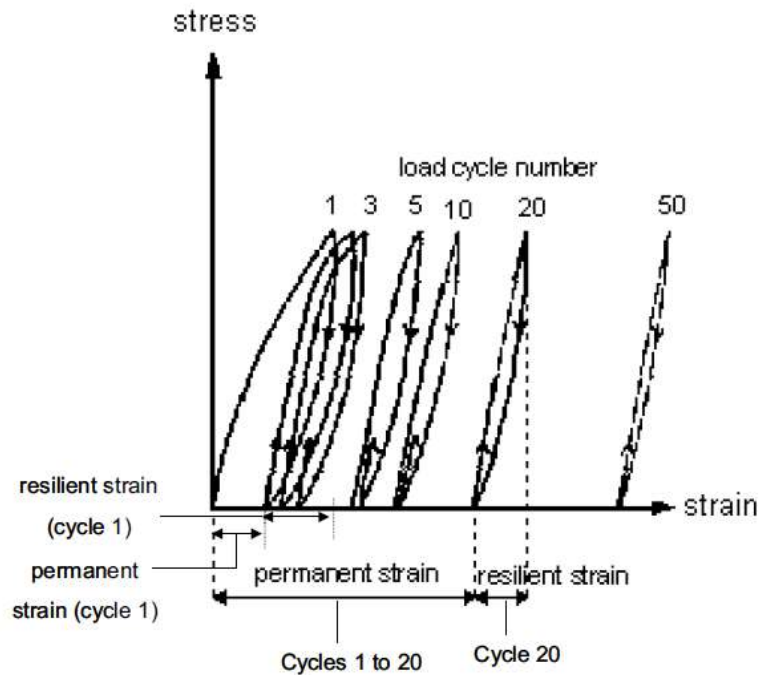


Figure 2- 28: Stress-Strain Relation for a Granular Material under Repeated CBR loading (van Niekerk, 2002)

Due to its simplicity, repeatability and cost, the CBR test is extensively used; however, when used for testing UGM's, problems arise. The main issue regarding UGM's is the ratio of mould and plunger geometry in relation to maximum particle size of the UGM to be tested (Araya, 2011). Again, as mentioned in Subsection 2.3.2, modified gradings are used in order to reduce the influence of maximum particle size on the CBR test results, therefore no true in situ bearing capacity is measured. In addition, the CBR test does not simulate cyclic traffic loading nor does it simulate the stress dependent behaviour of UGM's (Edwards, 2007).

2.3.3.2 K-Mould

C.J. Semmelink (Semmelink, 1991), a South African, developed the K-mould for rapid evaluation of the elastic and shear properties of road building materials. As shown in Figure 2-27, the K-mould consists of eight circular segments, each spring loaded and allowed to move in a radial direction.

Other than the CBR, the K-mould more accurately simulates the pavement stresses in an unbound granular layer due to traffic loading. Semmelink states that, one of the advantages of the K-mould is that its supporting stiffness is infinity variable. The spring system can, be locked in place to prevent any radial deformation or, allowed to apply variable confinement to the specimen. Note that, for the K-mould variable

confinement is a function of specimen deformation. Further advantages include the ease of the test setup and instrumentation and that only one specimen is required for the determination of the failure envelope as explained in Paragraph 2.3.1.1.

The K-mould however, has also come under scrutiny by other researchers with regard to its geometry and spring mechanism. Van Niekerk (2002) states:

“Disadvantages of the K-mould are its present limited height to diameter (h/d) ratio and the fact that the rigid steel wall segments and springs result in a uniform deformation and thus most likely a non-uniform horizontal stress over the height of the specimen.”

If further reading, into the development of the K-mould, is required, refer to Semmelink (1991).

2.3.3.3 Tri-axial Test

The Texas Department of Transport (TxDOT, 2002) defines a tri-axial test, as a test wherein stresses are applied in three mutually perpendicular directions, as shown by Figure 2-29. These stresses include the major principal stress σ_1 and the minor principal stresses σ_2 and σ_3 . Note that no shear stress develops on the sides of the tested specimen.

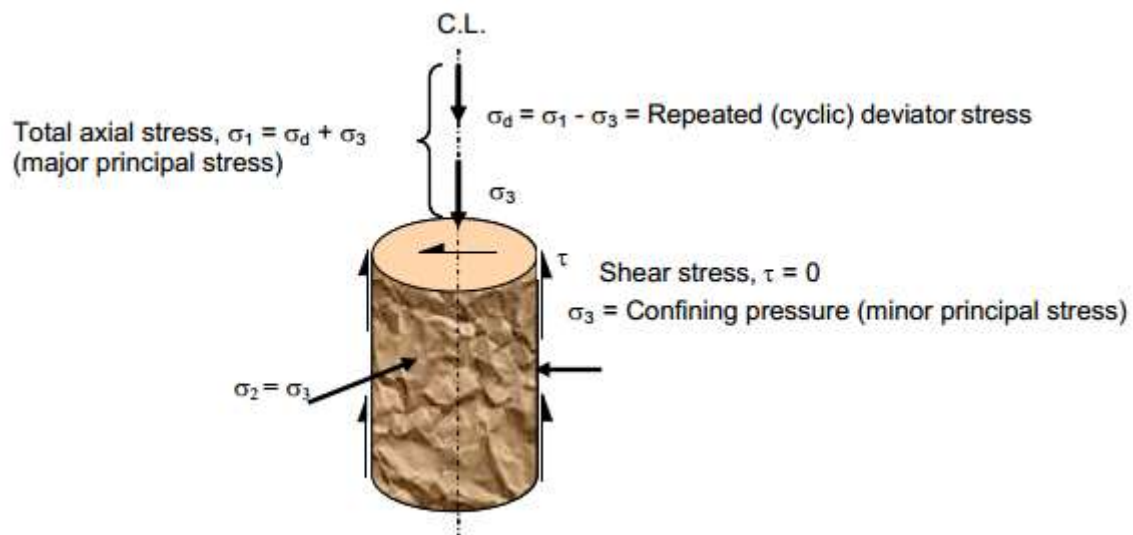


Figure 2- 29: Principal of Tri-axial Test (Anochie-Boateng et al., 2009)

In the current state and age of material characterisation, three tri-axial tests exist: the Hollow Cylinder Apparatus (HCA), the monotonic load and the cyclic load tri-axial. All of these tests accurately simulate the stresses and loading conditions that occur

within a pavement although, the monotonic load test does not simulate cyclic traffic loading. For this thesis however, only monotonic and cyclic tri-axial test will be utilised therefore, if further reading, with regard to the HCA tri-axial, is required, refer to Chan (1990) and Lee et al. (2002).

Monotonic Tri-axial Test

The basic principle that formulates the monotonic tri-axial test is an increase in the applied principal stress σ_1 in excess of the applied minor principal stresses σ_2 and σ_3 . The applied principal stress increased until excessive deformation occurs i.e. the specimen has failed in shear or strain. The test is carried out under various minor principal stresses σ_3 (confining pressure in tri-axial cell) conditions and the stress-strain relation for each recorded, as shown in Figure 2-30.

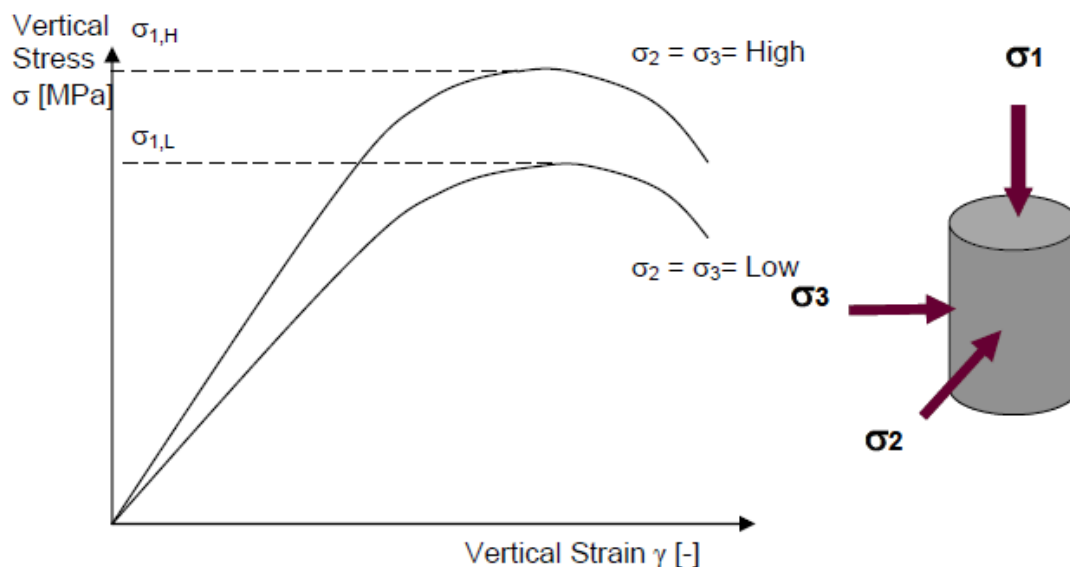


Figure 2- 30: Schematic representation of monotonic tri-axial tests results for two specimens tested at low and high confining pressure respectively (Jenkins, 2010)

By conducting a series of monotonic tests, at different confining pressures, on specimens produced from a single material to comparable standard, the shear parameters of the tested material can be determined. Mohr-Coulomb circles, as explained in Paragraph 2.3.1.1, represent the stress conditions at which shear failure occurs. As mentioned a tangent line to the Mohr-Coulomb circles represent a linear estimation of the true failure envelope of the tested material.

The monotonic test, even though it is an accurate measure of the failure envelope of unbound granular, and other materials, does not simulate cyclic traffic conditions. Under cyclic traffic loading, where the applied major principal stress σ_1 is far less than

the major principal stress at failure σ_1^f , failure will not occur instantly rather deformation will accumulate with repeated loading. Therefore, a more representative testing method, one that simulated the large amount of smaller repeated traffic loads, had to be developed.

Cyclic Tri-axial Test

As mentioned above, the monotonic tri-axial test allows an understanding of a materials failure envelope however; it does not accurately simulate a materials response to cyclic traffic loading. The cyclic tri-axial test, developed to simulate cyclic traffic loading, tests a materials response to different levels of cyclic stress for a range of confining pressures.

Data from the cyclic tri-axial test gives an accurate indication of the Resilient Modulus and permanent deformation characteristics of a pavement material under traffic loading, as explained in Paragraph 2.3.1.2

Tri-axial Test Apparatus

Tri-axial testing apparatus, used for monotonic and cyclic testing, must be capable of applying the required loading for the respective tests. Although several test set-ups exist, ranging in sample size to the type of confining fluid used, all need to incorporate the common features of a tri-axial testing apparatus, as shown in Figure 2-31 (a) and (b) below.

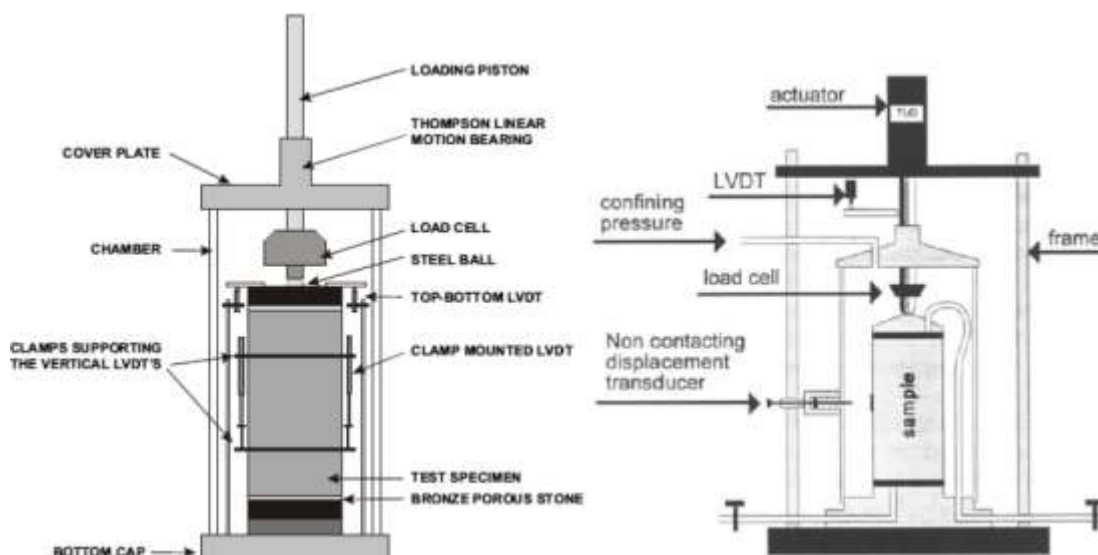


Figure 2- 31: Schematic Representation of a Typical Tri-axial Test Set-up, (a) Detailed Cell with Measuring Equipment and (b) Broader Representation of Tri-axial Test Set-up (IDOT, 2009 and Molenaar, 2010 respectively)

As illustrated by Figures 2-31 (a) and (b), the most common features found in a tri-axial testing apparatus are:

- Tri-axial cell;
- Actuator; and
- Measuring devices that include load cell and linear variable displacement transducers (LVDT's)

Other instrumentation not shown in the figures include:

- Control system;
- Data acquisition system; and
- A method of applying confinement to the specimen

The tri-axial cell is a fluid (air or water) tight cell in which the tri-axial specimen is tested. The cell must be capable of withstanding the high confining pressures applied, being air or water pressure, and should be easily opened to allow replacing of specimens and measuring devices. In addition, the internal dimensions of the cell should be to the extent that it can accommodate the specimen, the bulging (deformation) of the tested specimen together with the applied measuring equipment.

Modern actuators, operated by a servo-controlled hydraulic pressure system, are capable of displacement (monotonic) and load controlled (cyclic) testing (Mulusa, 2009). The system, which is a closed loop feedback system, can exert either a ramp or cyclic load on the specimen depending on the test type. In addition, concerning the geometry of the testing system and placement of the actuator, Mulusa (2009) states:

“The preferred geometry of testing system is such that the moving actuator is situated above the tri-axial cell with the fixed reaction point situated below the tri-axial cell. Inverted set-ups result in limitations on the maximum frequency of the dynamic load testing.”

Measuring devices include the load cell, which accurately measures the applied force, and LVDT's that measure the displacement of the specimen during testing. Note that the LVDT's on the specimen itself is not required for monotonic testing since this test only requires measurement of the applied force and the displacement of the actuator. Using the displacement of the vertical actuator however means that edge effects are included in the displacement measurements, which can significantly

influence the evaluated shear parameters. Therefore, it is recommended that additional measuring equipment be utilised to reduce the influence of edge effects. Furthermore some test set-ups incorporate electronic pressure gauges although, mechanical gauges are sufficient.

Tri-axial testing apparatus, although not shown in the figures, require a control system that allows for human-machine interaction. In addition, the set-up requires a data capturing system that captures the required data during testing. Modern computers, incorporating modern hardware and software, combine both control and data capturing system into one test system.

Tri-axial Test Protocol

Currently, many tri-axial testing protocols exist for both monotonic tri-axial and cyclic tri-axial testing. These protocols, each developed based on different experience and testing equipment available, differ in the sense that they incorporate different properties, as summarised below.

- Material (maximum aggregate size);
- Specimen preparation method (compaction);
- Condition of specimen (density and moisture content);
- Sample geometry (small versus large);
- Measuring equipment (number of LVDT's and position);
- Applied confinement;
- Confinement medium (water, air or oil);
- Specimen conditioning;
- Load type and frequency;
- Testing sequence; and
- Results

Protocols change over time however, for the purpose of this review, Table 2-1 presents a summary of existing Resilient Modulus (short duration cyclic tri-axial test) protocols, as summarised by Anochie-Boateng et al. (2009). Although the summary gives the reader some indication of the differences in existing protocol properties, Section 3.4 presents the specific protocols used within this research project for both monotonic (shear properties) and short duration cyclic (deformation properties) tri-axial tests.

Table 2- 1: Summary of Different Resilient Modulus Test Protocol Properties (Anochie-Boateng et al., 2009)

Property	EN 13286-7 (2004)	AASHTO T307-99 (2005)	NCHRP I-28A (2004)	CSIR Transportek (2002)	University of Stellenbosch (2007)	University of Illinois (1998)	Australia AG:PT/053 (2007)
Material types	Max aggregate size < 0.2 sample diameter	1. (Max size < 70% < 2.0 mm < 20% < 0.075, PI < 10%) 2. all others	1. (Max size > 9.5; > 25.4 scalped) 2. (Max size < 9.5; < 10% < 0.075) 3. (Max size < 9.5; > 10% < 0.075) 4. Thin wall undisturbed	No details – Borrow pit or test pit Max size 37.5 mm	Unbound and bound granular materials Max size 19 mm duplicate specimens	Unbound aggregates and subgrade soils Max size 25 mm	Max size 19 mm – oversize discarded (not more than 5%)
Specimen preparation	Vibro-compression (1 layer) Vibratory hammer (6 – 7 lifts)	1. Vibratory hammer (6 lifts) 2. Static (5 lifts) or pneumatic kneading (5 lifts)	Type 1: Impact (Proctor) / vibratory hammer (or rotary) Type 2: vibratory Type 3: Impact/ kneading	Vibratory table 3-lifts in split mould	Not finalized	Standard pneumatic concrete vibratory compactor 3-lifts in split mould	Standard and modified Proctor methods at (5 or 8 lifts)
Specimen compaction state	Moisture content and density reps of field conditions 6 specimens (OMC – 4, 2.1% and 100, 97, 95% density)	In situ wet density and moisture content or standard and modified Proctor	Desired density and moisture content	2 levels of density (95-98% & 102-105% Mod) and moisture content (Sr 45, 75%)	Specified moisture content and density	Optimum moisture content and max dry density	Optimum moisture content and max dry density
Height : diameter	2 ± 2% Diam > 5 times max particle size; (160 x 320 mm)	2.0 70 mm diam (subgrade); Min diam = 5 times max size (base /subbase)	2.0 70 mm diam (fine-grained), 100 – 150 mm diam (coarse-grained)	2.0 150mm diam x 300 - 305 mm high	2.0 150 mm diam x 300 m high	2.0 50mm diam (subgrade soils); 150mm diam (base/subbase)	2.0 100 diam x 200 mm high for fine and coarse-grained
Response measurement	Load cell Internal 3 axial LVDTs measuring centre 100 mm of sample at 120°, attached to membrane	Load cell external 2 external axial LVDTs	Load cell internal 2 Internal axial LVDTs	Load cell On sample full length	Load cell On specimen LVDTs over middle third	Load cell internal; 2 external axial LVDTs	Load cell external or internal 2 axial LVDTs

Table 2- 1 (cont.): Summary of Different Resilient Modulus Test Protocol Properties (Anochie-Boateng et al., 2009)

Property	EN 13286-7 (2004)	AASHTO T307 (2005)	NCHRP I-28A (2004)	CSIR Transportek (2002)	University of Stellenbosch (2007)	University of Illinois (1998)	Australia AG:PT/053 (2007)
Confining pressure	Variable and Constant (vacuum option) up to 600 kPa	Constant up to 140 kPa	Constant up to 140 kPa	Constant up to 200 kPa	Constant up to 200 kPa	Constant up to 140 kPa	Constant up to 500 kPa
Chamber medium	Water, air or silicon oil	Air	Air	Air	Air or water	Air	Silicon oil or water covering sample, together with air for pressure
Specimen conditioning	70 kPa confining, and axial deviator stress of 200 - 340 kPa; 20 000 reps	103.4 kPa confining, and axial deviator stress of 103.4 kPa; 500 - 1000 reps	27.6 -103.5 kPa confining for subgrade, base /subbase at 1000 reps; axial deviator stress of 50.8 - 227.7 kPa	200 kPa confining and axial deviator stress of $0.45\sigma_d$ at failure; 500 - 1000 reps	200 kPa confining and 20 kPa axial deviator stress, 5000 reps	103.4 kPa confining at deviator stress of 310.5 kPa; 1000 reps	50 kPa confining and axial deviator stress of 100kPa ; 1000 reps
Load type	Frequency of axial load (0.2 -10Hz)	Haversine, 0.1s load and 0.9s rest (hydraulic); 0.9 to 3s rest (pneumatic)	Haversine, 0.1s load, 0.9s rest period (base /subbase); 0.2s load, 0.8s (subgrade)	Haversine, 0.2s load and 0.8s rest period	Haversine, 0.5s load, 0.5s rest period	Haversine, 0.1s load, 0.9s rest period	3s vertical force wave with load of 1s and rise and fall of 0.3s
Test sequence	100 reps at 29 stress states; confining of 20 - 150 kPa and axial deviator stress of either 30 - 475 kPa or 20 - 300 kPa	100 reps at 15, stress states confining of 20.7- 138 kPa and max axial deviator stress of 20.7 - 276 kPa	100 reps at 30 stress states (Type 1); 20 stress states (Type 2) and 16 stress states (Type 3); confining of 20.7 to 138 kPa and deviator of 20.7 to 993 kPa cyclic	100 reps at 14 stress states; confining of 20 - 200 kPa and axial deviator stress of 0.08 to 0.81 times the failure stress	100 reps at 15 stress states; confining of 20 - 200 (coarse) 140 (fine) kPa and axial deviator stress of 0.1 - 0.9 times the failure stress	100 reps at 8 stress states; confining of 34.5 - 207 kPa and axial deviator stress of 69 - 414 kPa	At least 50 reps at 66 stress states; confining of 20 -150 kPa and axial deviator stress of 100 - 600 kPa
Results	Average of last 10 cycles use to computed M_R	Average of last 5 cycles use to computed M_R	Average of last 5 cycles use to computed M_R	Average of all load cycles use to compute M_R	Average of all load cycles use to compute M_R	Average of last 50 cycles use to computed M_R	Average of last 6 cycles use to computed M_R

Sample Preparation

Table 2-1 shows that, several compaction methods exist for compaction of samples in the laboratory. The most commonly used compaction methods are, the application of a static load or the use of a dynamic hammer (Mgangira et al. 2011). Other methods of compaction include a kneading action or using vibratory compaction methods e.g. vibratory hammer or vibratory table. Below, follows a discussion of the most commonly used steps of laboratory sample preparation and compaction whereas, Section 3.4 presents a discussion of the tri-axial sample preparation method used for this research.

The first step, in the laboratory sample preparation method, is the determination of the materials maximum achievable dry density and its associated moisture content (known as the optimum moisture content) as set in Method A7 of the TMH1. The method allows for the determination of the maximum dry density and optimum moisture content (OMC) by establishing a moisture-density relation curve, using compaction data of the material when prepared and compacted at the Modified AASHTO compaction effort at different moisture contents, as illustrated by Figure 2-32. Note that, for field evaluation purpose, samples shall be prepared to in-situ conditions i.e. in-situ moisture content and density, therefore Method A7 will not be incorporated.

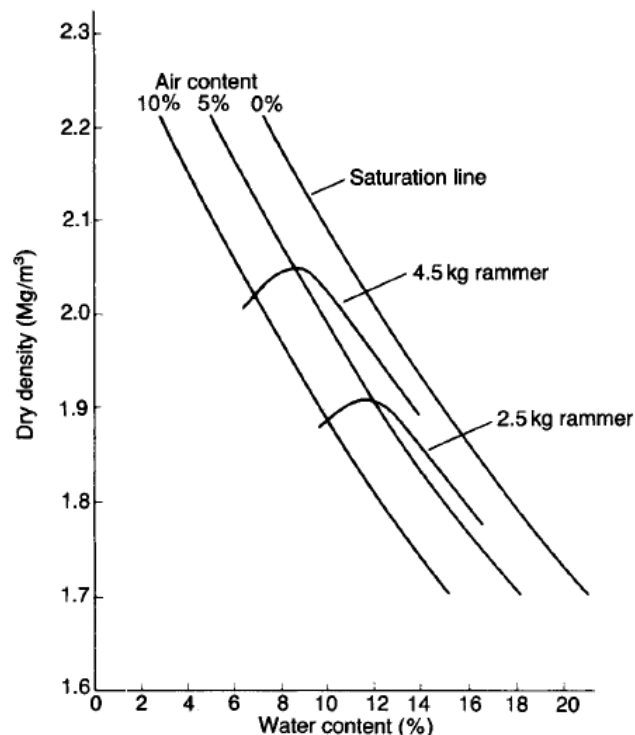


Figure 2- 32: Moisture-Density Relation Curve for Different Compactive Effort (Craig, 2004)

Interestingly, Figure 2-32 also illustrates that compactive effort influences the density achieved. Greater compactive effort (4.5kg compared to 2.5kg rammer) results in higher densities obtained at lower moisture contents.

Secondly, water is admixed to the material until the total moisture content within the material, is equal to the OMC. Note that dry material contains some amount of moisture (known as the hygroscopic moisture content) therefore; the amount of water to be admixed is the difference between the OMC and the hygroscopic moisture content. The hygroscopic moisture content, similar to any other moisture content calculation, is determined as set in Method A7 of the TMH1.

Finally, using material mixed to the desired moisture content, compaction can commence. As mentioned, different protocols enforce different compaction methods, therefore no discussion of a specific compaction method will follow, rather, presented in Chapter 3, follows a discussion of the compaction method utilised in this research.

2.4 Unbound Granular Layer Construction

The quality of layer construction within a pavement structure (unbound or treated layer) is a critical aspect that requires consideration. It is well understood that the quality of the constructed pavement layers influence the overall performance of the pavement structure therefore, standards and specifications exist in order to control the quality during the construction process.

This Subsection will introduce some of the material classification systems and their specification, to allow quality control of unbound pavement layers (in particular South African unbound layers) and discuss some of the field compaction methods applied to achieve the specified layer densities.

2.4.1 Classification and Specifications

Several material classification systems exist throughout the world. Some systems use the visual appearance of the material and results of different tests to make the classification more objective (SAPEM, 2013). Although other classification systems exist (AASTHO and Unified), in South Africa, the TRH14 (1985) classification system is most commonly used for UGM's.

The TRH14 system classifies granular materials according to three material types, each consisting of different material classes (ranging from G1 to G10):

- Graded crushed stone: G1, G2 and G3;
- Natural gravels (which include modified and processes gravels): G4, G5 and G6; and
- Gravel-soil: G7, G8, G9 and G10

The TRH14 requirements for G1 to G10 materials are set in relation to the following specifications:

- Grading i.e.: sieve size, grading modulus, flakiness index and crushing strength;
- Atterberg limits i.e.: liquid limit, plasticity index and linear shrinkage; and
- Bearing strength and swell i.e.: California Bearing Ratio (CBR) and swell

For further reading concerning classification systems used elsewhere in the world (AASHTO and Unified) reference is made to AASHTO M145-91 (2008 cited SAPEM, 2013), ASTM D3282 (2009, cited SAPEM, 2013) and Craig (2004) respectively.

In addition to the material classification systems, different material classes have different specifications to adhere too. In terms of compaction specifications set in the manual of the Committee of Land Transport Officials (COLTO, 1998), Table 2-2 summarises the minimum density of graded crushed stone in relation to the apparent density (AD), bulk density (BD) and maximum dry density (MDD) of the associated material class.

Table 2- 2: Guidelines for Compaction Specifications of Granular Base Layers (COLTO, 1998)

Base Class	Minimum % Apparent Density (AD)	Minimum % Bulk Density (BD)	% MDD
G1	86 to 88	89	–
G2	–	85	100 to 102
G3	–	–	98 to 100

Apparent and bulk density, also referred to as apparent relative density (ARD) and bulk relative density (BRD), refers to the density of the parent material. Several methods exist for calculating the density of the parent material however, Botha and Semmelink (2004) developed a more user friendly, non-operator dependant and repeatable method.

Furthermore, many other material specifications exist, all of which differ. It is important to apply the appropriate specifications, from the relevant documentation, for the specification of the particular project. The South African Pavement

Engineering Manual (SAPEM, 2013) gives a wide range of specifications for different materials as used in South Africa.

2.4.2 Field Compaction Methods

The compaction process is undoubtedly the most important process during the construction of UGM layers because of its critical influence on the performance of the material (refer to Paragraph 2.3.2.2). Semmelink (1995) states that field compaction deserve to get more serious attention than has very often been the case.

The results of laboratory compaction tests are not directly applicable to field compaction because of the differences in compactive effort and the manner in which the compaction effort is applied (Craig, 2004). Furthermore, as mentioned, most laboratory tests are performed on adjusted material grading where the larger particles are removed from the original material. However, the densities achieved in laboratory tests, using different compactive effort, is similar to the densities achieved by field compaction methods.

Two methods of compaction, *method* and *end-method* compaction exist (Graig, 2004). In *method* compaction, the compactive type and effort, layer thickness and total passes are specified in order to reach an acceptable density. This method however is not without drawbacks as variability in material properties and lubrication (moisture content) can result in over or under compaction. Total passes generally range between 3 and 12 although it is variable depending on the compactive type and effort, layer thickness, moisture content and material to be compacted.

The *end-method* compaction approach, which is more commonly used, specifies a target dry density after compaction. This target dry density is usually presented in relation to the maximum dry density (*MDD*) of the material to be compacted.

Interestingly, although extensively used, researchers argue against the method of specifying a target density, emphasising that compaction should commence until no further densification is achievable. Semmelink states that:

“Rolling should preferably only stop when there is little or no change in the in situ density with successive roller passes. By rolling to this point much premature rutting of the pavement can be avoided.”

Pavement layers should thus, rather be compacted until refusal density is reached.

Different compaction methods exist, some more appropriate than others depending on the type of compaction required and the material to be compacted. Below follows a short discussion on the preferable use of different compaction methods.

Wirtgen, in their Cold Recycling Manual (Wirtgen, 2004) presents a guide for roller selection depending on the material to be compacted.

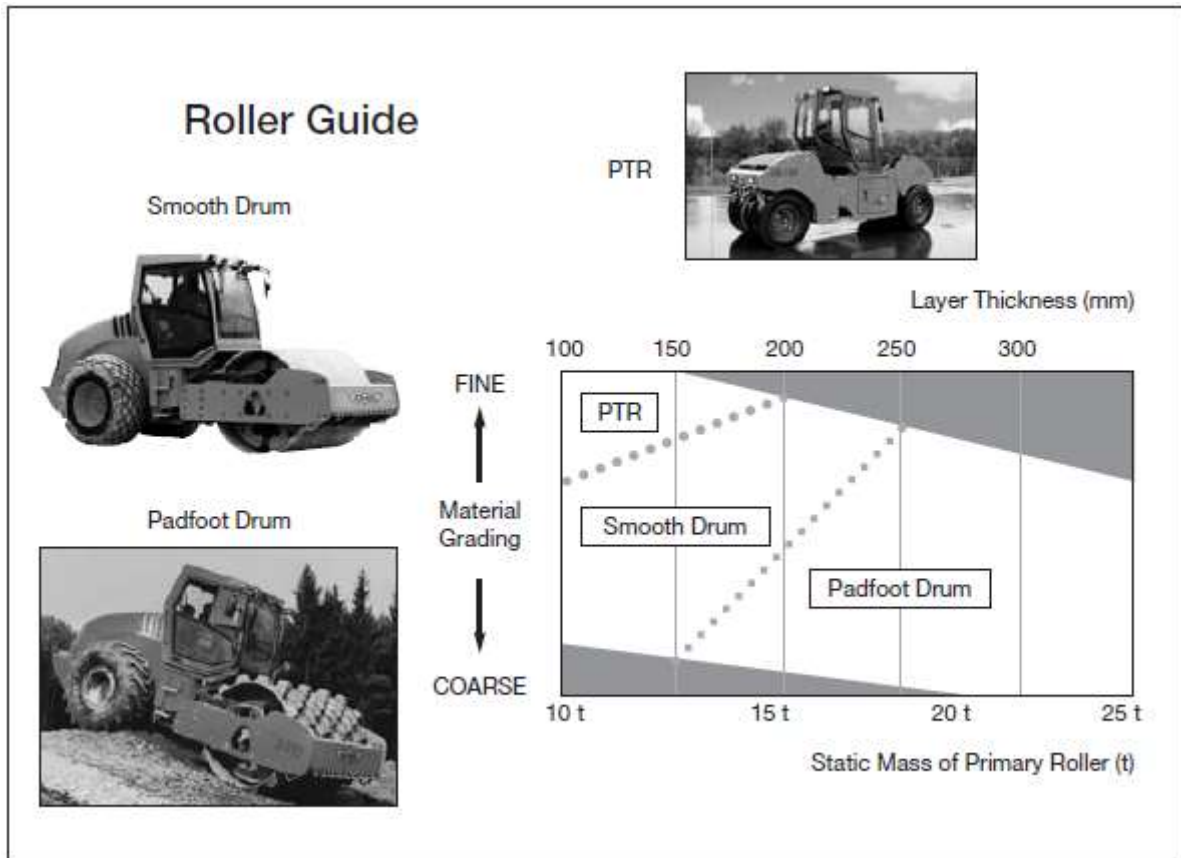


Figure 2- 33: Primary Roller Selection Guide (Wirtgen, 2004)

From Figure 2-33, it is clear that more compactive energy is required to compact thicker material layers.

2.5 Conclusion

Based on the literature reviewed, this section presents a summary of the conclusions drawn.

- Generally, South Africa utilises a lightly cemented subbase as support for an unbound granular base layer.
- The wearing or surfacing course has little load spreading capabilities and adds little strength to the pavement structure; rather the wearing or surfacing layer acts as a waterproofing layer.

- UGM layers are used as load spreading layers; therefore, an understanding of the load spreading properties is required.
- Current laboratory characterisation methods, used to characterise material strength and load spreading capabilities, show that moisture content, degree of compaction, grading and aggregate size, applied stress (stress dependent) and specimen geometry does significantly influence the behaviour of UGM's.
- The suction induced by moisture within a material contributes to the effective stress of the material (Theyse, 2007). Higher moisture content results in less suction, or even pore pressure, thereby reducing the effective stress. Van Niekerk (2002) and Araya (2011) found that mechanical performance properties (Shear Strength and Resilient Modulus) of UGM's tend to increase with increased moisture content however, Araya (2011) found that a tipping point exists where excessive moisture content results in reduced performance. This reduced performance can be linked to Theyse (2007) where an excessive increase in moisture content results in reduced effective stress within the material thereby reducing performance.
- Performance of UGM's tend to increase with increased compaction or density. Thom (1988) found that increased density yielded better shear resistance and reduced permanent deformation. His results however showed that density had no significant influence on the Resilient Modulus of the tested material. Lekarp et al. (2000) through their review of literature concluded that the literature is somewhat ambiguous regarding the influence of density on the resilient response of granular materials. Several reviewed studies showed a general increase in Resilient Modulus with increasing density whereas some literature stated that the effect of density is relatively insignificant. In more recent studies however (van Niekerk, 2002 and Araya, 2011), researching materials similar to that researched in this research study, both studies showed that Resilient Modulus increased with increased density. In addition Cohesion and Friction Angle was also shown to have increased due to an increase in density.
- UGM's are stress dependent. Without exception, an increase in the minor principal stress (confining pressure in tri-axial cell) results in an increase in the shear strength and Resilient Modulus and reduces Poisson's Ratio (Uzan, 1985 and Sweere, 1990). The effect of the major principal stress however

varies. Van Niekerk (2002) found that at lower stress regimes, an increase in the applied major principal stress results in an increase in Resilient Modulus (material stiffening). This increase however, is short lived, as a further increase in the applied major principal stress, approaching the failure stress, results in a reduction in stiffness (material softening).

- General trends show that the strength and Resilient Modulus decreases when an excess amount of fines (passing 75 micron) is present. Furthermore, well-graded materials tend to have higher strength and Resilient Moduli than that of uniformly graded materials. Lekarp et al. (2000) and van Niekerk (2002) argues that higher large particle-to-particle contact area yields higher friction between material particles. This in turn allows the material to take up a greater deviator stress for equal deformation (i.e. higher stiffness).
- Specimen geometry does influence the performance of UGM's although the influence is complex and not yet clearly understood. However, to prevent effects stemming from particle size in relation to specimen geometry, a minimum ratio, of specimen diameter to maximum aggregate size, of 6-7 needs to be maintained.
- Several infield compaction methods exist, some applying static energy, vibratory energy and even impact energy. The most commonly used infield compaction method however applies vibratory energy.
- Most laboratory characterisation methods apply the standard Modified AASTHO compactive effort (impact compaction) for specimen preparation. This however does not simulate infield construction methods and the current trend is to move from impact energy to a more representative vibratory energy method.
- To prevent effects stemming from the ratio between specimen diameter and maximum particle size, laboratory characterisation techniques require the true in-situ grading to be adjusted to fit the minimum ratio between specimen diameter and maximum particle size. This however does not allow accurate testing of the true material grading. Further research is required to establish the effects of evaluating performance properties based on adjusted material gradings.

CHAPTER 3: RESEARCH DESIGN AND METHODOLOGY

3.1 Introduction

This chapter presents a discussion on the research design and methodology followed in this research study. Included are; the experimental design developed to achieve the research objectives, material procurement, preliminary material testing, testing methodology and trouble shooting required to allow for the execution of the experimental design.

3.2 Experimental Design

To achieve the objectives of the research, an experimental plan had to be developed that would allow for the comparison, of the performance properties, of specimens prepared using similar grading curves but with different sized specimens as well as similar sized specimens prepared using different grading curves. Figure 3-1, on the following page, shows a summary of the experimental design developed for this study.

The experimental design as shown is broken up into 5 sections namely; Material, Sample Size, Grading Curve, Tri-axial Tests and Performance Properties, of which a short explanation on each is presented below.

- Material: Due to the nature of this research, time constraints and the size of specimens to be prepared and tested, only one representative parent material was selected.
- Specimen Size: Two sample sizes were selected for testing; a 150mm diameter with height 300mm (from here on referred to as small-size) and a larger 300mm diameter with height 600mm (referred to as large-size). Note that the specimen sizes are also represented symbolically as shown by Figure 3-1. By comparing small- and large-size specimens prepared under similar conditions, an understanding of the effect of sample geometry can be obtained. In addition, the large-size specimens will allow testing of grading curves containing larger (greater than 19mm) aggregates without the maximum particle size to specimen diameter influencing the results.
- Grading Curve: To gain an understanding of the influence of grading curve and the accuracy of the methods used in laboratories to adjust the in-situ grading (scalping and crushing) the experimental design incorporates three

grading curves. For the first grading curve (referred to as “S19”), the parallel-scalping method is used to remove all aggregate particles retained on the 19mm sieve (i.e. all particles greater than 19mm are removed). For the second grading curve (referred to as “G19C”), the scalp-add-back method is incorporated. In this method, all particles retained on the 19mm sieve is removed where after an equal mass, equal to that of the scalped material, is added back as particles passing the 19mm, but retained on the 13.2mm sieve. Finally, a full scale grading (referred to as “Full”) is utilised as the benchmark grading within the experimental design. Note that the grading curves are also represented through the symbols shown by Figure 3-1.

- Tri-axial Tests: Both monotonic and dynamic tri-axial tests were used to test the performance properties of the various specimens.
- Performance Properties: Results from monotonic tri-axial tests are used to evaluate the shear strength performance through the material’s Cohesion (C) and internal Friction Angle (ϕ). Cyclic tri-axial tests are performed to gain an understanding of the tested material’s performance under dynamic loading through its Resilient Modulus (M_r).

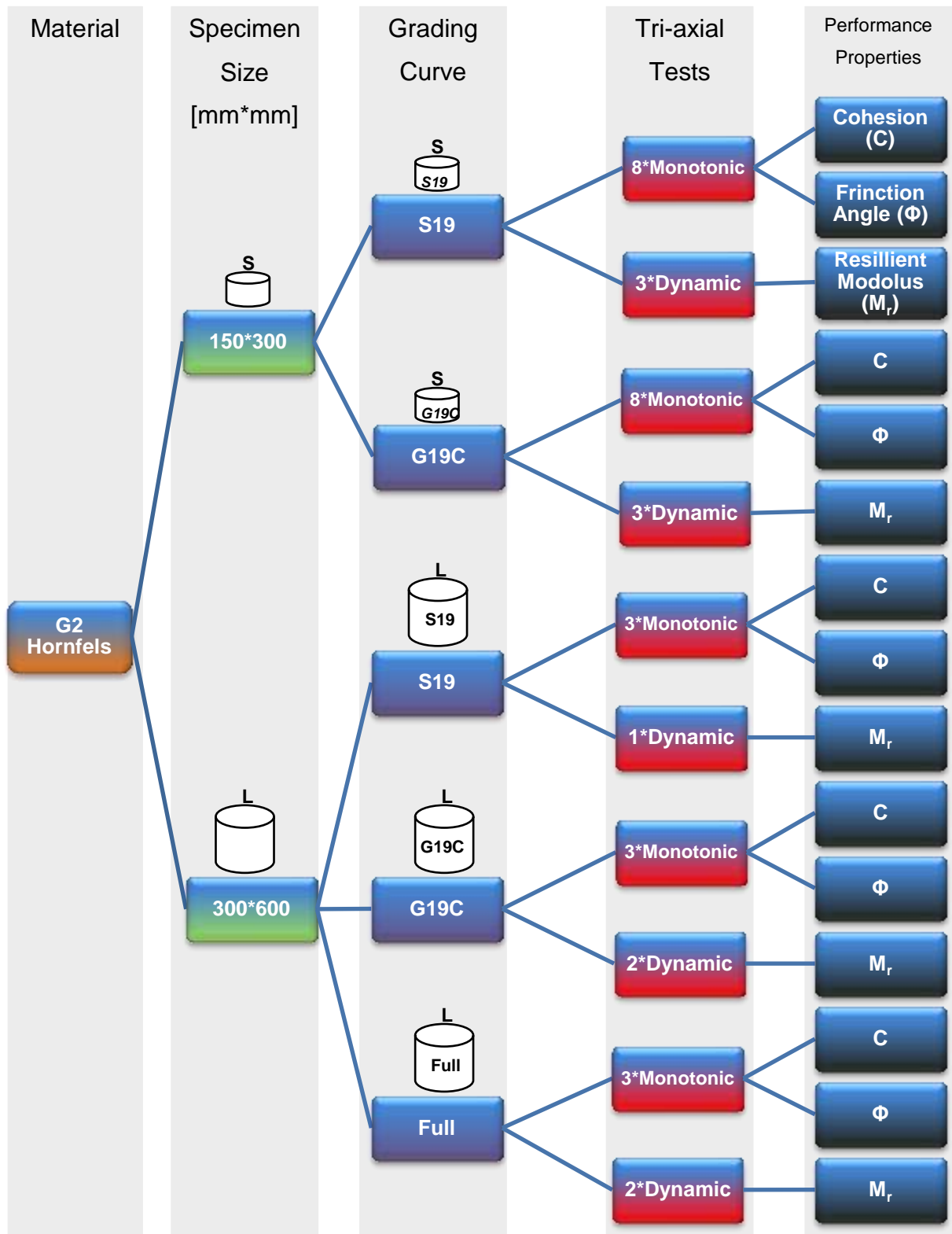


Figure 3- 1: Flow Chart of the Experimental Design

Note that the experimental design allows for the investigation of the influence of grading curve on the performance properties through the comparison of the adjusted grading curves (S19 and G19C) to that of the Full grading curve. In addition, the

influence of sample geometry can also be investigated through the comparison of different sized specimens prepared using similar grading curves and tested under similar conditions.

3.3 Material Procurement and Testing

Only one material type was selected for testing, see Section 3.2. Four tons of G2 graded crushed hornfels stone was delivered to Stellenbosch University by Lafarge Aggregates situated at the Tygerberg Quarry. The material, delivered by truck, was stockpiled and covered for future use.

Three grading curves were selected for testing. The initial material grading was broken down through sieving the material into various fractions, which, at a later stage, would be reconstituted to create the required grading curves. The material therefore had to be air-dried to allow for the sieving. The material was spread on the floor in a room with sufficient ventilation and left to dry. Once the material dried out sufficiently it was placed in bags, sealed and moved to the sieving room. This allowed for careful control of specimen preparation.

3.3.1 Sieving

Sieving commenced once the material reached sufficient moisture content (air-dried). A large-scale vibratory sieve, shown in Figure 3-2 was used to sieve the material into the fractions shown in Table 3-1 to the right.

The various fractions were then bagged and labelled accordingly.

Table 3- 1: Sieve Sizes

Sieve Size [mm]
26.5
19
13.2
9.5
4.75
2.36
1.18
0.6
0.425
0.3
0.15
0.075



Figure 3- 2: Vibratory Sieve

3.3.2 Grading

Once the material was sieved and bagged the various material fractions were combined to create the desired grading. As mentioned, three grading curves were selected for testing (*S19*, *G19C* and *Full*). The *S19* and *G19C* grading curves originate from the *Full* grading as explained below.

3.3.2.1 S19

As explained in Section 3.2, the *S19* grading is obtained from the *Full* grading, by scalping and removing all material particles retained on the 19mm sieve. The modification, which is shown by Figure 3-3, is a common method used in laboratory sample preparation as it allows for material specimens, with large particles, to be tested using small-size testing equipment

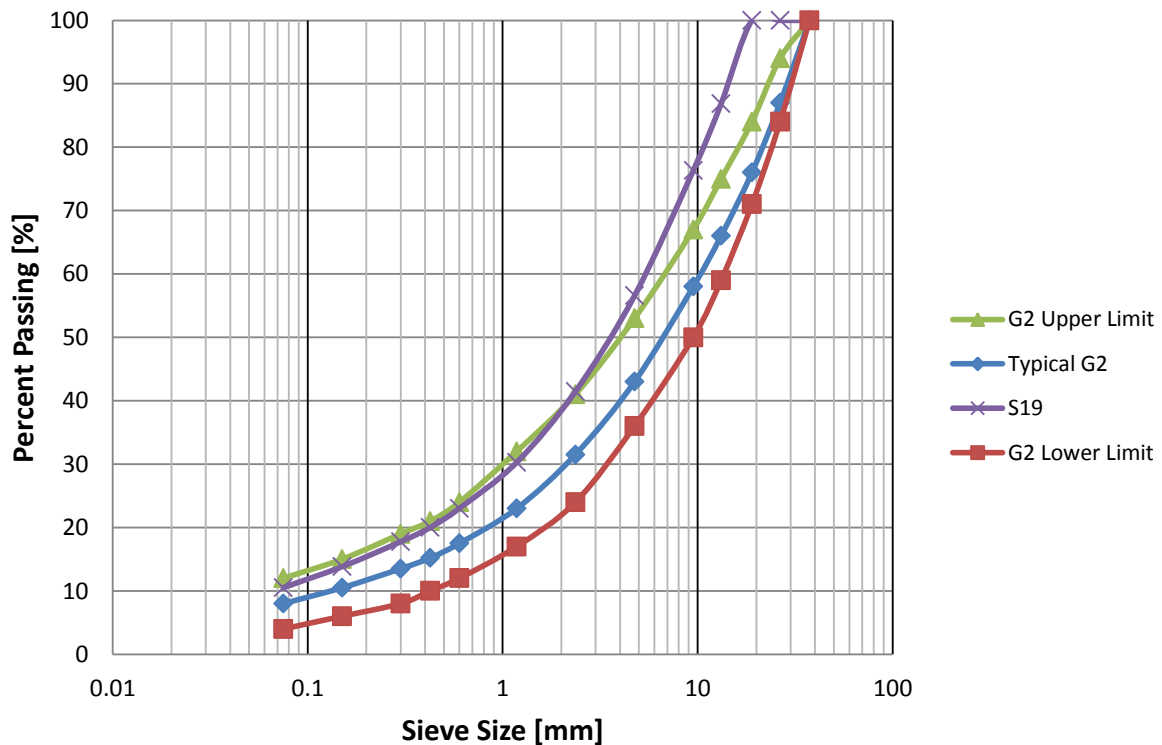


Figure 3- 3: S19 Grading Curve

Note that, although the parallel-scalping method, represented by the *S19* grading shown in Figure 3-3, is a commonly used method to manipulate the true grading curve, it exhibits drawbacks. As can be seen from Figure 3-3, implementation of this modification method results in an upward movement of the grading envelope, parallel to that of the original grading and thereby makes the grading finer.

The reason for the common use and implementation of this grading modification however, is the scale of common testing equipment. Most research institutes utilise small-scale testing equipment and therefore, to allow for the minimum recommended ratio between sample diameter and maximum particle size, remove the larger material particles. The easiest and most efficient method used to remove these particles is the parallel-scalping method, which, as mentioned, results in a finer

grading, not representative of the true in-situ grading. Therefore, a more accurate representation of the typical grading is required.

3.3.2.2 G19C

The *G19C* grading curve, which is also derived from the *Full* grading and an alternative to the *S19*, is shown in Figure 3-4. This grading curve is obtained by scalping the particles greater than 19mm and adding the mass scalped back as particles retained on the 13.2mm sieve but passing the 19mm sieve, see Section 3.2.

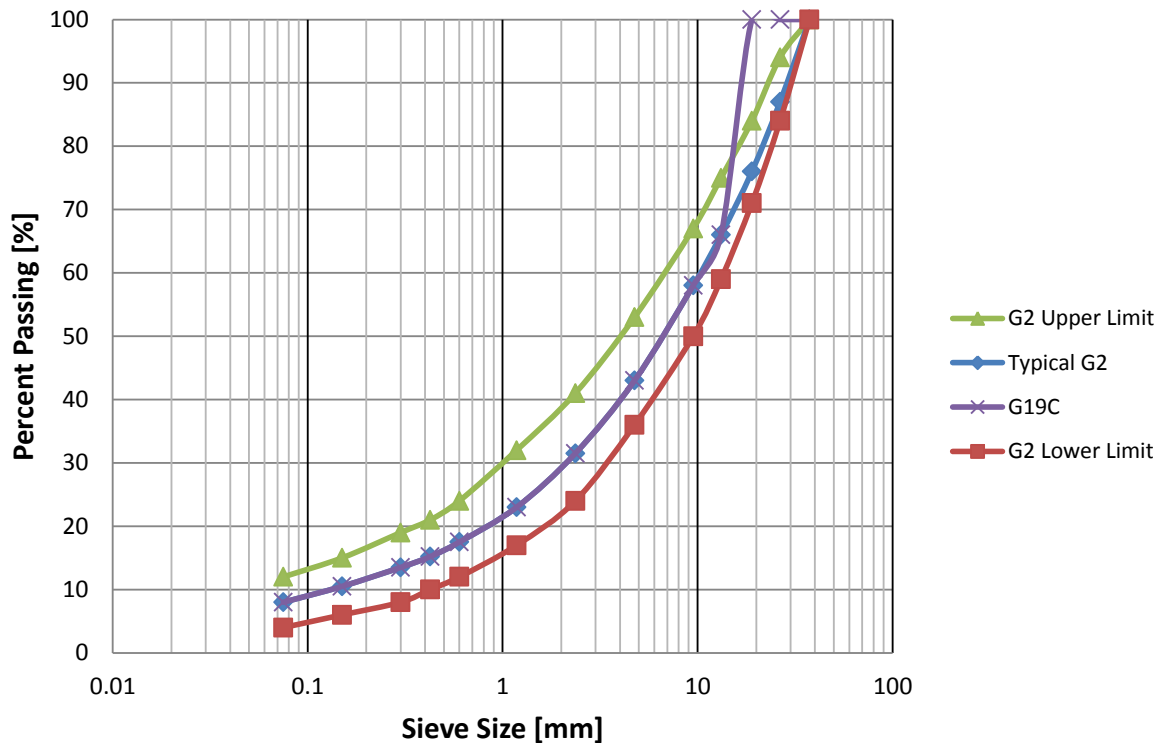


Figure 3- 4: G19C Grading Curve

Note that, except for the material fraction greater than 13.2mm, the *G19C* grading curve fits that of the *Typical/Full* G2 grading precisely. In addition, the mass of the scalped particles is replaced by the addition of particles with similar characteristics to that of the original particles retained on the 19mm sieve.

3.3.2.3 Full

The *Full* grading curve is an unmodified curve simulating that of the original grading. None of the material fractions are removed or reduced thus, the *Full* grading, shown in Figure 3-5, fits that of the *Typical* G2 grading precisely.

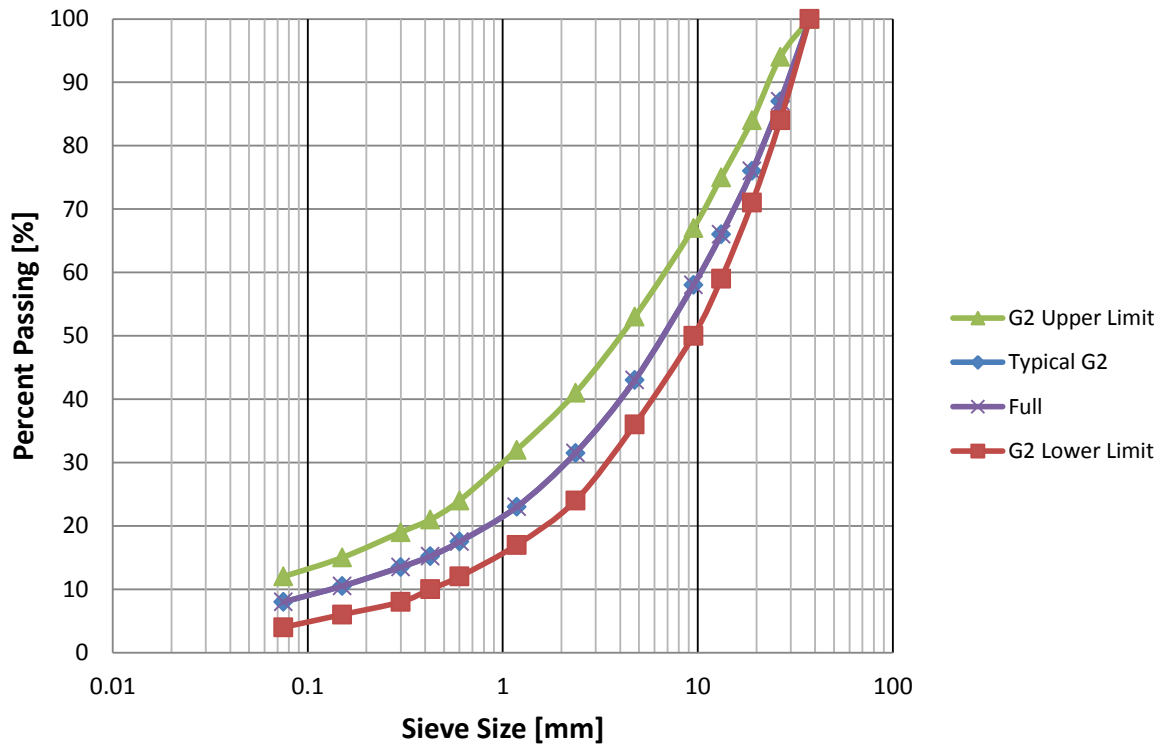


Figure 3- 5: Full Grading Curve

3.3.3 Moisture-Density Relation

From the literature reviewed (see Subsection 2.3.2), it is clear that compaction plays an important role in the performance of unbound granular materials. The literature also showed that the moisture content (MC) of the material specimen being compacted influences the density achieved. By applying equal compactive energy on material specimens containing different MC 's, a Density-Moisture relationship can be established. From this relationship, shown in Figure 3-6 below, the maximum dry density (MDD) of the material specimen, under the respective compactive energy, can be established. Note that at optimum moisture content (OMC), the material specimen is compacted to its MDD for the applied compactive energy.

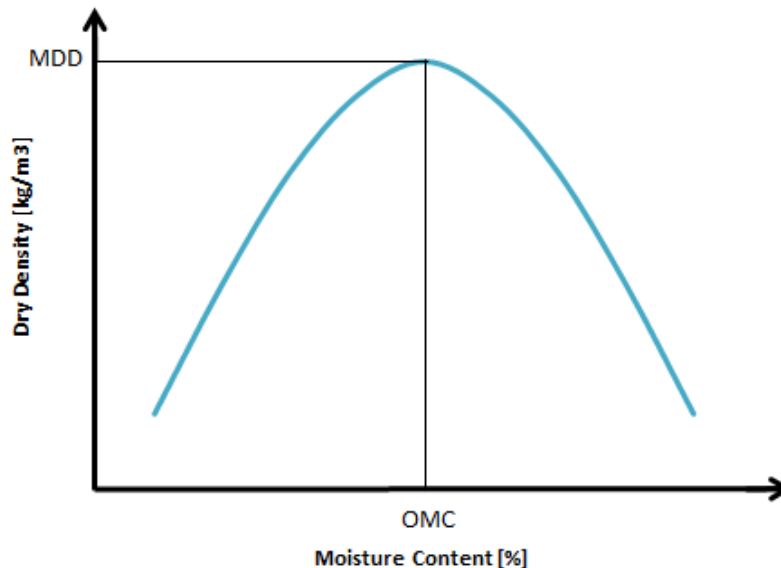


Figure 3- 6: Typical Density-Moisture Relationship Curve

The standard method for establishing a Density-Moisture relationship is presented in Method A7 of the TMH1 (1986). In this method, the Modified AASHTO compaction method, which applies impact energy, is used for testing. This however does not accurately simulate infield construction conditions as the most commonly used compaction method for crushed stone materials applies vibratory energy. It is believed that laboratory characterisation needs to incorporate methods that simulate infield conditions. Therefore, for a more accurate simulation of infield compaction, the impact energy applied by the Modified AASHTO compaction method, used in Method A7, is replaced with vibratory energy from a vibratory hammer compaction apparatus.

As mentioned, this research will compare different grading curves and samples sizes. In addition, the literature reviewed showed that density and moisture content influence the performance properties of unbound granular materials. Therefore, Density-Moisture relationships, for each grading curve associated with each sample size, had to be developed. From these different Density-Moisture relationships an universal moisture content had to be selected that could be used to achieve equal densities for each of the grading curves tested at each specimen size. In other words, all specimens had to be prepared with equal moisture content and compacted to the same density.

3.3.3.1 Density-Moisture Relationship for Small-size Specimens

The Density-Moisture relationship for small-size specimens (150mm Φ * 300mm H), was established using a method similar to Method A7 of the TMH1 (1986) with the Modified AASHTO compaction apparatus being replaced with the vibratory hammer apparatus shown in Figure 3-7.



Figure 3- 7: Small-scale Vibratory Hammer Setup with Bosch Hammer

As shown in Section 3.2, two grading curves (*S19* and *G19C*) are tested using small-size specimens. The procedure used during this research for establishing the Density-Moisture relationship for small-size specimens follows:

- Step A1: Combine the required material fractions to obtain roughly 5kg of the required grading curve.
- Step A2: Measure the required mass of dry material (± 5 kg per moisture variable) as well as the moisture to be added.
- Step A3: Add the moisture and mix thoroughly.
- Step A4: Weight off 2500gr of wet material and keep remaining material for calculation of the *MC*.

Step A5: Place 2500gr of wet material in vibratory hammer mould and compact until refusal density (no further increase in density) is achieved.

Step A6: Remove compacted specimen and note the mass in grams (M), average of three height measurements in mm (h) and the diameter in mm (D). Use Equation 3-1 below together with the noted measurements to determine the specimen density in kg/m^3 .

$$\text{Density [kg/m}^3] = \frac{M}{\pi * (\frac{D^2}{4}) * h} * 10^6 \quad 3-1$$

Step A7: Use the remaining material to determine the MC of the mixed material using Method A7 of the TMH1 (1986).

Step A8: Once the MC is determined using Step A7, use the density calculated in Step A6 and Equation 3-2 below to determine the dry Density in kg/m^3 (DD).

$$\text{Dry Density} = \frac{\text{Density}}{1 + \frac{MC\%}{100}} \quad 3-2$$

Step A9: Repeat steps A1-A8 for three additional MC 's (increments of 1%) and plot each DD (vertical axis) versus its associated MC (horizontal axis) as shown by Figure 3-6. This plot, referred to in this report as the initial Density-Moisture relation, contains 4 point.

Step A10: Once all four points have been plotted, identify the MC that would yield the MDD and repeat steps A1-A8 to confirm the density. Add this 5th point to the initial Density-Moisture curve to obtain the final Density-Moisture relation curve.

As mentioned, two grading curves ($S19$ and $G19C$) are tested using the small-scale vibratory hammer. The initial (before the 5th point of Step A10 was plotted) Density-Moisture relationship curves for these two grading curves are shown by Figure 3-8 below. As reference, Appendix A provides the raw data from the associated testing.

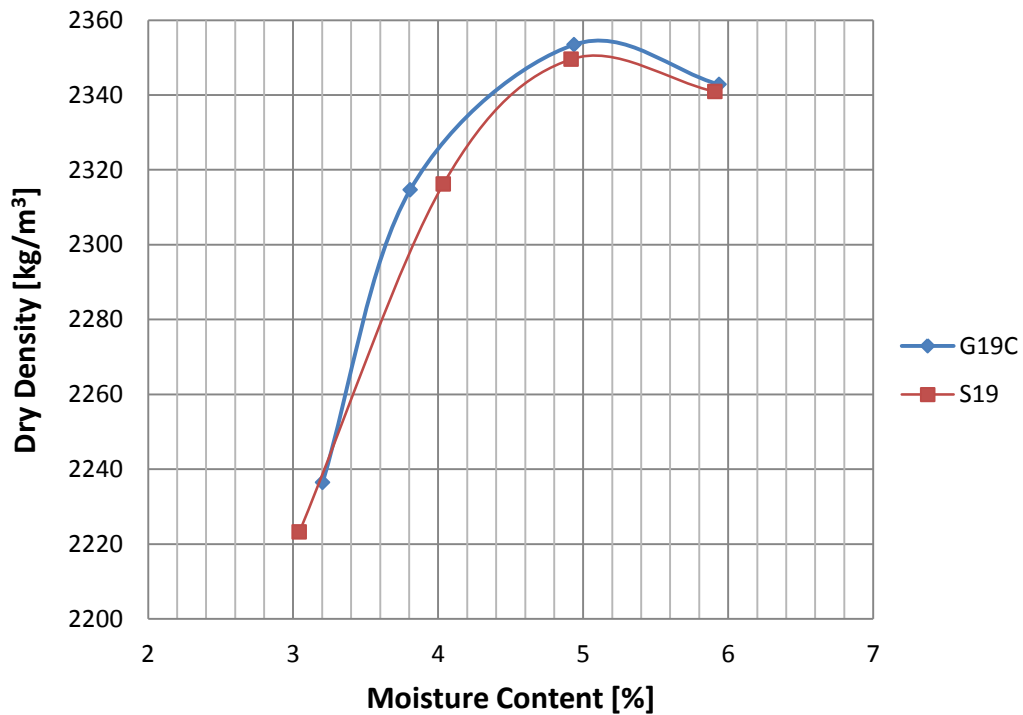


Figure 3- 8: Initial Density-Moisture Relationship Curve for Small-scale Vibratory Hammer

It should be noted from Figure 3-8 above that the *MDD*, for both grading curves, would be achieved at a *MC* close to 5.1%; or this would at least have been the case if the Modified AASHTO compaction method were used. However, during compaction with the vibratory hammer, as shown by Figure 3-9, it was noted that, at both 5.0 and 6.0% moisture, a material slush was forced from the mould. This indicated that there was an excess of moisture. Therefore, although the *OMC* seemed to be at 5.1%, a 5th point at 4.7% moisture was tested.



Figure 3- 9: Material Slush Forced from Mould at Excessively High Moisture Contents

Because of the material slush being forced from the mould, Step A10 was carried out using 4.7% moisture. Figure 3-10 shows the addition of the 4.7% moisture.

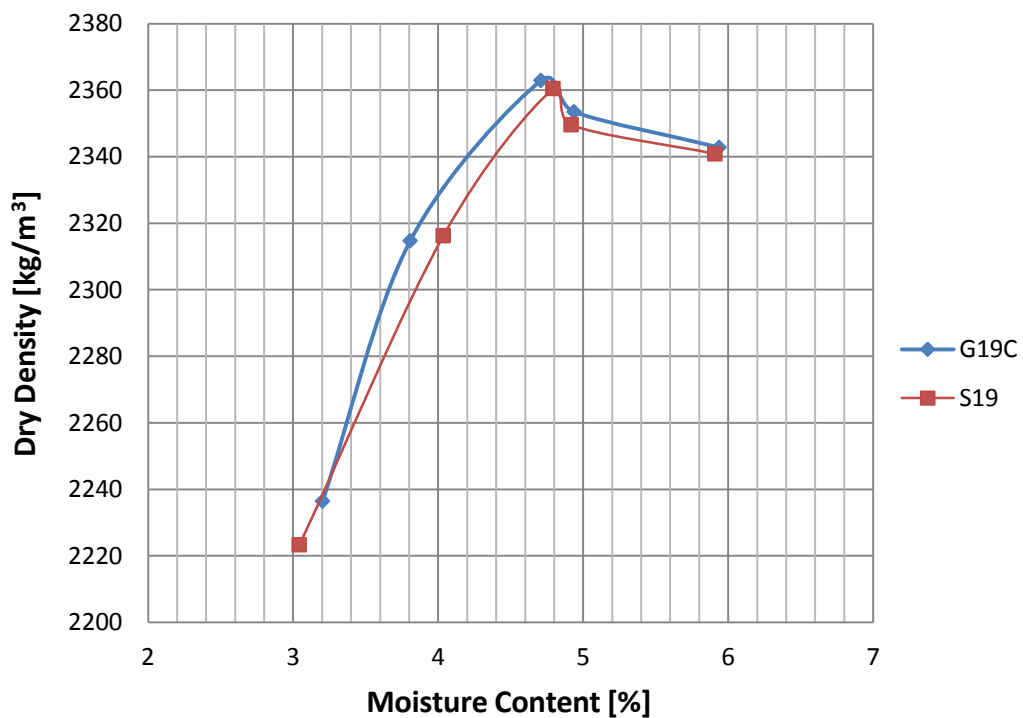


Figure 3- 10: Final Density-Moisture Relationship Curve for Small-scale Vibratory Hammer

Note that Figure 3-10 confirms the belief that the *OMC* for both grading curves is less than 5.0%. At 5% moisture both grading curve yield dry densities of about 2350kg/m³ whereas *MDD*'s of around 2360kg/m³ is reached at 4.7% moisture.

Interestingly, a significant and sudden decrease in dry density is noted for an increase in moisture from 4.7 to 5.0%. This shows that the compaction achieved for a

crushed stone material, using a vibratory hammer, is very sensitive to moisture variations close to the materials *OMC*.

A further point to note is the shape of the relationship curve for moisture contents below and above *OMC*. A significant increase in density is noted as the moisture content is increased from 3% up to the *OMC*. A further increase in moisture content however, above that of the *OMC*, sees only a slight change in density with the relationship curve flattening as the moisture content is increased further.

As mentioned earlier, excessive high moisture contents, higher than the *OMC*, result in slushing of fines during compaction. With only fines being slushed from the mould, a further increase in moisture content does not result in a significant change in density as

3.3.3.2 Density-Moisture Relationship for Large-size Specimens

Similar to the determination of the Density-Moisture relationship for small-size specimens, a variation to Method A7 of the TMH1 (1986) was used to establish the relation between density and *MC* for large-size (300 mm ϕ * 600 mm H) specimens. The Modified AASHTO compaction method was again replaced with a vibratory hammer. The vibratory hammer used to compact the large specimens is shown in Figure 3-11 below.



Figure 3- 11: Large-scale Vibratory Hammer

As shown in Section 3.2, three grading curves are incorporated into the experimental design for the large-size specimens (*S19*, *G19C* and *Full*). The procedure followed to establish the Density-Moisture relationship for the large-size specimens follow that set out in Paragraph 3.4.3.1 above with the only variation being the mass of material required. Instead of the 5kg of dry material required for small-size testing, 25kg of dry material is required for large-size testing.

For ease of testing, the full Density-Moisture relationship (five testing points) was only determined for the *Full* grading curve. Whereas, for both the *S19* and *G19C* grading curves only one point was tested at an *OMC* close to that of the small-size samples and the large-size *Full* grading curve. The results of the *Full* grading curve are shown in Figure 3-12 below together with the results of the additional two points tested at 4.7% moisture.

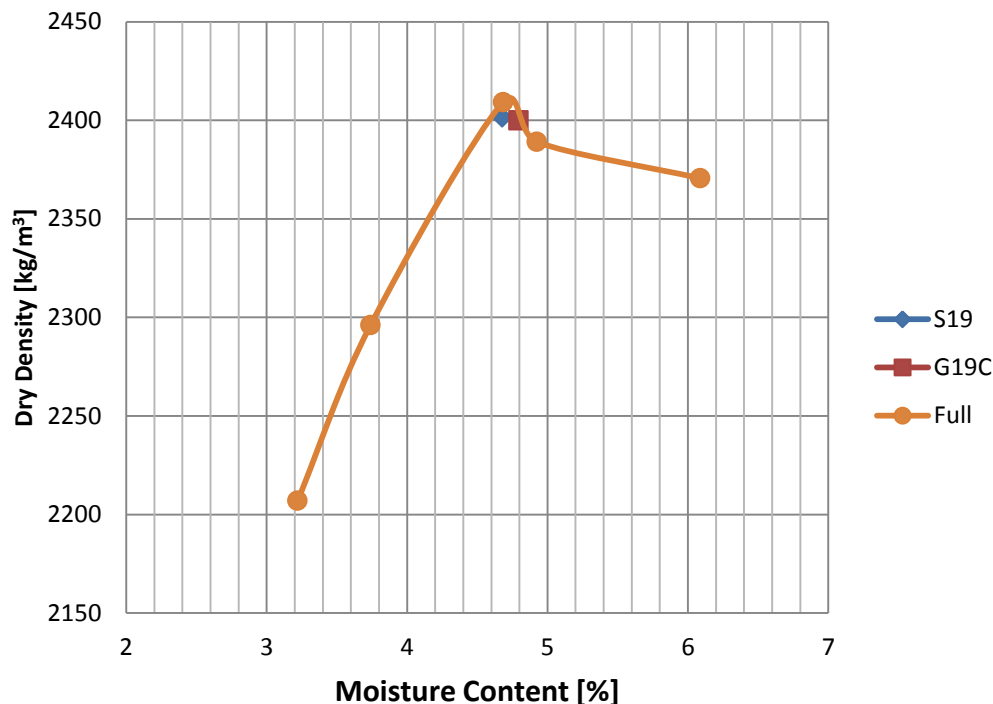


Figure 3- 12: Final Density-Moisture Relationship Curve for Large-scale Vibratory Hammer

Note that the Density-Moisture relationship curve of the *Full* grading curve also shows a sudden decrease in density when compacted with a vibratory hammer at a *MC* slightly greater than the *OMC*. In addition, it should be noted that for the large-scale vibratory hammer compaction, similar densities could be achieved at similar *MC*'s.

3.3.3.3 Comparison

As mentioned, the primary objective of this research study is to establish the influence of grading curve on the performance of an unbound granular material, through monotonic and dynamic tri-axial testing. Therefore, to allow for the comparison of performance properties tested on various grading curves, the tested specimens had to be prepared in an equal manner.

From the literature reviewed in Chapter 2, it is clear that both density and moisture content influence the performance of unbound granular materials. In addition, moisture in the material specimen also influences compaction. Therefore, for the purpose of this study, a single moisture content had to be selected that would allow various grading curves to be compacted to equal densities for both small and large-size specimens.

By combining all of the Density-Moisture relationship curves shown previously, a moisture content common to all of the tested grading curves can be identified that would result in equal densities being achieved during compaction. Figure 3-13 shows the Density-Moisture relationship curves for all of the tested specimens.

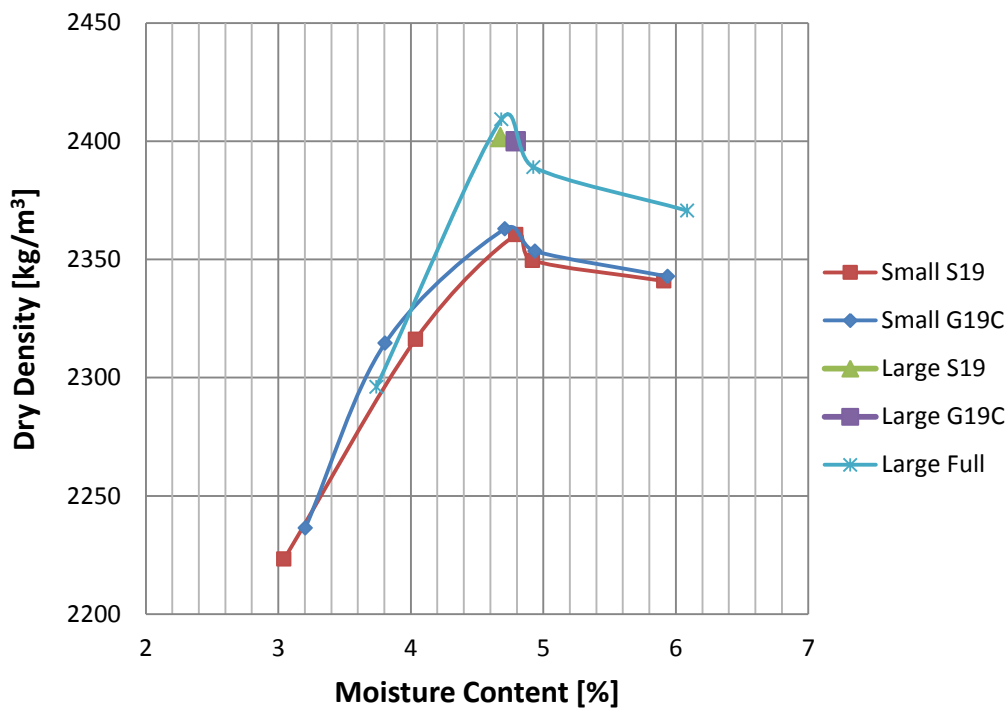


Figure 3- 13: Combined Density-Moisture Relationship Curves

Interestingly, higher densities, at similar *MC*'s, were achieved for specimens compacted using the large-scale vibratory hammer. It is believed (with reference to Craig, 2004) that the compactive energy applied to the material when using the large-scale vibratory hammer is greater than that of the small-scale hammer. As a result, greater densities can be achieved.

This research study requires all specimens to be compacted to an equal density therefore, the density achieved when using the large-scale hammer had to be reduced. As mentioned, the Density-Moisture relationships were established by compacting specimens until refusal density was reached (in other words, the maximum possible compaction that could be achieved using the applied compactive energy). Therefore, lower densities can be achieved by reducing the time that the compactive energy is applied.

Taking all of the above into consideration, a moisture content of 4.7% was identified that could be used and would allow all specimens to be compacted to a target dry density (*TDD*) of 2340kg/m³. Therefore, these two values were used as the compaction moisture content and target dry density for all specimens.

3.4 Testing Methodology

The testing methodology followed in this research study consisted of the following steps:

- Material preparation;
- Mixing of material and moisture;
- Compaction of specimens;
- Curing of specimens to be tested;
- Testing of specimens;
- Determination of moisture content and dry density at testing; and
- Data processing

3.4.1 Material Preparation

As mentioned, the G2 graded crushed hornfels, delivered by Lafarge, was air-dried, sieved into various material fractions, bagged and labelled accordingly. For ease of preparation, the various material fractions were combined, prior to mixing, in bags to contain the mass of material required during mixing.

Due to the limitation of the available mixing equipment, only 25kg of material could be mixed at a time. Therefore, for large-size specimens ($\pm 104\text{kg}$ when wet), five bags of material had to be prepared for each specimen. Each of these bags contained 23kg of dry material of which $\pm 20\text{kg}$ would be used for the specimen itself and $\pm 3\text{kg}$ for moisture calculations. For the small-size specimens on the other hand, only 15kg dry material was required for both the specimen and moisture calculations.

Table 3-2 below gives a breakdown of how the material fractions were combined to yield the required grading and mass of dry material.

Table 3- 2: Breakdown of Material Fraction Combinations for Each Grading and Sample Size

Sieve Size [mm]	S19 Small		G19C Small		S19 Large		G19C Large		Full Large	
	Percent Passing [%]	Mass Retained [gr]	Percent Passing [%]	Mass Retained [gr]	Percent Passing [%]	Mass Retained [gr]	Percent Passing [%]	Mass Retained [gr]	Percent Passing [%]	Mass Retained [gr]
37.5	100.0	-	100.0	-	100.0	-	100.0	-	100.0	-
26.5	100.0	0.0	100.0	0.0	100.0	0.0	100.0	0.0	87.0	2990.0
19.0	100.0	0.0	100.0	0.0	100.0	0.0	100.0	0.0	76.0	2530.0
13.2	86.8	1973.7	66.0	5100.0	86.8	3026.3	66.0	7820.0	66.0	2300.0
9.5	76.3	1578.9	58.0	1200.0	76.3	2421.1	58.0	1840.0	58.0	1840.0
4.75	56.6	2960.5	43.0	2250.0	56.6	4539.5	43.0	3450.0	43.0	3450.0
2.36	41.4	2269.7	31.5	1725.0	41.4	3480.3	31.5	2645.0	31.5	2645.0
1.18	30.3	1677.6	23.0	1275.0	30.3	2572.4	23.0	1955.0	23.0	1955.0
0.60	23.0	1085.5	17.5	825.0	23.0	1664.5	17.5	1265.0	17.5	1265.0
0.425	20.0	453.9	15.2	345.0	20.0	696.1	15.2	529.0	15.2	529.0
0.300	17.8	335.5	13.5	255.0	17.8	514.5	13.5	391.0	13.5	391.0
0.150	13.8	592.1	10.5	450.0	13.8	907.9	10.5	690.0	10.5	690.0
0.075	10.5	493.4	8.0	375.0	10.5	756.6	8.0	575.0	8.0	575.0
Pan	0.0	1578.9	0.0	1200.0	0.0	2421.1	0.0	1840.0	0.0	1840.0
Total Mass [gr]:		15000		15000		23000		23000		23000

3.4.2 Mixing

Uniform distribution of the moisture within a material specimen plays an important role in the performance uniformity of a tested specimen. The literature reviewed showed that moisture within material influences the performance thereof. Non-uniform distribution of the moisture within a material specimen could lead to premature failure or results not representative of the true behaviour. Therefore, the mixing process used had to be such that uniform distribution of the moisture within the material could be achieved.

For the mixing of both small- and large-size specimen, the pan mixer shown by

Figure 3-14 was used.



Figure 3- 14: Pan Mixer used to Mix Material

The process that was followed to get a uniform distribution of the moisture consists of:

- Add dry material to pan;
- Determine the required moisture using Equation 3-3 and measure out (1081gr and 705gr for large- and small-size specimens respectively);

$$W = DM * \frac{MC}{100} \quad 3-3$$

Where: W = mass of moisture [gr]
 DM = mass of dry material [gr]
 MC = moisture content [%]

- Turn on mixer and start mixing the dry material;
- Once dry material is thoroughly mixed, gently add the moisture whilst mixing commences;
- Continue mixing once all the moisture has been added whilst using a small garden spade (see Figure 3-14) to ensure all dry material is loosened from the pan; and

- Finally, switch off the mixer and remove pan containing mixed material

Note that it is important to add the moisture gently. This will assist the uniformity of the mix. A sudden addition of the moisture will result in lumps of wet material forming thereby, leaving some material dry.

3.4.3 Compaction

From the literature reviewed in Chapter 2, it was concluded that compaction has a significant influence on the performance of unbound granular materials. Therefore, to evaluate the influence of grading curve and sample geometry accurately, specimens had to be compacted to equal density.

In addition, it is believed that methods used to prepare laboratory specimens need to simulate in-field construction methods. Furthermore, according to the Interim Technical Guideline 2 of the Asphalt Academy (2009), vibratory hammer compaction yields similar particle orientation to that of construction methods. Therefore, for compaction of both small- and large-size specimens, tested in this research study, the vibratory hammers shown by Figure 3-7 and 3-11 were utilised.

Because of the 2:1 ratio between the height and diameter of tri-axial specimens, uniform compaction cannot be achieved through single layer compaction. Therefore, specimens were compacted in five layers. In addition, as mentioned in Subsection 3.4.3 the material specimens will not be compacted up to refusal density. Therefore, an important part of the compaction procedure used in this research study, is the implementation of a measuring device as an indication of the density achieved during compaction.

Since the final height of small- and large-size specimens need to be 300 and 600 mm respectively, and the diameter of each mould is known, a simple calculation (Equation 3-4 below) can be used to determine the mass of wet material required to yield the desired density at the target layer thickness shown in Table 3-3 (60 and 120 mm per layer for small and large-size specimens respectively). By adding a known mass of wet material, with known moisture content, to a mould with fixed diameter, and controlling the layer thickness to which the material is compacted, the target density can be achieved.

$$WM = TDD * \left(1 + \frac{MC}{100}\right) * \pi * \left(\frac{D^2}{4}\right) * LT * 10^{-6} \quad 3-4$$

Where: WM = mass of wet material [gr]
 TDD = target dry density [kg/m^3]
 MC = moisture content [%]
 D = specimen diameter [mm]
 LT = layer thickness [mm]

Table 3-3 below gives a summary of the layer thicknesses used during compaction, the mass of wet material added to reach the specified layer thicknesses and the cumulative layer thickness and mass, for each specimens size. Furthermore, Figure 3-15 shows the measuring tape placed on the small-scale vibratory hammer (see right hand side) as a form of controlling the layer thickness/density during compaction (see explanation below, Figures 3-15, 17, 18 and 20)

Table 3- 3: Layer Thickness and Mass Data

Layer nr.	Small-Scale (150*300mm)				Large-Scale (300*600mm)			
	Layer Thickness [mm]	Wet Material Mass per Layer [gr]	Cumulative Layer Thickness [mm]	Cumulative Material Mass [kg]	Layer Thickness [mm]	Wet Material Mass per Layer [gr]	Cumulative Layer Thickness [mm]	Cumulative Material Mass [kg]
1	60	2597.68	60	2.60	120	20781	120	20.78
2	60	2597.68	120	5.20	120	20781	240	41.56
3	60	2597.68	180	7.79	120	20781	360	62.34
4	60	2597.68	240	10.39	120	20781	480	83.13
5	60	2597.68	300	12.99	120	20781	600	103.91



Figure 3- 15: Tape Measure Placed on Vibratory Hammer to Control Layer Thickness/Density

Once moisture has been added and the material thoroughly mixed, the wet material was weighed according to the “*Material Mass per Layer*” column in Table 3-3, bagged and sealed to ensure no loss of moisture. These bags were then moved to the specific compactor, ready to be placed in the moulds and compacted.

The next step in the compaction process is the preparation of the specimen mould. For both small- and large-size specimens a split mould system was used as shown in Figures 3-16 (a) and (b) respectively. Prior to adding the mixed material, each mould was cleaned and lubricated to ensure that the compacted specimen could easily be removed from the mould without damage. Cook and spray was used to lubricate the small mould whereas a plastic sheet was placed along the inner surface of the large mould (see Figure 3-19) to separate the material from the moulds’ surface.



Figure 3- 16: (a) Small-scale Split Mould and (b) Large-scale Split Mould

Once the mould is assembled, the vibratory hammer is lowered into the mould until the foot piece rests on the mould’s base plate where after the “zero line” is marked out at the base of the sleeve as shown by Figure 3-17. The material for the first layer is then added and compacted to the ‘Target Dry Density Marker, Layer 1’, as illustrated by Figure 3-18.

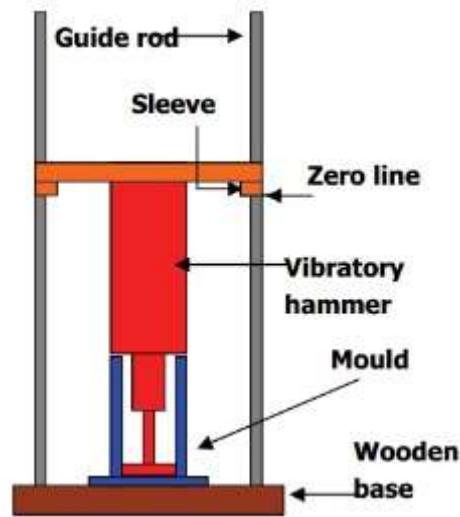


Figure 3- 17: Marking off of Zero Line (Kelfkens, 2008)

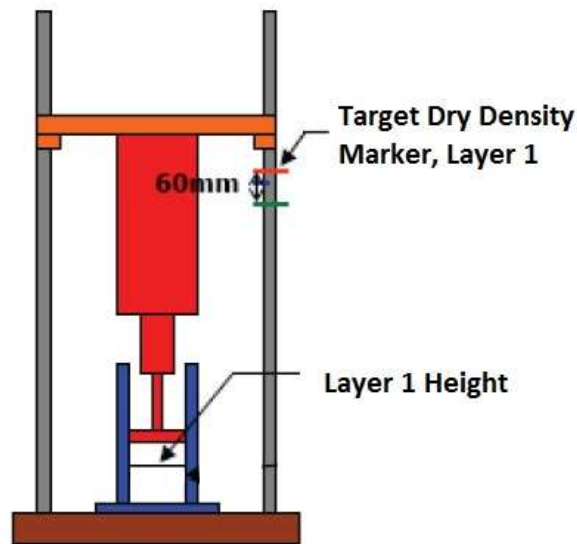


Figure 3- 18: Indicating the Target Dry Density Line (adjusted from Kelfkens, 2008)

As mentioned, both small- and large-size specimens were compacted in five layers. Therefore, to achieve continuity in the bonding between layers, the top of layers 1, 2, 3 and 4 were scarified/broken up before the material for the subsequent layer was added and compacted. The scarifying tool used on large-size specimen layers is shown in Figures 3-19. Note that the tool used for small-size specimens is a scaled down version of the one shown in Figure 3-19.



Figure 3- 19: Scarifying Tools used to Loosen Top of Compacted Layers

After scarification, the material for the subsequent layer is added and compacted to the 'Target Dry Density Marker, Layer 2', as shown by Figure 3-20.

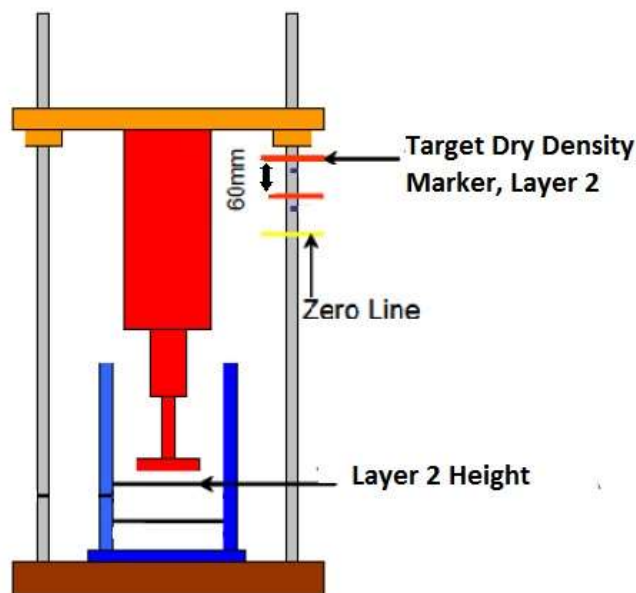


Figure 3- 20: Dry Density Mark for Layer 2 (adjusted from Kelfkens, 2008)

The top of the layer is again scarified to ensure continuity in bonding of layers where after the next layer is compacted. This procedure is performed until the fifth and final layer is added and compacted. Note that no scarification is performed on the top of

the final layer rather, at this stage the compacted specimen is removed from the mould. Importantly, care should be taken when removing specimens from mould in order to limit any damage to the specimen.

Once the specimen has been removed from the mould, specimen measurements had to be noted. These measurements include:

- The exact mass of the specimen;
- The diameter of the specimen to the nearest mm; and
- Three height measurements taken at an offset of 120° around the circumference of the specimen

The measurements noted above were then used to compute the Bulk Density using Equation 3-5 below where after, the true moisture content determined in Sub-section 3.5.2 was incorporated into Equation 3-5 to determine the achieved dry density using Equation 3-6 below.

$$BD = \frac{Mass}{\pi * h * \frac{D^2}{4}} * 10^6 \quad 3-5$$

$$DD = \frac{BD}{1 + \frac{MC}{100}} \quad 3-6$$

Where: BD = bulk density [kg/m³]
 $Mass$ = mass of specimen [gr]
 h = average of three height measurements [mm]
 D = diameter of specimen [mm]
 DD = dry density [kg/m³]
 MC = moisture content [%]

3.4.4 Curing

No standard curing methods, such as the methods used for stabilised materials, were used in this research study. In addition, no accelerated curing (oven drying) was implemented, as no oven that could fit the large-size specimens was available. Rather, for this research study, both small- and large-size specimens were compacted, sealed and left for 24 hours, to allow for redistribution of moisture and initial development of Cohesion, before testing.

It should be noted that the 24 hours curing method does not simulate infield curing processes and does not yield equilibrium moisture content. Further research is required to establish a robust curing method that would yield typical infield moisture contents.

3.4.5 Testing and Data Processing

To achieve the objectives set for this research study, large-size testing equipment capable of testing aggregated greater than 19mm in size, is required. Using small-size equipment for testing large-size aggregate particles yields non accurate results as these results are influenced by the ratio between specimen geometry and maximum particle size. Therefore, to eliminate the influence of this ratio, equipment capable of testing large-size material particles are required. Such equipment, at Stellenbosh University, exist in the form of a large-size tri-axial therefore only tri-axial tests were used to establish the influence of grading curve and specimen geometry on the performance of the tested material.

3.4.5.1 Testing Equipment and Consumables

For both small- and large-size tri-axial testing, a closed loop servo-hydraulic press system, controlled by a MTS Flextest 40 Digital Controller, as shown in Figure 3-21, was used. MTS Multipurpose TestWare software was used to allow interaction between the user and the MTS controller thereby enabling the user to control the devices shown in Figure 3-22 below.



Figure 3- 21: MTS Flextest 40 Controller used for both Small- and Large-size Testing



Figure 3- 22: Small-scale (Left) and Large-scale (Right) Tri-axial Testing Device

It must be emphasised that the two testing devices shown above are not exact

scaled versions of each other. Rather, the large-size testing device is far more modern, with more functionality, than what its small-size counterpart is. Table 3-4 below summarises the important similarities and differences between the two devices shown above.

Table 3- 4: Comparison between Small- and Large-Size Tri-axial Testing Devices

Comparison	Tri-axial Testing Device	
	Small-scale Device	Large-scale Device
Controllable Channels	1 (100kN actuator to apply vertical load)	2 (500kN actuator to apply vertical load and 50kN actuator to apply confinement)
Method of Control	Displacement, Force or Stress	Displacement, Force, Stress with the addition of Confinement for the 50kN actuator
Temperature Control	Yes (0 to 60 °C)	No
Confinement Medium	Air	Water
Confinement Control Method	Manual	Controlled by Actuator
Maximum Vertical Load	100kN	500kN
Maximum Confinement Pressure	250kPa	250kPa
Maximum number of measuring equipment connectable	2* Circumferential and 3* Vertical LVDT's	2* Circumferential and 3* Vertical LVDT's

For both sizes of testing, the MTS Controller allow rapid data capturing of up to 512Hz. The system also allows the user to select the data to be captured and the format thereof. For the purpose of this research study, data was captured at 512Hz and stores as comma-separated files, which could be imported into Excel at a later stage.

Consumables

For both monotonic and dynamic tri-axial tests, to be performed using the equipment shown above, consumable exists. These consumables include:

- O-rings and grease used to seal the tri-axial cell;
- Ribbons and springs used to attach circumferential LVDT's for the small- and large-size testing apparatus respectively; and
- Latex membranes used to cover the entire specimen, allowing confinement pressure to be applied

Except for the latex membranes, all of the other consumables are readily available at spare shops. The latex membranes however had to be manufactured at Stellenbosch as buying these membranes is expensive. Both small- and large-size membranes

were manufactured using latex fluid and the apparatus shown in Figure 3-23.



Figure 3- 23: Equipment used for the Manufacturing of small Latex Membranes

Note that for large-size membranes a larger PVC pipe was used.

The process used to manufacture these membranes is as follows:

- Pour latex fluid into tray;
- Start the motor that turns the PVC pipe;
- Lift the tray containing the latex fluid until the PVC pipe is roughly 10mm deep in the latex fluid;
- Once the entire pipe is covered with latex, lower the tray;
- Keep motor turning at a steady pace (this allows the latex to be distributed evenly around the pipe);
- Remove excess latex fluid from tray and clean the tray thoroughly; and
- Keep motor revolving for 24 hours, allowing the latex to dry, before adding the next layer similarly to that of the first layer

For this research study, to yield a strong yet flexible membrane, three layers of latex were applied to the PVC mould. Figure 3-24 shows the dried first layer of latex where after the second layer is added.



Figure 3- 24: First Layer of Large-size Membrane after Drying

Once the third and final layer has been left for 24 hours, the membrane is removed. Due to the sticky nature of the latex, workability is limited. Therefore, both the inside and outside of the membrane is covered with baby powder which reduces the stickiness and increase workability.

3.4.5.2 Monotonic Tri-axial Test

The monotonic tri-axial test is a simple test, which is commonly used to characterise the shear strength parameters (i.e. Cohesion C and internal Friction Angle ϕ) of pavement materials.

For the purpose of this research study, eight small-size monotonic tests were performed for each of the two small-size grading curve. For the large-size grading curves however, due to the size of specimens and difficulty of testing, only three specimens were tested for each of the three large-size grading curves. Note that, this is discussed further and that the effect of the reduced amount of specimens is taken into account.

Specimen Assembly

The determination of shear strength parameters are such that only the vertical load applied to a specimen and the vertical displacement as a result of the applied load, need to be noted. Therefore, no additional measuring equipment such as LVDT's need to be placed on the tested specimen.

As mentioned, both small- and large-size specimens were cured for 24 hours where after testing commenced. Assembly of small-size specimens occurred as follows:

- Place specimen on the baseplate of the tri-axial cell;
- Cover the specimen with the respective size latex membrane;
- Place top plate on top of the specimen;
- Seal the specimen by placing O-rings and grease on the foot- and top plate;
- Fit outer Perspex cover on top of the tri-axial cells footplate;
- Secure the lid of the tri-axial cell by fastening the necessary nuts and bolts;
- Place tri-axial cell, which now contains the specimen, into the MTS testing equipment;
- Connect pressure hose to cell; and
- Run test

Figure 3-25 shows a small-size tri-axial specimen assembled for monotonic testing.



Figure 3- 25: Small-scale Tri-axial Specimen Assembled for Monotonic Testing

Note that the setup shown contains no additional measuring equipment. Thus, the only data that can be captured is the displacement and force applied of the vertical actuator.

Due to the mass and size of the large-size tri-axial specimens to be tested in this research study, the assembly thereof is not as simple as that of the small-size counterpart.

The first major difference in the assembly of large-size specimens is that the specimens are compacted on top of the baseplate, as shown in Figure 3-26 below.



Figure 3- 26: Large-size Tri-axial Specimen Compacted On Top of Baseplate

Once compaction is complete, the top plate is placed on top of the specimen as shown by Figure 3-26 where after the latex membrane is placed over the specimen and sealed for 24 hours before testing.

The next variation to the procedure explained earlier, is that a two-ton portable crane is used to lift the specimen and place it on top of the tri-axial cell's baseplate. Figure 3-27 below shows a specimen already placed on the baseplate of the cell.

Similarly, to the assembly of the small specimens, the outer Perspex cover is placed on top of the cell's baseplate. Once the Perspex cover has been placed, the six steel bars are screwed into the holes shown on the baseplate where after the top plate is fitted, sealed with grease and fastened to ensure an airtight cell.



Figure 3- 27: Large-scale Tri-axial Specimen Placed on Baseplate

Once the entire cell has been assembled, as shown in Figures 3-28 and 30-31, the cell needs to be placed under the vertical actuator of the large-size tri-axial testing apparatus. This procedure is performed using the two-ton portable crane, a trolley specifically designed and built for this purpose and the vertical actuator itself. The procedure follows:

- Fasten the entire tri-axial cell to the crane (see Figure 3-28);
- Lift the cell until the required height is reached;
- Place the trolley on top of the extended platform of the tri-axial test apparatus (see Figure 3-29);
- Slowly lower the cell onto the trolley and disconnect the crane (see Figure 3-30);
- Push the trolley forwards until the specimen is directly under the vertical actuator;
- Connect the cell to the actuator;
- Use the hydraulic actuator to lift the entire cell from the trolley (see Figure 3-

31);

- Remove trolley from under the hanging cell (see Figure 3-31);
- Slowly lower the cell into place using the actuator (see Figure 3-32);
- Connect pressure hose from 50kN actuator and pressure transducer to cell;
- Fill the cell with water; and
- Run test



Figure 3- 28: Large-size Tri-axial Cell Connected to Portable Crane



Figure 3- 29: Trolley Designed and Built to Assist Moving of Tri-axial Cell



Figure 3- 30: Large-size Tri-axial Cell On Top of Trolley



Figure 3- 31: Large-size Tri-axial Cell being Lifted by the Actuator



Figure 3- 32: Large-size Tri-axial Cell Lowered into Position using Vertical Actuator

Note that even though Figure 3-29 shows additional measuring equipment attached to the specimen, no additional measuring equipment is required. As mentioned on Page 46, the only measurements used to evaluate the shear performance through monotonic testing are that of the vertical actuators applied force and displacement. The use of the vertical actuators displacement however includes the influence of edge effects into the measurement, which affects the measured performance. Therefore, it is recommended that additional measuring equipment be added to monotonic testing apparatuses to limit the influence of edge effects.

Furthermore, since the confinement pressure of the large-size test apparatus is controlled by the MTS system and a pressure transducer, the pressure is also captured for quality control purposes.

Monotonic Test

Once the test specimen has been assembled and the tri-axial cells placed, testing commenced.

As mentioned, eight small-size specimens were tested for each of the two small-size grading curves whereas three large-size specimens were tested for each of the three

large-size grading curves. For small-size testing, two specimens were tested under each of the following confining pressures:

- 25 kPa;
- 50 kPa;
- 100 kPa; and
- 200 kPa

For large-size testing on the other hand, only three specimens were tested under 50, 100 and 200 kPa confinement.

For all of the above confinement pressures and both small- and large-size monotonic tests, a test protocol was programmed into MTS's Multipurpose TestWare that utilises the displacement-controlled mode to apply a constant strain rate of 1% strain. During the test both the displacement of the vertical actuator and the force applied thereof is captured at 512Hz. Additionally, since the large-size tri-axial test apparatus automatically controls the confining pressure, the large-size test protocol had to include a function that utilised a pressure-controlled mode to control the pressure within the cell.

In addition, the test function programmed into the MTS system for both small- and large-size specimens utilised a "Break-detect" function. This function was programmed to end the test once the load applied by the vertical actuator has reached 80% of the failure load. For example, if the maximum applied load was equal to 10kN then the test will end when the applied load reaches 8kN.

To summarise, the basic procedure to perform a monotonic test on the small-size tri-axial test apparatus follows:

- Assemble the cell;
- Manually increase the confinement pressure to the desired pressure; and
- Run the MTS Flextest function programmed for small-size monotonic tests

The procedure used for large-size tri-axial testing is slightly different and includes:

- Assemble the cell; and
- Run the MTS Flextest function programmed for large-size monotonic tests

The final step in the testing of monotonic tri-axial specimens is the determination of

the moisture content at testing. This moisture content is computed by destroying the specimens and using Method A7 of the TMH1 (1986).

Data Processing

The data captured during both small- and large-size monotonic tri-axial tests were processed according to the steps set out in Mgangira et al. (2011).

Step 1: From the data captured, note the maximum applied (P_a^f) for each of the specimens tested. Using the failure load, calculate the applied failure stress ($\sigma_{a,f}$) using Equation 3-7 as shown.

$$\sigma_{a,f} = \frac{P_a^f}{A} \quad 3-7$$

Where: $\sigma_{a,f}$ = applied failure stress [kPa]
 P_a^f = applied failure load [kN]
 A = circular cross-sectional area before test [m²]

Step 2: Calculate the major principal stress at failure ($\sigma_{1,f}$) for each specimen using Equation 3-8. The major principal stress at failure is defined as the sum of the confining stress (σ_3), the stress caused by the dead weight on top of the specimen (σ_{dw}) and the applied failure stress ($\sigma_{a,f}$).

$$\sigma_{1,f} = \sigma_3 + \sigma_{dw} + \sigma_{a,f} \quad 3-8$$

Where: $\sigma_{1,f}$ = major principal failure stress [kPa]
 σ_3 = applied confinement pressure [kPa]
 σ_{dw} = stress caused by dead weight [kPa]

Step 3: Both the Cohesion (C) and internal Friction Angle (φ) can be computed once the relationship between the confining stress (σ_3) and the major principal failure stress ($\sigma_{1,f}$) is known.

According to Mgangira et al. (2011), the relationship is given by Equation 3-9.

$$\sigma_{1,f} = A * \sigma_3 + B \quad 3-9$$

Where: $A = \frac{1+\sin \varphi}{1-\sin \varphi}$ and $B = \frac{2*\cos \varphi}{1-\sin \varphi}$

From the data, $\sigma_{1,f}$ and σ_3 of the tested specimens, a regression analysis is performed to determine the values of A and B .

Step 4: With A and B known, the Cohesion and internal Friction Angle is computed using Equations 3-10 and 3-11.

$$\varphi = \sin^{-1} \left(\frac{A-1}{A+1} \right) \quad 3-10$$

$$C = \frac{B*(1-\sin \varphi)}{2*\cos \varphi} \quad 3-11$$

Where: C = Cohesion [kPa]
 φ = Friction Angle [°]

In addition to the above, which represents the Mohr-Coulomb Model for determining the shear parameters, an additional method, the Drucker-Prager Model in p-q space, can also be used to compute the shear parameters. Although not used to evaluate the influence of grading curve and specimen geometry on the shear performance in this research study, the Drucker-Prager Model does add value in that it considers intermediate principal stresses (Rani et al. 2014). Furthermore, for the Mohr-Coulomb criterion, the major principal stress σ_1 is independent of the intermediate principal stress σ_2 , which leads to underestimating the yield strength of the material (Al-Ajmi and Zimmerman, 2005). This also disagrees with test results reflecting the influence of σ_2 to the strength of the tested material in many cases. A further disadvantage of the Mohr-Coulomb criterion is that the cross-section of the Mohr-Coulomb criterion is six-faceted, due to the irregular hexagon deviatoric plane, rather than smooth as in the case of the Drucker-Prager criterion (Erkens, 2002).

For the purpose of this study, the Drucker-Prager Model is ignored and only shear parameters calculated by means of the Mohr-Coulomb Model is used to evaluate the influence of specimen geometry and grading curve.

3.4.5.3 Short Duration Dynamic Tri-axial Test

The short duration dynamic tri-axial test is a complex test that requires several small measurements, on the tested specimen, during testing. These measurements are used to compute the Resilient Modulus (M_r) of the tested material.

For this research study, three small-size specimens were tested for each of the two small-size grading curves whereas two short duration dynamic tri-axial tests were

performed for each of the three large-size grading curves.

Sample Assembly

The assembly of both small- and large-size tri-axial specimens for dynamic testing follows the same procedure as that of monotonic specimens. The only difference in the procedure is the assembly of the additional measuring equipment required.

As mentioned, the Resilient Modulus is determined by measuring displacements on a specimen when dynamically loaded. The displacement of the middle third of the specimen is required. Therefore, three vertical LVDT's are placed at an offset of 120° around the circumference of the specimen. Note that the two fixed points of each of these LVDT's are at a height of 100 and 200mm, and 200 and 400mm for small- and large-size specimens respectively.

In addition to the vertical LVDT's, two circumferential LVDT's are placed around the centre of the specimens to be tested. The measurements from these LVDT's are used to compute the Poisson's Ratio of the tested specimen.

Figure 3-33 shows a small-size tri-axial specimen assembled and ready for dynamic testing. Note that the assembly of the large-size specimen is similar.

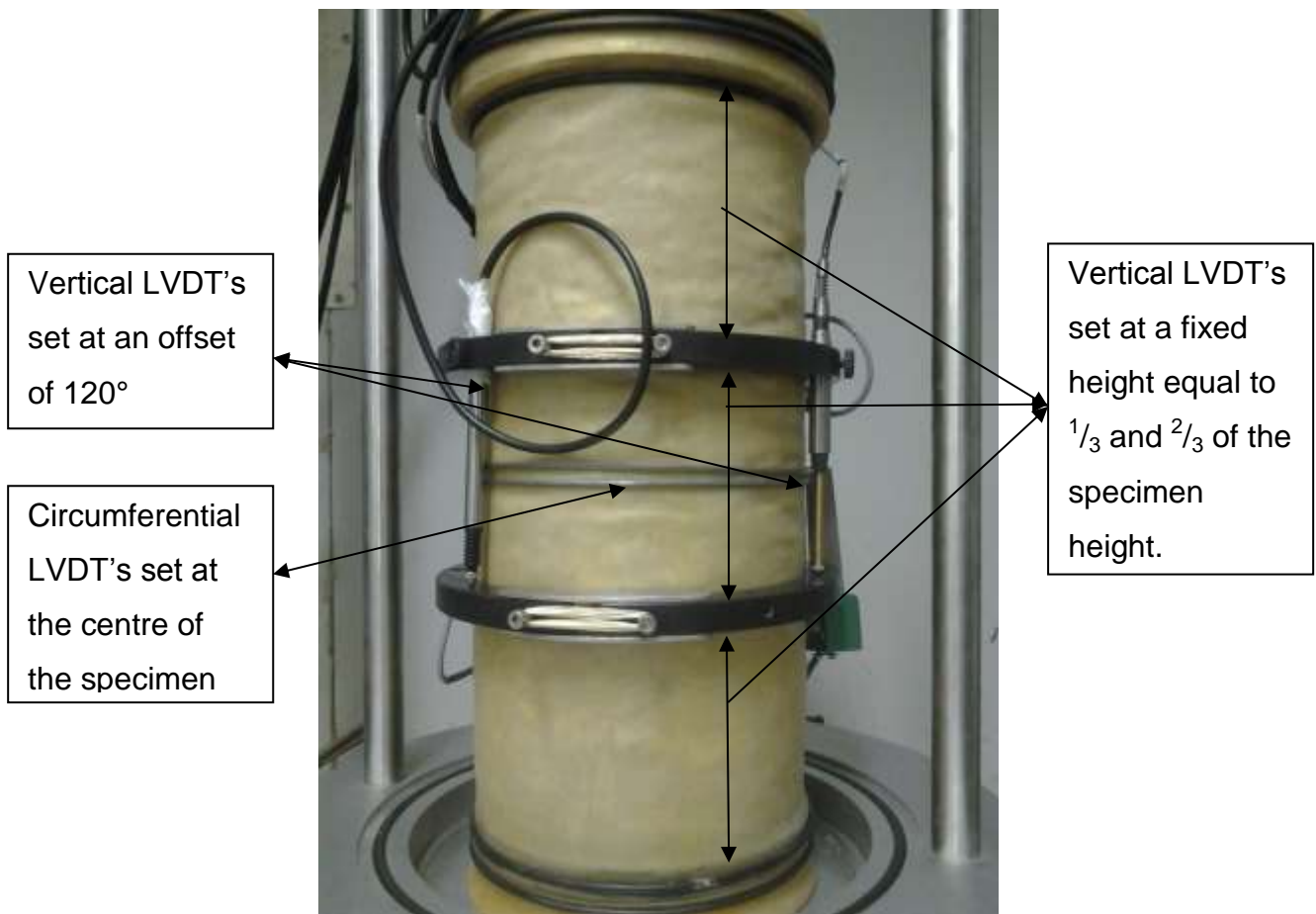


Figure 3- 33: Small-size Specimen Assembled for Dynamic Tri-axial Test

In summary, the specimen assembly process for both small- and large-size specimens are:

- Place specimen into tri-axial cell;
- Place three vertical LVDT's at an offset of 120° apart in the centre third of the specimen;
- Place two circumferential LVDT's at the centre of the specimen;
- Fit the top plate of the tri-axial cell whilst connect the cables for each measuring device to the cables connected to the MTS Controller;
- Places assembled cell in the chamber or onto the platform for small- and large-size testing apparatus respectively;
- Connect the pressure hoses; and
- Run Test

Short Duration Dynamic Test

Once the test specimen has been assembled and the tri-axial cell placed, testing commenced.

As mentioned, three small-size specimens were tested for each of the two small-size grading curves whereas two short duration dynamic tri-axial tests were performed for each of the three large-size grading curves.

All of the above-mentioned specimens were tested using a pre-programmed MTS function that incorporates a haversine load phase combined with a resting period, as shown by Figure 3-34 below. The one-second load cycle shown, consists of:

- A 0.05 seconds loading phase; followed by
- A 0.05 seconds unloading phase; and finally
- A 0.9 seconds resting period

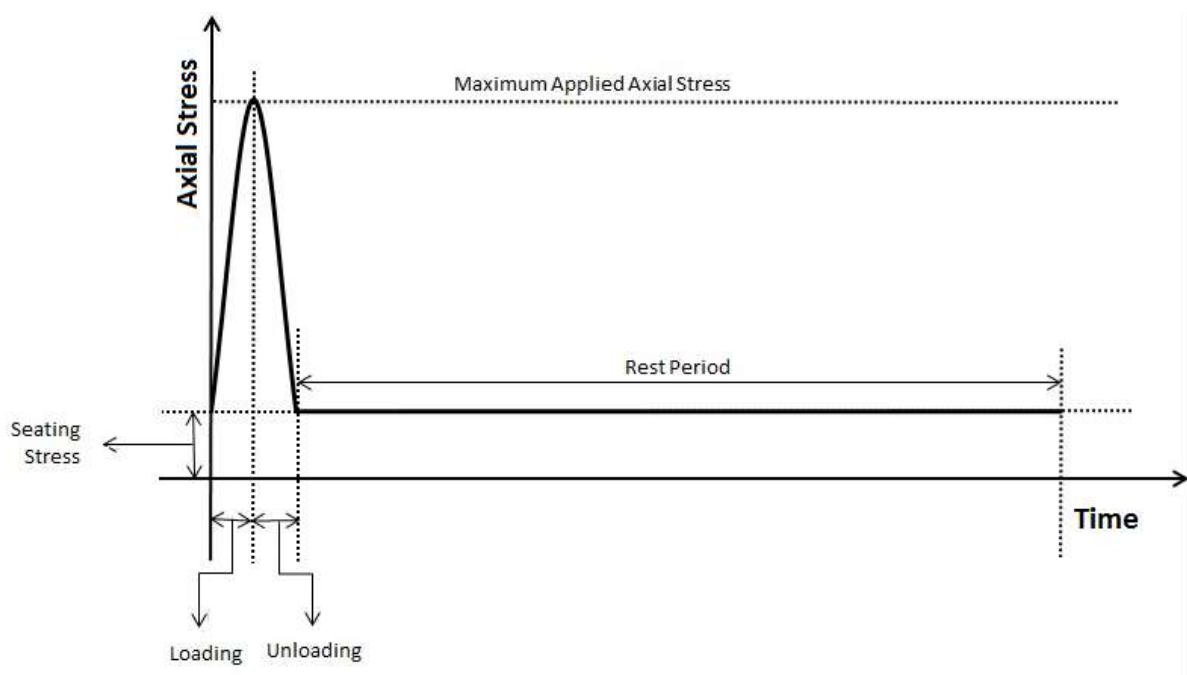


Figure 3- 34: A Single Load Cycle for the Short Duration Dynamic Tri-axial Test

Furthermore, the programed MTS function consists of a conditioning phase, where 750 load cycles are applied to the specimen, using a force-controlled mode, under a constant confinement pressure of 200 kPa. During this phase, the 750 load cycles are distributed by five Stress Ratios (10, 20, 30, 40 and 55% of the maximum failure stress computed through monotonic testing at the specific confinement) as illustrated in Table 3-5 below.

Table 3- 5: Loading Regime for Short Duration Dynamic Tri-axial Test

Test Phase	Confinement Pressure [kPa]	Stress Ratio as Percentage of Monotonic Failure Stress				
		10%	20%	30%	40%	55%
Conditioning	200	100 cycles	100 cycles	150 cycles	200 cycles	200 cycles
Production	200	100 cycles	100 cycles	100 cycles	100 cycles	100 cycles
	150	100 cycles	100 cycles	100 cycles	100 cycles	100 cycles
	100	100 cycles	100 cycles	100 cycles	100 cycles	100 cycles
	50	100 cycles	100 cycles	100 cycles	100 cycles	100 cycles
	25	100 cycles	100 cycles	100 cycles	100 cycles	100 cycles

Once the conditioning of the test specimen has completed, the MTS function allows the production phase to start. In this phase, as shown by Table 3-5, 100 load cycles are applied to the specimen, again using the force-controlled mode, for each of the five increasing Stress Ratios and their respective confining pressures (starting at 200 kPa and working down to 25 kPa).

In addition to the above, the MTS programed function is programed such that it will required specimen specific input variables from the user. These variables include 25 maximum applied loads, each representing the five Stress Ratios and their five respective confining pressures. Note that these variables are specimen specific and are computed from the respective specimen's monotonic test results. The procedure used to compute these variables is explained below, followed by Table 3-6 which presents a summary of the loading schedule used for each short duration dynamic tri-axial test.

The load variables required during short duration dynamic tri-axial testing are computed as follows:

- Determine the specimen's shear parameters (C and φ) using monotonic tri-axial test results;
- Compute the confinement specific failure stress using the shear parameters determined above, each of the five confining pressures and Equation 3-12.

$$\sigma_d^f = \sigma_3 * \tan^2\left(\frac{\varphi}{2}\right) + 2C \tan\left(45 + \frac{\varphi}{2}\right) \quad 3-12$$

Where:

- σ_d^f = Failure stress [kPa]
- σ_3 = Confinement pressure [kPa]
- φ = internal Friction Angle [°]
- C = Cohesion [kPa]

- Determine the maximum applied load, for each of the specific Stress Ratios and the respective confining pressures, using Equation 3-13.

$$L_{max} = SR * \sigma_d^f * \pi * \frac{D^2}{4} / 10^8 \quad 3-13$$

Where:

- L_{max} = maximum applied load [kN]
- SR = Stress Ratio [%]
- σ_d^f = failure stress from Equation 3-11 [kPa]
- D = diameter of specimen [mm]

Note that Table 3-6 gives two values for the minimum applied load or seating load during each load cycle. A value of 0.4 and 1.5 kN is used for small- and large-size specimens respectively. In addition, Table 3-6 further provides the load cycles to be recorded. Note that for each loading phase and its respective confinement and Stress Ratio, the data during the first and final five loading cycles are recorded. For both small- and large-size testing, data is captured at a rate of 512Hz and include the following data points:

- Three vertical LVDT readings [mm];
- Two circumferential LVDT readings [mm];
- Vertical displacement of vertical actuator [mm];
- Force applied by vertical actuator [kN]; and
- Time/duration of test [s]

As stated earlier, the confining pressure for small-size testing needs to be controlled manually whereas the large-size apparatus utilises an actuator to control confinement. Therefore, for large-size testing the confining pressure applied [kPa], by the 50kN actuator is also captured.

Table 3- 6: Summary of Loading Schedule used for Short Duration Dynamic Tri-axial Test

Cycles	Loading Phase	Confining Pressure [kPa]	Stress Ratio [%]	Maximum Applied Force [kN]: Equation 3-11 and 3-12	Minimum Applied Force or Seating Load [kN]	First and Last Five Cycles to be Recorded	
0-100	Conditioning	200	10	$\sigma_f^d(200)*0.1*\pi*(D^2/4)$	0.4 or 1.5	0-5, 96-100	
101-200			20	$\sigma_f^d(200)*0.2*\pi*(D^2/4)$	0.4 or 1.5	101-105, 196-200	
201-350			30	$\sigma_f^d(200)*0.3*\pi*(D^2/4)$	0.4 or 1.5	201-205, 346-350	
351-550			40	$\sigma_f^d(200)*0.4*\pi*(D^2/4)$	0.4 or 1.5	351-355, 546-550	
551-750			55	$\sigma_f^d(200)*0.55*\pi*(D^2/4)$	0.4 or 1.5	551-555, 746-750	
751-850	Production	200	10	$\sigma_f^d(200)*0.1*\pi*(D^2/4)$	0.4 or 1.5	751-755, 846-850	
851-950			20	$\sigma_f^d(200)*0.2*\pi*(D^2/4)$	0.4 or 1.5	851-855, 946-950	
951-1050			30	$\sigma_f^d(200)*0.3*\pi*(D^2/4)$	0.4 or 1.5	951-955, 1046-1050	
1051-1150			40	$\sigma_f^d(200)*0.4*\pi*(D^2/4)$	0.4 or 1.5	1051-1055, 1146-1150	
1151-1250			55	$\sigma_f^d(200)*0.55*\pi*(D^2/4)$	0.4 or 1.5	1151-1155, 1246-1250	
1251-1350		150	150	10	$\sigma_f^d(150)*0.1*\pi*(D^2/4)$	0.4 or 1.5	1251-1255, 1346-1350
1351-1450				20	$\sigma_f^d(150)*0.2*\pi*(D^2/4)$	0.4 or 1.5	1351-1355, 1446-1450
1451-1550				30	$\sigma_f^d(150)*0.3*\pi*(D^2/4)$	0.4 or 1.5	1451-1455, 1546-1550
1551-1650				40	$\sigma_f^d(150)*0.4*\pi*(D^2/4)$	0.4 or 1.5	1551-1555, 1646-1650
1651-1750				55	$\sigma_f^d(150)*0.55*\pi*(D^2/4)$	0.4 or 1.5	1651-1655, 1746-1750
1751-1850		100	100	10	$\sigma_f^d(100)*0.1*\pi*(D^2/4)$	0.4 or 1.5	1751-1755, 1846-1850
1851-1950				20	$\sigma_f^d(100)*0.2*\pi*(D^2/4)$	0.4 or 1.5	1851-1855, 1946-1950
1951-2050				30	$\sigma_f^d(100)*0.3*\pi*(D^2/4)$	0.4 or 1.5	1951-1955, 2046-2050
2051-2150				40	$\sigma_f^d(100)*0.4*\pi*(D^2/4)$	0.4 or 1.5	2051-2055, 2146-2150
2151-2250				55	$\sigma_f^d(100)*0.55*\pi*(D^2/4)$	0.4 or 1.5	2151-2155, 2246-2250
2251-2350		50	50	10	$\sigma_f^d(50)*0.1*\pi*(D^2/4)$	0.4 or 1.5	2251-2255, 2346-2350
2351-2450				20	$\sigma_f^d(50)*0.2*\pi*(D^2/4)$	0.4 or 1.5	2351-2355, 2446-2450
2451-2550				30	$\sigma_f^d(50)*0.3*\pi*(D^2/4)$	0.4 or 1.5	2451-2455, 2546-2550
2551-2650				40	$\sigma_f^d(50)*0.4*\pi*(D^2/4)$	0.4 or 1.5	2551-2555, 2646-2650
2651-2750				55	$\sigma_f^d(50)*0.55*\pi*(D^2/4)$	0.4 or 1.5	2651-2655, 2746-2750
2751-2850	25	25	10	$\sigma_f^d(25)*0.1*\pi*(D^2/4)$	0.4 or 1.5	2751-2755, 2846-2850	
2851-2950			20	$\sigma_f^d(25)*0.2*\pi*(D^2/4)$	0.4 or 1.5	2851-2855, 2946-2950	
2951-3050			30	$\sigma_f^d(25)*0.3*\pi*(D^2/4)$	0.4 or 1.5	2951-2955, 3046-3050	
3051-3150			40	$\sigma_f^d(25)*0.4*\pi*(D^2/4)$	0.4 or 1.5	3051-3055, 3146-3150	
3151-3250			55	$\sigma_f^d(25)*0.55*\pi*(D^2/4)$	0.4 or 1.5	3151-3155, 3246-3250	

To summarise, the basic procedure used to perform a small-size, short duration, dynamic tri-axial test, follow:

- Assemble the specimen and tri-axial cell;

- Manually increase confinement to 200kPa for conditioning;
- Run the MTS Flextext function programmed for small-size dynamic testing;
- Input the variables required by the MTS test function; and
- Manually change confining pressure when required to

The procedure used for large-size testing is less complex and include the following steps.

- Assemble the specimen and tri-axial cell;
- Run the MTS Flextext function programmed for small-size dynamic testing; and
- Input the variables required by the MTS test function

Finally, similar to that of the monotonic test, the moisture content and dry density at testing is determined from the tested specimens.

Data Processing

As mentioned, the short duration dynamic tri-axial test was used to evaluate the resilient response of the tested material. The Resilient Modulus was used as an indicator of the resilient response and the determination thereof was based on the definition shown in Figure 3-35 below.

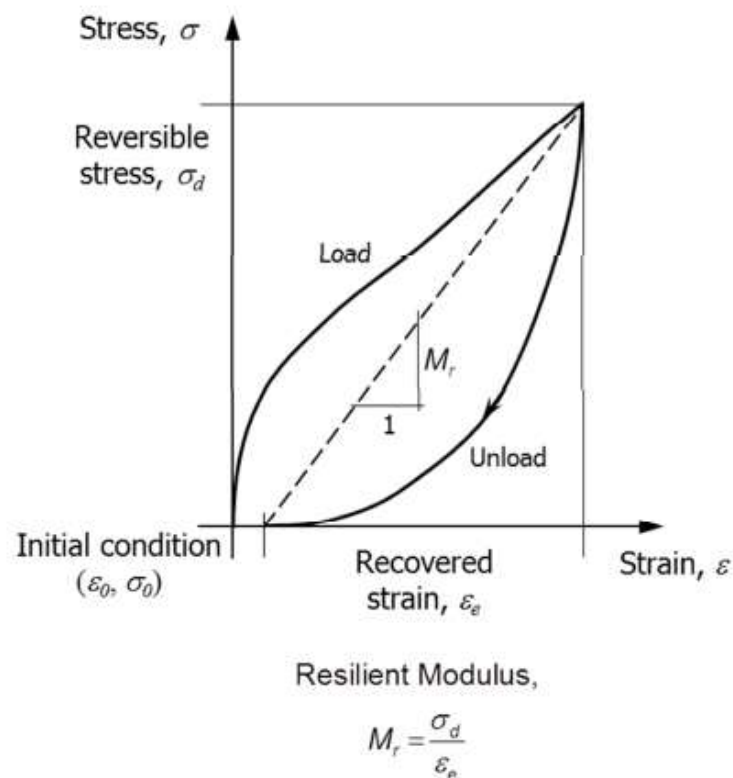


Figure 3- 35: Resilient Modulus Definition and Calculation (Theyse, 2012)

The procedure used to compute the Resilient Modulus as set in Figure 3-35 follows the method explained by Mgangira et al. (2011). Within this method it is required that, for each of the last five load cycles of every applied Stress Ratio and every confining pressure level, the following shall be determined.

- The minimum (LVDT_{min}) and maximum (LVDT_{max}) deformation reading for each of the three on specimen LVDT's:

This allows for the calculation of the average axial deformation, of the middle third of the specimen, during each load cycle, using Equation 3-14.

$$\Delta\delta_{a(N)} = \frac{\sum_{i=1}^{i=3}(LVDT_{i,max} - LVDT_{i,min})}{3} \quad 3-14$$

Where:

$\Delta\delta_{a(N)}$	= average axial deformation per load cycle N [mm]
$LVDT_{i,max}$	= maximum deformation on i^{th} LVDT [mm]
$LVDT_{i,min}$	= minimum deformation on i^{th} LVDT [mm]
N	= cycle number [-]
i	= LVDT number [-]

- The resilient axial strain per load cycle:

The resilient axial strain is calculated using Equation 3-15.

$$\epsilon_{a(N)} = \frac{\Delta\delta_{a(N)}}{L_g} \quad 3-15$$

Where:

$\epsilon_{a(N)}$	= resilient axial strain [-]
$\Delta\delta_{a(N)}$	= average axial deformation per load cycle N [mm]
L_g	= gauge length [mm]

Note that, gauge length is defined as the length between the fixed LVDT points. For this research study, 100mm and 200mm gauge lengths were used for small- and large-size testing respectively.

- The cyclic stress per load cycle:

The cyclic stress per load cycle is defined as the difference in maximum - and minimum stress applied to the specimen. As mentioned, fixed seating loads of 0.4 and 1.5kN were used as the minimum load on small- and large-size specimens respectively whereas the maximum loads applied to the specimens

are shown in Table 3-6. Equation 3-16 can be used to determine the cyclic stress per load cycle.

$$\sigma_{cyclic(N)} = \frac{L_{max(N)} - L_{min(N)}}{A} \quad 3-16$$

Where: $\sigma_{cyclic(N)}$ = the Nth cycle's cyclic stress [kPa]
 $L_{max(N)}$ = maximum load during Nth cycle [kN]
 $L_{min(N)}$ = minimum load during Nth cycle [kN]
 A = circular cross-sectional area of specimen [m²]

- Resilient Modulus per load cycle:

As defined by Figure 3-35, the Resilient Modulus for each load cycle shall be calculated using Equation 3-17.

$$M_{r(N)} = \frac{\sigma_{cyclic(N)}}{\epsilon_{a(N)} * 1000} \quad 3-17$$

Where: $M_{r(N)}$ = Resilient Modulus per load cycle [MPa]
 $\sigma_{cyclic(N)}$ = the Nth cycle's cyclic stress [kPa]
 $\epsilon_{a(N)}$ = resilient axial strain [-]

- The average Resilient Modulus of the last five load cycles per loading sequence:

As mentioned, the data for the last five load cycles of each loading sequence is captured. Therefore, to incorporate each of the five cycles' data, an average Resilient Modulus is computed using Equation 3-18.

$$M_r = \frac{\sum_{j=1}^{j=5} M_{r(N)}}{5} \quad 3-18$$

From the data processing shown above, several graphs were prepared. These graphs are shown in the following chapter where the results are analysed and discussed.

3.5 Trouble Shooting

As mentioned in the introduction to this dissertation, the objectives of this research study could only be achieved through the further development of an existing large-size tri-axial testing apparatus. This section is dedicated to introduce the reader to

the some preliminary testing that was done and to briefly explain the modifications that were made to the existing apparatus.

3.5.1 Preliminary Testing

Since the capabilities of the existing large-size tri-axial apparatus was unknown, several preliminary tests were performed, together with Mrs Chantal Rudman, lecturer at the Stellenbosch University's Civil Engineering Department, to become acquainted with the apparatus and its capabilities.

The tests ranged from low to high frequency pressure tests and incorporated both static and dynamic, vertical loading and pressure control. A draft report (Rudman, 2012), has been drafted based on initial testing which shows and explains all modifications made to allow commissioning and testing of large tri-axial apparatus.

A key element mentioned in the draft report, which should be highlighted, is the positioning of the pressure transducer during variable confinement testing. During the first preliminary test conducted, it was observed that, at high frequencies, the actual pressure within the tri-axial cell did not correspond to that of the pressure demand. An investigation was launched and it was concluded that the cell pressure was in fact lower than the pressure measured by the pressure transducer. Figure 3-36 shows the layout of the testing apparatus.

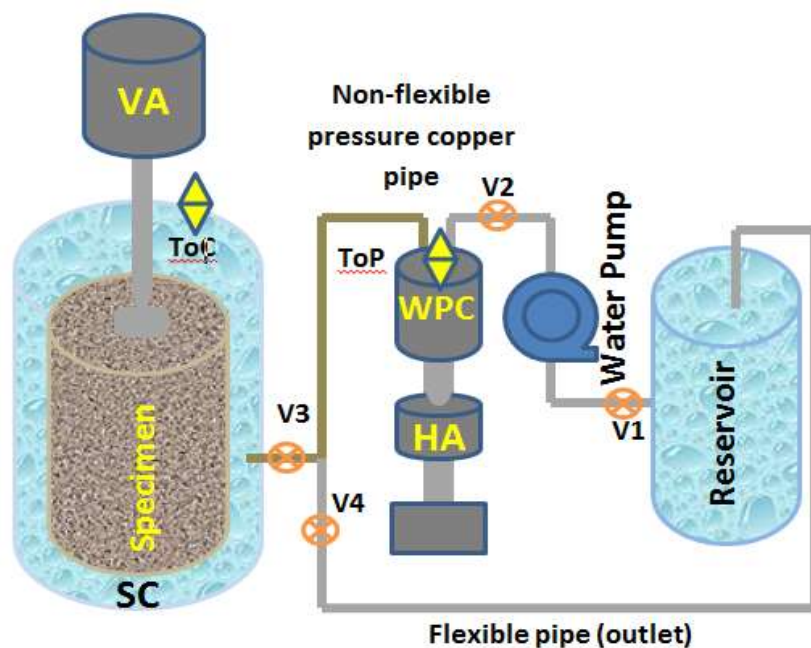


Figure 3- 36: Layout of Large-size Tri-axial Testing Apparatus (Rudman, 2012)

Initially, with the pressure transducer attached directly above the 50kN actuator (which controls the cell pressure) on top of the Top of Pressure Cylinder (ToP in Figure 3-36), variable confinement demands were not transferred to the tri-axial cell. Rather, due to friction within the pipe system connecting the pressure controller to the tri-axial cell, a premature pressure built-up existed before the pressure could be transferred to the cell itself (i.e. the pressure transducer measured the demanded pressure before the demanded pressure reached the cell).

The pressure transducer was repositioned on the Top of the Specimen Cylinder (ToC in Figure 3-36) and it was observed that the internal cell pressure was equal to that of the commanded pressure for both static and variable confinement pressures. At this stage, both static and dynamic tri-axial test could be performed without hassle.

With the above modification made, more tests were performed and it was confirmed that:

- Monotonic tri-axial test could be performed with accurate control of the confining pressure up to 350 kPa and applying a vertical force up to 250 kN.
- Dynamic control of the confinement pressure was capable for confining pressures up to 300 kPa at frequencies up to 10 Hz.
- Application of a dynamic vertical load was possible up to load of 100 kN at frequencies up to 5 Hz.

3.5.2 Dynamic Tri-axial Testing

After the successful testing of all large-size monotonic tri-axial specimens, large-size short duration dynamic tri-axial tests were performed. The test apparatus, at low Stress Ratios (forces lower than 100 kN) and low frequencies (less than 5 Hz), seemed to perform as expected. However, the test protocol applied required forces in excess of 100 kN at frequencies of 10 Hz to be applied. The combination of great forces at high frequencies resulted in successive movement in the support structure. The movement caused by high Stress Ratios resulted in movement of the entire tri-axial cell which in turn caused water leaks in the pipe system. In addition, such excessive movement is dangerous and could cause damage to the testing apparatus. Therefore, modifications were made to increase the rigidity of the support frame.

The modifications that were brought to the large-size tri-axial apparatus include:

- Placing of spacer blocks to level the existing platform (see Figure 3-37 below);
and



Figure 3- 37: Spacer Blocks used to Level Tri-axial Platform

- Increasing rigidity of existing platform by fixing it to the support structure below (see Figures 3-38 and 39)



Figure 3- 38: Drilling of Holes through Platform and Support Beams



Figure 3- 39: Fixing of Platform to Support Beams to Increase Rigidity

The above-mentioned modifications increased the rigidity thereby reducing movement of the tri-axial cell. To confirm this, a dynamic test was performed and even at the highest Stress Ratio of 55% the test was conducted in a safe manner without any excessive movement. Dynamic loading could be performed under safe conditions for the following:

- Dynamic loading up to 200 kN for frequencies up to 10 Hz.

For further reading on the trouble shooting of the large-size tri-axial test apparatus please refer to Rudman (2012).

3.6 Summary

Chapter 3 is summarised as follows:

- An experimental design was developed that incorporates two specimen sizes (small *S* and large *L*) and three grading curves (*S19*, *G19C* and *Full*) to allow for investigation of the influence of grading curve and specimen size.
- Small-size specimens were prepared using the two adjusted gradings (i.e. *S-S19* and *S-G19C*) whereas large-size specimens were prepared using the two adjusted gradings and the full in-situ G2 grading (*L-S19*, *L-G19C* and *L-Full*).
- The G2 material procured was dried and sieved into various material fractions to allow for accurate control of specimen preparation.
- Moisture-Density relationship curves were developed, using vibratory

compaction, for all grading curves and used to identify a single moisture content that would yield a single target dry density for both specimen sizes.

- All material gradings were mixed by adding 4.7% moisture and mixing it through with a pan mixer.
- Once the material has been thoroughly mixed, the wet material, for both specimen sizes, was placed in split moulds and compacted to the desired density using the measuring apparatus mentioned in Sub-section 3.4.3.
- Importantly, since the material tested is an UGM, no standard curing method was applied; rather, material specimens were left for 24 hours to allow redistribution of moisture and development of initial Cohesion.
- Two types of performance tests were performed to evaluate the performance of the selected material gradings; monotonic and dynamic tri-axial tests.
- Monotonic tri-axial tests were used to evaluate the shear performance (Cohesion and Friction Angle) and short duration dynamic tri-axial tests to evaluate the resilient response (Resilient Modulus) of the tested specimens.
- Monotonic test results were compared for specimens tested for a range of 50, 100 and 200 kPa confining pressures.
- Short duration dynamic tri-axial test were performed for a range of confining pressures reducing from 200 to 150, 100, 50 and 25 kPa for Stress Ratios increasing from 10 to 20, 30, 40 and 55%.
- Adjustments and improvements were brought to the large-size tri-axial testing apparatus to allow safe performing of tests and to ensure that test results were uninfluenced by the testing apparatus.

CHAPTER 4: ANALYSIS AND DISCUSSION OF RESULTS

4.1 Introduction

This chapter is dedicated to present, interpret and discuss all test results relevant to the experimental design. In addition, this chapter also presents results of additional testing, performed to gain a better understanding of the representative parent material's behaviour.

Firstly, quality control results are presented and discussed where after, with reference to the research objectives, the material shear parameters, evaluated through monotonic tri-axial testing, are analysed. In the final section of this chapter, dynamic tri-axial test results are presented and discussed.

4.2 Quality Control

As mentioned in earlier sections of this report, both moisture content and density significantly influences the performance of UGM's. Therefore, to allow accurate comparison of performance properties, for specimens with different geometry and grading curve, both the moisture content within specimens and the densities to which these specimens are compacted, had to be similar.

For all specimens prepared and tested the mixing moisture content, dry density after compaction and moisture content after testing was computed and noted. From these results, graphs were prepared showing the consistency of the moisture content in relation to the target moisture content of 4.7% and the density achieved as a percentage of the target dry density of 2340 kg/m³, as determined in Sub-section 3.3.3.

4.2.1 Small-size Specimens

Figure 4.1 shows a graph illustrating the mixing and compaction quality control that was implemented for both grading curves of small-size specimens. Note that Figure 4-1 summarises the data for more small-size specimens than were originally set out in the experimental design. These extra specimens were used for additional testing which will be explained at a later stage in this chapter.

It is clear from Figure 4.1, that small-size specimens were compacted to close proximity to the target dry density (see vertical axis on left). For the quality control purposes of this research study, a variation of $\pm 1\%$ in relation to the target dry density

was allowed (i.e. an upper dry density limit of 2360 and a lower limit of 2320 kg/m³ was set).

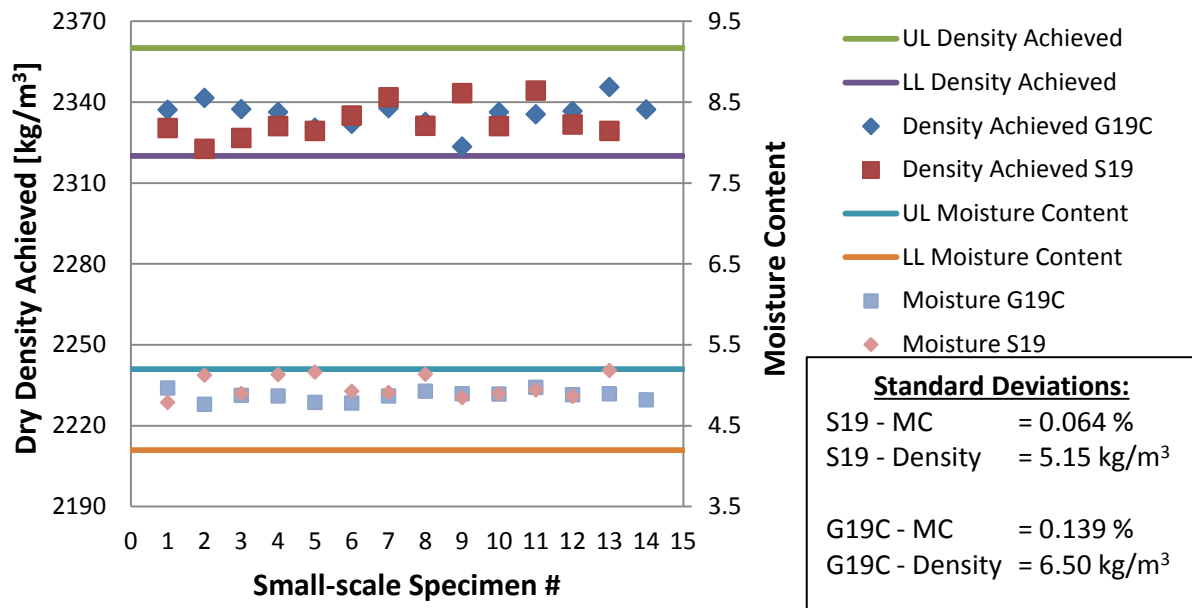


Figure 4- 1: Small-size Specimen Quality Control Summary

In addition to the high level of density control (standard deviations of 5.15 and 6.50 kg/m³ for *S19* and *G19C* grading curves respectively), the mixing/compaction moisture content (see vertical axis on right) was also carefully controlled (standard deviations of 0.064 and 0.139 % moisture for *S19* and *G19C* grading curves respectively). Only specimens with moisture contents within 0.5% moisture either side of the target moisture content, were tested (i.e. an upper limit of 5.2% and a lower limit of 4.2% moisture was set).

It should be noted that, for both grading curves, the mixing moisture content, although within the limits set, is closer to the upper limit than the lower limit (i.e. slightly higher than the target moisture content). This phenomenon, although not explained in Chapter 3, most likely results from the incorporation of the material's hygroscopic moisture content into the mixing moisture content.

The hygroscopic moisture content for each material grading curve was determined and accounted for by removing the computed mass of hygroscopic moisture from the moisture to be added during mixing. The hygroscopic moisture contents however were computed using material that was air dried for a longer period to that of material used during specimen preparation. As a result, it is plausible that the material used during specimen preparation contained slightly higher hygroscopic moisture contents

than the material used during the testing of the hygroscopic moisture content. This, in turn, will slightly increase the moisture content during mixing and compaction by the difference in tested hygroscopic moisture content and true hygroscopic moisture content. e.g. If the tested hygroscopic moisture content is 0.2% then only 4.5% moisture needs to be added during mixing to reach the target 4.7% moisture. If however, the hygroscopic moisture content during specimen preparation is 0.3%, then the addition of 4.5% moisture will yield a mixing and compaction moisture content of 4.8%, 0.1% higher than the target moisture content.

Although the influence of moisture content on the performance of UGM's is significant, the impact of the variation in hygroscopic moisture content is so small that it would have an insignificant influence on the findings of this report. However, a specimen prepared with a variation in moisture content that results in the mixing and compaction moisture content of a specimen falling outside of the set limits, would have been removed from the testing envelope and repeated.

Once compacted, specimens were sealed and left standing for 24 hours before testing. This is done to allow the unbound material to develop some initial cohesion before testing. Therefore, to allow for accurate comparison of tested specimens, the effect of curing on the moisture content at testing had to be controlled. For the purpose of this study, the moisture content after testing was used as an indication of the variability in curing.

Figure 4-3 shows the variation in moisture content of specimens after testing. When compared to Figure 4-1 for the same specimens, a reduction in moisture content is evident. This shows that even though the specimens were sealed directly after compaction, using plastic bags, the 24 hour curing process does result in a slight reduction in moisture content.

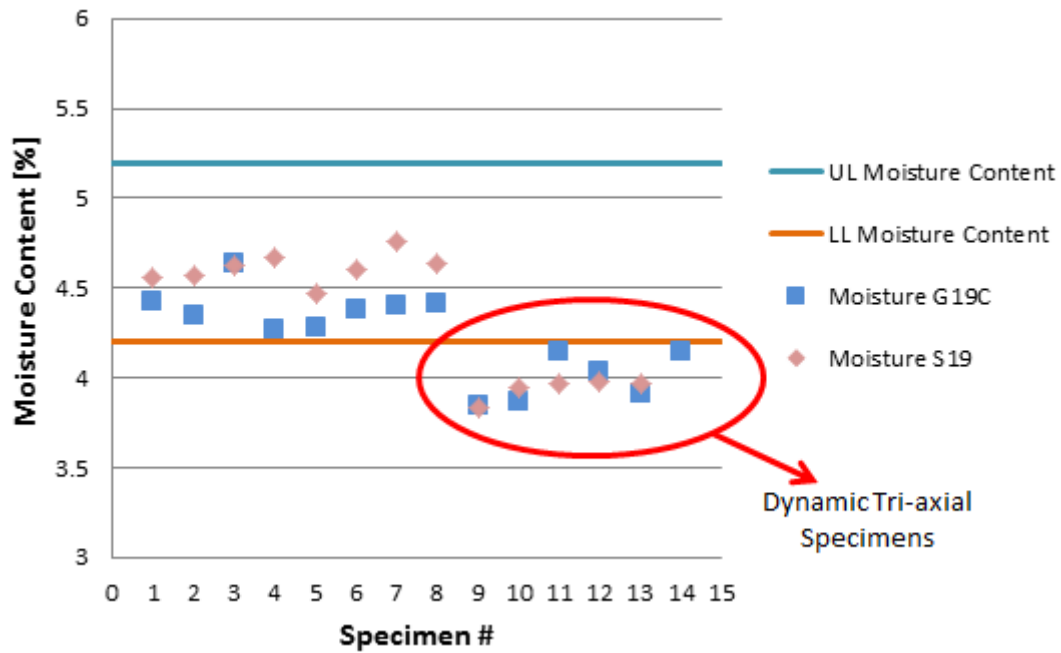


Figure 4- 2: Small-size Specimen Moisture Variation after Testing

Figure 4-3 shows the small-size specimens sealed in plastic. Note that some moisture, originally added to the specimens, adheres to the plastic bag’s surface thereby reducing the moisture content within the specimen. This reduction in moisture prior to testing will influence the moisture content after testing, as seen in Figures 4-1 and 4-2.



Figure 4- 3: Moisture Adhering to Plastic Surface during Curing

Interestingly, Specimens 9 to 14 yields much lower moisture contents after testing than Specimens 1 to 8. This is due to the nature of the tests performed on the specific specimens. Specimens 1 to 8 were used for monotonic tri-axial testing purposes whereas Specimens 9 to 14 were utilised for dynamic tri-axial testing.

During dynamic tri-axial testing, cyclic loads are applied to the specimen ranging from low to high Stress Ratios. As these loads are applied, the plasticity of the material reduces. In addition to the reduction of plasticity, further compaction is achieved by the re-packing and settling of material particles. This increase in compaction caused by dynamic loading, forces some moisture out of the specimen thereby reducing the moisture content of the specimen during testing. This phenomenon, shown in Figure 4-4, was noted during dynamic tri-axial testing and explains the reduced final moisture content for dynamic tri-axial specimens. This shows the importance of measuring the moisture content before and after testing.



Figure 4- 4: Moisture Extruded from Specimen during Dynamic Loading

Note that the effect of reduced moisture content during dynamic loading will be discussed further in Section 4.4.

4.2.2 Large-size Specimens

Figure 4-5, similar to Figure 4-1, illustrates the control of quality for large-size tri-axial specimens based on compaction moisture content and density achieved.

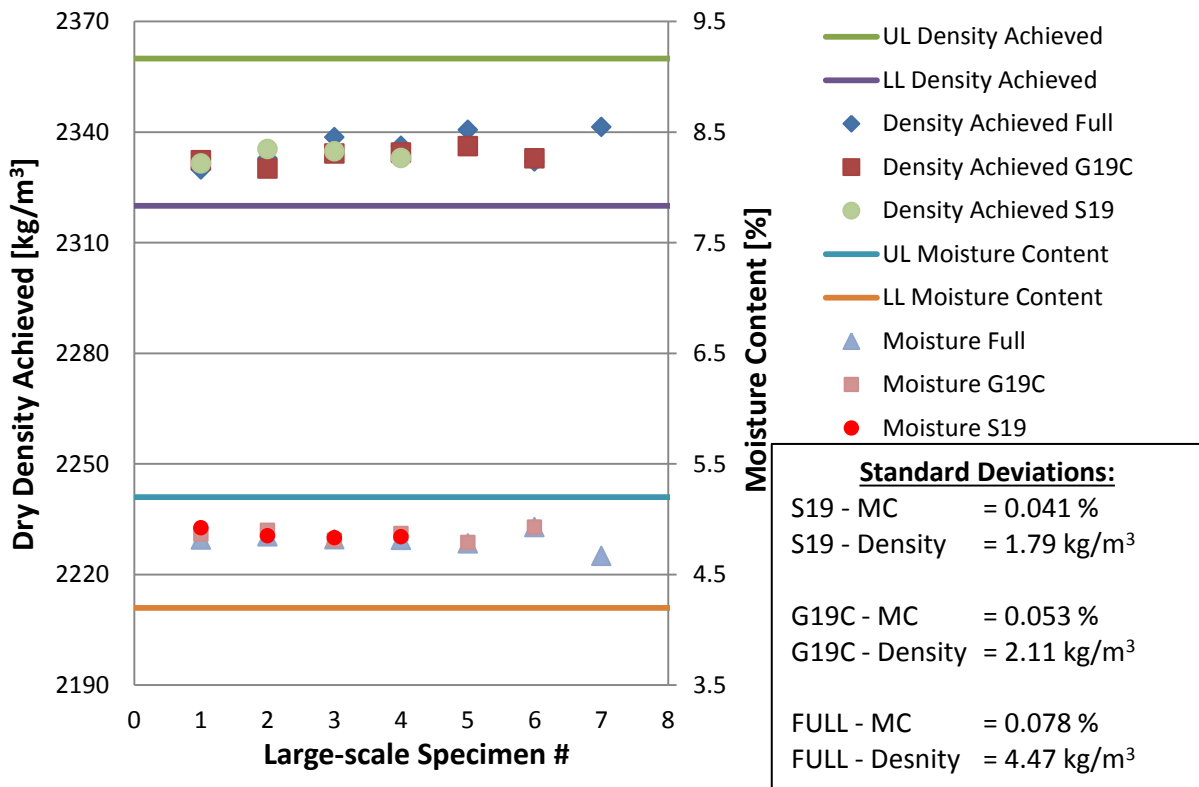


Figure 4- 5: Large-size Specimen Quality Control Summary

Again, all large-size specimens used for testing fell within the limits set for this research study. Furthermore, and more important, when comparing Figure 4-1 and 4-5, one should note that the moisture content during compaction and densities achieved for both small and large-size specimens are similar. This allows for accurate comparison of the respective sized testing equipment.

It is interesting that, when comparing the standard deviations of the specimens prepared, large-size specimens show lower standard deviations in both moisture content and dry densities achieved. Table 4-1 summarises the standard deviations achieved for all of the specimens prepared for this research study.

Table 4- 1: Summary of Standard Deviations

Specimen Scale	Grading Scale	Standard Deviations	
		Moisture Content [%]	Dry Density [kg/m ³]
150mm ϕ * 300mm H	S19	0.064	5.15
	G19C	0.139	6.50
300mm ϕ * 600mm H	S19	0.041	1.79
	G19C	0.053	2.11
	FULL	0.078	4.47

Note that the higher standard deviations observed for the small-size specimens could impact on the results obtained from small-size testing.

Furthermore, the phenomenon of reduced moisture contents for dynamic specimens is also noted for large-size specimens. Figure 4-6 shows, for dynamic Specimens 4 to 7, lower moisture contents after testing than that of monotonic tri-axial Specimens 1 to 3. When comparing the reduction in moisture content from before testing to after testing for monotonic specimens alone, a slight difference in the magnitude of the reduction in moisture contents is noted between the two grading curves. Table 4-2 summarises the average moisture contents for all grading curves of each specimen size.

Table 4- 2: Summary of Moisture Content during Compaction and After Testing

Specimen Scale	Grading Scale	Average Moisture Content During Compaction [%]	Average Moisture Content After Testing [%]	Reduction in Moisture Content [%]	Average Reduction [%]
Small	S19	5.01	4.61	0.40	0.51
	G19C	4.85	4.22	0.63	
Large	S19	4.87	4.70	0.16	0.14
	G19C	4.86	4.72	0.14	
	Full	4.83	4.70	0.12	

An average reduction in moisture content for small-size specimens during the curing process of 0.51% is noted whereas a reduction of only 0.14% is noted for large-size specimens. The primary factor influencing the variation is likely to be the difference in curing, although this was not specifically investigated. As mentioned, small-size specimens are sealed using plastic bags which, as has already been shown, results in moisture adhering to the plastic. Large-size specimens on the other hand are sealed within the specimen's mould, thereby not allowing moisture to escape the specimen itself.

4.3 Monotonic Tri-axial Testing

Monotonic tri-axial tests were utilised to determine the shear properties of the selected material. Both the Cohesion C and Friction Angle Φ were computed using the results obtained from monotonic tri-axial tests.

A minimum of three tri-axial specimens, with equal properties, tested at three different confining pressures are required to determine the shear parameters of a

material specimen. For the purpose of this study however, eight small-size specimens and three large-size specimens were tested at four and three confining pressures respectively.

4.3.1 Presentation of Initial Test Results

Monotonic tri-axial test results can be plotted to show the stress-strain relationship of the tested specimens, at the respective confining pressures, as shown in Figure 4-6. Note that only the small-size *S19* stress-strain relationships are shown and that all other stress-strain relationship curves are presented in Appendix B.

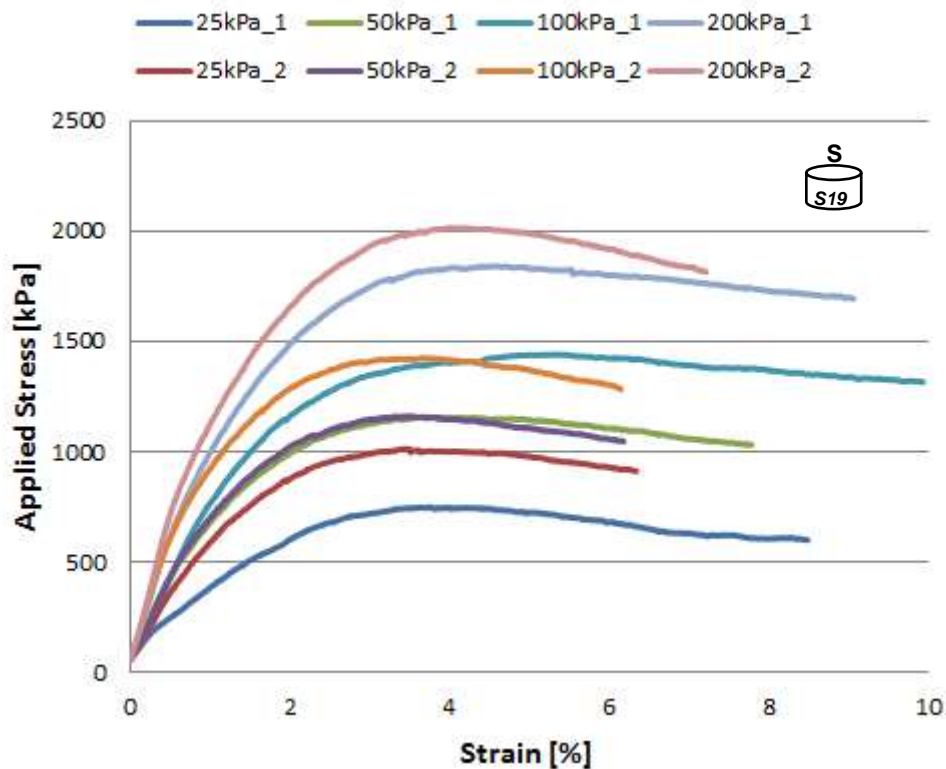


Figure 4- 6: Stress-Strain Relationship Curve for Small-size S19 Specimens

In addition to the above stress-strain relationship curves, the monotonic tri-axial test results can be plotted in the Mohr-Coulomb representation, as shown in Figure 4-7.

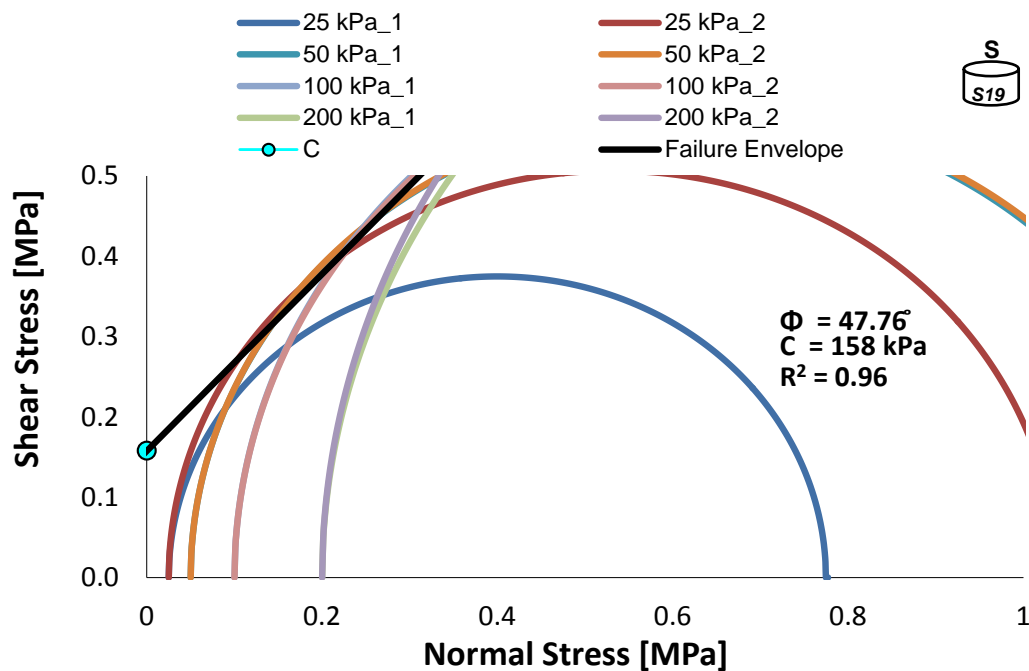


Figure 4- 7: Mohr-Coulomb Representation of Small-size S19 Monotonic Test Results

The shear parameters are computed by fitting a failure envelope to the Mohr-Coulomb representation shown above. The slope of the failure envelope, a linear line tangent to all of the Mohr circles, is known as the Friction Angle Φ [in degrees] whereas the failure envelope's intercept with the shear stress axis is known as the Cohesion C [in kPa].

Note that only the small-size *S19* grading curve's Mohr-Coulomb representations are shown and that all other Mohr-Coulomb representations are presented in Appendix C together with their respective stress-strain relationship curves.

The shear parameters, computed as set out above, for all combinations of grading curves and specimen geometries are summarised in Table 4-3.

Note that Table 4-3 shows the Cohesion and Friction Angle for two confining pressure ranges, 25, 50, 100 and 200 kPa and 50, 100 and 200 kPa respectively. As mentioned, only three large-size tri-axial specimens are tested to determine the shear parameters of large-size specimens whereas eight small-size specimens are tested. The effect of the reduced number of specimens needs to be accounted for since the confinement pressure range for small-size testing is different to that of large-size testing.

Table 4- 3: Summary of Cohesion and Friction Angle for Various Grading and Specimen Sizes






Symbol	Average Density [kg/m ³]	25 - 200 kPa Confinement Range		R ²	50 - 200 kPa Confinement Range		R ²
		Cohesion [kPa]	Friction Angle [°]		Cohesion [kPa]	Friction Angle [°]	
	2331	157.59	47.76	0.96	184.73	45.90	0.98
	-				245.49	47.65	
	2336	93.97	51.00	0.96	109.47	49.96	0.96
	-				176.43	50.89	
	2334	-	-	-	174.11	47.78	1.00
	2332	-	-	-	109.15	51.73	1.00
	2334	-	-	-	127.49	49.77	0.99

Table 4-3 shows that reducing the number of specimens for small-size testing from eight specimens, over a confinement range of 25, 50, 100 and 200 kPa, to six specimens, over a confinement pressure range of 50, 100 and 200 kPa, results in a significant increase in Cohesion and a reduction in Friction Angle. This shows that Cohesion is more accurately defined by considering a confinement pressure range of 25 and 50 kPa although this confinement range was not used to determine the Cohesion for this study. In addition, Figure 4-8 shows the change in Friction Angle and Cohesion as a percentage of the initial shear parameters computed with eight specimens and a confinement pressure range of 25, 50, 100 and 200 kPa.

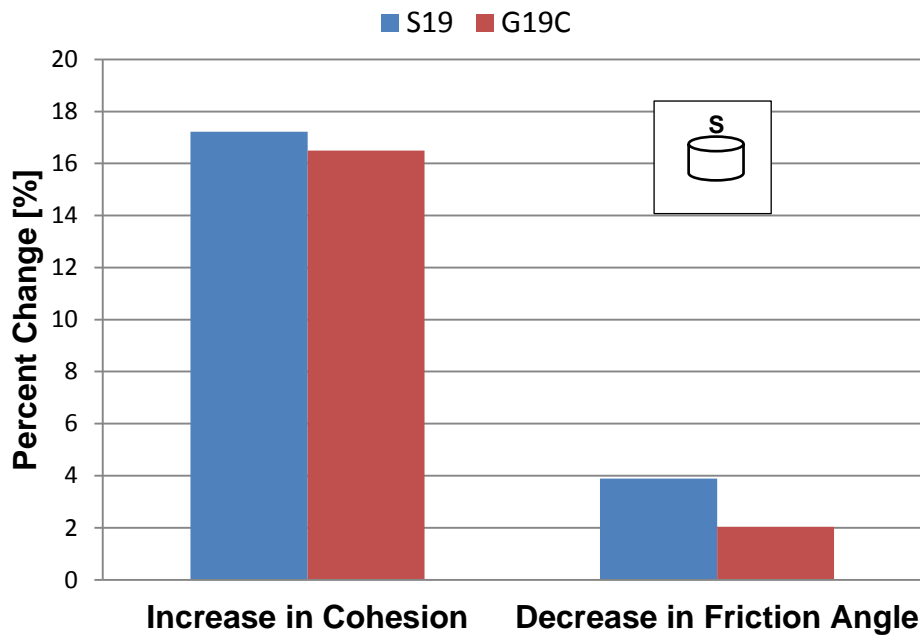


Figure 4- 8: Percentage Change in Shear Parameters when Changing the Confinement Pressure Range for Small-size Tri-axial

It is thus clear that, to allow for accurate comparison of, shear parameters, the confinement pressure range under which the specimens were tested needs to be equal. Therefore, to accommodate this, the 25 kPa confinement pressure is removed from the testing scope. I.e. the results from only six of the eight small-size monotonic tri-axial specimens, tested over a confinement pressure range of 50, 100 and 200 kPa will be used for further comparisons.

A further interesting point to take note of from Table 4-3 is the correlation coefficient R^2 values. It is clear that larger specimens yield more repeatable results since the obtained coefficients of variance are higher however less large-size specimens were tested and a different R^2 could have been achieved if more specimens were tested.

4.3.2 Influence of Specimen Geometry

The influence of specimen geometry on the material's shear parameters can be evaluated through the comparison of the shear parameters from similar grading curves yet different specimen sizes.

Figure 4-9 shows the influence of specimen geometry on the Cohesion of both the S19 and G19C grading curves.

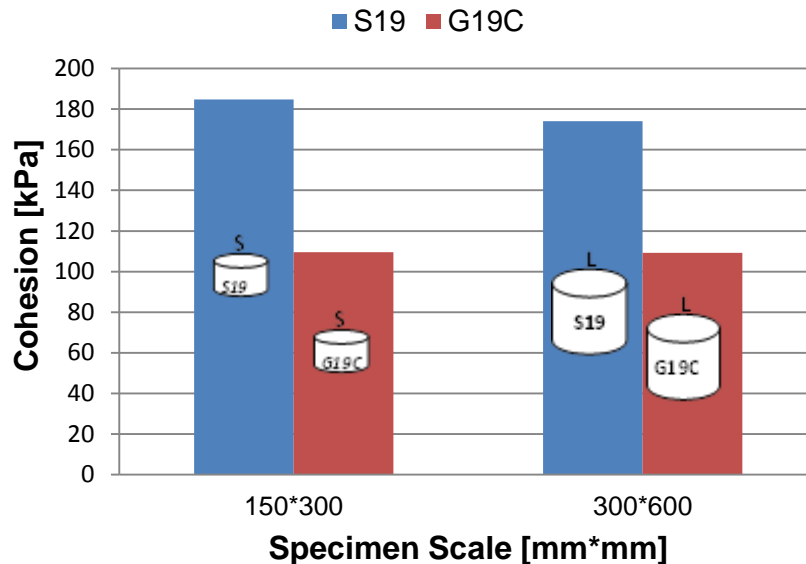


Figure 4- 9: Influence of Specimen Geometry on Cohesion

Note that there is a definite decrease (5.8%) in Cohesion for the *S19* grading curve, whereas the *G19C* grading curve shows a mere 0.3% decrease in Cohesion as the specimen size is increased. This shows that a lower Cohesion can be expected for larger specimens however the magnitude of the change is influenced by the grading curve.

It could be argued that this decrease in Cohesion, due to an increase in specimen size, is caused by material variability however, it is believed that specimen variability is so small that its influence on the results are insignificant. Therefore, it is believed that the decrease in Cohesion results from the increased specimen size. In addition, the decrease in Cohesion is noted for both grading curve which supports the conclusion that the change in Cohesion is related to the change in specimen size.

Figure 4-10 illustrates the influence of specimen geometry on the Friction Angle of the tested grading curves. The results show that for both the *S19* and *G19C* grading curves the larger specimen size yields higher internal Friction Angles. For the *S19* grading curve an increase in Friction Angle of 4.1% is noted whereas, the *G19C* grading curve shows a smaller increase of 3.5% when comparing the smaller specimen's results to that of its larger counterpart. This shows that an increase in Friction Angle can be expected with an increase in specimen size. Interestingly, the *G19C* grading curve is again less influenced by the change in specimen geometry when compared to the *S19* grading curve.

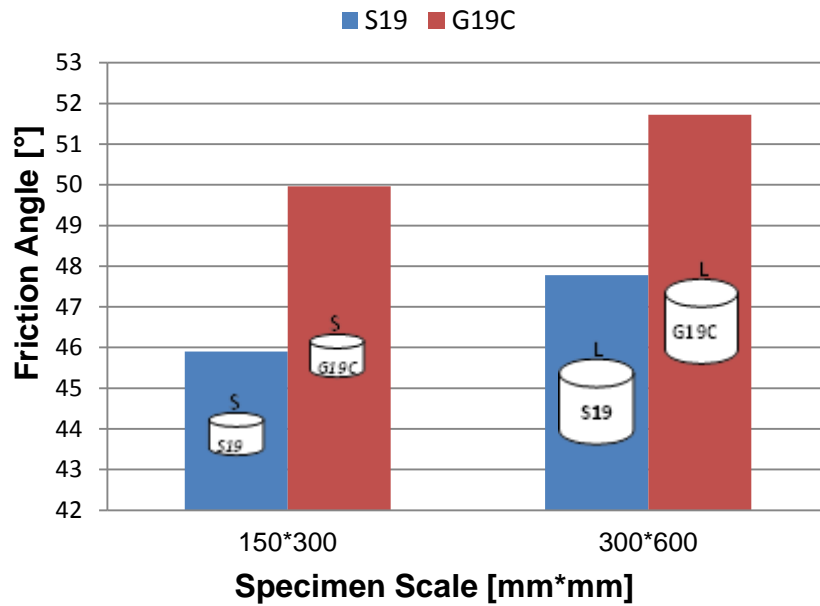


Figure 4- 10: Influence of Specimen Geometry on Internal Friction Angle

It is plausible that the increase in Friction Angle observed in Figure 4-10, due to an increase in specimen size, results from improved material packing. For larger specimens, which exhibit larger cross-sectional area and larger material volume per compacted layer (see Sub-section 3.4.3), increased particle movement can be expected during compaction. This leads to better particle orientation thereby improving packing and increasing particle-to-particle friction. Increased friction between material particles result in increased Friction Angles for larger specimens.

4.3.3 Influence of Grading Curve

The influence of grading curve, on the material's shear parameters can be evaluated through the comparison of the shear parameters from specimens prepared with different grading curves yet similar specimens sizes.

Figure 4-11 shows the influence of grading curve on the Cohesion of the tested specimens.

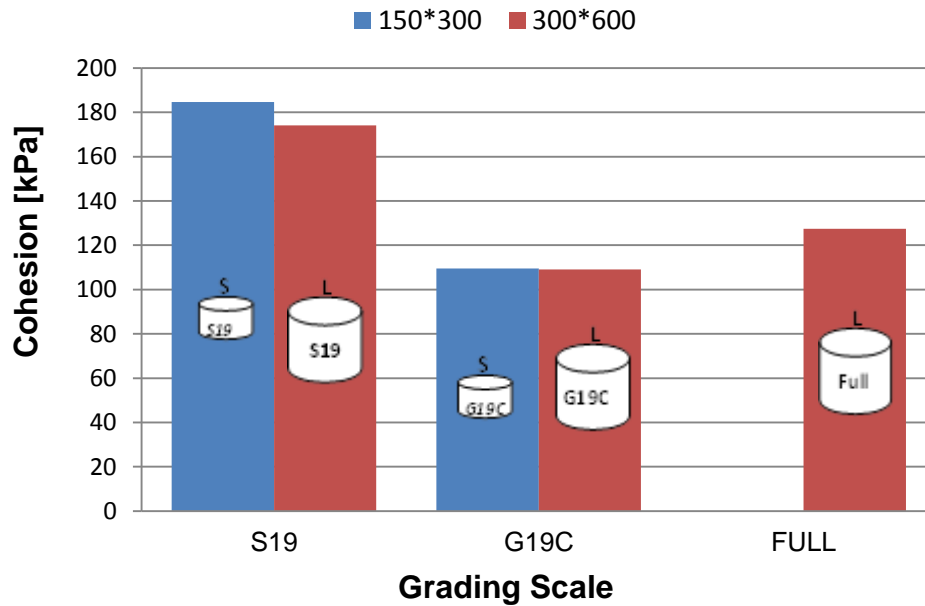


Figure 4- 11: Influence of Grading Curve on Cohesion

As expected, a clear decrease in Cohesion is noted for both small and large-size specimens as the grading becomes coarser (i.e. from *S19* to *G19C*). For the large-sized specimens the Cohesion of the *Full* grading curve is slightly lower than that of the *S19* grading yet higher than that of the *G19C* grading curve.

The change in Cohesion can be attributed to the coarseness of the grading. The finer *S19* grading, in comparison to the coarser *G19C* grading, yields increased capillary suction, due to reduced void size and increased number of voids, thereby increasing the effective stress within the material specimen. Increased effective stress results in increased shear performance, i.e. increased Cohesion. In addition, friction between small aggregate particles could also add to the improved Cohesion however, the influence of suction should be the dominant factor here.

The influence of grading curve on the Friction Angle is illustrated in Figure 4-12. As expected, due to improved aggregate interlocking, the coarser *G19C* grading curve, for both sized specimens, yields a higher Friction Angle when compared to the finer *S19* grading curve. Furthermore, as illustrated by Figure 2-26, excess fines within the material specimen, as is the case for the *S19* grading, cause “floating” of larger particles thereby reducing large particle-to-particle friction. Therefore, the finer *S19* grading yields lower Friction Angles when compared to the coarser *G19C* grading.

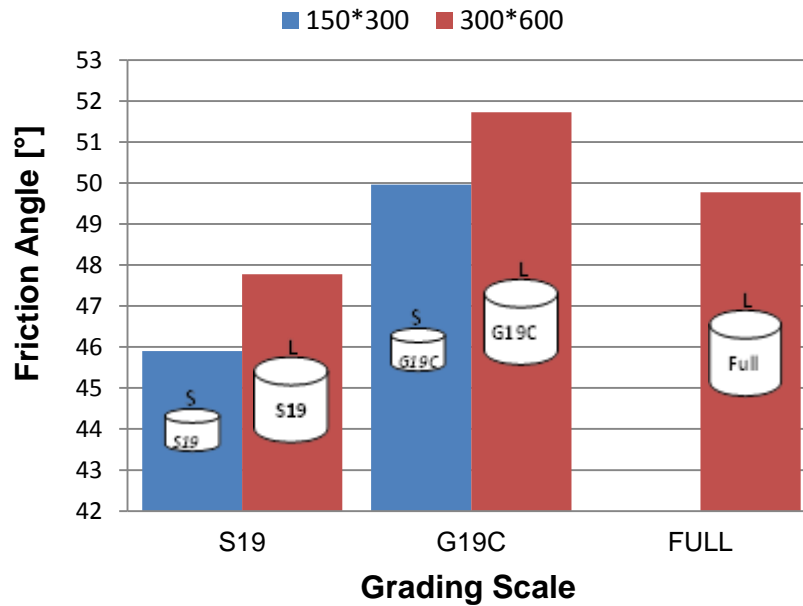


Figure 4- 12: Influence of Grading Curve on the Friction Angle

Interestingly, it is observed again that the large-sized *Full* grading yield results between that of the two adjusted grading curves. The Friction Angle is lower than both the *G19C* grading curves yet greater than that of the *S19* grading curves.

4.3.4 Comparison

Although the objectives of this research study are to evaluate the influence of both grading curve and specimen geometry, on the performance properties of the tested material, it is important to identify which of the adjusted grading curves yield the most representative results when compared to the true *Full* in-situ grading curve.

Assuming that the large-size specimens, prepared using the *Full* grading curve, are most representative of the in-situ material shear parameters, a comparison can be made. Using the large-size, *Full* grading curve test results as a benchmark and normalising all monotonic test results thereto, allows comparison. Figure 4-13 shows all of the normalised monotonic tri-axial test results for this research study.

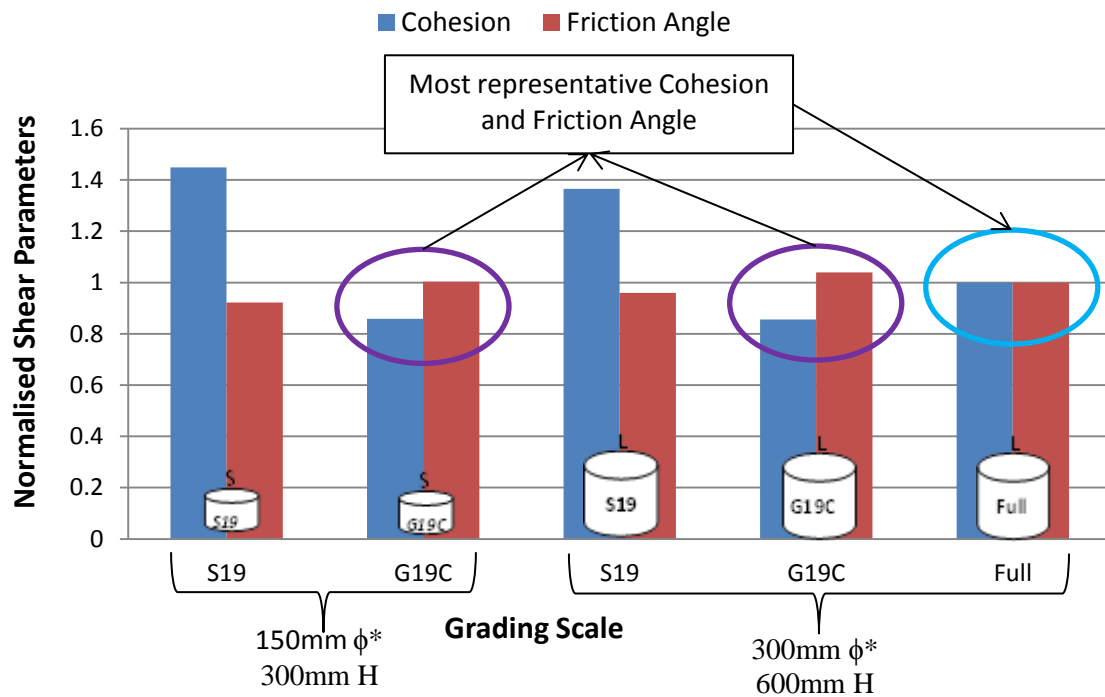


Figure 4- 13: Normalised Monotonic Tri-axial Test Results

Note that, Figure 4-13 above allows comparison of the two testing apparatuses based on monotonic tri-axial results. In addition, Figure 4-13 also gives an indication of which adjusted grading curve represents the full grading curves test results best.

It is clear from Figure 4-13 that the two testing apparatuses yield similar results for both Friction Angle and Cohesion, with only slight differences observed. This is evident for both modified grading curves (i.e. *S19* and *G19C*) as the normalised Cohesion values for the *S19* grading curve are 1.45 and 1.37; and the normalised Friction Angle values are 0.92 and 0.96 for the small and large-size apparatus respectively.

For the *G19C* grading curve, normalised Cohesion values of 0.86 and 0.86 are shown whereas the normalised Friction Angle values are 1.00 and 1.04, for the small and large-size specimens respectively.

Figure 4-13 together with the normalised values above confirm that the two sized testing apparatuses yield similar results when testing similar specimens and that they are comparable. In addition Figure 4-13 shows, based on the normalised values, that, for both sized specimens, the *G19C* grading curve yield more representative shear parameters, when compared to the *Full* grading curve.

Figure 4-14 adds value to the results and conclusions shown above. The *Full* grading is represented in Figure 4-14 b) which shows that the grading is balanced in the amount of fines and larger particles.

The *S19* grading curve, a fine grading, can be represented by Figure 4-14 c) which clearly has an excess amount of fines thereby reducing large grain-to-grain contact area. This in turn reduces Friction Angle, due to the “floating” nature of large particles within the fines. The *S19* grading curve also yields higher Cohesion. The “gluey” mastic resulting from the excess fines and moisture causes this. In addition, finer gradings yield more surface area and reduced voids within the mix. This results in a thinner layer of moisture covering the material particles, which in turn increase capillary suction. Increased capillary suction results in increased Cohesion and Friction Angle.

The *G19C* grading, which is also represented by Figure 4-14 b) also has a balance in fine and coarse material particles. Therefore, Figure 4-14 adds thereto that the *G19C* grading curve is more representative of the *Full* grading curve.

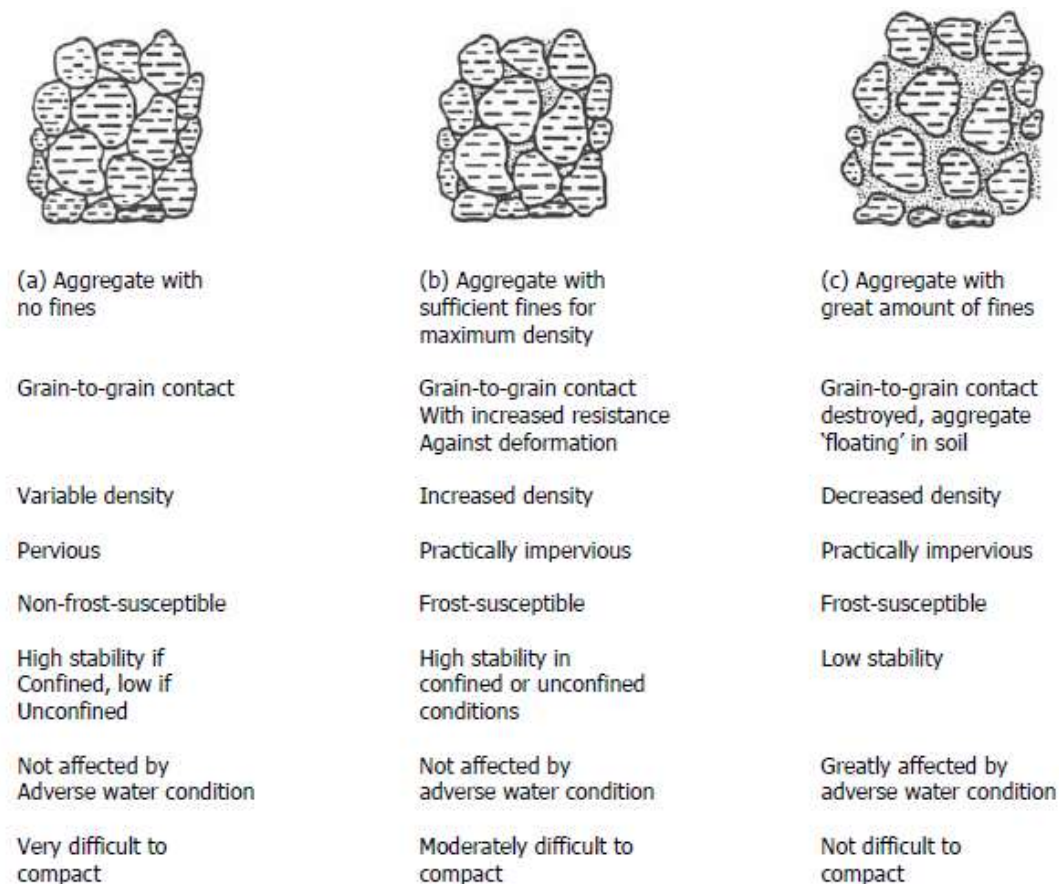


Figure 4- 14: Three Physical States of Aggregate Particle Distribution (Molenaar, 2010)

4.3.5 Additional Testing

As mentioned in Section 4.2, additional specimens, outside of the original; experimental design's scope, were prepared. These specimens were tested under different conditions to that of the specimens set out in the experimental design, in order to gain a better understanding of the tests themselves and the material's performance properties.

As illustrated in the experimental design, three small-size specimens are used for small-size dynamic tri-axial tests. In order to gain some understanding of the effect of dynamic loading, small-size monotonic tri-axial tests were performed at a range of confinement pressures namely 50, 100 and 200 kPa. The tests on these three specimens were performed once dynamic tests were complete thereon. This was done for both small-size gradings and the results compared to the monotonic tri-axial test results from the initial six specimens (for a similar confinement range, before dynamic loading), as shown in Figure 4-15.

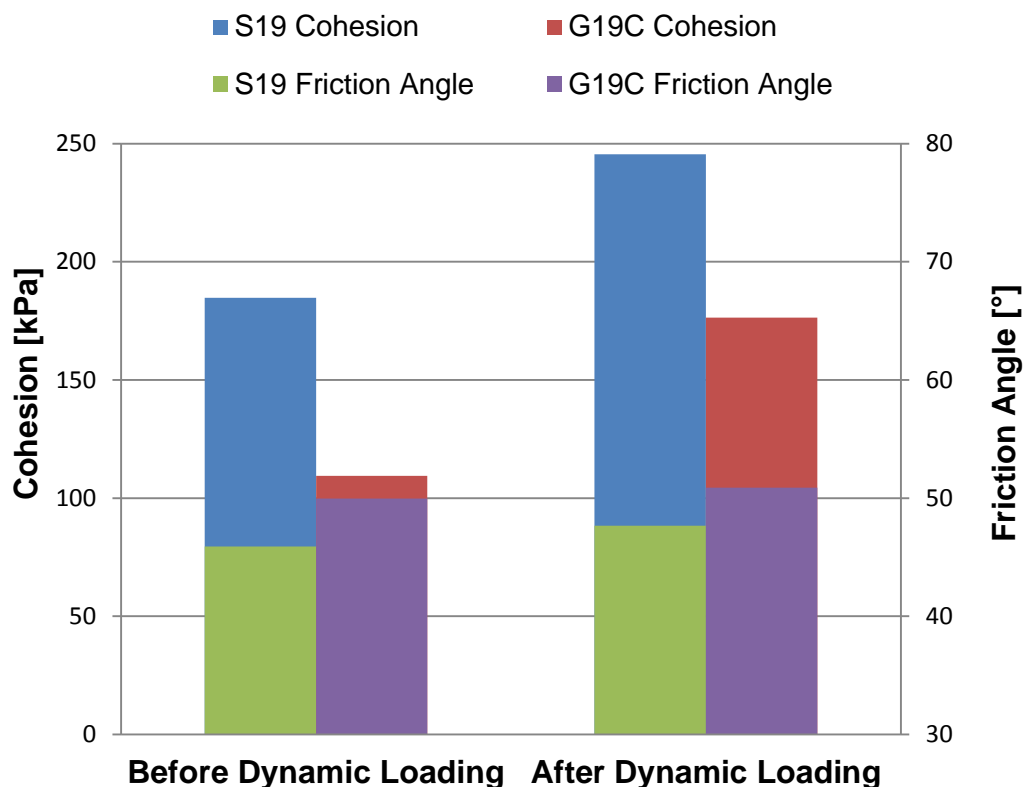


Figure 4- 15: Comparison of Small-size Shear Parameters Prior and Post Dynamic Loading

Interestingly, a significant increase in both Cohesion and Friction Angle is noted for both grading curves when comparing values before and after dynamic loading. This

increase in shear properties confirms the anticipated behaviour, mentioned in Section 4.2, that the reduction in moisture content (see Figure 4-2 and 4-4) is caused by an increase in density resulting from dynamic loading and improved particle packing.

An increase in density yields more contact points and higher internal contact area between aggregate particles, as illustrated by Figure 4-16, thereby increasing the Friction Angle within the tested specimens. Furthermore, as mentioned earlier, reduced moisture content results in increased suction, thereby increasing the Cohesion of the tested specimens.

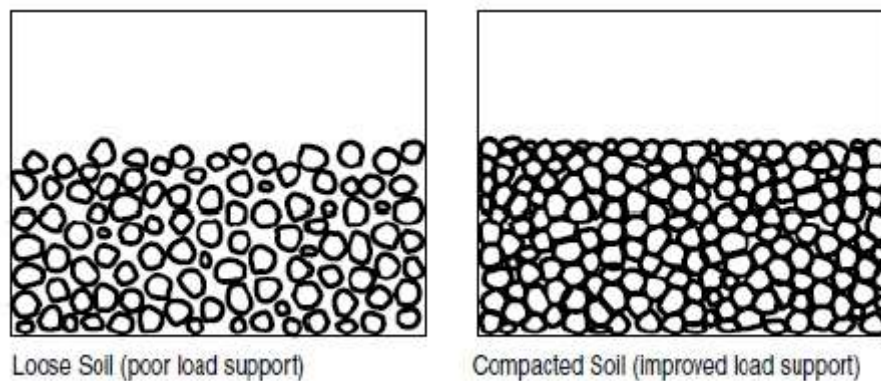


Figure 4- 16: Change in Soil Structure due to Increased Compaction/Density (Multiquip, 2011)

Even after dynamic loading, the Cohesion and Friction Angle are similarly influenced by grading curve as the results shown in Sub-sections 4.3.2, 4.3.3 and 4.3.4. The *G19C* grading curve again yields lower Cohesion and higher Friction Angle than that of its finer *S19* counterpart.

4.4 Dynamic Tri-axial Testing

Dynamic tri-axial tests were used to evaluate the resilient response of the tested material. The Resilient Modulus M_r of the tested specimens was computed using the results obtained from short-term dynamic tri-axial tests.

For the purpose of this study, three small-size specimens, for each of the two small-size grading curves, were tested whereas one large-size specimen was tested for the *S19* grading curve and two large-size specimens each, for the *G19C* and *Full* grading curves. An initial conditioning phase was performed on each tested specimen, which consisted of Stress Ratios ranging from a minimum of 10% to a maximum of 55%, to remove the materials plasticity without causing premature failure. A 200 kPa confinement pressure was applied to the specimen during all Stress Ratios of the

conditioning phase, where after the loading phase commenced. The combination of a 200 kPa confining pressure and the applied Stress Ratios, result in high Bulk Stresses, allowing rapid removal of material plasticity without damaging the specimen.

The loading phase consists of five confinement pressures ranging from 200 to 25 kPa. For each confinement pressure, five Stress Ratios are applied ranging from an initial 10% to the final 55%.

4.4.1 Presentation of Initial M_r Test Results

Dynamic tri-axial test results can be plotted to show the relationship between the Resilient Modulus of the specimen to the applied confinement pressure and the associated Stress Ratios. Figure 4-17 shows a typical illustration of the Resilient Modulus test results obtained from dynamic tri-axial testing.

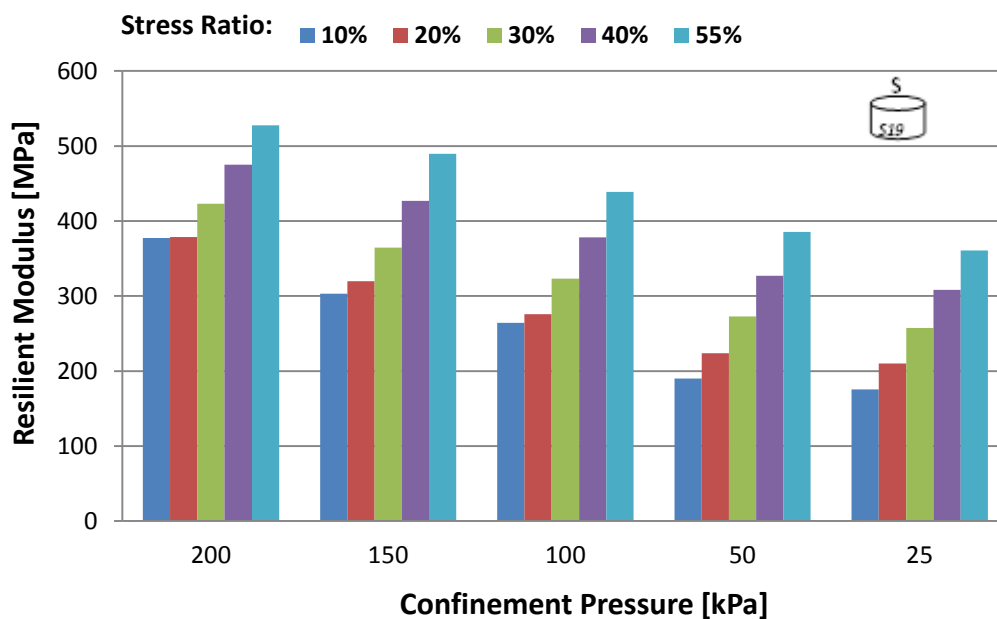


Figure 4- 17: Typical Resilient Modulus Values for Small-size S19 Specimen 1

It is clear from Figure 4-17 that the Resilient Modulus of the tested specimen is stress dependent. From the evaluation of the influence of confining pressure on the Resilient Modulus, a clear increase in Resilient Modulus is noted for an increase in confining pressure. This increase in Resilient Modulus, resulting from an increase in confinement pressure, is noted for all applied Stress Ratios.

Furthermore, when evaluating the influence of Stress Ratio, a clear increase in the Resilient Modulus is noted for an increase in Stress Ratio. Again, this increase in

Resilient Modulus, as a result of increased Stress Ratios, is noted for all confinement pressure ranges.

Note that Figure 4-17 only shows the results obtained from testing a small-size specimen (Specimen 1), prepared using the *S19* grading curve. All other specimens tested also showed an increase in Resilient Modulus for an increase in confinement pressure and an increase in applied Stress Ratio. The results are presented in Appendix C.

It is clear that both confinement pressure and applied Stress Ratio influences the resilient response of a tested specimen. Therefore, to account for the influence of both confinement pressure and Stress Ratio simultaneously, the Resilient Modulus values are presented in relation to the applied Bulk Stress Θ in kPa.

The Bulk Stress, defined as the sum of all principal stresses ($\sigma_1 + \sigma_2 + \sigma_3$), influences the Resilient Modulus values of the small-size *S19* tri-axial specimen as illustrated in Figure 4-18. Note that the values of both the Resilient Modulus and associated Bulk Stress are plotted on a double-logarithmic scale.

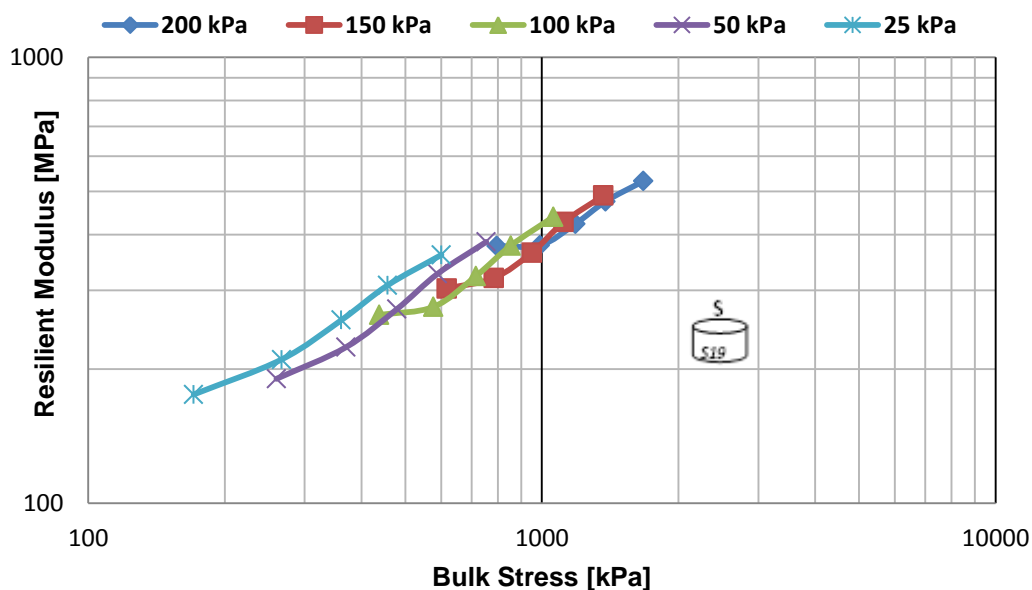


Figure 4- 18: Resilient Modulus – Bulk Stress Relationship, Small-size *S19*, Specimen 1

With σ_2 and σ_3 representing the applied confinement pressure and σ_1 , the sum of the applied confinement and the applied vertical stress (a function of the applied Stress Ratio), an increase in Resilient Modulus is expected for an increase in Bulk Stress. As mentioned, the Bulk Stress is a function of σ_1 , σ_2 , and σ_3 . Therefore, an increase

in the confinement pressure (increase in σ_1 , σ_2 and σ_3) and/or the applied Stress Ratio (increase in σ_3) will result in an increase in the Bulk Stress thus, an increase in the Resilient Modulus.

Figure 4-18 and the figures presented in Appendix C, confirm that the resilient behaviour of the tested material is stress dependent. Higher Resilient Modulus values were obtained at greater applied Bulk Stress. This increase in Resilient Modulus, as shown in Figure 4-18, was noted for all of the tested specimens of which the results are presented in Appendix C.

Even though it has now been shown that, the tested material's resilient behaviour is stress dependent, the magnitude of its dependency on the sum of the applied stresses (Bulk Stress) is not yet known. Therefore, material models need to be developed to allow for a better understanding of the degree of stress dependency.

4.4.2 Modelling of Resilient Behaviour

As has been shown above, the resilient behaviour of all the specimens tested (see Appendix C) is stress dependent. The degree of stress dependency, for the different specimen and grading curves however is not known. Therefore, material models need to be calibrated that gives an indication of the material stress dependency.

Many material models exist that allows the evaluation of stress dependent resilient behaviour. For the purpose of this study however, two material models were used.

Equation 4-1 represents the more basic M_r - θ model whereas Equation 4-2 represents the more accurate M_r - θ - $\frac{\sigma_d}{\sigma_f}$ model.

$$M_r = k_1 \left(\frac{\theta}{\sigma_0} \right)^{k_2} \quad 4-1$$

$$M_r = k_3 \left(\frac{\theta}{\sigma_0} \right)^{k_4} \left(1 - k_5 \left(\frac{\sigma_d}{\sigma_f} \right)^{k_6} \right) \quad 4-2$$

Where:

M_r	= Resilient Modulus [MPa]
θ	= Bulk Stress ($\sigma_1 + \sigma_2 + \sigma_3$) [kPa]
σ_0	= reference stress (1) [kPa]
k_1	= material regression coefficient [MPa]

- k_2 = material regression coefficient [-]
- σ_d = deviator stress [kPa]
- σ_d^f = deviator stress at failure [kPa]
- k_3 = material regression coefficient [MPa]
- k_4, k_5, k_6 = material regression coefficients [-]

Using a non-linear regression analysis, both models were calibrated to best fit the obtained Resilient Modulus values for all combinations of similar specimens (i.e. data from all three small-size S19 specimens were combined and the model calibrated thereto).

Figures 4-19 and 4-20 shows both the calibrated models, fitted to the results obtained from the three small-size S19 tri-axial tests. The results from all other specimens calibrated to fit the $M_r-\theta$ and $M_r-\theta-\frac{\sigma_d}{\sigma_d^f}$ models are presented in Appendix D and Appendix E respectively.

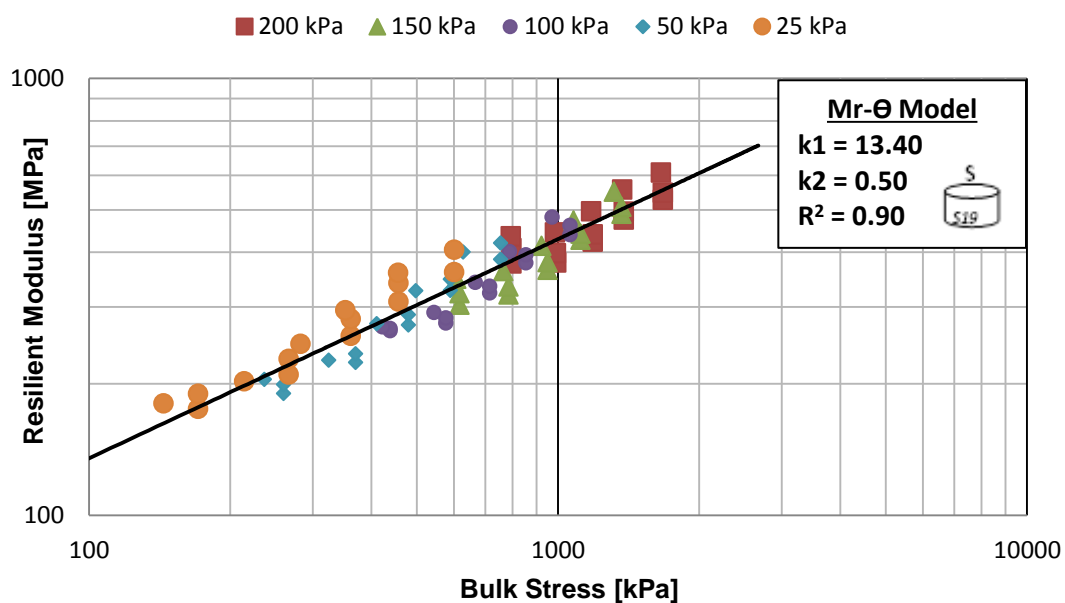


Figure 4- 19: $M_r-\theta$ Model Calibrated to Fit Small-size S19 Resilient Modulus Results

Note that there is little variation between the Resilient Modulus results obtained from testing the three specimens. At 25 kPa confinement the specimens yield Resilient Modulus values ranging between 175 and 190 MPa when tested at 10% Stress Ratio whereas the specimens show Resilient Modulus values ranging between 528 and 609 MPa when tested at 200 kPa confinement at 55% Stress Ratio.

In addition, the model coefficients k_1 and k_2 varies little to that of previous research

done on similar material (van Niekerk, 2002).

Although Figure 4-19 shows a high coefficient of variation between the tested results and that of the calibrated model ($R^2 = 0.90$), the model only accounts for the influence of Bulk Stress and does not account for the deviator Stress Ratio as in the case of the $M_r-\Theta-\frac{\sigma_d}{\sigma_f}$ model. Figure 4-20 shows the $M_r-\Theta-\frac{\sigma_d}{\sigma_f}$ model calibrated to fit the results obtained from the three small-size S19 dynamic tri-axial tests.

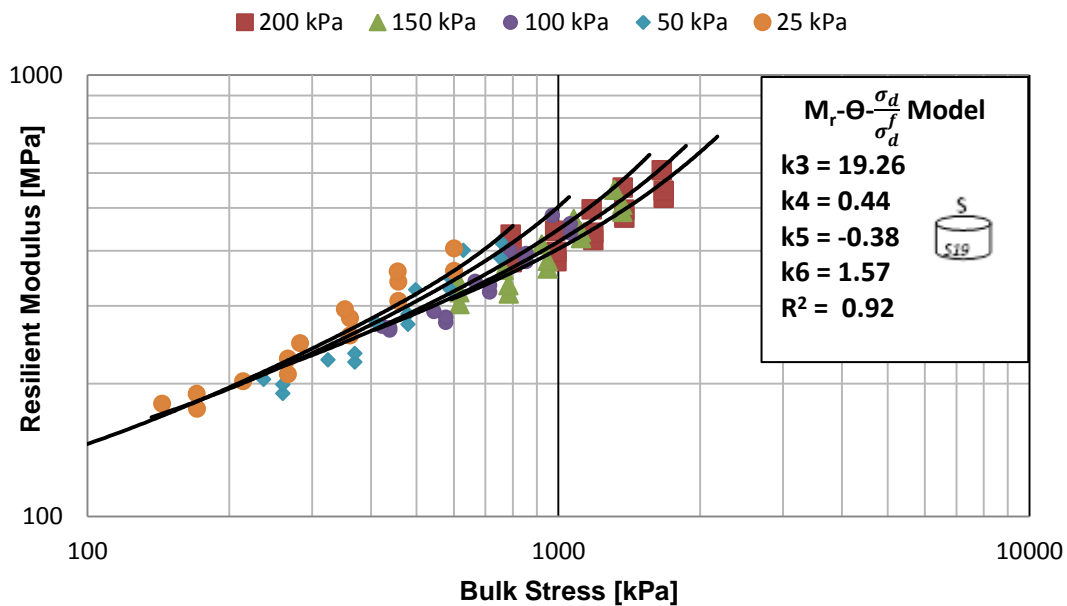


Figure 4- 20: $M_r-\Theta-\frac{\sigma_d}{\sigma_f}$ Model Calibrated to Fit Small-size S19 Resilient Modulus Results

Immediately, because it accounts for the influence of the deviator Stress Ratio, the $M_r-\Theta-\frac{\sigma_d}{\sigma_f}$ model fits the obtained results better (see Table 4-5 below).

Interestingly, the $M_r-\Theta-\frac{\sigma_d}{\sigma_f}$ model shows material stiffening ($k_5 < 0$) for the range of Stress Ratios tested. One would expect the material’s Resilient Modulus to reduce with increased deviator stress however, for the material tested and the range of Stress Ratios applied, the Resilient Modulus increases with increased deviator Stress Ratio.

It is believed that this stiffening occurs as a result of the increased density and reduced moisture content during dynamic loading. As explained in Chapter 4.2 and 4.3, Sections 4.2.1, 4.2.2 and 4.3.5, the dynamic loading of both small and large-size specimens results in an increase in density which, in turn forces moisture from the

specimen thereby reducing moisture content and increasing suction within the material specimen. Literature shows that the effect of increased density and reduced moisture content is increased Resilient Modulus (see Paragraphs 2.3.2.1 and 2.3.2.2).

Note that material stiffening was observed for all specimens tested ($k_5 < 0$) as illustrated in Table 4-4 and Appendix E.

Table 4- 4: Summary of Material Coefficients and Correlation Coefficients for Calibrated Models

Specimen Scale	Grading Scale	Number of Specimens	Mr- θ Model			Mr- θ - $\frac{\sigma_d}{\sigma_f}$ Model				
			k1 [MPa]	k2 [-]	R ²	k3 [MPa]	k4 [-]	k5 [-]	k6 [-]	R ²
150mm Φ * 300mm H	S19	3	13.40	0.50	0.90	19.25	0.44	-0.38	1.57	0.92
	G19C	3	19.17	0.47	0.90	28.31	0.39	-0.60	1.62	0.98
300mm Φ * 600mm H	S19	1	16.42	0.48	0.98	17.07	0.47	-0.08	1.98	0.98
	G19C	2	11.13	0.54	0.94	15.64	0.48	-0.48	2.09	0.97
	Full	2	14.62	0.51	0.92	18.75	0.46	-0.30	1.28	0.94

Interestingly, when comparing the k_5 material coefficients, the large-size specimens seem to undergo less material stiffening in comparison to that of the small-size specimens.

Concerning all other material coefficients, for the $M_r\theta$ model, no definite trend can be observed regarding the influence of grading curve or specimen geometry. When comparing the two specimen sizes of the S19 grading curve, the small-size specimens yield lower k_1 coefficients yet higher k_2 coefficients. The complete opposite however is noted when comparing the two specimens sizes of the G19C grading curve where the larger specimens now yields lower k_1 coefficients yet higher k_2 coefficients.

A further interesting point when comparing the two models, as shown by Figure 4-21, is that the $M_r\theta$ - $\frac{\sigma_d}{\sigma_f}$ model yields slightly higher Resilient Modulus values for Bulk Stress values less than 300 kPa, at low deviator Stress Ratios SR_d (less than 0.1). For a Bulk Stress greater than 300 kPa, at $SR_d < 10\%$, the $M_r\theta$ - $\frac{\sigma_d}{\sigma_f}$ model shows lower Resilient Modulus values than that of the $M_r\theta$ model.

This however changes as the effect of the deviator Stress Ratio is incorporated into

the $M_r-\Theta-\frac{\sigma_d}{\sigma_f}$ model. As mentioned the tested material shows stiffening with increased deviator Stress Ratio. Thus, for an equal Bulk Stress, an increase in deviator Stress Ratio results in an increase in Resilient Modulus. Furthermore Figure 4-21 shows that, at $SR_d = 50\%$, both models yield comparable Resilient Modulus values whereas a further increase in deviator Stress Ratio, for the $M_r-\Theta-\frac{\sigma_d}{\sigma_f}$, yields greater Resilient Modulus values than that of the $M_r-\Theta$ model.

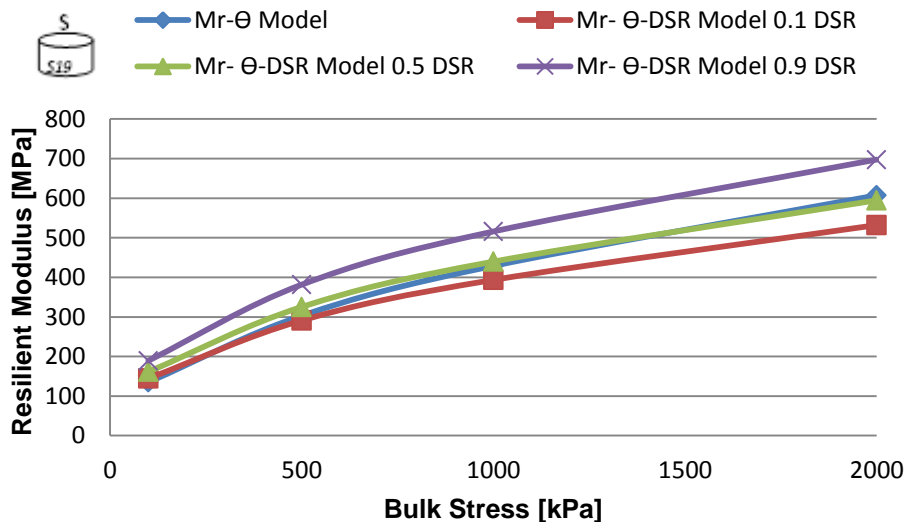


Figure 4- 21: Comparison of Models at $SR_d = 10, 50$ and 90% for Small-size S19 Specimens

Note that, although Figure 4-20 only shows the change in Resilient Modulus as a result of an increase in deviator Stress Ratio for the small-size S19 specimens, all other specimens (see Appendix H) showed similar trends to that illustrated above.

4.4.2.1 Influence of Specimen Geometry

The influence of specimen geometry on the resilient response of the tested material can be evaluated by using the calibrated models and plotting their results in relation to various Bulk Stress values and, in the case of the $M_r-\Theta-\frac{\sigma_d}{\sigma_f}$ model, also the applied Stress Ratio. Figure 4-22 shows the estimated Resilient Modulus values, estimated using the calibrated $M_r-\Theta$ model at four Bulk Stress values.

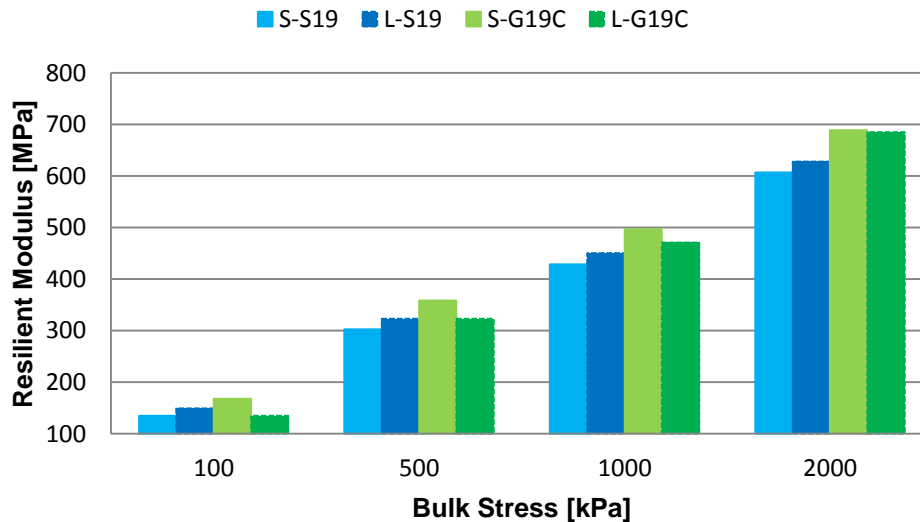


Figure 4- 22: Estimated Resilient Modulus Values for the $M_r-\Theta$ Model

It is clear from Figure 4-22 that the $M_r-\Theta$ model is influenced by specimen geometry however; the influence is not constant for both grading curves. When comparing the small and large-size S19 results, the larger specimens yield higher resilient moduli, for the full range of Bulk Stress values. On the other hand, the small-size G19C results show higher resilient moduli than that of the large-size results. Thus, no certain influence of specimen size can be established for all grading curves.

Again, when evaluating the influence of specimen geometry on the $M_r-\Theta-\frac{\sigma_d}{\sigma_f}$ model, it is clear that the model is influenced by specimen geometry however no certain trend can be established. From Figure 4-23, showing the results obtained from the calibrated model for a $SR_d = 10\%$ and Figure 4-24, showing the results obtained for a $SR_d = 50\%$, no clear trend is noted. From Figure 4-25 however, it is clear that, for a $SR_d = 90\%$, small-size specimens yield higher Resilient Modulus values than larger specimens do.

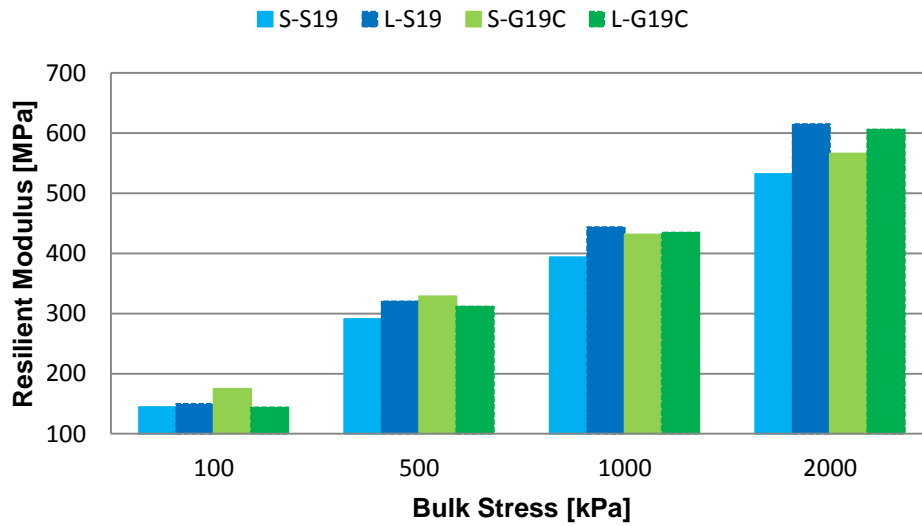


Figure 4- 23: Estimated Resilient Modulus for the $M_r-\theta-\frac{\sigma_d}{\sigma'_d}$ Model with $SR_d = 10\%$

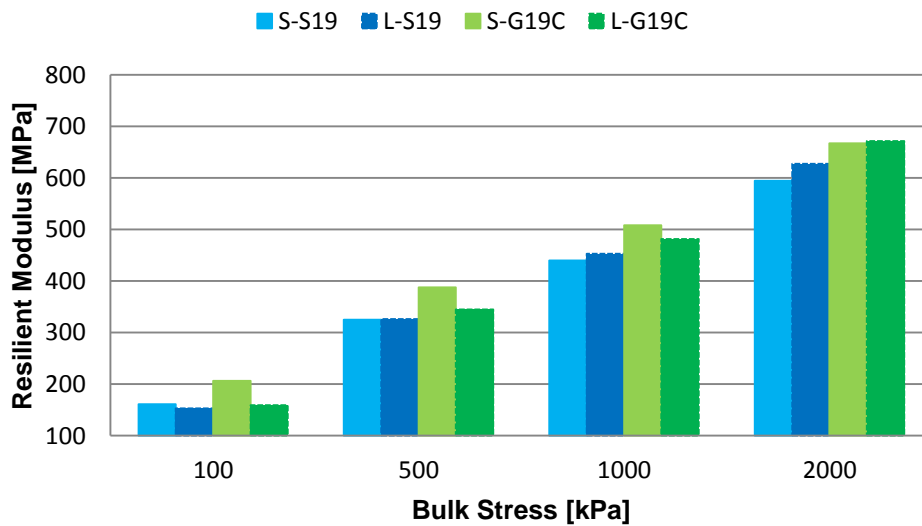


Figure 4- 24: Estimated Resilient Modulus for the $M_r-\theta-\frac{\sigma_d}{\sigma'_d}$ Model with $SR_d = 50\%$

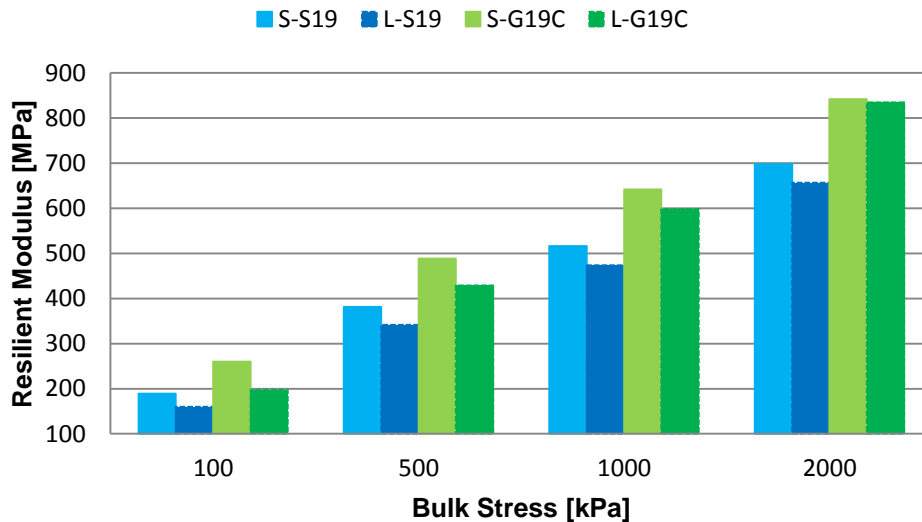


Figure 4- 25: Estimated Resilient Modulus for the $M_r-\theta-\frac{\sigma_d}{\sigma_f}$ Model with $SR_d = 90\%$

Interestingly, although no certain trend can be established regarding the influence of specimen geometry on the Resilient Modulus values obtained from the $M_r-\theta-\frac{\sigma_d}{\sigma_f}$ model another significant trend is observed. As the deviator Stress Ratio increases, a more significant increase in Resilient Modulus is noted for both grading curves of the small-size specimens. This shows that small-size specimens show greater material stiffening at high deviator Stress Ratio when compared to large-size specimens. This phenomenon is confirmed by the material coefficient k_5 in Table 4-5 where the k_5 values for small-size specimens are more negative than that of the larger specimens. A more negative k_5 value indicates that the scale of material stiffening is greater than that of a less negative value.

It is clear that the no certain influence of specimen geometry can be established. It has been shown by Figure 4-22 that different grading curves are influenced differently by specimen geometry. In addition, Figures 4-23, 4-24 and 4-25 not only show that different grading curves are influenced differently by specimen geometry, but that the effect of the applied deviator Stress Ratio influences different specimen sizes differently.

4.4.2.2 Influence of Grading Curve

The influence of grading curve on the resilient response of the tested material can be evaluated by using the calibrated models and plotting their results in relation to various Bulk Stress values and, in the case of the $M_r-\theta-\frac{\sigma_d}{\sigma_f}$ model, the applied Stress

Ratio. Figure 4-26 shows the estimated Resilient Modulus values, using the calibrated $M_r-\Theta$ model at four Bulk Stress values.

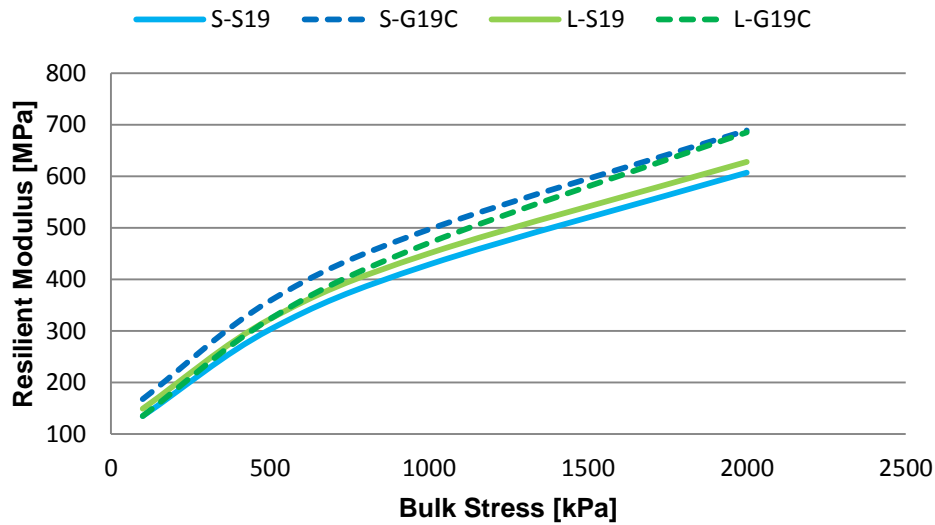


Figure 4- 26: Estimated Resilient Modulus Values for the $M_r-\Theta$ Model

Figure 4-26 shows, except for the large-size specimens at Bulk Stresses less than 500 kPa, that the coarser *G19C* grading curve yields higher Resilient Modulus values than the finer *S19* grading curve when estimated using the $M_r-\Theta$ model.

When evaluating the influence of grading curve on the Resilient Modulus of the tested specimen estimated using the $M_r-\Theta-\frac{\sigma_d}{\sigma_f}$ model, a similar trend to that stated above is noted. Figures 4-27, 4-28 and 4-29 shows the $M_r-\Theta-\frac{\sigma_d}{\sigma_f}$ model's estimated Resilient Modulus values for applied $SR_d = 10, 50$ and 90% respectively, for a range of applied Bulk Stresses.

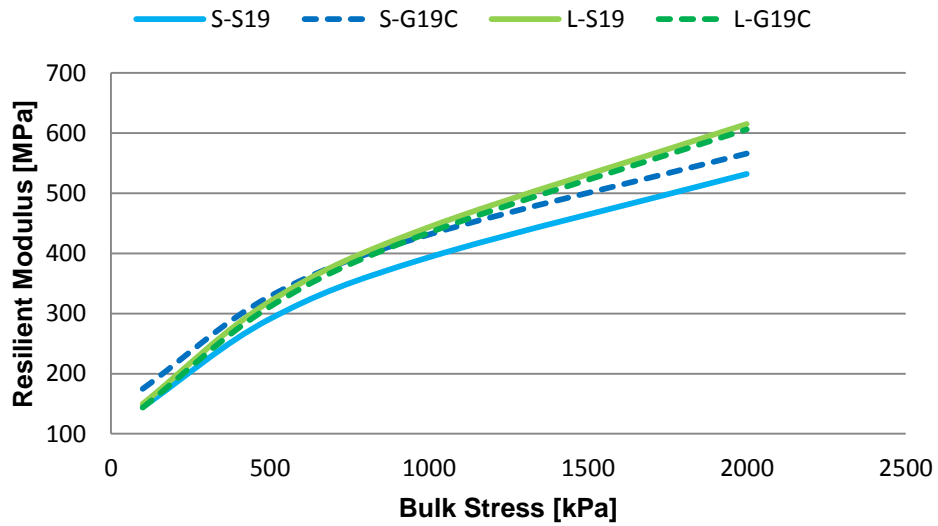


Figure 4- 27: Estimated Resilient Modulus for the $M_r-\theta-\frac{\sigma_d}{\sigma_f}$ Model with $SR_d = 10\%$

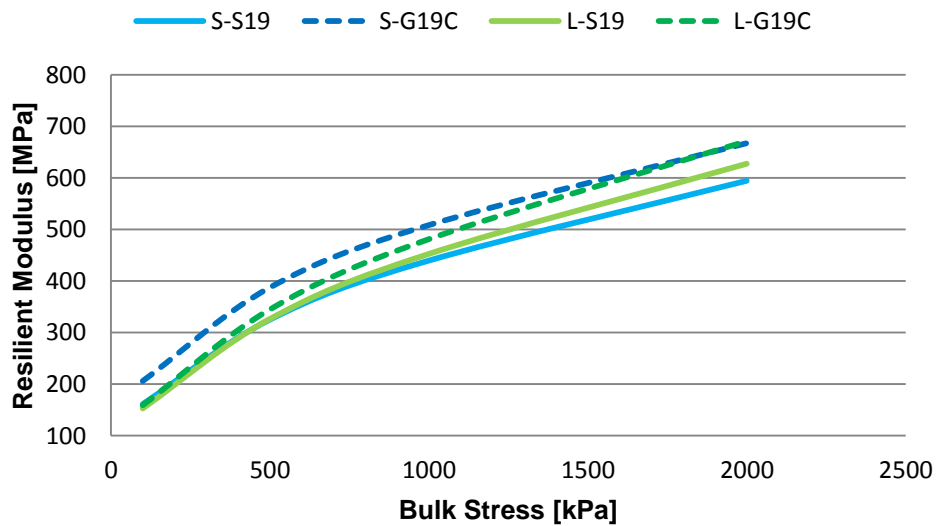


Figure 4- 28: Estimated Resilient Modulus for the $M_r-\theta-\frac{\sigma_d}{\sigma_f}$ Model with $SR_d = 50\%$

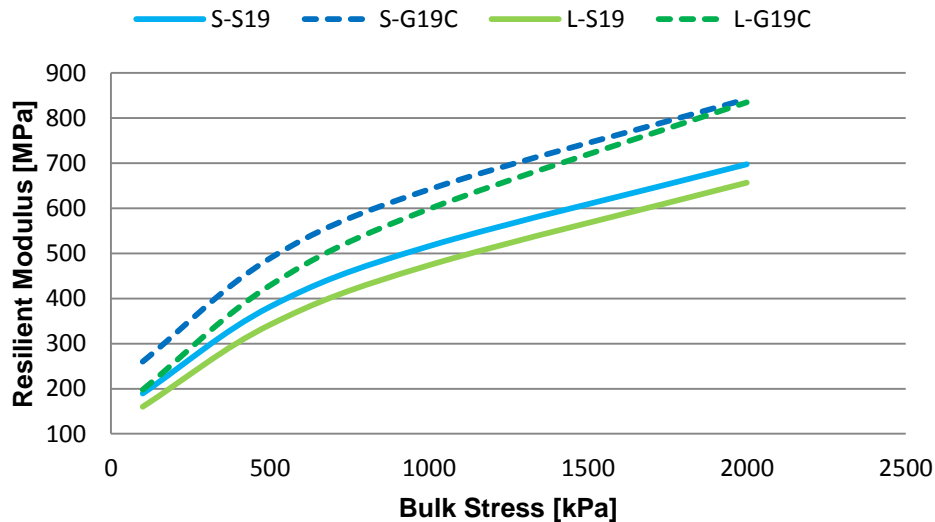


Figure 4- 29: Estimated Resilient Modulus for the $M_r-\theta-\frac{\sigma_d}{\sigma_d}$ Model with $SR_d = 90\%$

Interestingly, except for the large-size specimens, with an applied $SR_d = 10\%$ (see Figure 4-27), the coarser *G19C* grading curve yields higher Resilient Modulus values than the finer *S19* grading. Again, this is noted for both curves of specimens except at an applied $SR_d = 10\%$ where, for the large-size specimens, the finer *S19* grading curve yields slightly higher Resilient Modulus values than its coarser counterpart, *G19C*. In addition, note that there is a larger deviation in Resilient Modulus values at higher SR_d and for equal SR_d 's a greater variation in Resilient Modulus of the tested materials is noted at higher Bulk Stresses.

4.4.3 Comparison

As mentioned in Sub-section 4.3.4, grading curves are compared to show which of the two adjusted grading curves, *S19* or *G19C*, yield results that are more representative of the *Full* grading. By normalising all estimated Resilient Modulus values in relation to the estimated values of the *Full* grading curve, the best fitting grading curve can be established.

Figure 4-30 shows the $Mr-\theta$ model's values normalised in relation to the *Full* grading curves estimated Resilient Modulus values at four Bulk Stresses. Note that for all Bulk Stresses, except 100 kPa, both specimen sizes of the *G19C* grading curve yields results more representative to that of the *Full* grading curve.

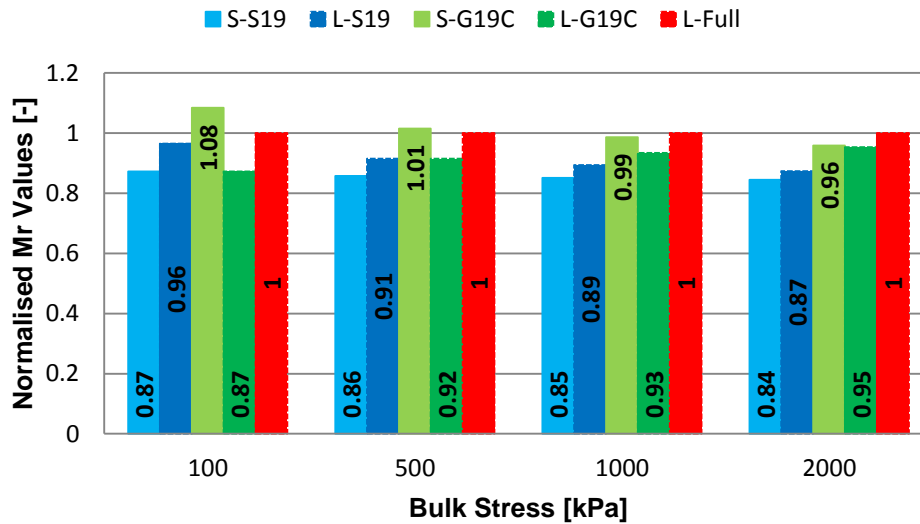


Figure 4-30: Normalised Resilient Modulus Values for $M_r-\Theta$ Model

A further interesting point to take note of from Figure 4-30, for the full range of applied Bulk Stresses, is that large-size *S19* specimens yields more representative results, to that of the *Full* grading curve, when compared to smaller specimens. For the *G19C* grading curve on the other hand, smaller specimens yield results that are more representative of the *Full* grading curve.

For the $M_r-\Theta-\frac{\sigma_d}{\sigma_f}$ model on the other hand, no best fit can be identified to fit the *Full* grading curve for the entire range of Bulk Stresses and applied deviator Stress Ratios. Figures 4-31, 4-32 and 4-33 shows the $M_r-\Theta-\frac{\sigma_d}{\sigma_f}$ model's values normalised in relation to the *Full* grading curves estimated Resilient Modulus values at four Bulk Stresses for $SR_d = 10, 50$ and 90% respectively.

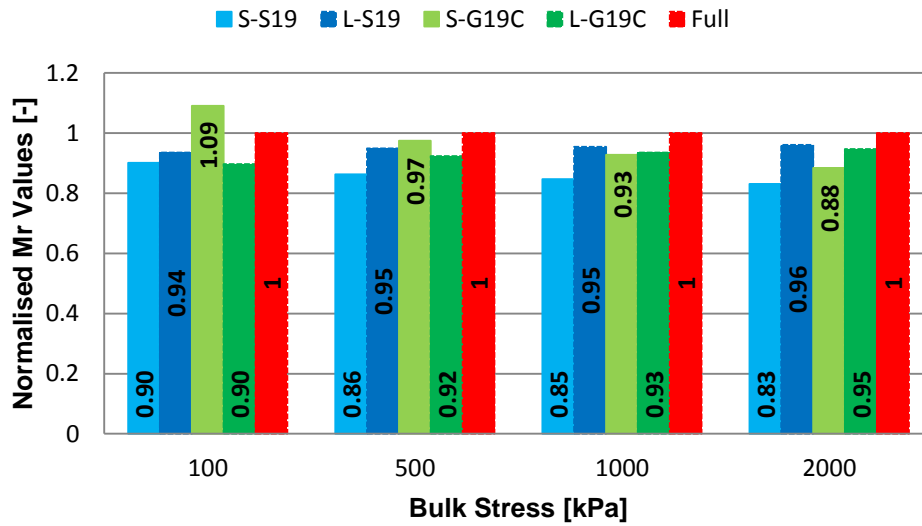


Figure 4- 31: Normalised Resilient Modulus Values for $SR_d = 10\%$, $M_r-\theta-\frac{\sigma_d}{\sigma_d}$ Model

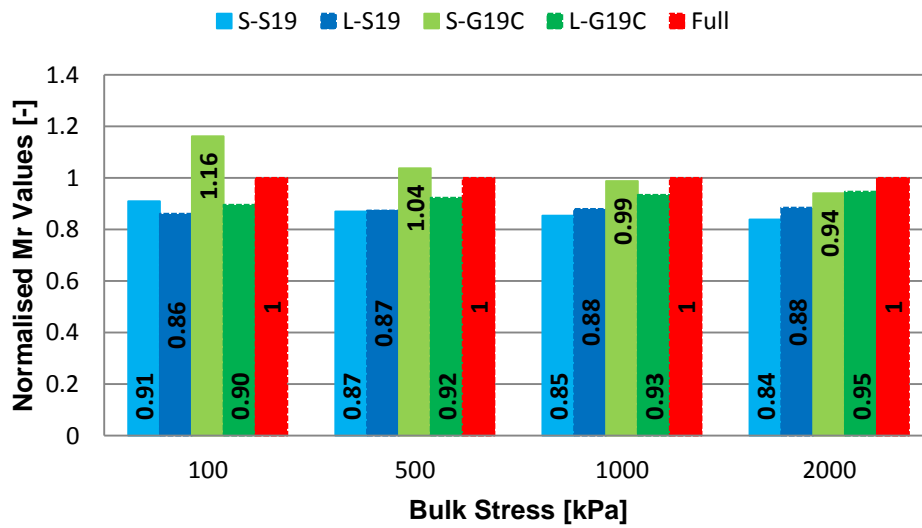


Figure 4- 32: Normalised Resilient Modulus Values for $SR_d = 50\%$, $M_r-\theta-\frac{\sigma_d}{\sigma_d}$ Model

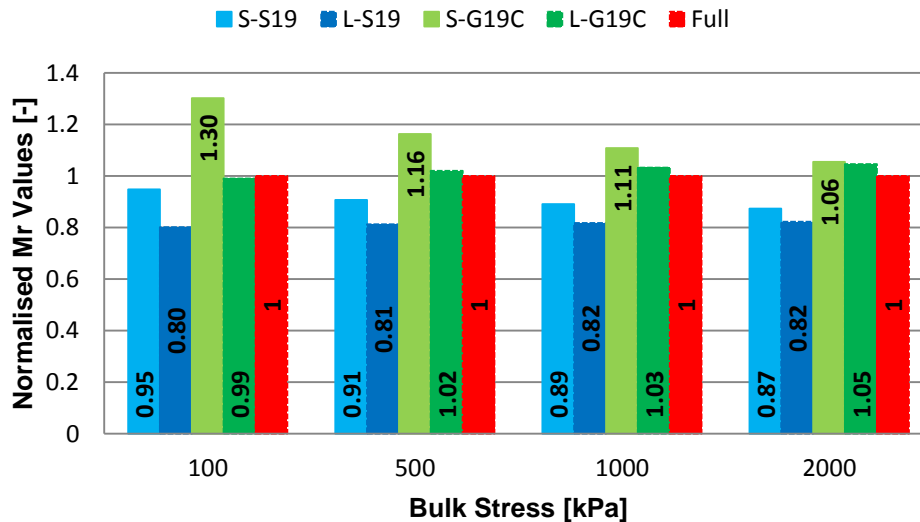


Figure 4- 33: Normalised Resilient Modulus Values for $SR_d = 90\%$, $M_r - \theta - \frac{\sigma_d}{\sigma'_d}$ Model

Note that neither of the two adjusted grading curves represents the results obtained from the *Full* grading curve best for the full range of applied Bulk Stress and deviator stress. It is only at an applied $SR_d = 50$ and 90% , for Bulk Stress values greater and/or equal to 500 kPa, that the *G19C* grading curve represents the *Full* grading curve's results best. For a $SR_d = 10\%$ no certain best fit is observed. For small-size specimens the *G19C* grading curve yields more representative results compared to the large-size *Full* grading curve's results. For the large-size specimens on the other hand the *S19* grading curve yields results that are more representative of the *Full* grading.

It is believed that the *G19C* grading curve is more representative of the *Full* in-situ grading. The stresses induced in typical pavement structures are in close proximity to Bulk Stresses of 1000 kPa and the critical $SR_d = 20$ to 50% . Therefore, the *G19C* grading curve would yield results more representative of the true in-situ grading.

Note that Chapter 5 presents a design analysis where a typical South African class B pavement structure is analysed. The results obtained will show the typical stresses and deviator stress ratios induced within the UGM layer due to loading, and could be used to show which grading curve best fits that of the *Full* in-situ grading.

4.4.4 Additional Testing

Initially, no additional dynamic tri-axial tests would have been performed. However, during testing it was observed that the tested material's response to dynamic loading

was instant. It therefore became questionable whether a 0.9 second resting period within one load cycle (refer to Figure 3-33) was required. Furthermore, to evaluate the influence of increased density during dynamic loading, additional load cycles were applied to some specimens after the initial dynamic tri-axial test was complete. The results are presented below.

4.4.4.1 Evaluation of Resting Period

Dynamic tri-axial test results were used to establish whether the tested material's response was rapid enough to allow for a shortened resting period. Figures 4-34, 4-35 and 4-36 shows the normalised applied stress and normalised LVDT readings, each normalised in relation to themselves (i.e. the applied stress cycle is normalised over the full second in relation to the maximum applied stress whereas each LVDT's strain measurement is normalised in relation to that specific LVDT's maximum strain measure over the one second load cycle).

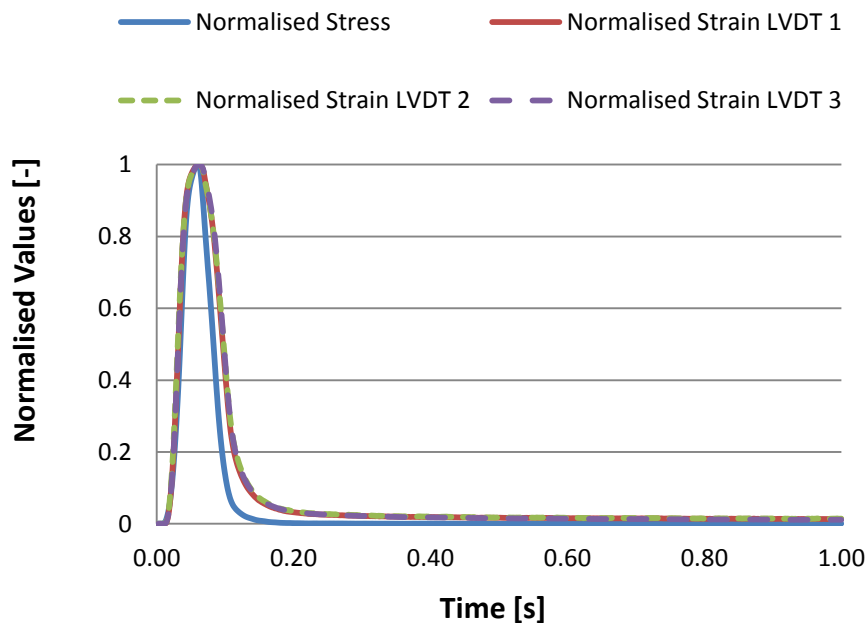


Figure 4- 34: Last 55% SR Conditioning Cycle, S-S19

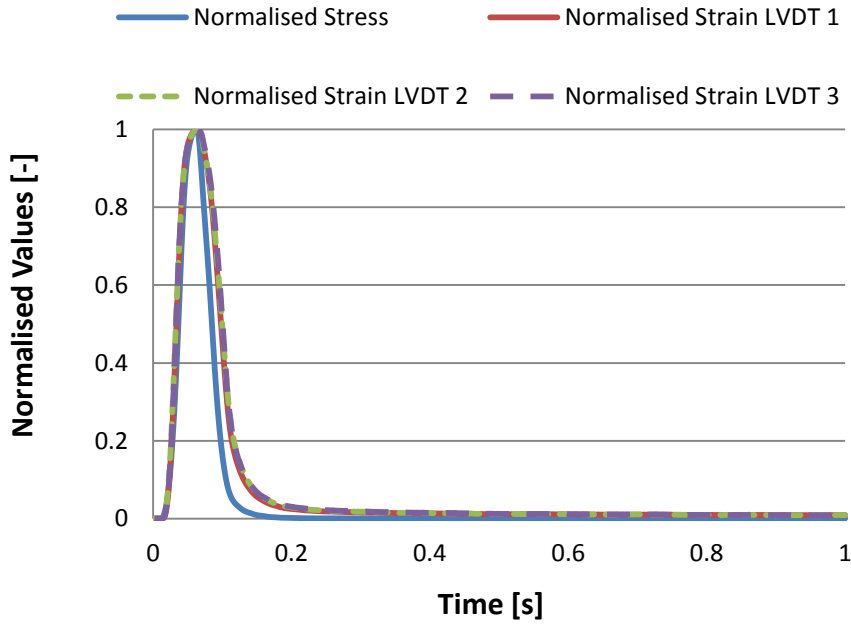


Figure 4- 35: Last 55% SR 200 kPa Load Cycle, S-S19

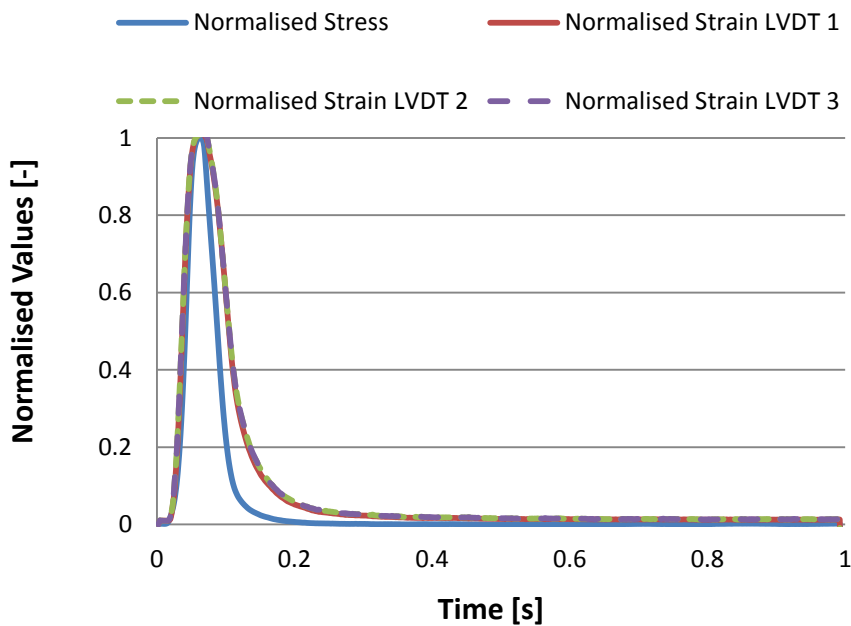


Figure 4- 36: Last 55% SR 25 kPa Load Cycle, S-S19

Note that, for the two loading phase scenarios shown in Figures 4-35 and 4-36, the last cycle of the 55% Stress Ratio during the 200 kPa loading phase and the last cycle of the 55% Stress Ratio for the 25 kPa loading phase, no notable change in LVDT measurements exist after 0.5 seconds. For the conditioning phase, see Figure 4-34 however, a slight change in LVDT measurements are noted after the 0.5 second mark. This shows that the response of the material is delayed if the material still

exhibits plastic behaviour. Once conditioning removes all plasticity, the material's response becomes more rapid. Therefore, no prolonged resting period is required during the loading phases.

Although Figures 4-34, 4-35 and 4-36 only show load cycles for a small-size *S19* specimens, the above phenomenon has been confirmed for all grading and specimen sizes tested. Appendix F presents the graphs shown above for all specimens with the addition of the 10% Stress Ratio data for the conditioning phase and the 200 and 25 kPa loading phase.

Note that, although large-size specimens also show that the 0.9 second resting period is not required, Figure 4-37 shows that the LVDT measurements are less stable which could influence the accuracy of test results. Improvements to the attachment mechanism will be required as the stability of the attached LVDT's could influence accuracy of the measured displacements.

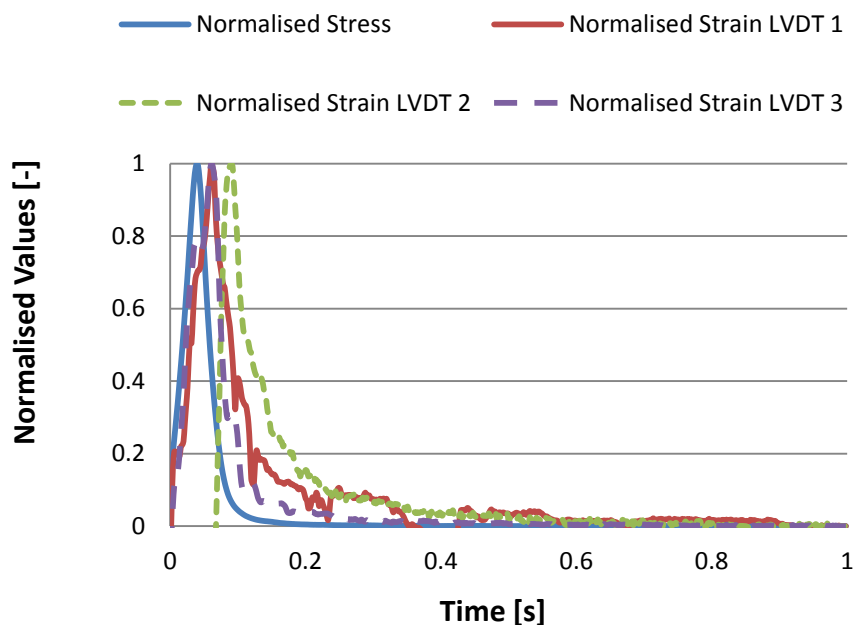


Figure 4- 37: Last 55% SR 200 kPa Load Cycle, L-S19

4.4.4.2 Evaluation of Loading and Unloading Phase

In addition to the above, an additional small-size *S19* specimen was prepared in which a more rapid load cycle was applied (see Figure 4-38). The load cycle consisted of a:

- 0.025 second loading phase; followed by a

- 0.025 second unloading phase; and finally a
- 0.95 second resting period

Interestingly, Figure 4-38, and the figures presented in Appendix G, again shows that the material's response is rapid. Furthermore, when comparing the normal 0.1 second loading phase to that of the rapid 0.05 second loading phase, no significant difference in Resilient Modulus is observed (see comparison between Figure 4-39 and 4-40).

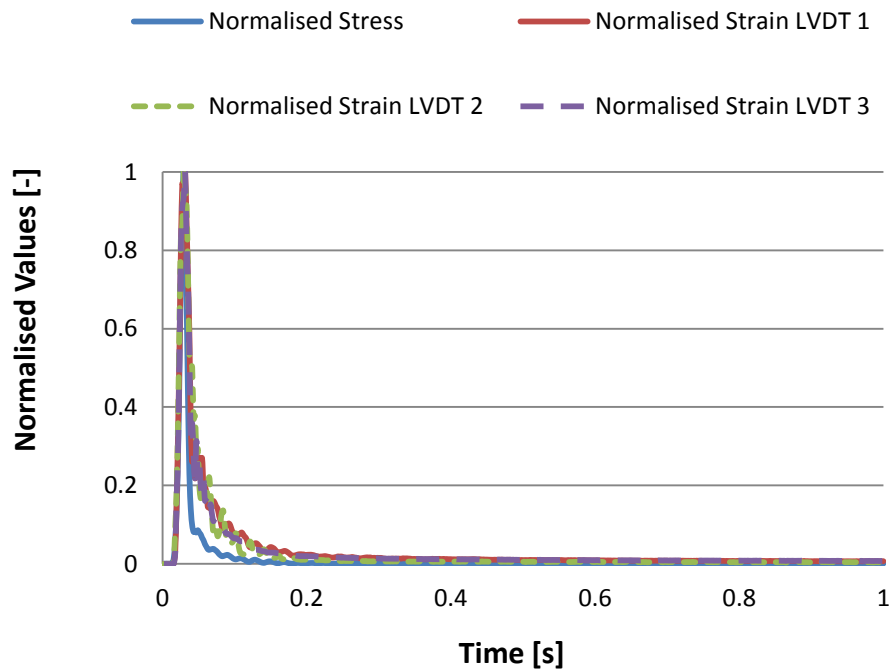


Figure 4- 38: Last Rapid 55% SR 200 kPa Load Cycle, S-S19

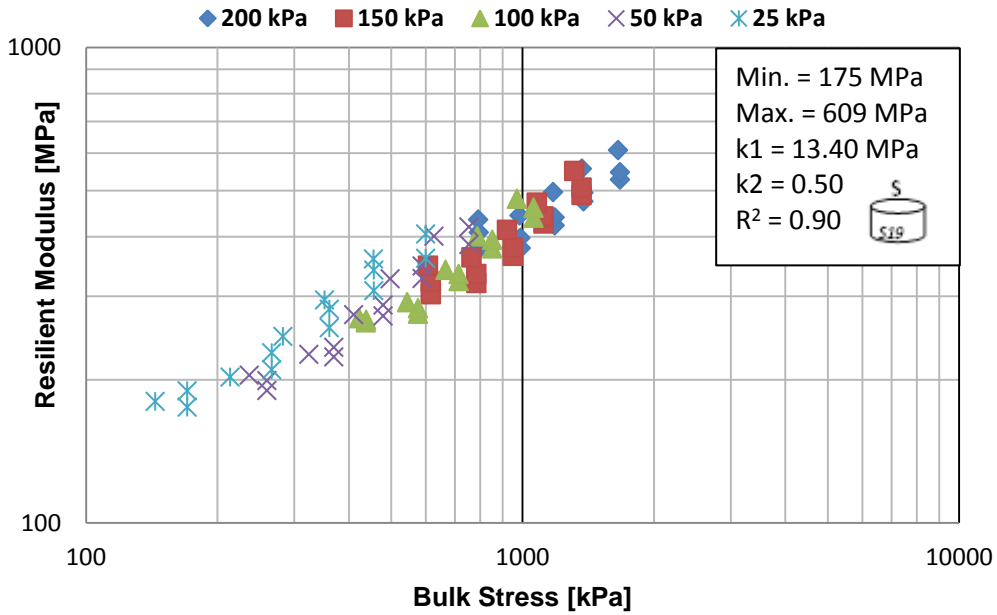


Figure 4- 39: Resilient Modulus vs Bulk Stress, Small-size S19, 0.1/0.9 Load Cycle

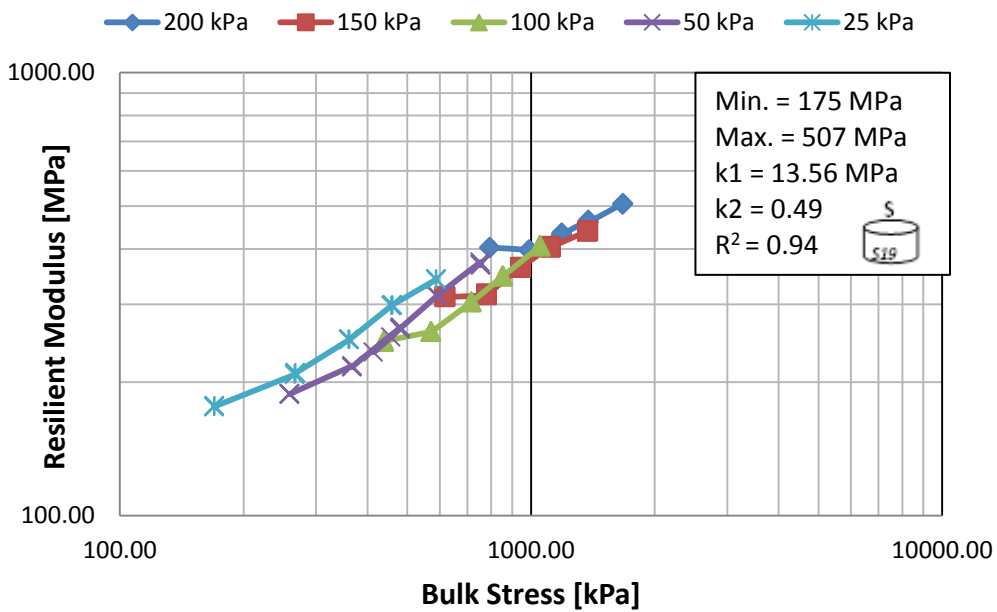


Figure 4- 40: Resilient Modulus vs Bulk Stress, Small-size S19, 0.05/0.95 Load Cycle

From Figures 4-39 and 4-40 it is clear that the model parameters, based on the $M_r-\theta$ model, is in close proximity and that similar Resilient Moduli will be predicted for equal Bulk Stresses. This confirms that the rapid load cycle does not influence the obtained resilient response of the material.

It was observed that the testing equipment was placed under severe strain when using the rapid loading cycle and continuous tuning of the controller was required to keep the testing apparatus in a stable condition. Therefore, although it could further

shorten testing duration, the use of rapid loading cycles is not recommended.

In addition, not all testing apparatuses are capable of applying both shortened loading phases and resting periods without influencing the results. Systematic loading errors could influence results. Therefore, a need to evaluate each machine's load dependent pulse wave exists.

4.4.4.3 Influence of Density Increase during Dynamic Tri-axial Testing

As has been mentioned in Sections 4.2 and 4.3, an increase in specimen density during dynamic loading was observed. Moisture was forced from specimens during dynamic loading (Section 4.2) and, in the case where monotonic tri-axial test were performed on specimens already dynamically loaded (Section 4.3), a clear increase in shear properties, due to the increase in density, was noted.

To further confirm the above observations additional load cycles were performed on large-size dynamic tri-axial specimens after the initial load cycles have been completed. The load cycles that were repeated included all five applied Stress Ratios at confinement pressure ranges of 200, 150 and 100 kPa. Figure 3-41 shows the results obtained for the large-size S19 specimen.

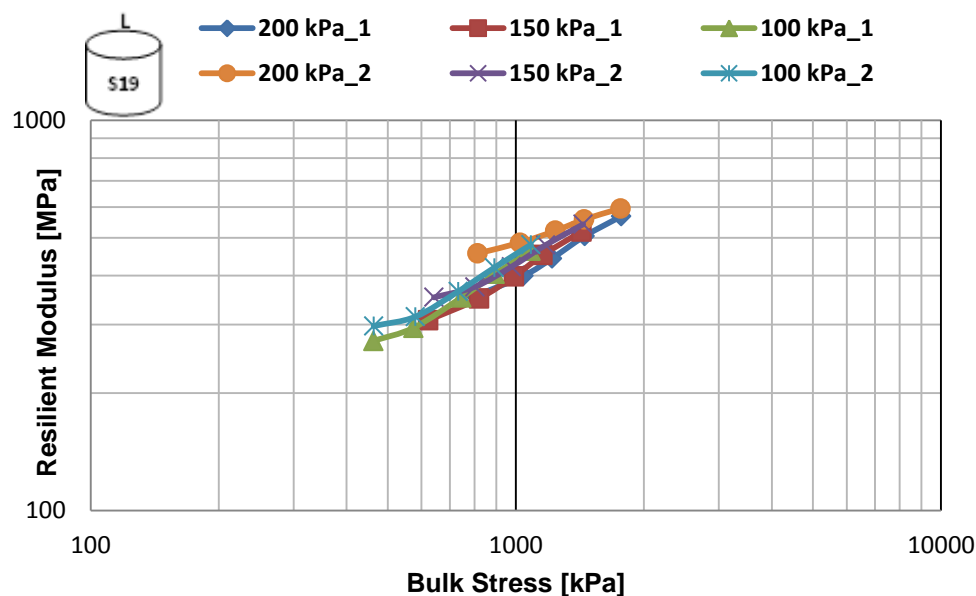


Figure 4- 41: Influence of Increased Density on Resilient Modulus of Large-size S19 Specimen

Note that, for all four applied confinement pressures, the Resilient Modulus obtained after initial dynamic loading is greater than that measured in the initial dynamic loading phase. The above was shown for all three large-size grading curves and the results are presented in Appendix I.

CHAPTER 5: DESIGN CONSIDERATION

The load applied to a pavement structure is transferred throughout the structure by the various pavement layers. Each of these layers transfers the applied load differently depending on the stiffness properties of the layers' associated parent material. Therefore, to understand load distribution within a pavement structure, a stress-strain analysis of the entire pavement structure is required. This chapter presents such an analysis based on the parent material and grading curves investigated in this research study in order to evaluate the influence of grading curve on the design of an unbound pavement layer.

5.1 Pavement Structure and Loading

The pavement structure selected for analysis is what can be typically expected in South Africa for a class B road. Figure 5-1 shows the structure and the load applied to the pavement structure.

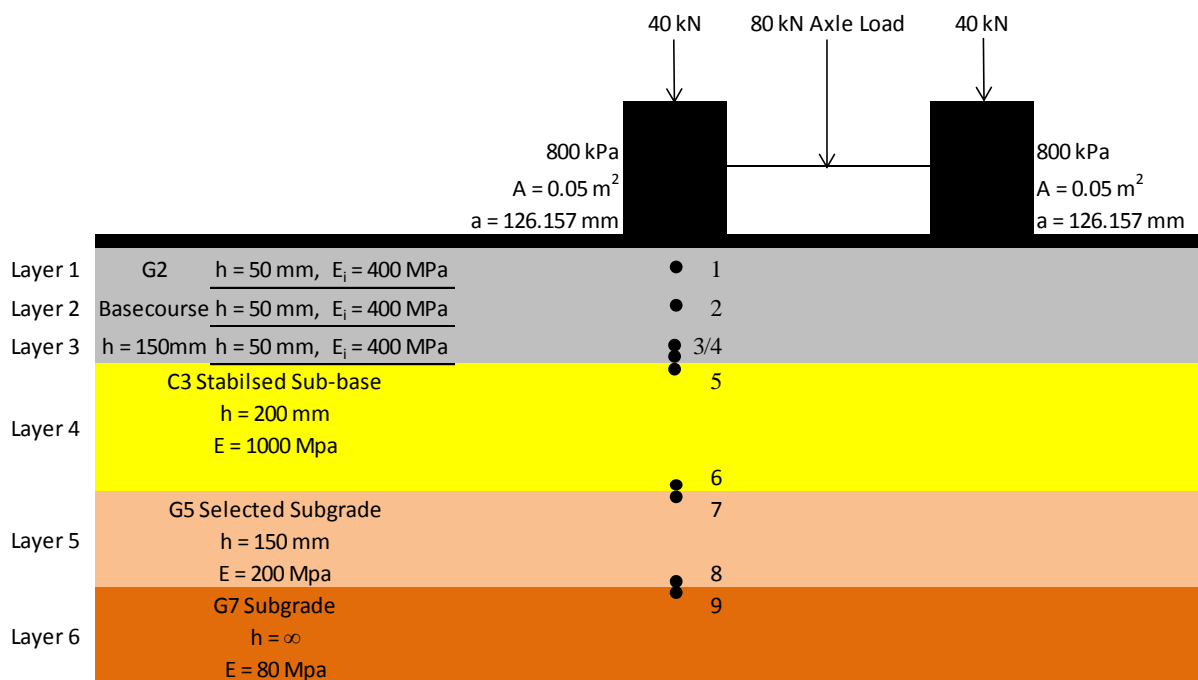


Figure 5- 1: Pavement Structure and Load Layout used in Stress-Strain Analysis

The pavement structure selected for analysis comprises a single seal that does not contribute to the structural strength of the pavement and can therefore be ignored in the analysis. Next, a 150 mm G2 crushed stone basecourse, similar to that of the material researched in this project, is selected. To simulate the stress dependent

nature of unbound granular materials, the 150 mm basecourse is divided into three 50 mm sub-layers, each with an initial assumed material stiffness of 400 MPa (Theyse, 1996). The sub-base comprises a selected G5 material, stabilised to a C3 type material with an assumed stiffness of 1000 MPa. Although Theyse (1996) recommends the stiffness values for a typical C3 to range between 1000 and 2000 MPa after construction, a lower value in the range was selected as the stiffness of cemented layers, due to fatigue cracking, reduces with time. Below the cemented layer, a 150 mm G5 selected subgrade layer with a stiffness of 200 MPa followed by the in-situ subgrade with a stiffness of 80 MPa is incorporated into the design analysis.

For the purpose of this comparative analysis, which is to ascertain the influence of grading on the laboratory determined Resilient Modulus properties and hence the structural performance of the granular base, only Phase I of the material stiffness properties is considered. Note that the selected layer moduli are realistic for such a scenario of an inverted pavement structure.

The load applied to the pavement structure, see Figure 5-1, comprises an 80 kN super single tyre, single axle load (i.e. 40 kN load on each tyre). This load, although not the standard 80 kN dual wheel axle load used in South Africa (SAPEM, 2013), is used to simplify the design but still meet the requirements of an equivalent standard 80 kN dual wheel, single axle load.

Morton et al. (2004) through a study of traffic loading on the N3 between Johannesburg and Durban, South Africa, has shown that, due to improved tyre manufacturing, the tyre pressures associated with current heavy vehicles range between 700 and 825 kPa. Therefore, for the purpose of this analysis, a tyre pressure of 800 kPa is utilised which, together with the 40 kN tyre load, yields a contact area of 0.05m^2 . The associated radius of the applied stress is 126 mm.

In addition to the above, Figure 5-1 also shows the points within the pavement structure that were analysed. Points 1, 2 and 3 are critical points taken in the centre of each of the three 50 mm unbound granular layers. At these points the principal stresses were analysed. Points 4 and 5 are taken at the bottom of the third unbound granular layer and at the top of the stabilised layer respectively. This shows the change in stress between two layers, at similar depths, within the pavement structure. Points 6 and 7 are taken at the bottom of the stabilised layer and the top of

the selected subgrade layer, whereas Points 8 and 9 are analysed at the bottom of the selected subgrade and top of the in-situ subgrade respectively. Point 6 is the critical point within the stabilised layer and the horizontal strain is analysed in order to evaluate fatigue cracking. Note that only Points 1, 2, 3 and 6 will be required for analysis of the pavements life expectancy however, to show an accurate distribution of stresses throughout the pavement structure more points are required.

5.2 Unbound Basecourse M_r Iteration

As confirmed in Chapter 4, the Resilient Modulus of the tested UGM is stress dependent. In addition, as shown by Figure 2-1, the pavement layers distribute the applied load throughout the pavement thereby reducing the stress with increased depth. Therefore, an iterative stress-strain analysis is required to obtain the Resilient Modulus associated with the applied stresses within the UGM basecourse.

For the purpose of this study, the design software developed by Shell, BISAR 3, was used to perform the iterative design. The iterative procedure is performed by using the initial assumed stiffness values and computing the associated stresses within Layers 1, 2 and 3. These stresses are then used to compute the Bulk Stress where after the material stiffness can be computed using the calibrated M_r model. As mentioned the $M_r-\Theta-\frac{\sigma_d}{\sigma_f}$ model used in this research, predicts material stiffening at high Stress Ratios. This however is inconsistent with true material performance, which softens or even fails at high Stress Ratios. Therefore, to limit the influence of predicted material stiffening, only the $M_r-\Theta$ model will be used in the Design Life analysis.

Once the new stiffness values are known, the design analysis is performed again using the newly computed stiffness values until the difference between consequent stiffness values are less than 10%. This is in order to meet the design reliability of 90% for a class B road (SAPEM, 2013). Table 5-1 shows the iterative procedure for the small-size S19 grading curve.

Table 5- 1: Iterative Design Method to Compute Resilient Modulus (Small-size S19 Specimens)

Iteration	Layer	BISAR 3 Input Mr [Mpa]	Values from BISAR 3			Θ [kPa]	k1 [MPa]	k2 [-]	Mr [Mpa]	Mr Deviation from Previous
			σ_1 [kPa]	σ_2 [kPa]	σ_3 [kPa]					
1	1	400.0	799.4	474.1	474.1	1747.6	13.40	0.50	560.2	40%
	2	400.0	725.5	236.7	236.7	1198.9			464.0	16%
	3	400.0	572.9	190.4	190.4	953.7			413.8	3%
2	1	560.2	797.5	504.2	504.3	1806.0			569.5	2%
	2	464.0	712.4	220.1	220.1	1152.6			454.9	-2%
	3	413.8	557.5	179.9	179.9	917.3			405.8	-2%
3	1	569.5	797.5	504.5	504.5	1806.5			569.5	0%
	2	454.9	712.2	218.2	218.3	1148.7			454.2	0%
	3	405.8	557.7	180.2	180.2	918.1			406.0	0%

Note that the iterative design for all other grading and specimen sizes are presented in Appendix J. Furthermore, note that the Resilient Modulus values obtained from the first iteration is used as the input Resilient Modulus values for the second iteration.

Table 5-2 presents a summary of the final Resilient Modulus values obtained from the iterative design procedure for all of the tested grading and specimen sizes.

Table 5- 2: Summary of Final M_r Values

Specimen Scale	Grading Scale	Layer	BISAR 3 Input Mr [MPa]	Θ [kPa]	k1 [MPa]	k2 [-]	Mr [MPa]	Mr Deviation from Previous [%]
150 mm ϕ * 300 mm H	S19	1	569.5	1806.5	13.40	0.50	569.5	0.0
		2	454.9	1148.7			454.2	0.0
		3	405.8	918.1			406.0	0.0
	G19C	1	655.7	1839.5	19.17	0.47	656.2	0.0
		2	527.1	1145.1			525.1	0.0
		3	466.0	889.0			466.2	0.0
300 mm ϕ * 600 mm H	S19	1	602.6	1819.7	16.42	0.48	602.8	0.0
		2	484.5	1148.0			483.2	0.0
		3	431.2	906.4			431.4	0.0
	G19C	1	643.1	1832.6	11.13	0.54	643.5	0.0
		2	499.7	1138.7			497.7	0.0
		3	437.4	897.7			437.7	0.0
	FULL	1	676.5	1845.4	14.62	0.51	677.1	0.0
		2	532.0	1139.0			529.4	0.0
		3	465.3	885.5			465.6	0.0

Interestingly, although the Bulk Stresses of the respective layers are in close proximity, the final Resilient Modulus values differ quite significantly. Normalising the obtained Resilient Modulus values in relation to the large-size *Full* grading curve specimens shows that both sizes of the *G19C* grading curve yields Resilient Modulus values more representative of the *Full* grading curve. This is illustrated by Figure 5-2.

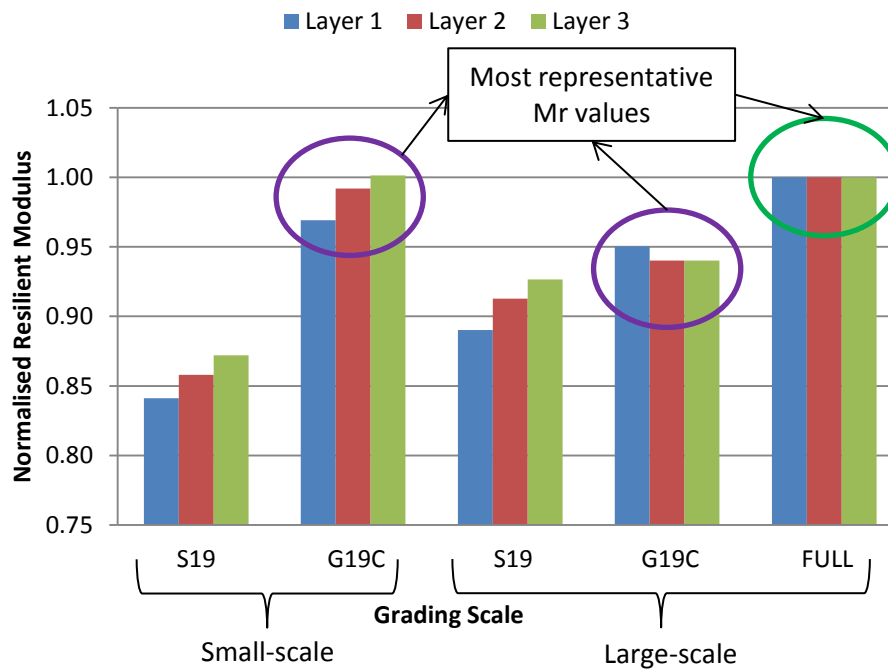


Figure 5- 2: Normalised Resilient Modulus Values after Iterative Design

It is very interesting, as it has been shown in Chapter 4, that at different Bulk Stresses and applied deviator Stress Ratios, different grading and specimen sizes represent the *Full* grading curve best. The above however shows that for a typical South African pavement structure, under typical South African loading conditions, with the associated parent material, that the *G19C* grading curve represents the Resilient Modulus of the *Full* grading curve best. This is confirmed by comparing the Bulk Stresses induced in the unbound base layer to the Bulk Stresses and their associated Resilient Modulus values in Chapter 4. It has been shown in Chapter 4 that for Bulk Stresses in close proximity to 1000 kPa and higher, that the *G19C* grading curve represents the *Full* grading best.

It is important to note however that the above was found to be true for the specific Stress Ratios (low, $\pm 20\%$) induced in the pavement analysis. It is plausible that the findings, at higher Stress Ratios, can be inconsistent to that observed above. However, it could be argued that the above observation hold true since a competent design should yield low Stress Ratios to ensure that the material does not become unstable (due to high Stress Ratios).

5.3 Design Life Calculations

To determine the design life of the pavement structures, the final Resilient Modulus values are used to determine the stresses and strains of the associated layers which is used in transfer functions to obtain the design life.

5.3.1 Unbound Granular Base Layer

Figures 5-3 and 5-4 show the development of horizontal and vertical stresses throughout the pavement structure as analysed in BISAR 3 for the associated base material.

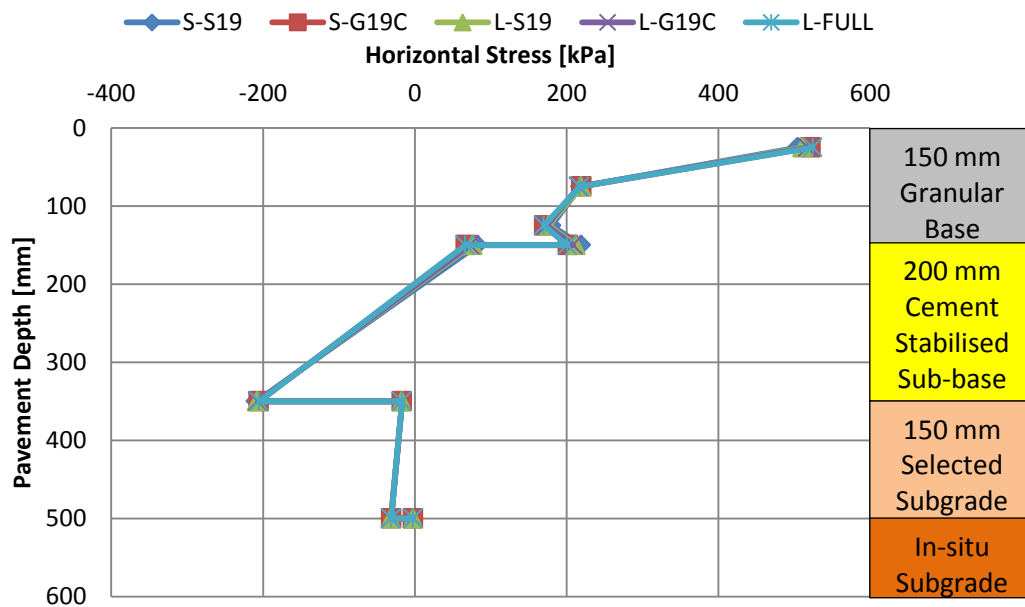


Figure 5- 3: Horizontal Stress Development in Pavement Structure

Note that for all specimen and grading curves, there is a constant change in horizontal stress with an increase in pavement depth. Further, note that at depths of 150, 350 and 500 mm there is a jump in the horizontal stress. This jump is caused by a change in the stiffness of the materials. With the strain being equal, a change in stiffness results in a change in stress (Hooke’s Law).

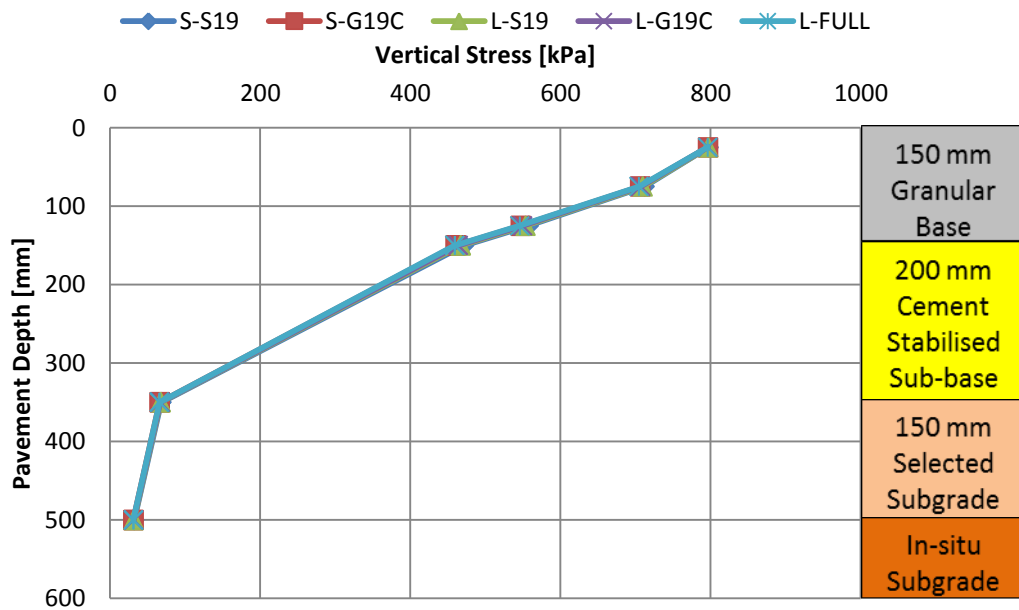


Figure 5- 4: Vertical Stress Development in Pavement Structure due to Loading

From Figure 5-4, it should be noted that, as expected, there is a decrease in vertical stress with increase in pavement depth. This confirms that the load applied to the pavement structure is distributed throughout the pavement structure by the pavement layers, thereby reducing the stress as the depth increases. Furthermore, this reduction in vertical stress contributes to the reduction in Resilient Modulus of the UGM basecourse. A reduction in vertical stress yields a lower Bulk Stress, which in turn yields a lower Resilient Modulus.

For the purpose of this research study, the South African Mechanistic Design Method (SAMDM) was used to establish the design life of both the base and subbase layer of the pavement structure.

For all three layers of the unbound base course the design safety factor, F is determined using Equation 5-1 (Theyse, 2000).

$$F = \frac{\sigma_3 \phi_{term} + C_{term}}{\sigma_1 - \sigma_3} \quad 5-1$$

Where: σ_3 = horizontal principal stress [kPa]

σ_1 = vertical principal stress [kPa]

$$\phi_{term} = K \left(\tan^2 \left(45 + \frac{\phi}{2} \right) - 1 \right)$$

$$C_{term} = 2KC \tan \left(45 + \frac{\phi}{2} \right)$$

- K = moisture condition constant (0.8 for moderate moisture)
- ϕ = Friction Angle [°]
- C = Cohesion [kPa]

Once the factor of safety F has been determined as shown above, the relationship between the estimated design life and F , shown by Equation 5-2 (Theyse, 2000), can be applied to establish the estimated design life N , of the material layer. Note that Equation 5-2 presents the transfer function for estimating the design life of class B roads.

$$N_B = 10^{(2.605122F+3.707667)} \tag{5-2}$$

Where: N_B = Estimated design life for class B roads [ESA]

Table 5-3 presents a summary of the design life calculations for each of the grading and specimen sizes analysed.

Table 5- 3: Summary of Design Life Calculation for Unbound Granular Basecourse Layer

Specimen Size	Grading Curve	C [kPa]	ϕ [°]	Position-Layer	σ_1 [kPa]	σ_3 [kPa]	$\sigma_{1,f}$ [kPa]	σ_d [kPa]	$\sigma_{d,f}$ [kPa]	DSR	C-term	ϕ -term	F	N_B [ESA]
Small	S19	184.7	45.9	Middle-1	797.5	504.5	3987.5	293.0	3483.0	0.08	729.76	4.08	9.5	3.0E+28
				Middle-2	712.2	218.2	2242.3	494.0	2024.1	0.24			3.3	1.8E+12
				Middle-3	557.7	180.2	2010.7	377.5	1830.5	0.21			3.9	6.5E+13
	G19C	109.5	50.0	Middle-1	796.5	521.5	4529.1	275.0	4007.6	0.07	480.72	5.23	11.7	1.2E+34
				Middle-2	706.1	219.5	2254.3	486.6	2034.8	0.24			3.3	2.6E+12
				Middle-3	547.2	170.9	1888.2	376.3	1717.3	0.22			3.7	1.7E+13
Large	S19	174.1	47.8	Middle-1	797.1	511.3	4332.2	285.8	3820.9	0.07	721.56	4.57	10.7	3.7E+31
				Middle-2	709.8	219.1	2371.9	490.7	2152.8	0.23			3.5	7.1E+12
				Middle-3	553.4	176.5	2086.1	376.9	1909.6	0.20			4.1	1.8E+14
	G19C	109.1	51.7	Middle-1	796.6	518.0	4931.0	278.6	4413.0	0.06	503.27	5.84	12.7	5.2E+36
				Middle-2	706.9	215.9	2422.1	491.0	2206.2	0.22			3.6	1.2E+13
				Middle-3	549.9	173.9	2073.3	376.0	1899.4	0.20			4.0	1.7E+14
	FULL	127.5	49.8	Middle-1	796.2	524.6	4608.1	271.6	4083.5	0.07	557.04	5.17	12.0	1.1E+35
				Middle-2	704.6	217.2	2315.9	487.4	2098.7	0.23			3.4	4.8E+12
				Middle-3	545.7	169.9	1963.2	375.8	1793.3	0.21			3.8	4.5E+13

Interestingly, Table 5-3 shows that the critical points of failure, for all of the specimens analysed are in the centre of the basecourse layer. This is confirmed by plotting the deviator Stress Ratio DSR in relation to the pavement depth as illustrated by Figure 5-5. Note, from Figure 5-5, that the maximum DSR is reached at a depth of 75 mm, which is at the centre of the basecourse.

Note that the Design Life calculations show that the granular base will last forever ($N = \pm 10^{12}$ ESA's). This however is a shortcoming of the SAMDM as highlighted by F.J. Jooste's in his re-evaluation of some aspects of the mechanistic-empirical design

approach (Jooste, 2004). Given the overall pavement balance, which is poor considering the Modular Ratio between the stiffness of the subbase and subgrade layers (Modular Ratio of 5 which is high), hence the low expected life of the subbase layer (see calculations in Sub-section 5.3.2), the low DSR in the granular base layer still lead to very high SF's and expected Design Life's. Therefore, it appears that the granular base will last forever, but this is actually not the case.

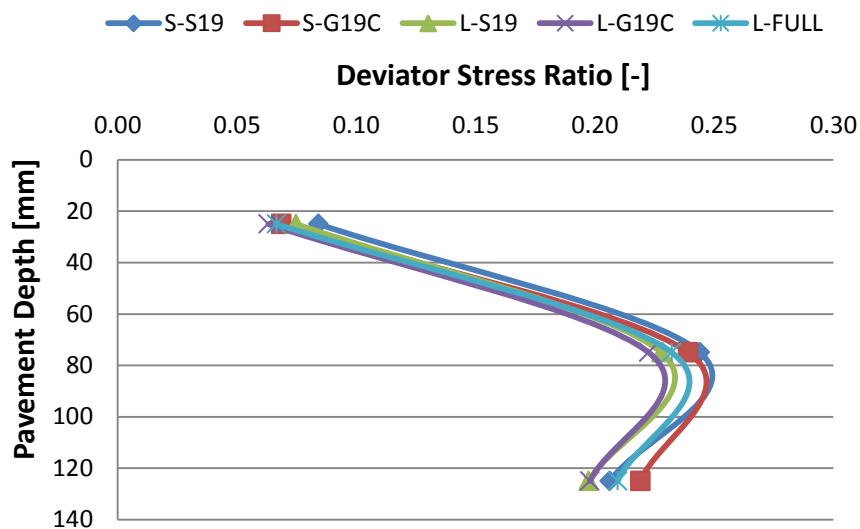


Figure 5- 5: Progression of DSR in Relation to Pavement Depth

5.3.2 Cement Stabilised Subbase Layer

The design life of the cement stabilised subbase layer is also computed using the method presented by the SAMDM. The mechanism of failure expected is that of fatigue cracking therefore the critical point of analysis is the tensile strain at the bottom of the stabilised layer (depth of 350 mm). BISAR 3 is again used to evaluate the strain and the fatigue relationship presented by Equation 5-3 (Theyse, 2000) is used to estimate the design life.

$$N_B = SF * 10^{6.84 \left(1 - \frac{\epsilon}{7.63 \epsilon_b}\right)} \quad 5-3$$

- Where:
- N_B = Estimated design life for class B roads [ESA]
 - SF = Layer thickness shift factor ($10^{0.00285h - 0.293}$)
 - ϵ = Tensile strain at bottom of stabilised layer [$\mu\epsilon$]
 - ϵ_b = Strain at break (125 $\mu\epsilon$ for C3 material)

Table 5-4 presents the calculations used to estimate the design life of the cements

stabilised subbase layer.

Table 5- 4: Summary of Design Life Calculations for Stabilised Subbase Layer

Specimen Scale	Grading Scale	ϵ [$\mu\epsilon$]	ϵ_b [$\mu\epsilon$]	h [mm]	SF	N_B [ESA]
150 mm ϕ *	S19	174	125	200	1.89	7.40E+05
300 mm H	G19C	170.5	125	200	1.89	7.84E+05
300 mm ϕ *	S19	172.5	125	200	1.89	7.58E+05
	G19C	171.7	125	200	1.89	7.68E+05
	FULL	170.2	125	200	1.89	7.88E+05

Note that there is a slight difference in the design life estimations for each of the evaluated grading and specimen sizes.

5.3.3 Comparison of Design Life

It is clear from Tables 5-3 and 5-4 and Figure 5-6 that pavement failure will be caused by a failure in the stabilised subbase. Cracking will occur due to the high tensile strains developed at the bottom of the layer.

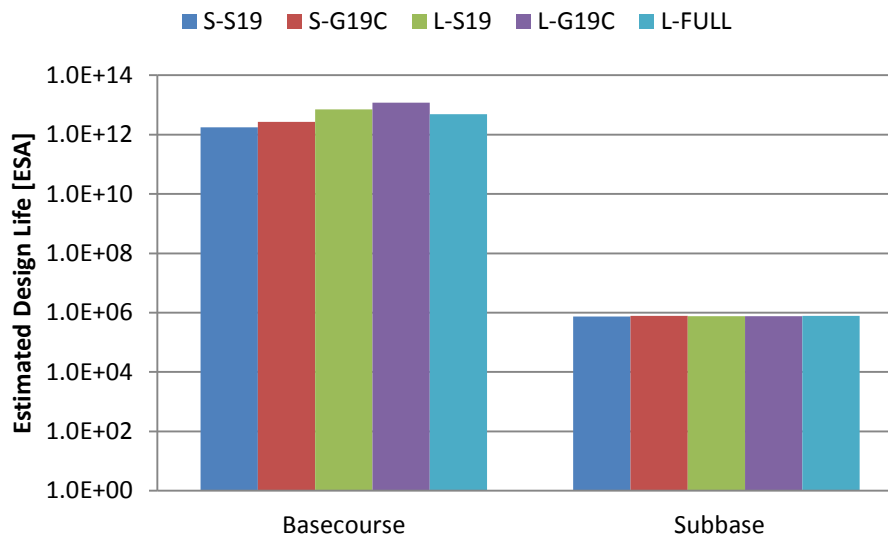


Figure 5- 6: Comparison of Estimated Design Life Values

A further interesting point to take note of is that, although the failure of the pavement structure will occur in the subbase, the estimated design life of the pavement structure that incorporates the *G19C* grading curves are more representative to that of the *Full* grading curve. This shows that for the design life analysis shown, that the analysis of the *G19C* grading curves are more representative to that of the *Full* grading curve. In addition it should be noted that results obtained by testing large specimens yield far greater expected design lives compared to small specimens

It is important to note that although the initial design life of the basecourse is high in comparison to that of the subbase, the stiffness of the subbase will decrease as it approaches failure. As the pavement finds more balanced Modular Ratios, the stiffness of the subbase will reduce, resulting in a reduced basecourse stiffness thereby reducing the design life of the granular base too. However, for the purpose of this comparison into the influence of the base layer's grading, it suffices to use the initial subbase stiffness for the stress distribution in this sensitivity analysis.

CHAPTER 6: CONCLUSIONS AND RECOMMENDATIONS

This final chapter presents a synthesis on the conclusions drawn from the research study. In addition, recommendations for future studies are presented as well as methods to improve the current testing protocols and testing equipment used for this study.

6.1 Conclusions

6.1.1 General Conclusions

The general conclusions that were made based on observations and results obtained in this study include:

- The most commonly used method of grading manipulation, the parallel-scalp-method, referred to as the *S19* grading curve in this thesis, yields a very fine grading that does not, at any stage along the grading curve, simulate the initial *Full* grading. Therefore, an alternative method, more representative of the true grading, needs to be implemented.
- The alternative to the *S19* grading curve, the *G19C* grading curve, yields a grading curve that fits the *Full* grading curve precisely except at sieve sizes greater than 13,2mm.
- Both sizes of specimen compaction equipment allowed for accurate control of density. This in turn allowed comparison of different sized specimens prepared under similar conditions.
- The large-size testing apparatus allows more accurate control of the applied confinement pressure. The pressure is controlled by the system itself and not manually as is the case with the small-size testing apparatus.
- The entire range of monotonic tri-axial specimens showed a decrease in moisture content due to the curing method implemented. Large-size monotonic specimens however showed a smaller reduction in moisture content (0.14%) when compared to small-size specimens (0.51% reduction). As mentioned, the implementation of plastic bags, to seal the small-size specimens, results in a build-up of moisture on the surface of the plastic thereby removing moisture from the specimens themselves. In addition, the volume to surface area ratio (30 and 60 for small- and large-size specimens respectively) could also influence the flow of moisture, resulting in increased

moisture loss for small-size specimens which has more surface area in relation to specimen volume when compared to large-size specimens.

- All sizes of specimens tested showed the material's stress dependent nature. Shear strength increased with increasing confinement pressure whereas all dynamically loaded specimens showed an increase in Resilient Modulus for an increase in confinement pressure, applied vertical stress and Bulk Stress.
- The number of specimens tested influences material shear parameters. Results show that reducing the number of small-size specimens monotonically tested from eight to six (i.e. removing the 25 kPa specimens) results in a significant increase in Cohesion and a decrease in Friction Angle. Therefore, to allow for comparison, a similar range of confinement pressures needs to be tested.
- All tests performed on specimens already dynamically loaded, showed an increase in both shear strength and resilient performance properties. Monotonic tri-axial tests were performed on small-size specimens that were dynamically tested up to a maximum Stress Ratio of 55% . The results showed an increase in both Cohesion and Friction Angle. In addition, additional load cycles were applied to large-size dynamically loaded specimens once the initial dynamic tri-axial test was complete. The results showed an increase in the Resilient Modulus of the tested material. Furthermore, all $M_r-\theta-\frac{\sigma_d}{\sigma_f}$ calibrated models showed material stiffening ($k_5 < 0$).

This stiffening results from an increase in density and a reduction in plasticity as a result of dynamic loading. Another factor that supported the phenomenon that dynamic loading causes an increase in density was the forcing out of moisture from the specimens during dynamic testing.

- Generally the $M_r-\theta-\frac{\sigma_d}{\sigma_f}$ model, which accounts for the influence of the deviator Stress Ratio, fits the measured Resilient Modulus values best. As mentioned however, the model predicts material stiffening. Although this is the case for the range of applied Stress Ratios, material softening or even failure is expected at severe Stress Ratios. Therefore, it is important to note that this conclusion is based on the range of Stress Ratios tested and different trends can be expected for more severe Stress Ratios.
- The dynamic tri-axial test results showed that for all sizes of specimens the one second load cycle can be shortened to a half second load cycle without

influencing the measured Resilient Modulus. The response of this specific material is so rapid that there is no need for a 0.9 second rest period. Although it has also been shown that the duration of the loading and unloading phase can also be halved, this does place severe strain on the testing equipment.

- Analysis of large-size dynamic tri-axial results show that the mechanism used to connect vertical LVDT's to the large-size specimens allows severe movement of the LVDT's which could influence the results obtained. An improvement to the current mechanism is required.
- For the typical pavement structure analysed, basecourse failure will occur in the centre of the basecourse layer.
- The design life analysis shows that the critical design life is that of the stabilised subbase layer which will fail long before failure in the basecourse occurs. Failure will occur due to tensile strains induced at the bottom of the stabilised subbase layer.

6.1.2 Influence of Specimen Geometry

To gain an understanding of the influence of specimen geometry, on the performance properties tested, two sizes of specimens were tested. The results were analysed and it was concluded that:

- The larger specimens, for both grading curves, showed lower Cohesion values when compared to small-size specimens. In terms of Friction Angle, both grading curves yielded greater angles of internal friction for larger specimens.

Although it is plausible that the influence is due to material variation, the variation in material specimens is small and that the influence thereof is insignificant. In addition, both grading curves showed the above influence of specimen geometry which adds to the believe that the observation is influenced by specimen geometry rather than material variation.

- With regard to Resilient Modulus and the $M_r-\theta$ model, it is clear that specimen geometry does influence the Resilient Modulus however, no certain and constant trend can be established.

For the *S19* grading curve, larger specimens yield larger Resilient Modulus values whereas the *G19C* grading curve yields higher Resilient Modulus

values for the small size specimens. The influence of specimen geometry is thus influenced by the grading of the tested specimens.

- The $M_r-\theta-\frac{\sigma_d}{\sigma_f}$ model also shows that the Resilient Modulus is influenced by specimen geometry and that no certain trend can be established. The model however adds to the $M_r-\theta$ model, in that it shows that the applied deviator Stress Ratio also affects the influence of specimen geometry and that the affect is not constant for all grading curves.

For a deviator Stress Ratio of 0.1, the *S19* grading curve yield higher Resilient Modulus values for large specimens over the entire range of Bulk Stresses. The *G19C* grading curve on the other hand yields lower Resilient Modulus values for large-size specimens for stresses equal and less than 500 kPa. For Bulk Stresses greater than 500 kPa the *G19C* grading curve yield greater Resilient Modulus values for larger specimens.

In summary, both grading curves, for an applied deviator Stress Ratio of 0.1 and applied Bulk Stresses greater than 500 kPa, yield higher Resilient Modulus values for large-size specimens. For Bulk Stresses 500 kPa and less, the *G19C* grading curve yield lower values for large-size specimens.

For a deviator Stress Ratio of 0.9 and the entire range of Bulk Stresses, the smaller specimens yield greater Resilient Modulus values for both grading curves.

- Large-sized specimens showed lower standard deviations and coefficients of variation, for both monotonic and dynamic tri-axial test, when compared to small-size specimens. It is believed that this is due to boundary conditions, caused by the moulding process, influencing the obtained results thereby showing that larger sized specimens are less influenced by boundary conditions caused by the split moulds used during specimen preparation.

6.1.3 Influence of Grading Curve

The influence of grading curve on the resilient response of the tested material can be evaluated by using the calibrated models and plotting their results in relation to various Bulk Stress values and, in the case of the $M_r-\theta-\frac{\sigma_d}{\sigma_f}$ model, the applied Stress

Ratio. From the plotted results, it can be concluded that:

- For both specimen sizes, the finer *S19* grading curve yield far greater Cohesion values when compared to that of the coarser *G19C* and *Full* grading curves.
- In terms of Friction Angle, the coarser *G19C* grading curve yields, as expected, higher angles of internal friction for both specimen sizes, when compared to the finer *S19* grading curve.
- With regards to the Resilient Modulus values, estimated with the $M_r-\theta$ model, the *G19C* grading curve yields greater Resilient Modulus values compared to its finer counterpart, the *S19* grading curve, for Bulk Stresses greater than 500 kPa. This confirms that grading curve does influence the Resilient Modulus of the tested material although the influence is affected by the applied Bulk Stress.
- The $M_r-\theta-\frac{\sigma_d}{\sigma_f}$ model also shows that grading curve influences the Resilient Modulus of the tested material. Except for an applied deviator Stress Ratio of 0.1, the *G19C* grading curve yield higher Resilient Modulus values when compared to the *S19* grading curve for both sizes of specimens. At a deviator Stress Ratio of 0.1 however, the large-size *S19* specimen yields greater Resilient Modulus values for the entire range of Bulk Stresses.

This confirms that the Resilient Modulus of the tested material is influenced by grading curve however; the applied deviator Stress Ratio also affects the influence.

6.1.4 Comparison of Grading Curves

Although not initially set as an objective of this thesis, a revised method of grading manipulation for small-size laboratory characterisation of pavement materials is recommended. Through analysis of test results and based on the assumption that the large-size *Full* grading curve specimen's best simulate true infield performance, the following can be conclude:

- In terms of the grading curve itself, the *G19C* grading curve fits a large portion of the *Full* grading curve whereas no part of the *S19* grading curve fits the *Full* grading curve. This in itself shows that the *G19C* grading curve is more representative of the *Full* grading.

- For both Cohesion and Friction Angle, the *G19C* grading curve yields more representative results to that of the *Full* grading curve. This is noted for both small and large-size specimens.
- With regard to the experimental Resilient Modulus and design results that were considered for the tested grading curves, none of the two adjusted grading curves yield results that are comparable to that of the *Full* grading for the full range of Bulk Stresses and applied SR_d . However, the *G19C* grading curve fits the *Full* grading best for a wider range of Bulk Stress and SR_d values.
- In terms of the design life analysis, the estimated pavement design life for both sizes of the *G19C* grading curves are more representative of the *Full* grading curve when compared to that of the finer *S19* grading curves. In addition, when comparing the Bulk Stresses induced in the granular base due to loading, the *G19C* grading fits the *Full* grading best. This shows that even though the *G19C* grading does not always fit the *Full* grading best, especially at low Bulk Stresses (<100 kPa) and Deviator Stress Ratios (<20%), it does however fit the *Full* grading best for typical South African pavement structures and the stresses induced therein due to typical South African loading conditions. Note that this is true for Phase 1 of the design and could have been different for Phase 2 (equivalent granular phase).

6.2 Recommendations

Although the research study yielded valuable information regarding the influence of specimen geometry and grading curve on the performance of the tested material, the research was not without drawbacks. Therefore, to improve future research into this topic and other topics involving similar testing protocols, recommendations are presented below.

6.2.1 Future Research

Recommendations for future research include:

- Only one representative parent material was selected for testing. Therefore, it is recommended that, future studies, investigating the influence of grading curve and specimen geometry, investigate the influences on more types of materials. This would show whether the influence is similar for various material types.

- One moisture content and target dry density was used for all grading curve. In doing this, some grading curves tested might not have been compacted to their maximum density at their optimum moisture content. Therefore it is recommended that future research evaluate specimens compacted to maximum density at their optimum moisture content. This would give a better understanding of the material infield performance when compacted to its maximum density.
- The literature reviewed showed that some practices use specimens previously dynamically loaded for evaluation of shear performance. This research however shows that an increase in shear performance can be expected when comparing results from virgin specimens to that of previously dynamically loaded specimens. It is therefore recommended that this practice only be used to evaluate the future expected shear performance of the material once dynamically loading and not during initial design phase testing.
- It has been shown that the commonly used parallel-scalping method (*S19* grading curve) does not yield results as representative of the true *Full* grading curve. Therefore, it is recommended that future research incorporate the more representative scalp-add-back method (*G19C* grading curve) for specimen preparation and testing.
- A robust method for achieving equilibrium moisture content is required for large-size specimens. Further research to develop such an method is required for future testing of large-size specimens.

6.2.2 Testing Protocols

The results show that, for the representative parent material tested, the current 0.9 second resting period within the prescribed loading cycle, is too long. The response of the material is rapid and after about 0.4 seconds no further change in the displacement measured by the vertical LVDT's is noted. Therefore, since there is no further change noted, there is no need for the prolonged resting period. It is recommended, based on the results obtained, that the loading cycle for dynamic tri-axial tests be revised to incorporate a 0.1 second loading phase followed by a 0.4 second resting period. This would halve the time required to perform both short duration dynamic and permanent deformation tri-axial tests.

Care should however be taken when shortening these load pulses. As mentioned, shortening the loading phase placed high strain on the apparatuses used.

Furthermore, not all tri-axial apparatuses are capable of applying shortened load pulses without influencing the obtained results. Therefore, it is advised that, if the route of shortening the load pulse is taken, the tester should perform a regime of tests to evaluate the equipment used load dependent pulse wave to confirm whether the apparatus used is capable of applying the shortened load without influencing the results.

6.2.3 Testing Apparatus

Although the testing apparatus' used for this research study performed as desired, slight changes to the equipment can improve future testing. Therefore, it is recommended that:

- The small-size tri-axial apparatus be upgraded to a system similar to that of the large-size apparatus. Currently the small-size apparatus requires the researcher to manually set the confinement pressure using a valve system. This however is not as accurate as the system implemented on the large-size apparatus, which is automatically controlled, by the control system, to yield the desired confinement pressure.
- The mechanism used to attach the vertical LVDT's to large-size specimens be changed to a similar method as that used on the small-size tri-axial apparatus. The small-size tri-axial apparatus implements a mechanism that is more rigid when compared to that of the large-size mechanism thereby yielding more stable displacement measurements.

REFERENCES

1. AASHTO. 2008. M145-91: *Standard Specification for Classification of Soils and Soil-Aggregate Mixtures for Highway Construction Purposes*. American Association of State and Highway Transportation Officials. Available from AASHTO Bookstore: bookstore.transportation.org, 2008.
2. Al-Ajmi, A.M., Zimmerman, R.W., 2005. *Relation between the Mogi and the Coulomb failure criteria*. Int. J. Rock Mech. Miner. Sci. 42 (3), 431–439., 2005.
3. Anochie-Boateng, J., Paige-Green, P., Mgangira M., 2009. *Evaluation of test methods for estimating resilient modulus of pavement geomaterials*. In Proceedings of the 28th Southern African Transport Conference, pp245 (Vol. 248), 2009.
4. Araya, A.A., 2011. *Characterisation of Unbound Granular Materials for Pavements*. PHD dissertation at Delft University of Technology. The Netherlands, 2011.
5. Asphalt Academy, 2009. *Bitumen Stabilised Materials Technical Guidelines (TG2)*, Asphalt Academy, Pretoria, South Africa, 2009.
6. ASTM. 2009. D3282-09. *Standard Practice for Classification of Soils and Soil-Aggregate Mixtures for Highway Construction Purposes*. Available from ASTM Webstore: webstore.ansi.org, 2009.
7. Austin, A., 2009. *Fundamental characterization of unbound base course materials under cyclic loading*. Dissertation. Faculty of the Louisiana State University and Agricultural and Mechanical College in partial fulfilment of the requirements for the degree of Master of Science in Civil Engineering in The Department of Civil and Environmental Engineering By Aaron Austin BS, Louisiana Tech University, 2009.
8. Brown, S. F., 1996. *Soil Mechanics in Pavement Engineering*, 36th Rankine Lecture: Géotechnique, Vol. 46, No. 3, pp 383-426, 1996.
9. Brown, S. F. and Pell, P. S., 1967. *An experimental investigation of the stresses, strains and deflections in a layered pavement structure subjected to dynamic loads*. In Intl Conf Struct Design Asphalt Pvmts, 1967.
10. Chan, F. W. K., 1990. *Permanent Deformation Resistance of Granular Layers in Pavements*. PhD Dissertation, University of Nottingham, United Kingdom, 1990.
11. Chilukwa, N. N., 2013. *Vibratory Hammer Compaction of Granular Materials*. Master of Engineering, Stellenbosch University, South Africa, 2013.

12. Committee of Land Transport Officials (COLTO). 1998. *Standard specifications for road and bridge works for state road authorities*. South African Institute of Civil Engineers. South Africa, 1998.
13. Craig R. F., 2004. *Craig's Soil Mechanics*. Seventh Edition. SPON Press, Oxon, UK, 2004.
14. Edwards, J. P., 2007. *Laboratory characterisation of pavement foundation materials*. Doctoral dissertation, Loughborough University, Nottingham, 2007.
15. Erkens, S. M. J. G., 2002. *Asphalt concrete response (ACRe): determination, modelling and prediction: Het gedrag van asfalt (ACRe): bepalen, modelleren en voorspellen*. Delft University of Technology. Delft, The Netherlands, 2002.
16. Huurman M., 1997. *Permanent Deformation in Concrete Block Pavements*. PhD Thesis. Delft University of Technology. Delft, The Netherlands, 1997.
17. Huurman, M. and Van Niekerk, A. A., 1995. *Establishing Complex Behaviour of Unbound Road Building Materials from Simple Material Testing*, Laboratory for Road and Railroad Research. Delft University of Technology, Delft, report, 7-95., 1995.
18. Jenkins J. K., 2000. *Mix design considerations for cold and half-warm bituminous mixes with emphasis on foam bitumen*. PHD dissertation, Stellenbosch University, South Africa, 2000.
19. Jenkins, J. K., 2010. *South African hot mix asphalt design*. Pavement material II lecture notes presented at Stellenbosch University, South Africa, 2010.
20. Jooste, F. J., 2004. *A Re-evaluation of Some Aspects of the Mechanistic-Empirical Design Approach*. In Proceedings of the 8th Conference on Asphalt Pavements for Southern Africa (CAPSA'04), Vol. 12, p. 16., 2004.
21. Kelfkens, R. W. C., 2008. *Vibratory Hammer Compaction of Bitumen Stabilised Material*. Dissertation for Master of Science in Engineering, Stellenbosch University, Stellenbosch, South Africa, 2008.
22. Lee, D. H., Juang, C. H., Lin, H. M., & Yeh, S. H., 2002. *Mechanical behavior of Tien-Liao mudstone in hollow cylinder tests*. Canadian geotechnical journal, 39(3), 744-756., 2002.
23. Lefevre, S. R. and Van Niekerk, A. A., 1998. *Compactive Behaviour of Mix Granulate Basecourse Materials in Relation to Physical Material Properties*. Delft University of Technology, Delft, Report: 7-98-200-20, ISSN 0169-9288, 1998.
24. Lekarp F., Isacsson U. and Dawson A., 2000. "State of the Art. 1: Resilient Response of Unbound Aggregates." *Journal of Transportation Engineering*, Vol.

- 126, No. 1. pp 71-72., 2000.
25. Lekarp, F., Isacsson, U., and Dawson, A., 2000. "State of the Art. II: Permanent strain response of unbound aggregates." J. Transp. Engrg., ASCE, 126(1), 76–83., 2000
 26. Lekarp, F., & Isacsson, U., 2001. *The Effects of Grading Scale on Repeated Load Triaxial Test Results*. International Journal of Pavement Engineering, 2(2), 85-101., 2001.
 27. Maree, J. H., 1979. *Die Laboratoriumbepaling van die Elastiese Parameters, die Skuifsterkteparameters en die Gedrag onder Herhaalde Belasting van Klipslagkroonlaagmateriale: Toetsmetodes en Apparaatbeskrywing*. Technical Report RP/11/78, NITRR, CSIR.
 28. Mgangira, M. B, Maina, J., Paige-Green, P., Theyse, H., Verhaeghe, B. and Jenkins, J.K., 2011. *Proposed protocol for resilient modulus and permanent deformation characteristics of unbound and bound granular materials*, Report No SANRAL/SAPDM/B1-c/2011-01, CSIR & Stellenbosch University, South Africa, 2011.
 29. Molenaar, A.A.A., 2010. *Cohesive and Non-Cohesive Soils and Undound Granular Materials For Base and Sub-Base in Roads*, Pavement Materials 1 Lecture Notes, Stellenbosch University, 2010.
 30. Morton, B. S, Lutting, E., Horak, E., Visser, A.T., 2004. *The effect of axle load spectra and tyre inflation pressures on standard pavement design methods*. Proceedings of the 8th conference on asphalt pavement for Southern Africa (CAPSA'04). Sun City. 2004.
 31. Multiquip, 2011. *Soil Compaction Handbook*. Multiquip Inc. Rev. A (0212_BD), Carson, 2011.
 32. Mulusa, W. K., 2009. *Development of a simple triaxial test for characterising bitumen stabilised materials*.
 33. Pavementinteractive, 2007. "Poisson's Ratio" Cited: 3 October 2013, Available: <http://www.pavementinteractive.org/article/poissons-ratio/>
 34. Rani. R. S., Prasad. K. N., Krishna. T. S., 2014. *Applicability of Mohr-Coulomb and Drucker-Prager Models for Assessment of Undrained Shear Behaviour of Clayey Soils*, Journal of Civil Engineering and Technology (IJCIET), ISSN 0976 – 6308 (Print), ISSN 0976 – 6316(Online), Volume 5, Issue 10, October (2014), pp. 104-123 © IAEME, 2014.
 35. Roman Roads, 2001. *Building, Linking, and Defending the Empire.*" Science and

- Its Times*. Ed. Neil Schlager and Josh Lauer. Vol. 1. Detroit: Gale, 2001. Gale World History. 2013.
36. Rondón, H. A., Wichtmann, T., Triantafyllidis, T., & Lizcano, A., 2009. *Comparison of cyclic triaxial behavior of unbound granular material under constant and variable confining pressure*. Journal of Transportation Engineering, 135(7), 467-478., 2009.
37. Rudman, C., 2012, *Trouble Shooting the Large Triaxial*, Draft Background Report, Faculty of Engineering, Department of Civil Engineering, Stellenbosch University, South Africa, 2012.
38. Seed, H.B., Chan, C.K and Lee, C.E., 1962. *Resilience characteristics of subgrade soils and their relations to fatigue in asphalt pavements*. Proceedings of International Conference on Structural Design of Asphalt Pavements. Ann Arbor, USA. Vol 1, pp 611-636., 1962.
39. Semmelink, C. J., 1991. *Use of the DRTT K-mould to determine the elastic and shear properties of pavement materials*, Department of Transport, Pretoria, South Africa, 1991.
40. Semmelink, C. J., 1995. *Optimal Compaction of Untreated Road Building Materials in South Africa*. Proceedings of the Fourth International Symposium on Unbound Aggregates in Roads (UNBAR 4). 17th – 19th July 1995, University of Nottingham, Nottingham, United Kingdom, 1995.
41. Semmelink C.J. and Botha P.B., 2004. *Determination of the Bulk Relative Density (BRD) and Apparent Relative Density (ARD) of granular materials in one test by means of the rice method (suitable for all types of material for both ≥ 4.75 mm and < 4.75 mm fractions)*. Proceedings of the 8th conference on asphalt pavements for Southern Africa (CAPSA'04). Sun city, South Africa, 2004.
42. South African Pavement Engineering Manual (SAPEM). 2013. South African Pavement Engineering Manual 1st edition. South Africa, 2013.
43. Sweere, G. T. H., 1990. *Unbound granular basis for roads*, PhD thesis, University of Delft, Delft, The Netherlands, 1990.
44. Technical Methods for Highways (TMH1). *Standard methods of testing road construction materials*. 2nd edition. Department of Transport, Pretoria, South Africa.
45. Technical Recommendations for Highways (TRH 14). 1985. *Guidelines for road construction materials*. Department of Transport, Pretoria, South Africa, 1985.
46. Theyse, H.L, De Beer, M., Rust, F.C., 1996. *Overview of South African*

- mechanistic pavement design method*. Transportation Research Record 1539. Transportation Research Board. Washington: 6-16., 1996.
47. Theyse, H.L., 1998. *Towards Structural Guidelines for the Structural Design of Pavements with Emulsion-treated Layers*, CR-97/045, CSIR Transportek, 1998.
48. Theyse, H. L., 2000. *Overview of the South African Mechanistic Pavement Design Methods*, South African Transport Conference, Pretoria, South Africa, 2000.
49. Theyse, H. L., 2007. *A Mechanistic-Empirical Design Model for Unbound Granular Pavement Layers*. PhD Thesis, University of Johannesburg, Johannesburg, South Africa, 2007.
50. Theyse, H. L., 2010. *Effective Stress in Partially Saturated Unbound Granular Layer*. Pavement material I lecture notes presented at Stellenbosch University, South Africa, Mei 2010.
51. Theyse H. L., 2012. *Revision of the South African Pavement Design Method – Project Focus Area: Resilient Response Models for Unbound Material – B-1a*. Draft Contract Report SANRALSAPDM-B1a-2012-01. SANRAL, South Africa. 2012.
52. Thom, N. H., 1988. *Design of road foundations*, PhD thesis, Department of Civil Engineering, University of Nottingham, Nottingham, United Kingdom, 1988.
53. Thom, N. H., Edwards, J. P. and Dawson, A., 2005. *A Practical Test for Laboratory Characterization of Pavement Foundation Materials*
54. TxDot, 2002. *Triaxial Compression for Disturbed Soils and Base Materials*. Texas Department of Transport, TxDot Designation: TEX-117-E, 2002 – 2009.
55. Uzan, J., 1985. *Characterization of granular material*. Transp. Res. Rec. 1022, Transportation Research Board, Washington, D.C., 52–59., 1985.
56. Vanapalli, S. K., Fredlund, D. G., Pufahl, D. E., & Clifton, A. W., 1996. *Model for the prediction of shear strength with respect to soil suction*. Canadian Geotechnical Journal, 33(3), 379-392., 1996.
57. Van Niekerk, A.A., Scheers, J. van and Galjaard P.J., 2000. *Triaxial testing of coarse grained mix granulates at scaled gradings and smaller specimen sizes*. Proc. UNBAR 5; pp. 161-170; University of Nottingham, Department of Civil Engineering; Nottingham, United Kingdom, 2000.

58. Van Niekerk, A.A. 2002. *Mechanical behaviour and performance of granular bases and sub-bases in pavements*. PHD dissertation at the Delft University of Technology. The Netherlands, 2002.
59. Werkmeister, S., 2003. *Permanent deformation behaviour of unbound granular materials in pavement constructions*. Von der Fakultät Bauingenieurwesen der Technischen Universität Dresden, 2003.
60. Werkmeister, S., Numrich, R., Dawson, A. R., & Wellner, F., 2003. *Design of granular pavement layers considering climatic conditions*. Transportation Research Record: Journal of the Transportation Research Board, 1837(1), 61-70., 2003.
61. Witczak, M.W. and Uzan, J., 1988. *The Universal Airport Pavement Design System Report I of V: Granular Material Characterization*. University of Maryland, Department of Civil Engineering, 1988.
62. Wirtgen GmbH, 2004. *Cold Recycling Manual*, 2nd edition published by Wirtgen GmbH, Windhagen, Germany, 2004

APPENDICES

Appendix A:**Material Densities Based on Vibratory Compaction****Table A- 1: Mod Results for Small-size S19 Grading Curve**

Target MC [%]	Mass [g]	Height [mm]	Density [kg/m ³]	Holder Ref	EM [g]	WM [g]	DM [g]	True MC [%]	Average MC [%]
3	2483.00	61	2290.91	Y9	237.10	933.90	912.90	3.11	3.04
		61		73	237.50	935.60	914.90	3.06	
		62		98	178.40	914.30	893.10	2.97	
4	2484.00	59	2409.70	X2	237.20	902.90	877.60	3.95	4.04
		58		84	224.10	937.50	909.30	4.12	
		58		43	228.50	957.00	928.70	4.04	
4.7	2477.00	57	2473.58	63	226.40	901.90	872.60	4.53	4.79
		56		12	203.10	925.20	891.20	4.94	
		57		70	197.80	974.60	938.30	4.90	
5	2454.00	56	2465.11	12	203.10	898.90	865.20	5.09	4.92
		57		13	226.50	979.20	944.60	4.82	
		56		80	193.80	977.00	940.80	4.85	
6	2395.00	55	2479.19	70	197.90	875.80	837.90	5.92	5.91
		55		6A	179.60	874.80	834.60	6.14	
		54		63	220.90	918.10	880.70	5.67	

Table A- 2: Mod Results for Small-size G19C Grading Curve

Target MC [%]	Mass [g]	Height [mm]	Density [kg/m ³]	Holder Ref	EM [g]	WM [g]	DM [g]	True MC [%]	Average MC [%]
3	2488.00	61	2308.07	60	222.60	954.00	930.50	3.32	3.20
		61		61	285.50	1046.60	1022.10	3.33	
		61		32	219.30	1001.00	978.50	2.96	
4	2491.00	59	2402.76	3B	187.40	898.00	871.70	3.84	3.81
		59		2	207.20	952.90	924.70	3.93	
		58		58	202.60	933.00	907.30	3.65	
4.7	2463.00	56	2474.15	44	179.50	893.60	862.10	4.61	4.71
		56		X2	237.00	1016.10	981.40	4.66	
		57		65	228.40	1040.90	1003.30	4.85	
5	2444.00	56	2469.68	53	215.10	917.60	884.50	4.94	4.94
		56		24	185.90	886.00	852.70	4.99	
		56		2	238.70	976.40	942.10	4.88	
6	2383.00	54	2481.91	14	198.50	938.90	897.30	5.95	5.94
		54		18	189.70	964.40	921.40	5.88	
		55		17	153.10	900.50	858.30	5.98	

Table A- 3: Mod Results for Large-size Full Grading Curve

Target MC [%]	Mass [g]	Height [mm]	Density [kg/m ³]	Holder Ref	EM [g]	WM [g]	DM [g]	True MC [%]	Average MC [%]
4	20934.00	124	2381.95	80	193.80	773.40	751.00	4.02	3.74
		125		65	228.50	898.70	876.20	3.47	
		124		70	197.80	888.30	863.50	3.73	
4.7	21155.00	118	2522.04	2A	187.40	858.90	828.90	4.68	4.68
		119		32	202.50	873.20	842.60	4.78	
		119		54	215.00	934.40	902.80	4.59	
5	20967.00	119	2506.67	73	237.40	882.60	850.70	5.20	4.92
		118		63	226.40	901.50	870.50	4.81	
		118		Y3	236.20	1024.20	988.40	4.76	
6	20858.00	117	2514.89	4A	236.80	967.50	929.20	5.53	6.09
		117		X1	236.50	978.30	932.00	6.66	
		118		20	172.00	992.90	945.90	6.07	

Appendix B:

Monotonic Tri-axial Test Results

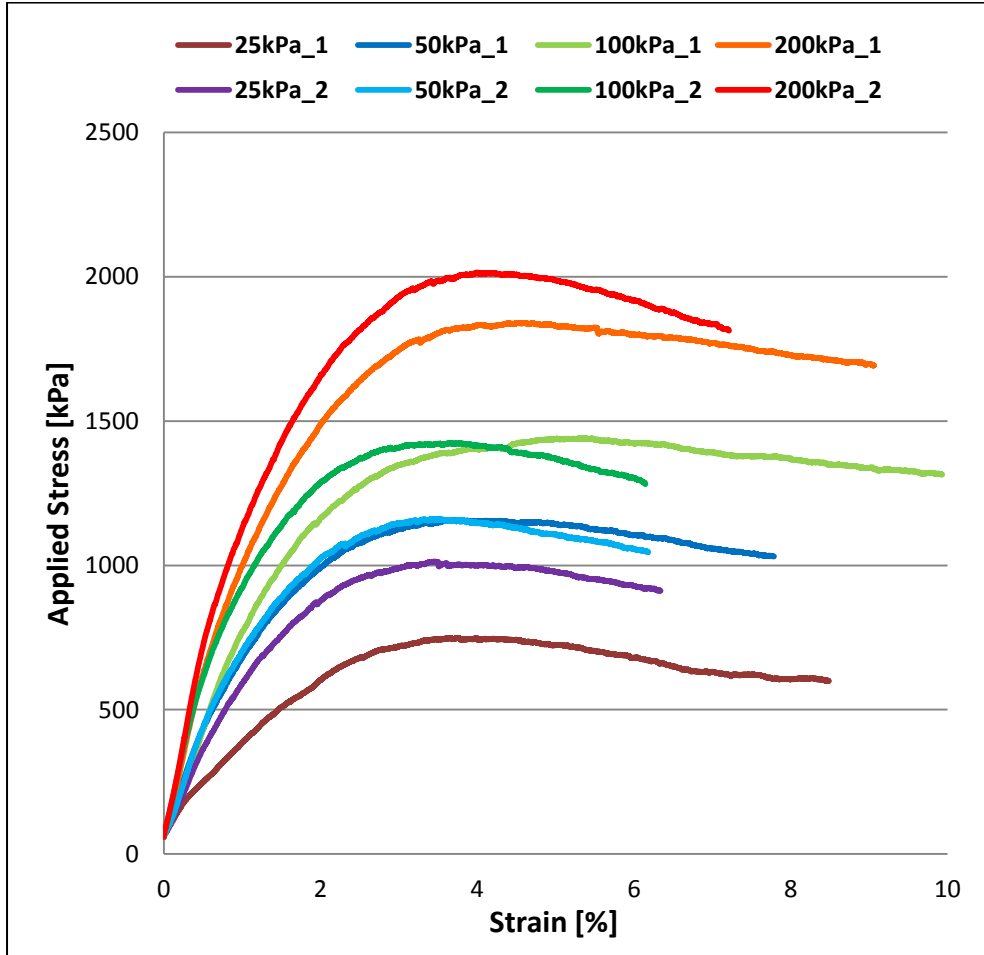


Figure B- 1: Stress-strain Relationship Curves, Small-size S19

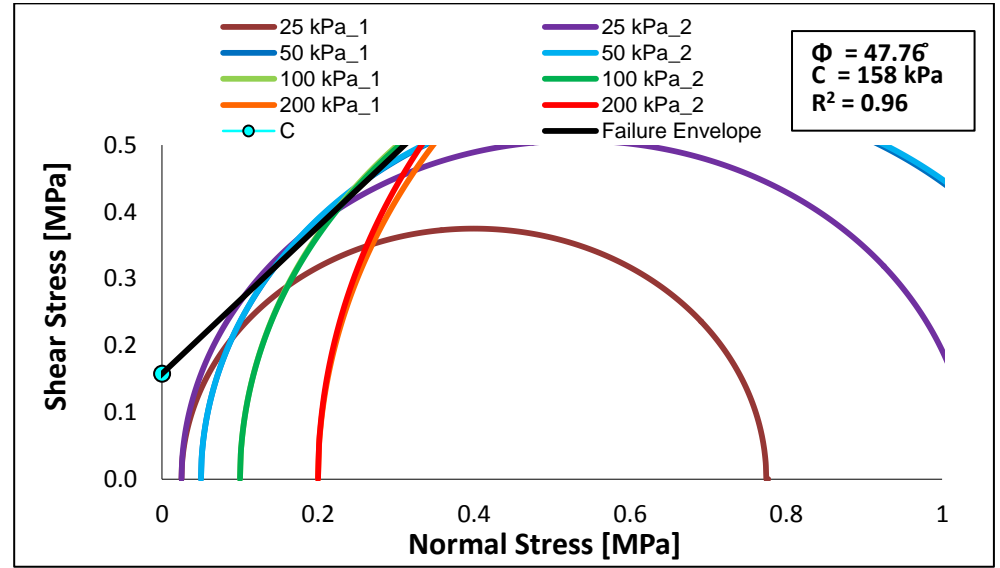


Figure B- 2: Eight Circle Mohr-Coulomb Representation, Small-size S19

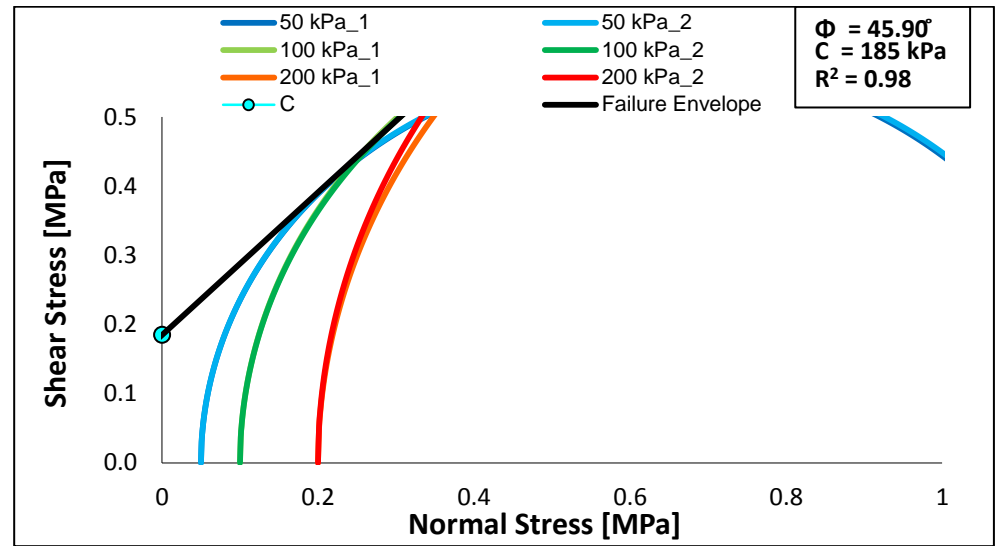


Figure B- 3: Six Circle Mohr-Coulomb Representation, Small-size S19

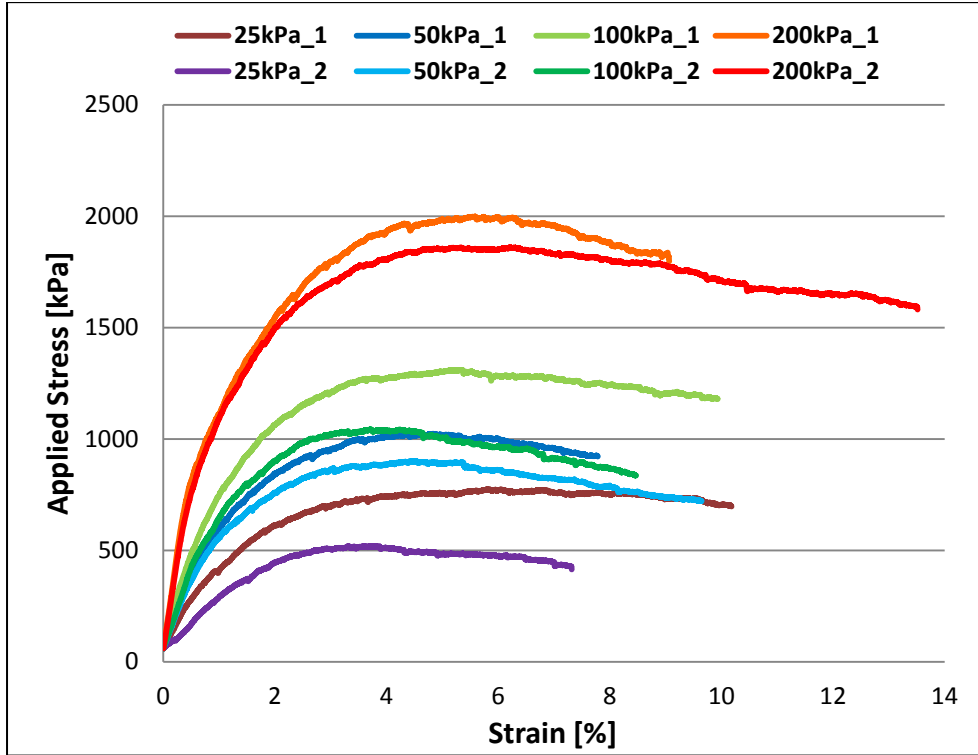


Figure B- 4: Stress-strain Relationship Curves, Small-size *G19C*

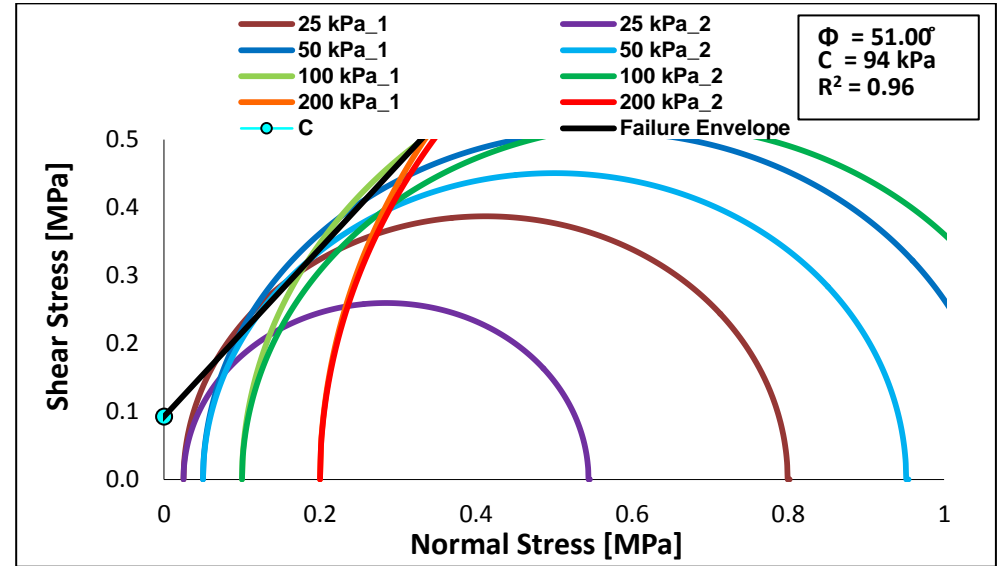


Figure B- 5: Eight Circle Mohr-Coulomb Representation, Small-size *G19C*

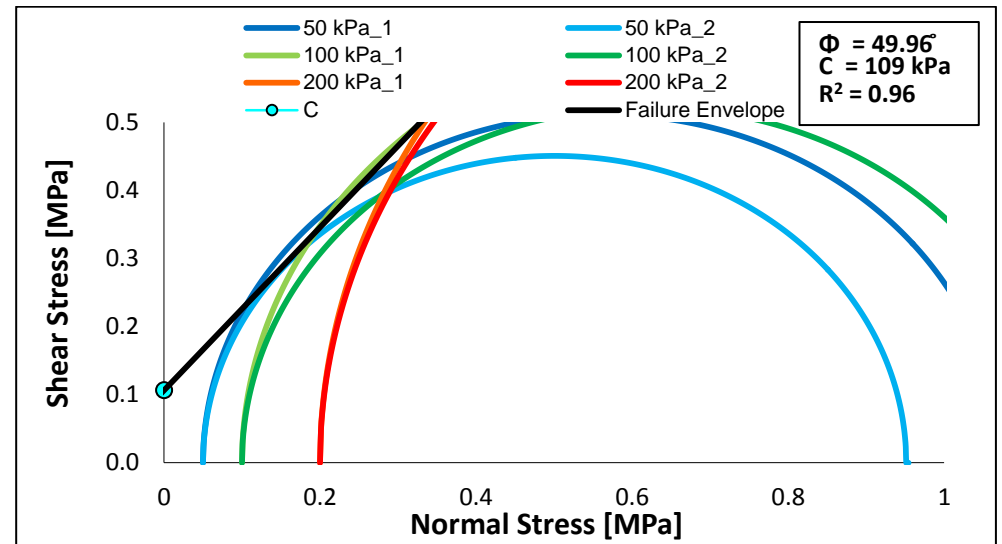


Figure B- 6: Six Circle Mohr-Coulomb Representation, Small-size *G19C*

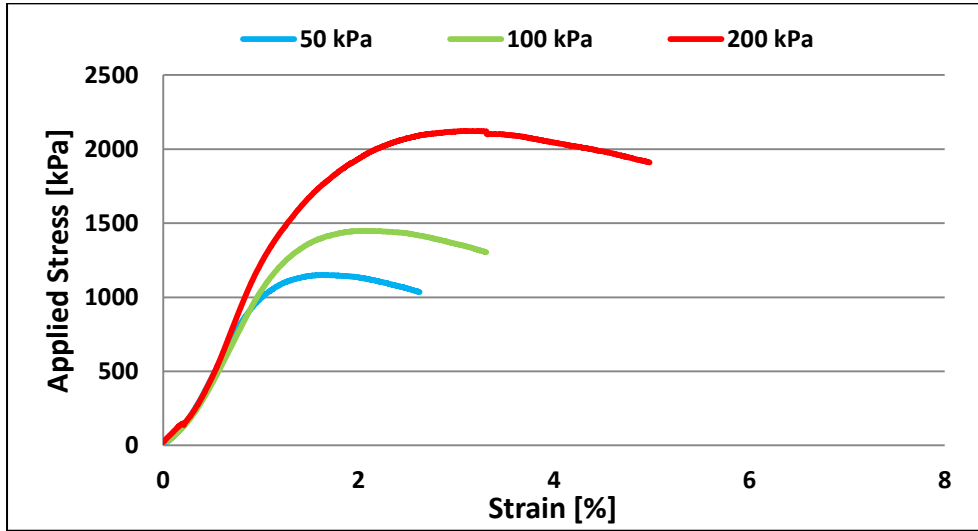


Figure B- 7: Stress-strain Relationship Curves, Large-size S19

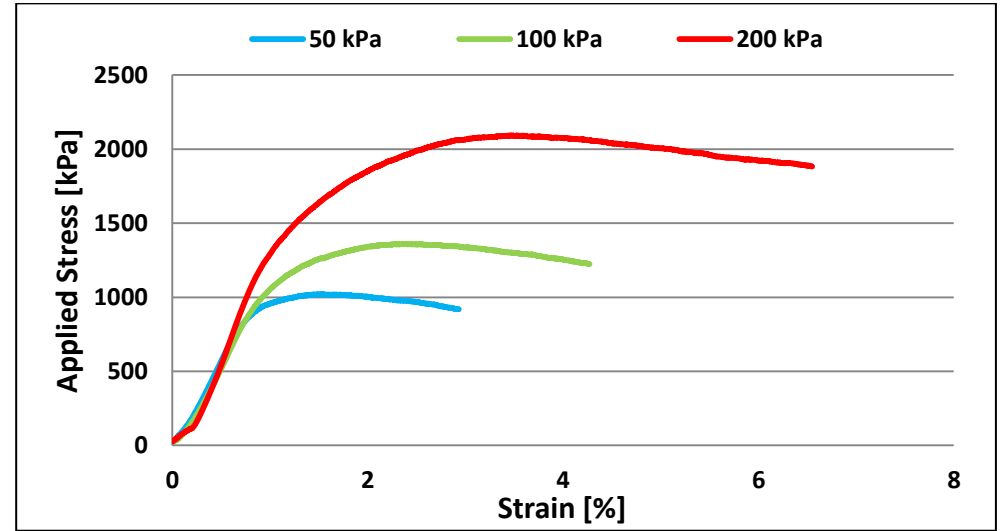


Figure B- 9: Stress-strain Relationship Curves, Large-size G19C

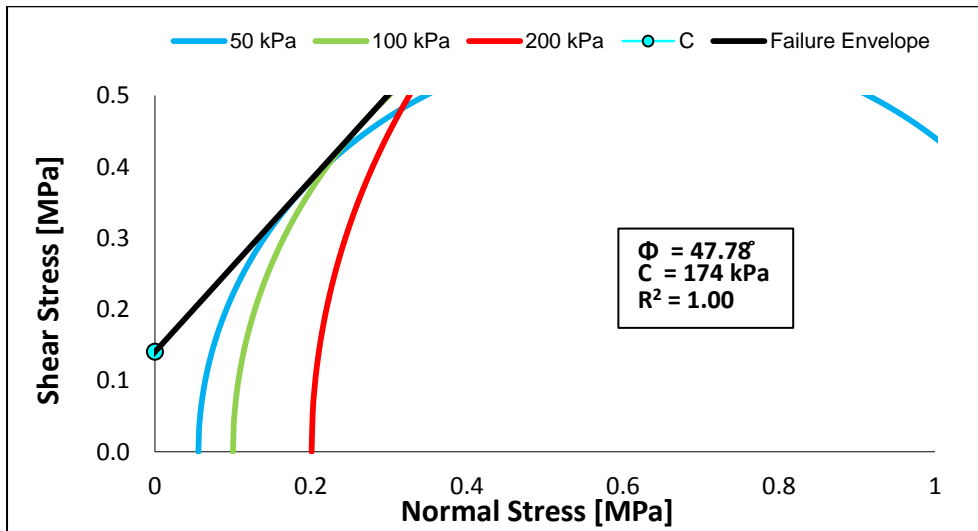


Figure B- 8: Three Circle Mohr-Coulomb Representation, Large-size S19

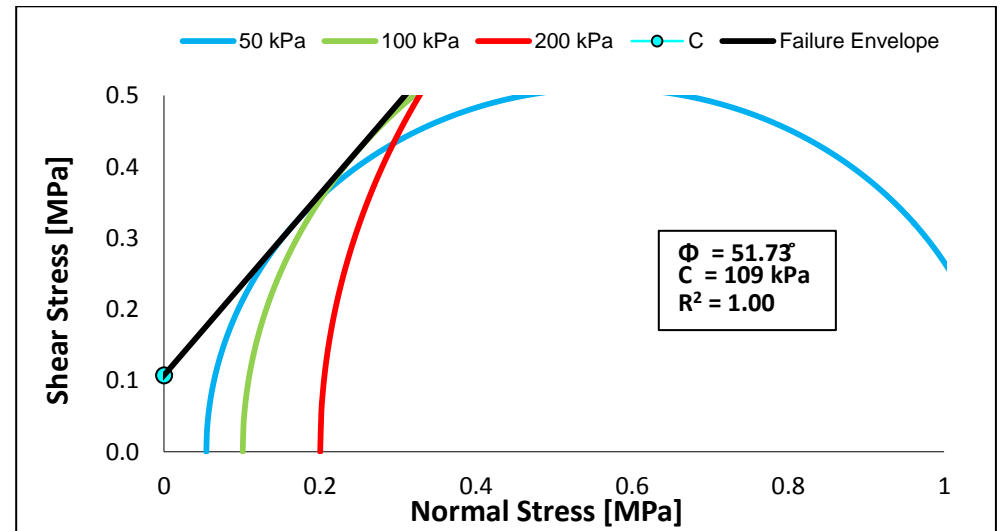


Figure B- 10: Three Circle Mohr-Coulomb Representation, Large-size G19C

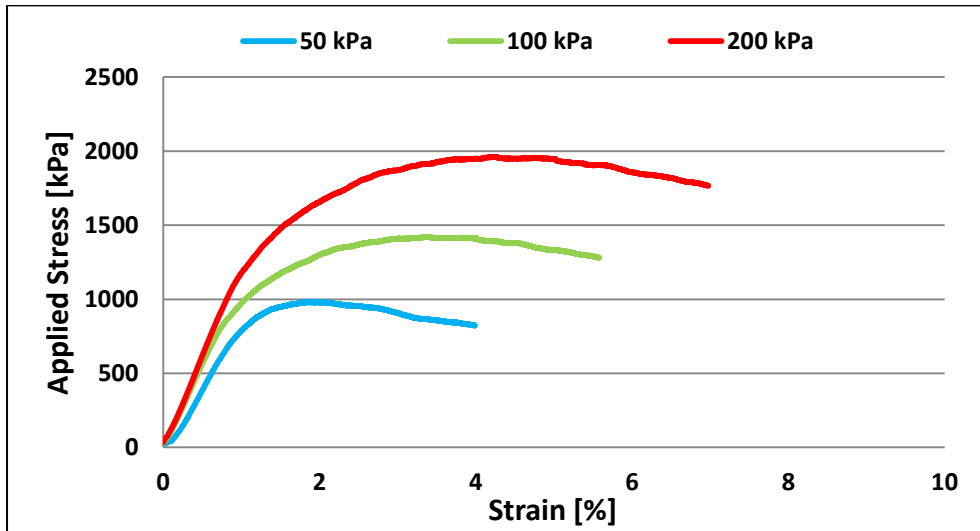


Figure B- 11: Stress-strain Relationship Curves, Large-size *Full*

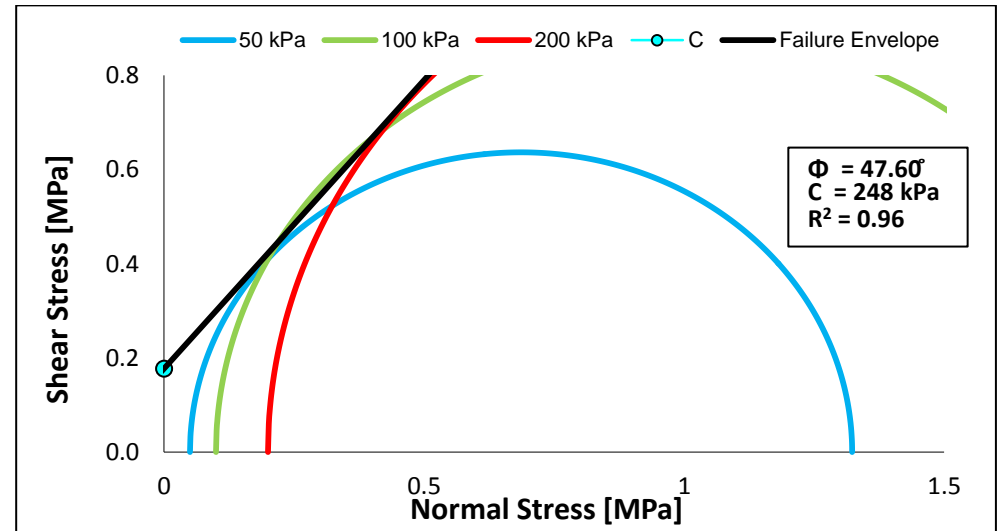


Figure B- 13: Mohr-Coulomb Representation, S-S19, Post Dynamic Loading

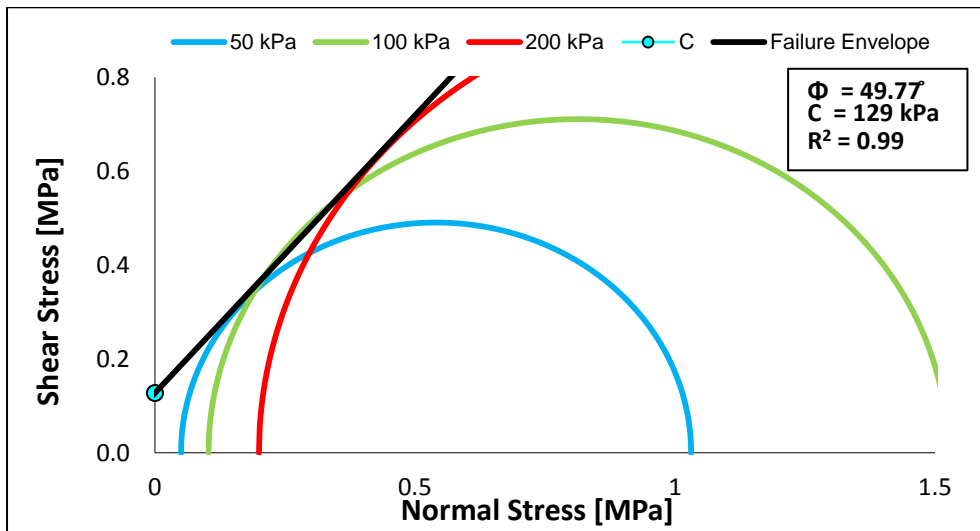


Figure B- 12: Three Circle Mohr-Coulomb Representation, Large-size *Full*

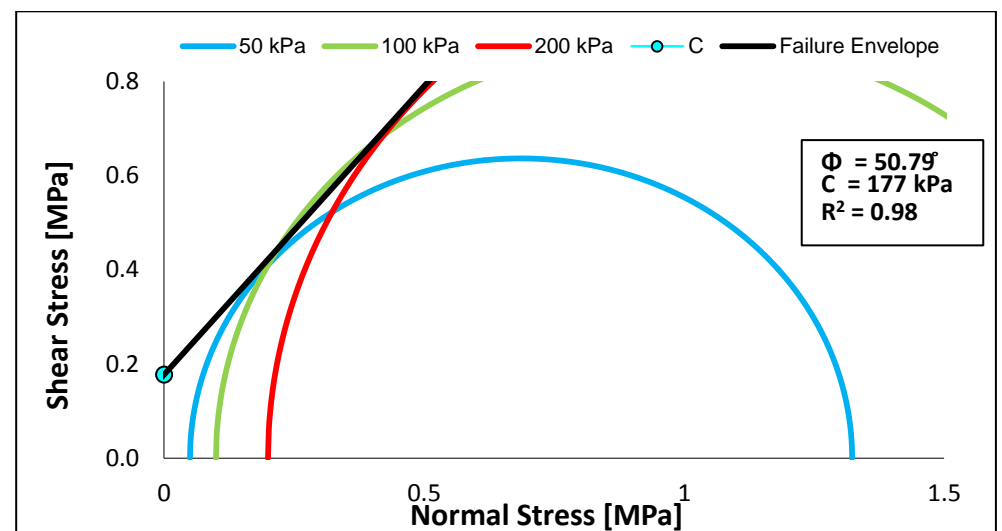


Figure B- 14: Mohr-Coulomb Representation, S-S19, Post Dynamic Loading

Appendix C:

Dynamic Tri-axial Test Results

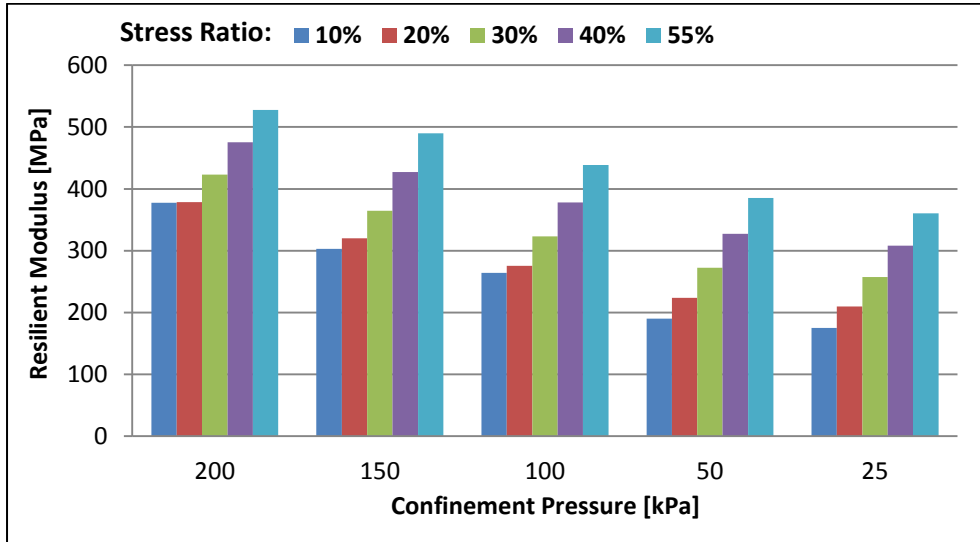


Figure C- 1: Small-size S19 Resilient Modulus Results, Specimen 1

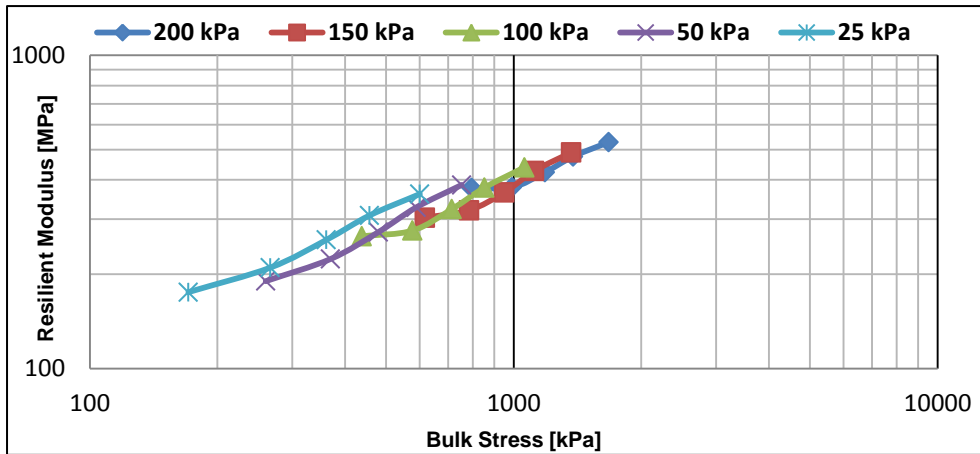


Figure C- 2: Resilient Modulus vs Bulk Stress, Small-size S19, Specimen 1

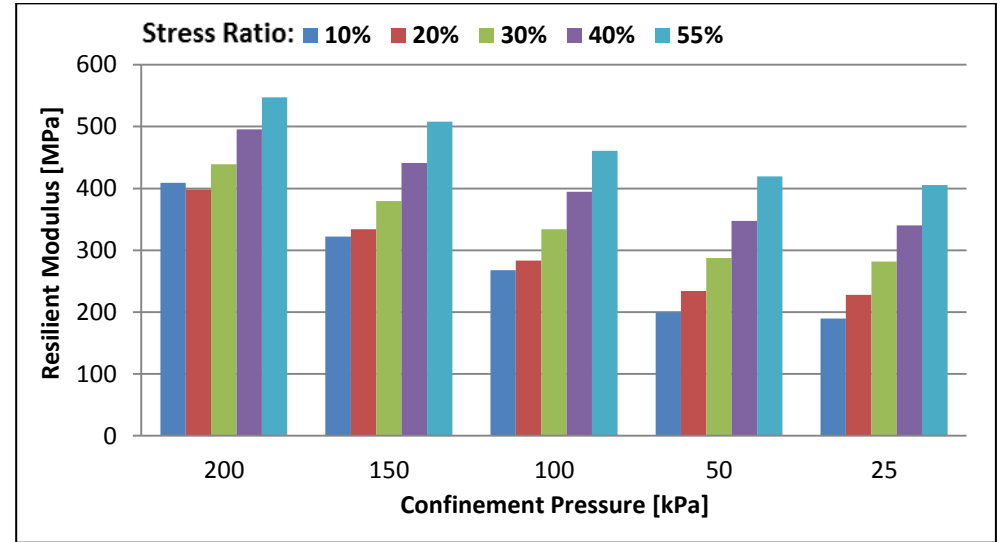


Figure C- 3: Small-size S19 Resilient Modulus Results, Specimen 2

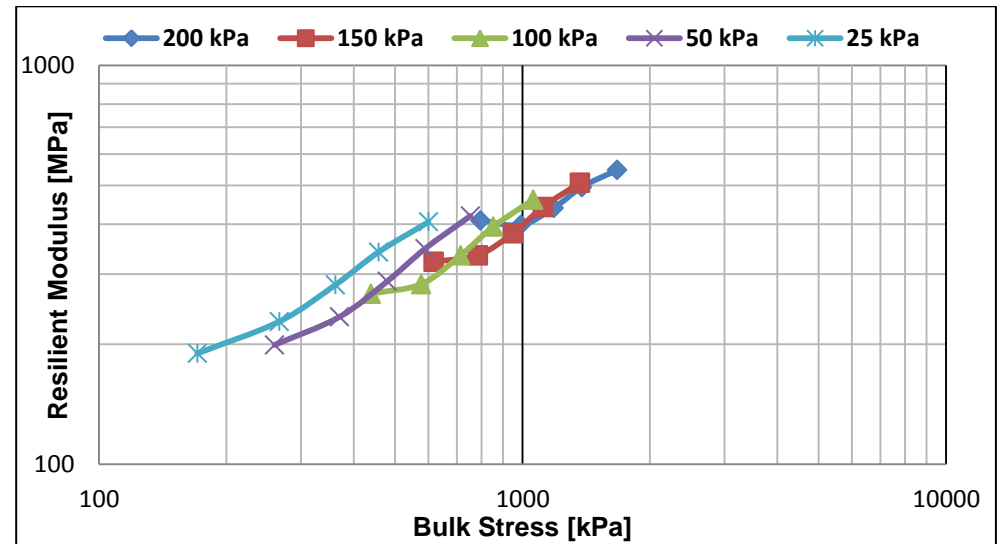


Figure C- 4: Resilient Modulus vs Bulk Stress, Small-size S19, Specimen 2

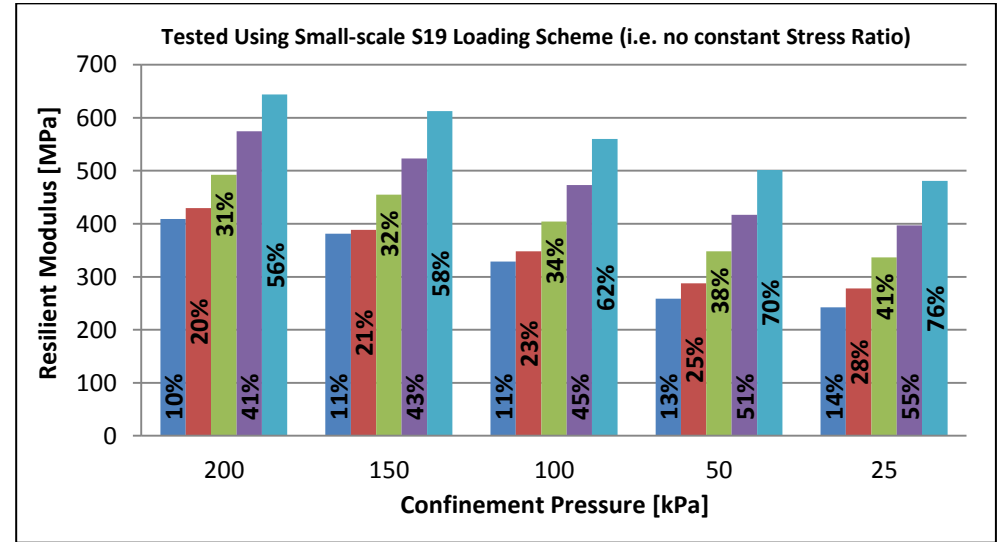
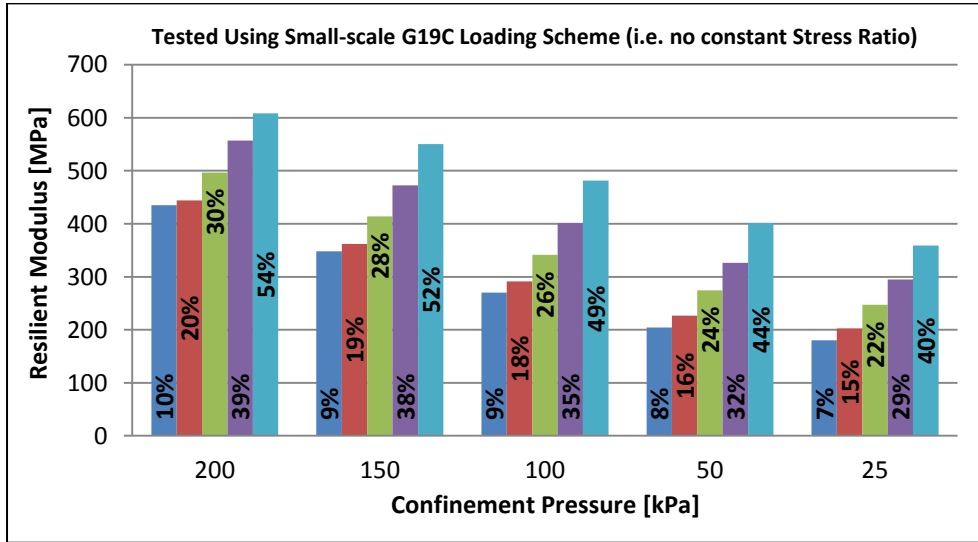


Figure C- 5: Small-size S19 Resilient Modulus Results, Specimen 3

Figure C- 7: Small-size G19C Resilient Modulus Results, Specimen 1

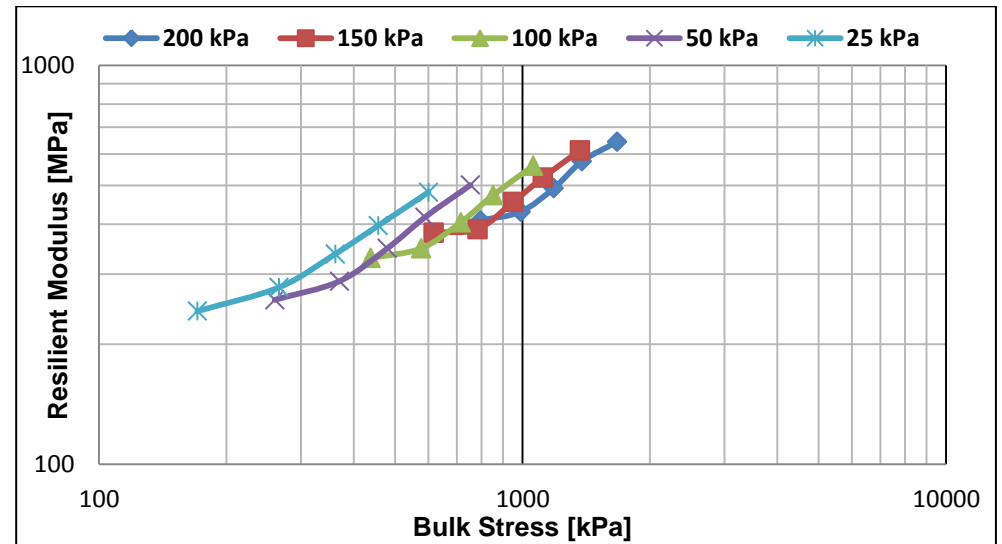
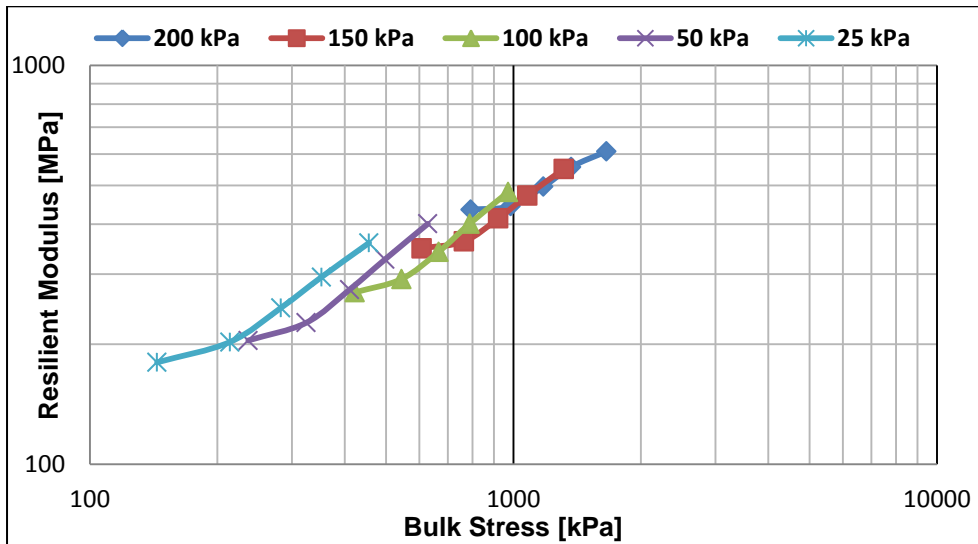


Figure C- 6: Resilient Modulus vs Bulk Stress, Small-size S19, Specimen 3

Figure C- 8: Resilient Modulus vs Bulk Stress, Small-size G19C, Specimen 1

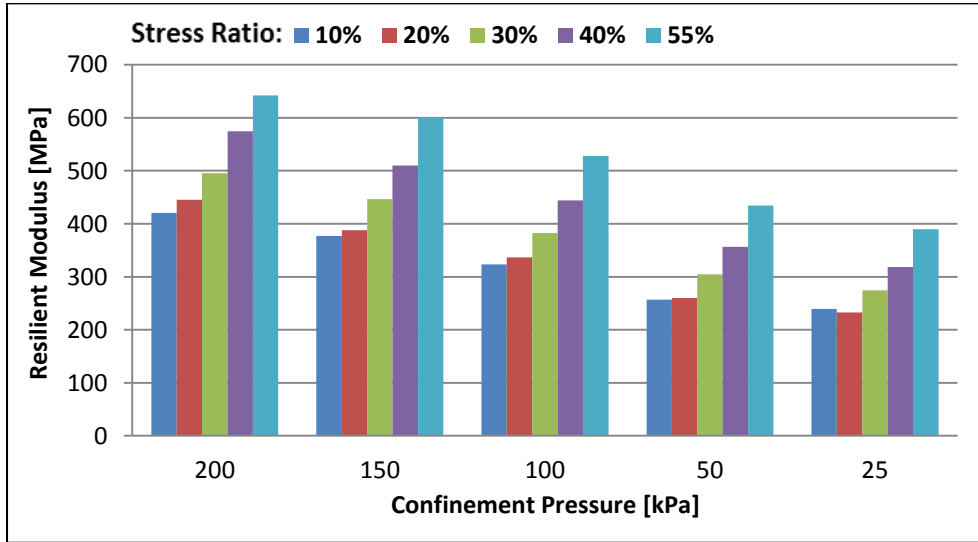


Figure C- 9: Small-size *G19C* Resilient Modulus Results, Specimen 2

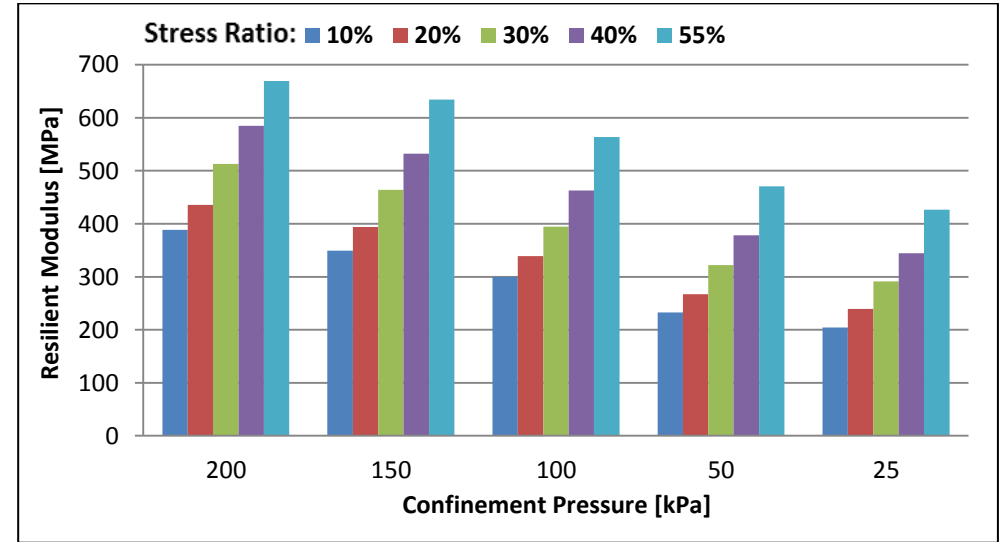


Figure C- 11: Small-size *G19C* Resilient Modulus Results, Specimen 3

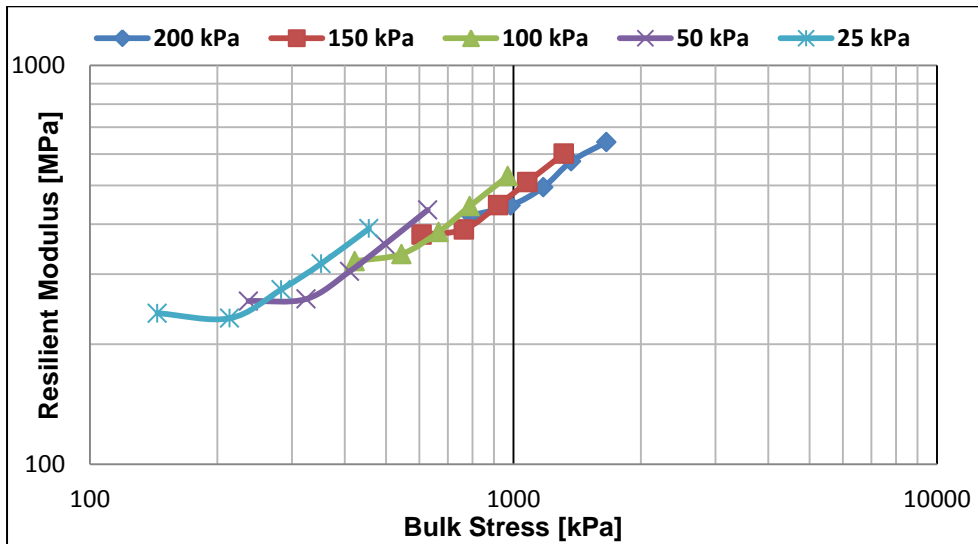


Figure C- 10: Resilient Modulus vs Bulk Stress, Small-size *G19C*, Specimen 2

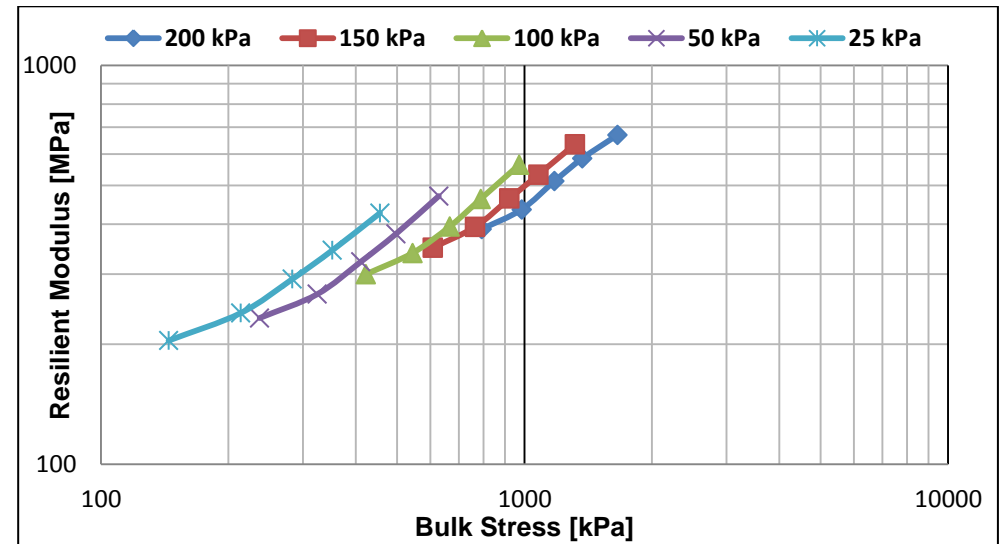


Figure C- 12: Resilient Modulus vs Bulk Stress, Small-size *G19C*, Specimen 3

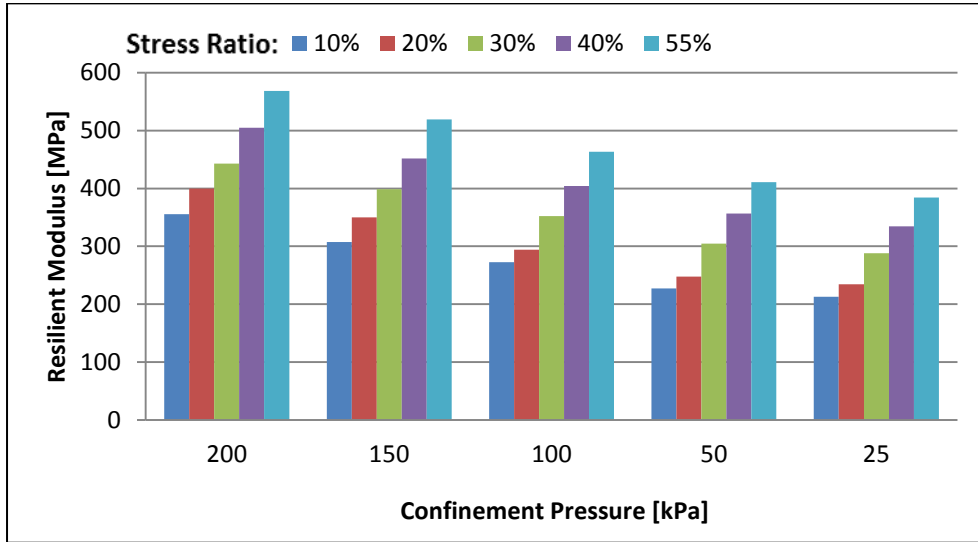


Figure C- 13: Large-size S19 Resilient Modulus Results, Specimen 1

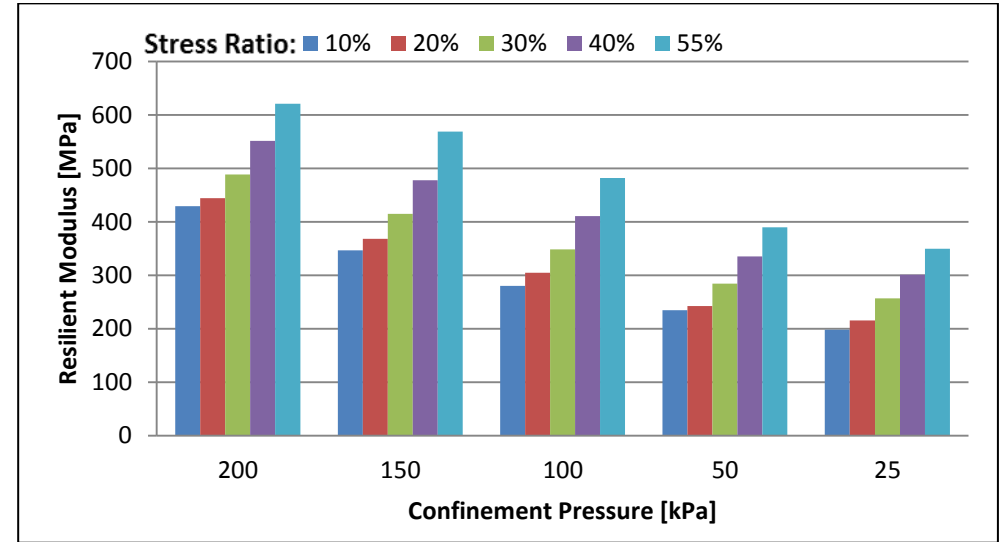


Figure C- 15: Large-size G19C Resilient Modulus Results, Specimen 1

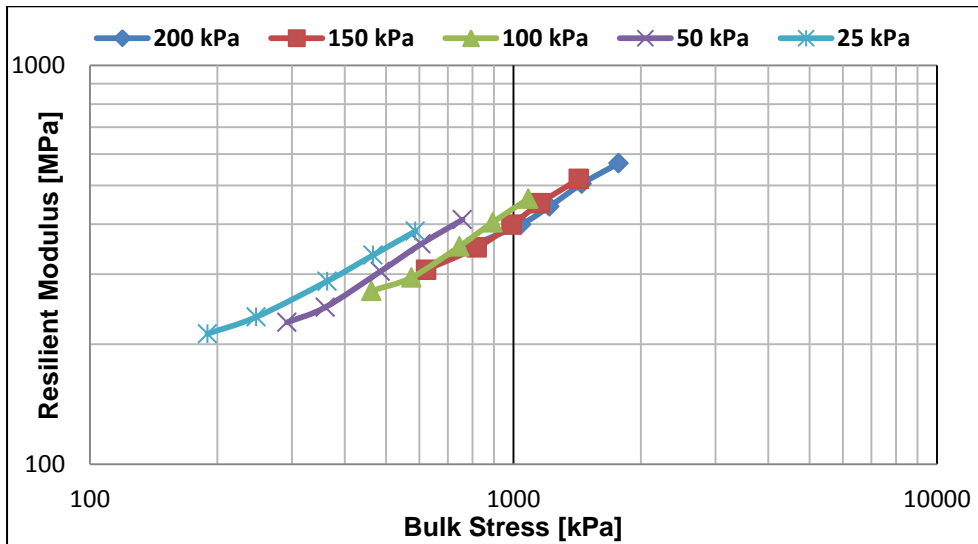


Figure C- 14: Resilient Modulus vs Bulk Stress, Large-size S19, Specimen 1

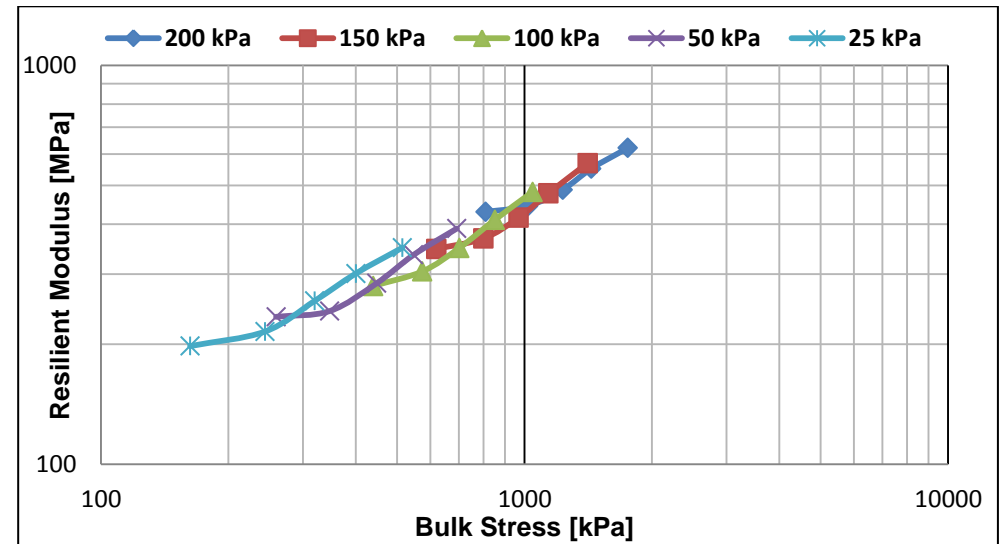


Figure C- 16: Resilient Modulus vs Bulk Stress, Large-size G19C, Specimen 1

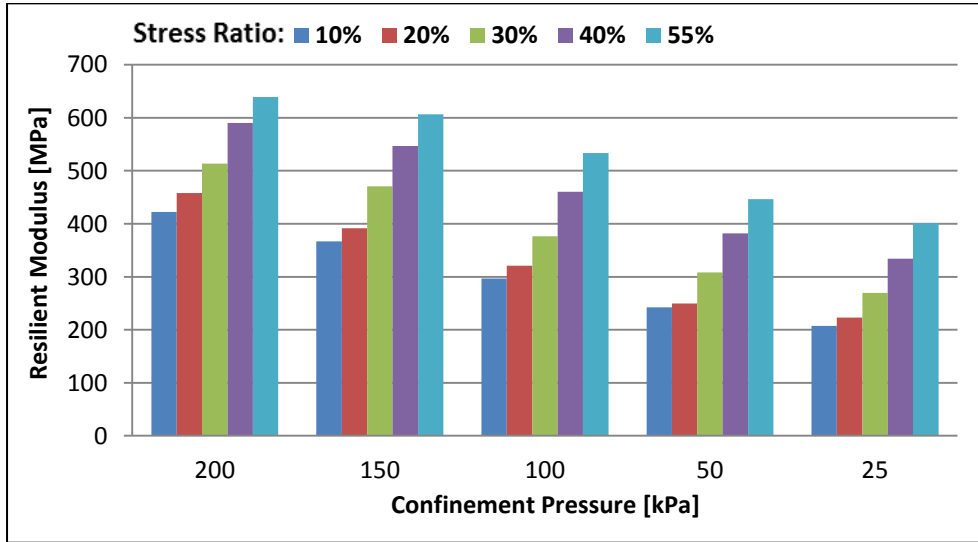


Figure C- 17: Large-size *G19C* Resilient Modulus Results, Specimen 2

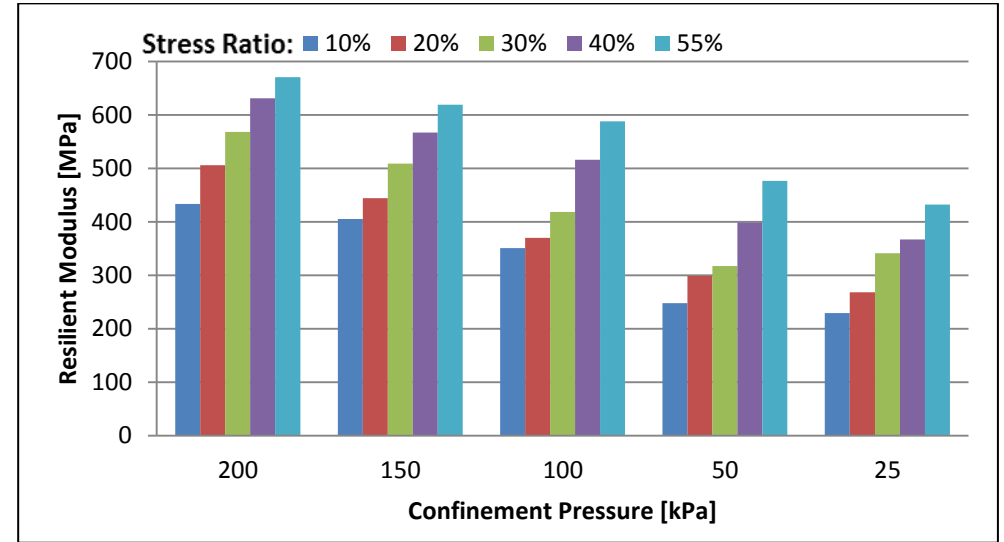


Figure C- 19: Large-size *Full* Resilient Modulus Results, Specimen 1

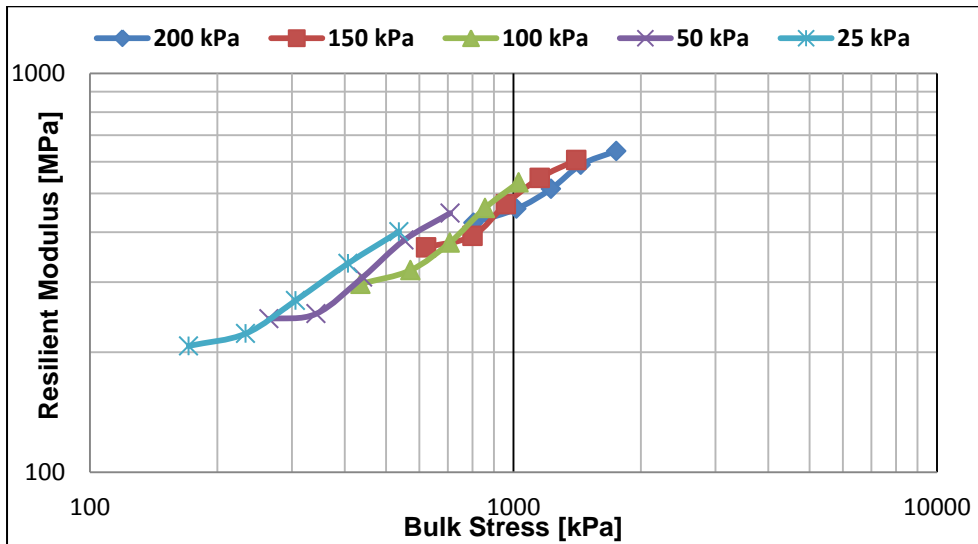


Figure C- 18: Resilient Modulus vs Bulk Stress, Large-size *G19C*, Specimen 2

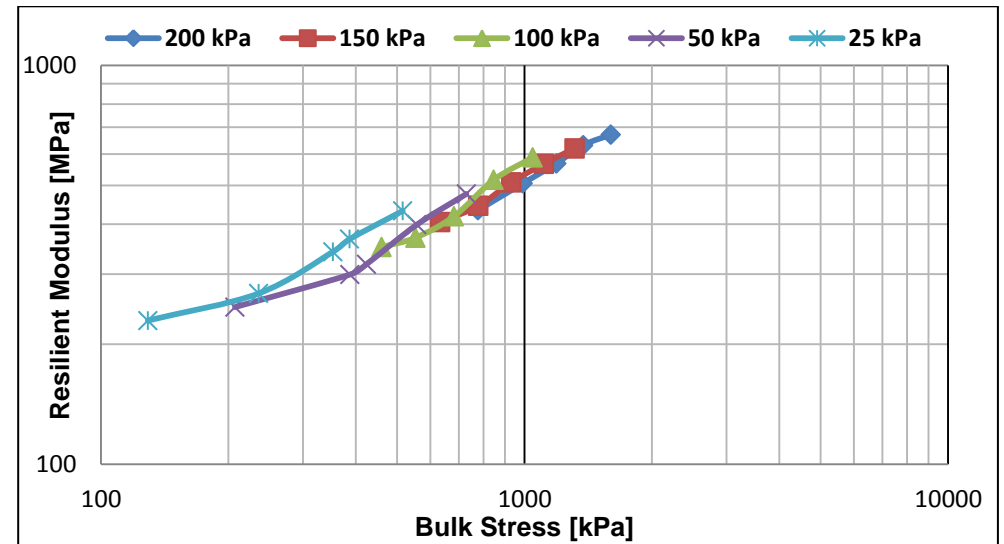


Figure C- 20: Resilient Modulus vs Bulk Stress, Large-size *Full*, Specimen 1

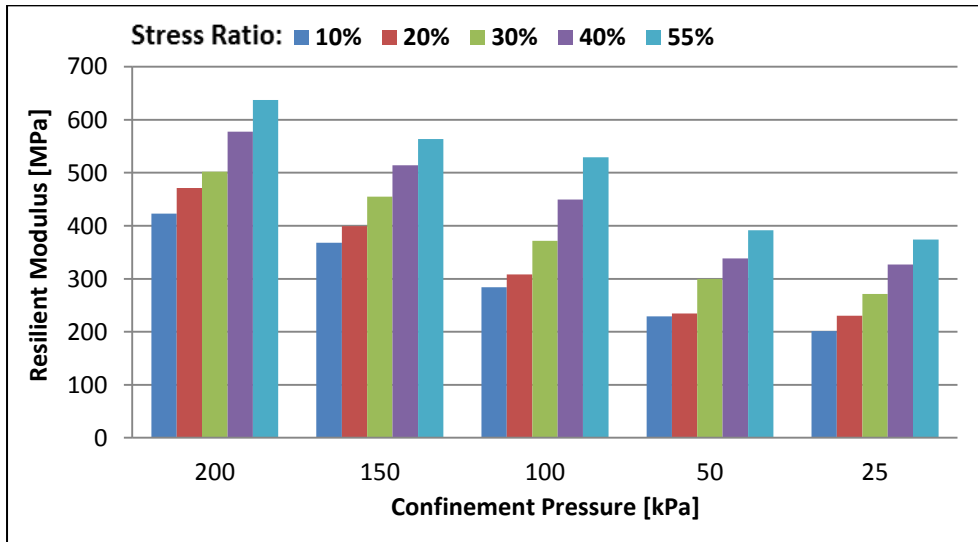


Figure C- 21: Large-size *Full* Resilient Modulus Results, Specimen 2

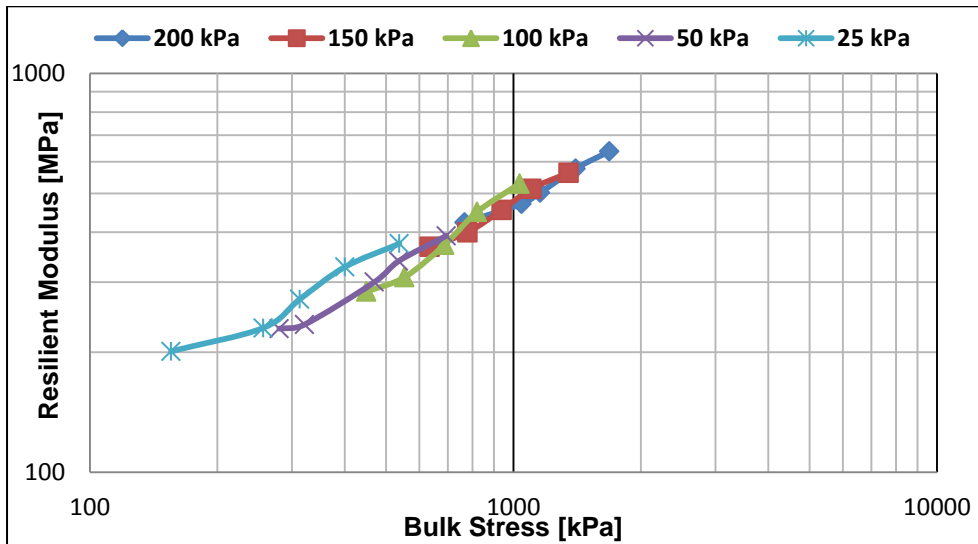


Figure C- 22: Resilient Modulus vs Bulk Stress, Large-size *Full*, Specimen 2

Appendix D:

Modelling of M_r - θ Model

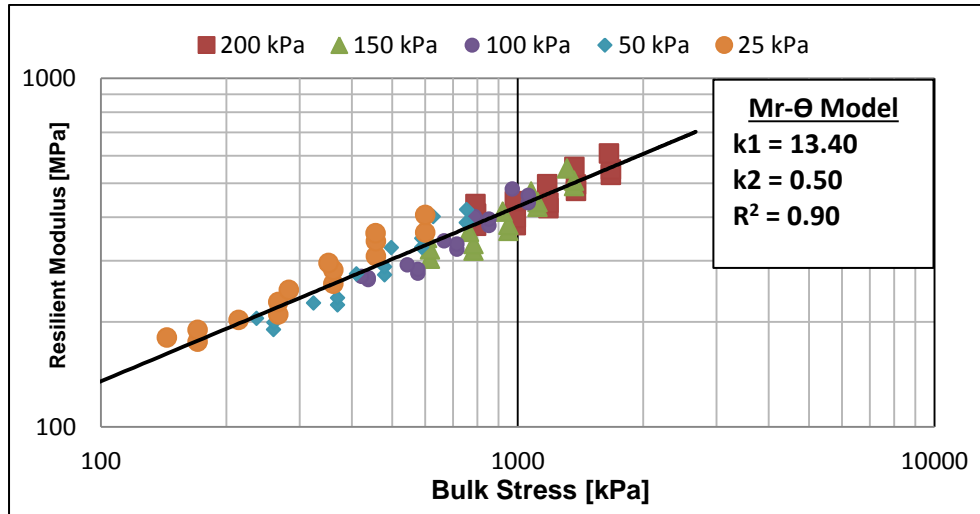


Figure D- 1: M_r - θ Modelling of Small-size S19 Resilient Modulus

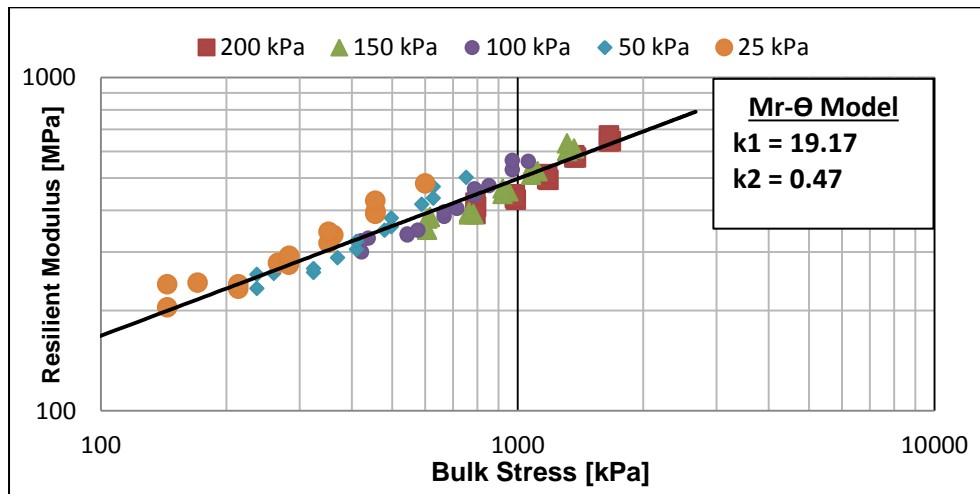


Figure D- 2: M_r - θ Modelling of Small-size G19C Resilient Modulus

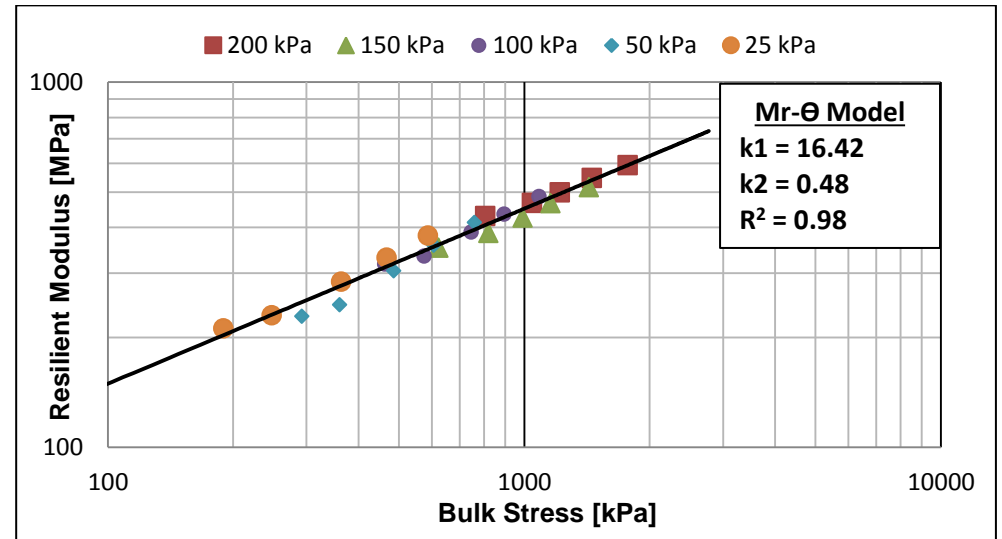


Figure D- 3: M_r - θ Modelling of Large-size S19 Resilient Modulus

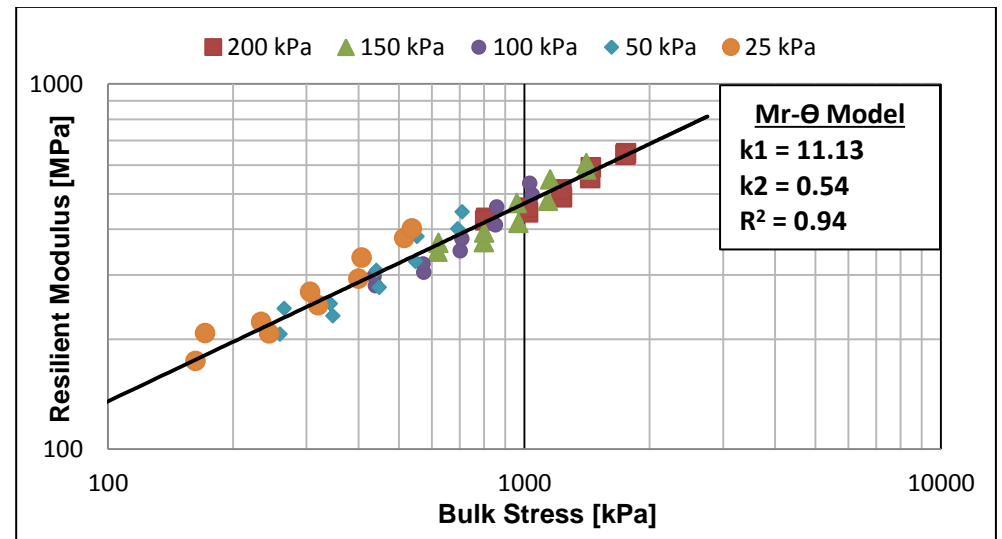


Figure D- 4: M_r - θ Modelling of Large-size G19C Resilient Modulus

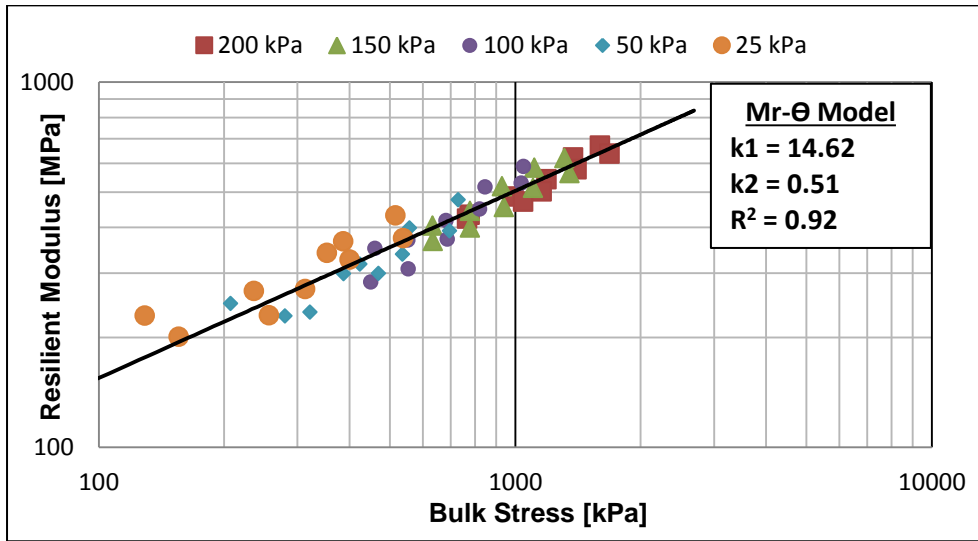


Figure D- 5: $M_r-\theta$ Modelling of Large-size *Full* Resilient Modulus

Appendix E:

Modelling of $M_r-\Theta-\frac{\sigma_d}{\sigma_f}$ Model

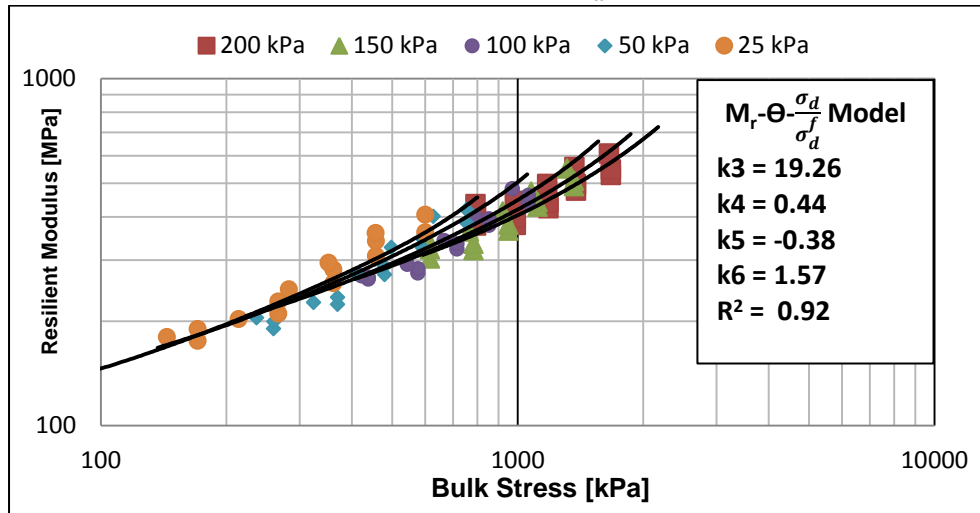


Figure E- 1: $M_r-\Theta-\frac{\sigma_d}{\sigma_f}$ Modelling of Small-size S19 Resilient Modulus

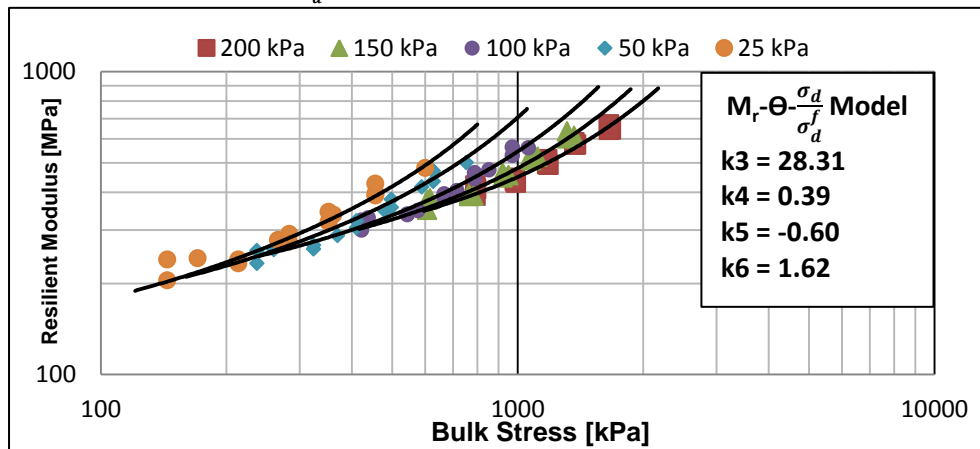


Figure E- 2: $M_r-\Theta-\frac{\sigma_d}{\sigma_f}$ Modelling of Small-size G19C Resilient Modulus

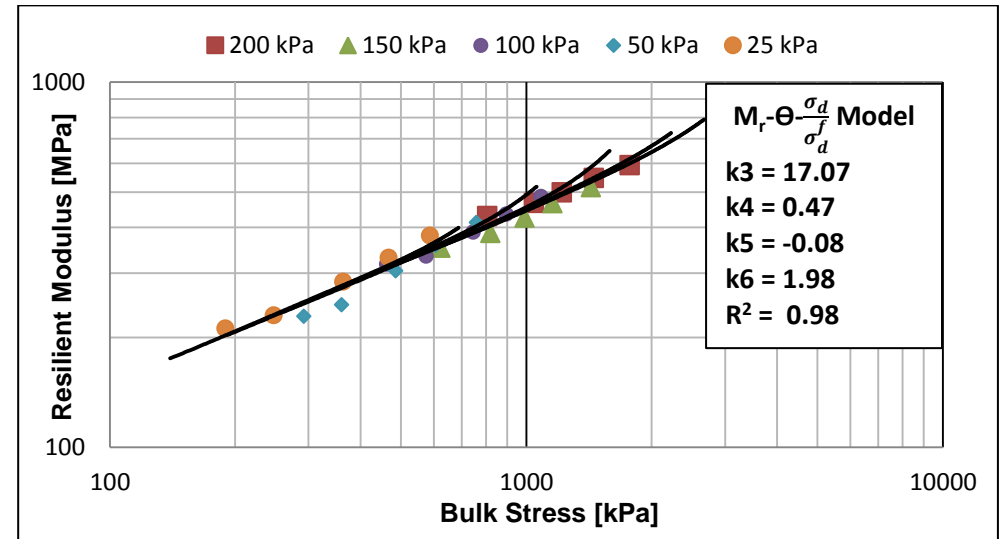


Figure E- 3: $M_r-\Theta-\frac{\sigma_d}{\sigma_f}$ Modelling of Large-size S19 Resilient Modulus

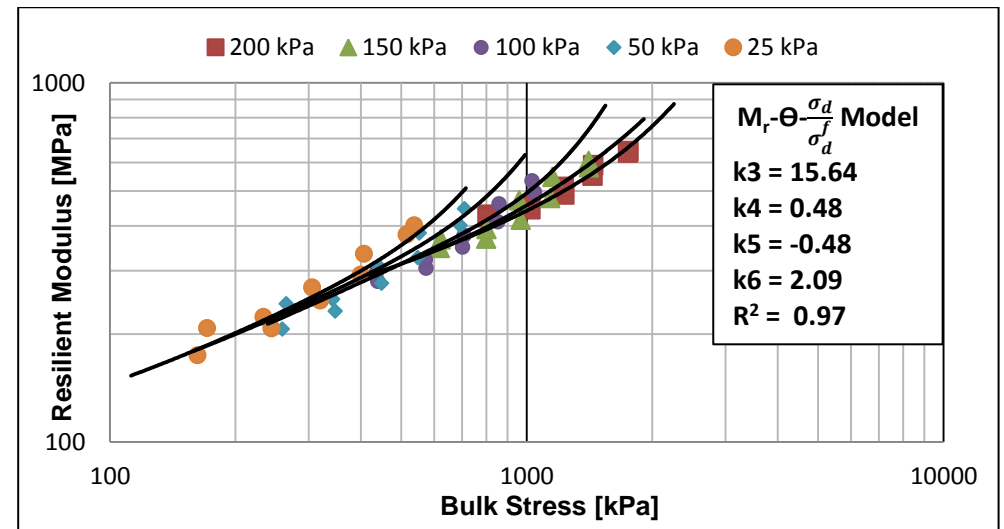


Figure E- 4: $M_r-\Theta-\frac{\sigma_d}{\sigma_f}$ Modelling of Large-size G19C Resilient Modulus

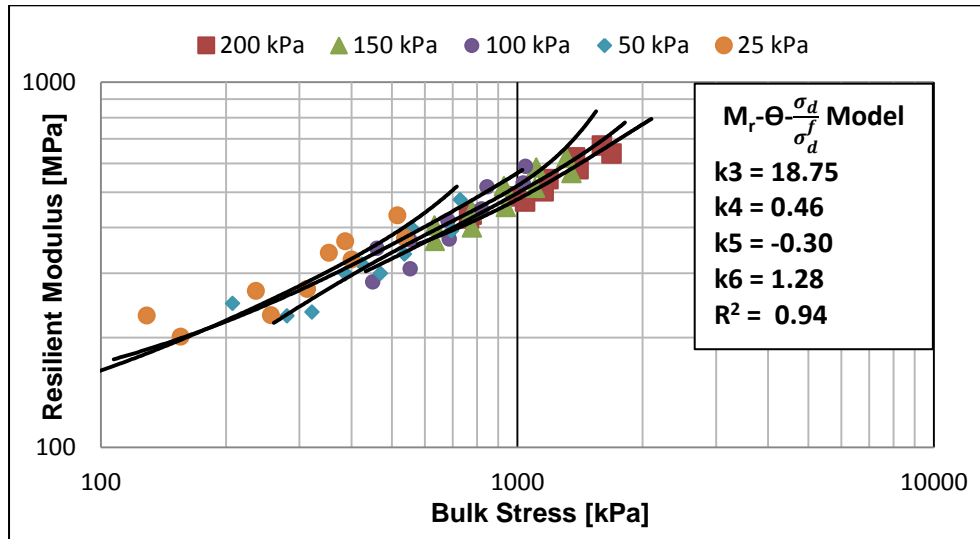


Figure E- 5: $M_r-\theta-\frac{\sigma_d}{\sigma'_d}$ Modelling of Large-size *Full* Resilient Modulus

Appendix F:

0.1 – 0.9 Loading Rate

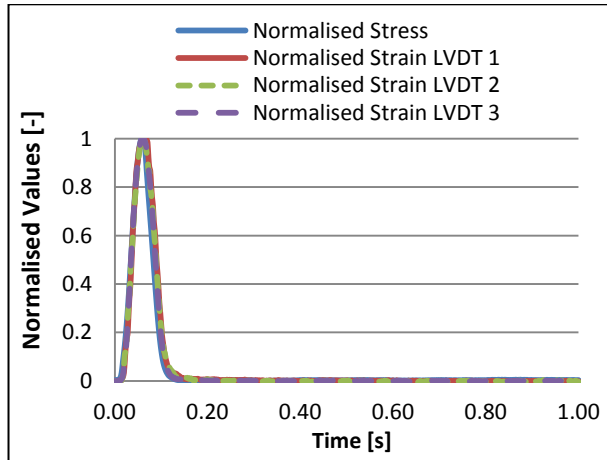


Figure F- 1: Last 10% SR Conditioning Cycle, S-S19

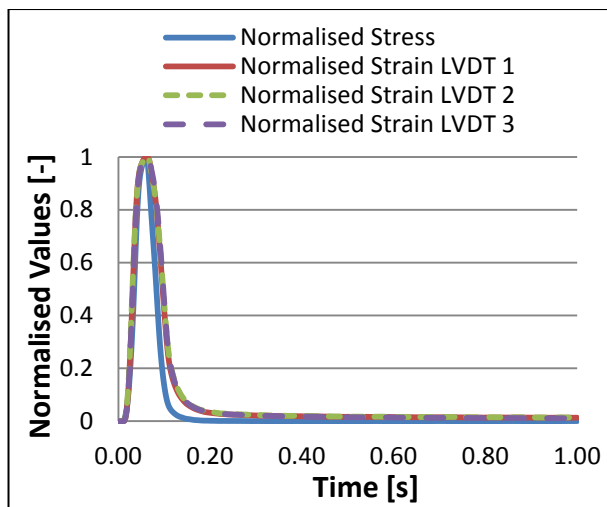


Figure F- 2: Last 55% SR Conditioning Cycle, S-S19

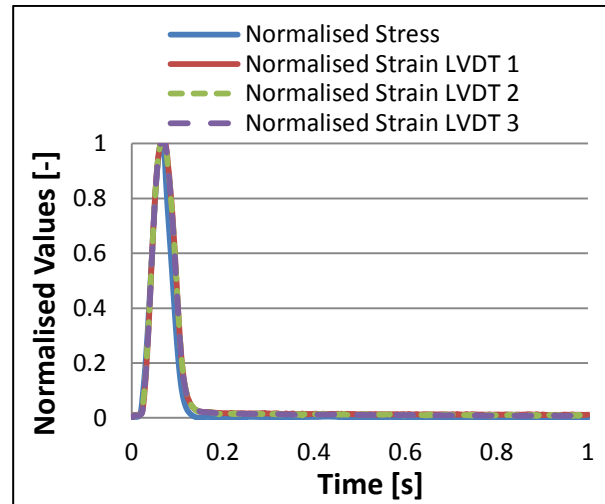


Figure F- 3: Last 10% SR 200 kPa Load Cycle, S-S19

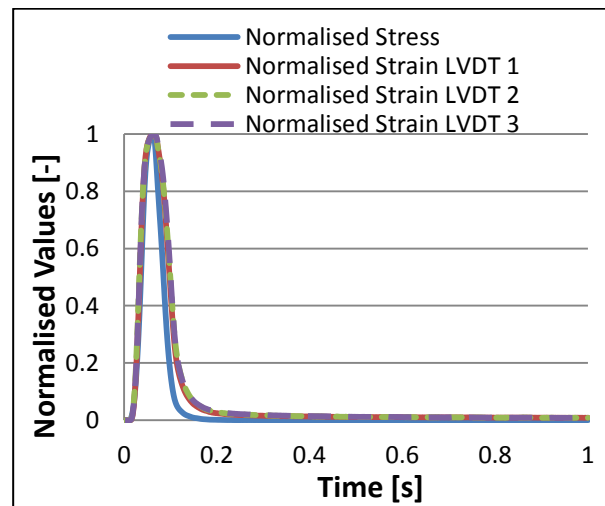


Figure F- 4: Last 55% SR 200 kPa Load Cycle, S-S19

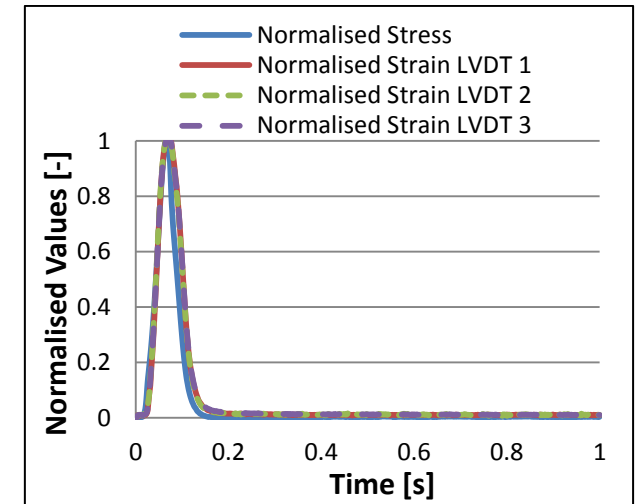


Figure F- 5: Last 10% SR 25 kPa Load Cycle, S-S19

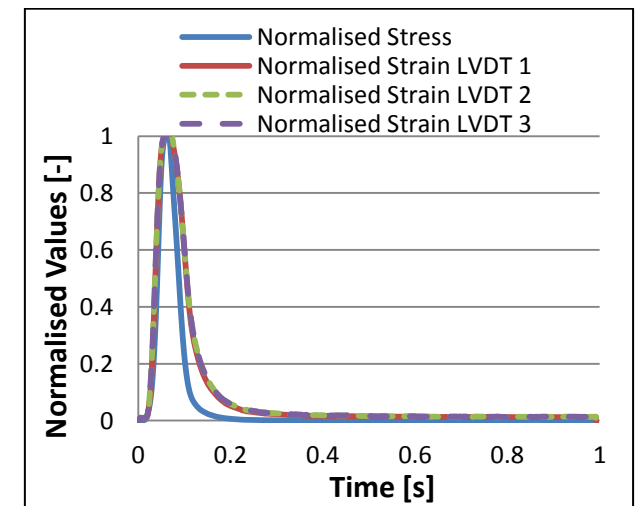


Figure F- 6: Last 55% SR 25 kPa Load Cycle, S-S19

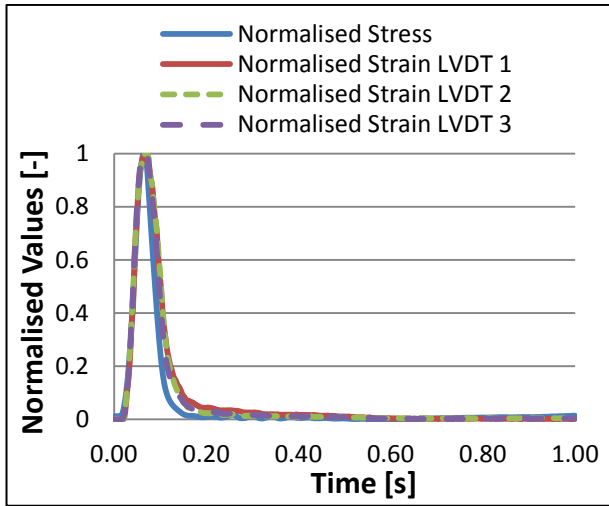


Figure F- 7: Last 10% SR Conditioning Cycle, S-G19C

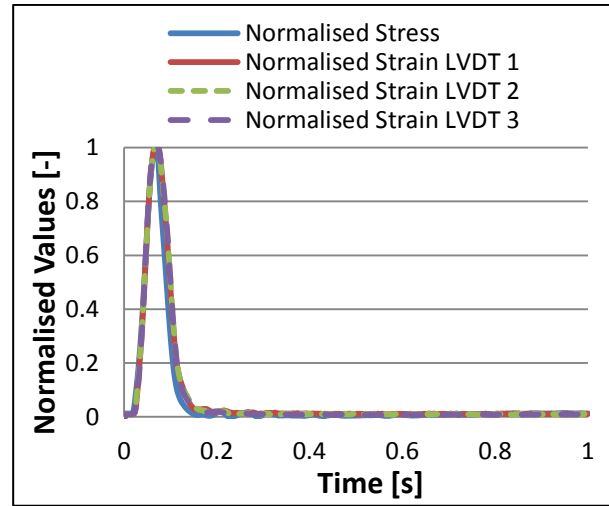


Figure F- 9: Last 10% SR 200 kPa Load Cycle, S-G19C

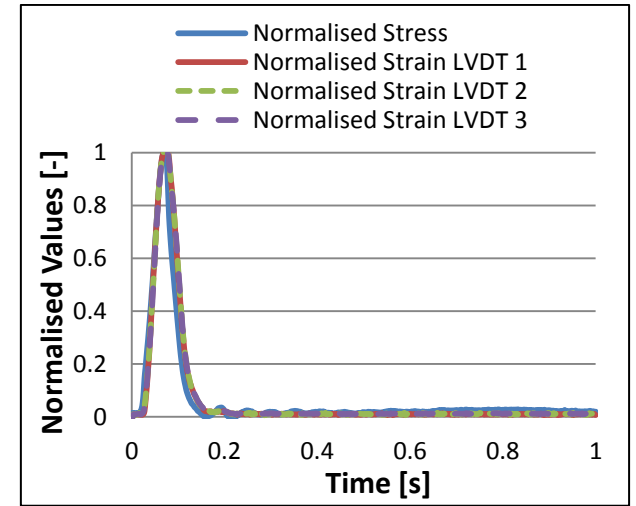


Figure F- 11: Last 10% SR 25 kPa Load Cycle, S-G19C

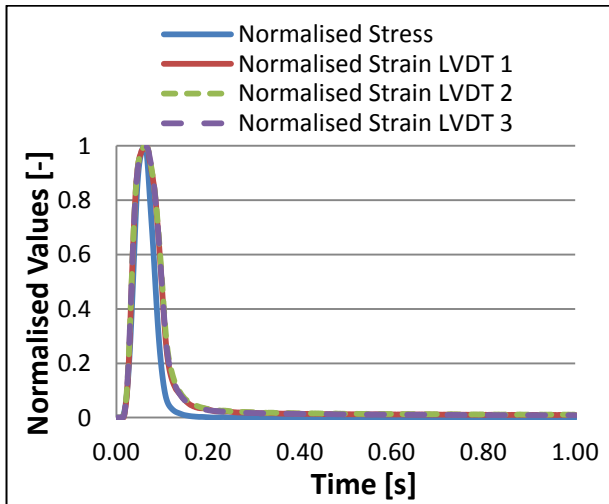


Figure F- 8: Last 55% SR Conditioning Cycle, S-G19C

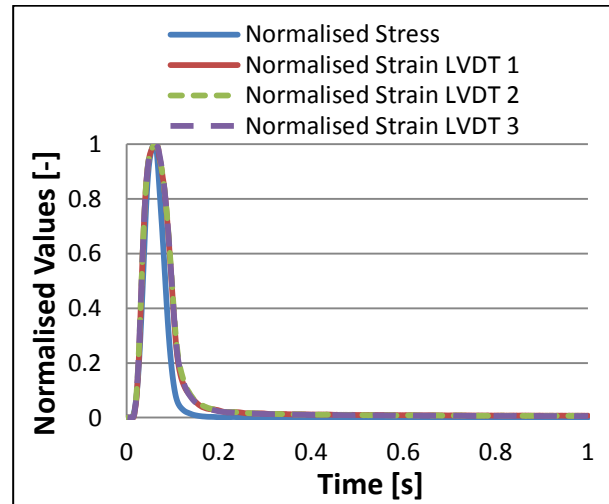


Figure F- 10: Last 55% SR 200 kPa Load Cycle, S-G19C

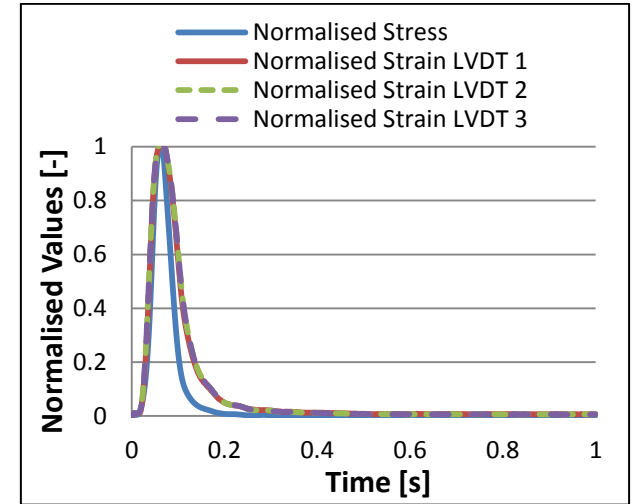


Figure F- 12: Last 55% SR 25 kPa Load Cycle, S-G19C

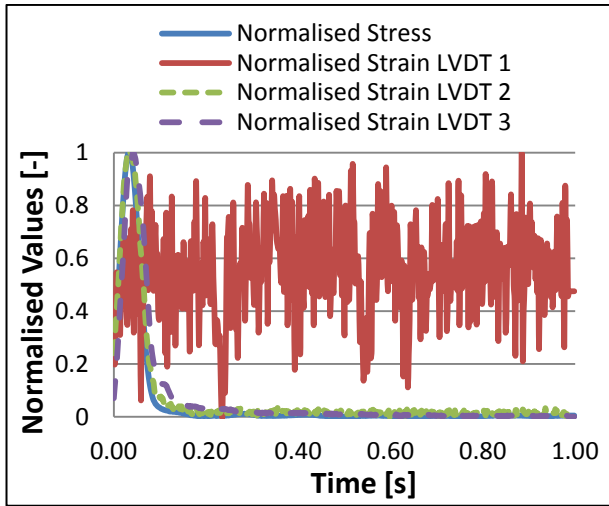


Figure F- 13: Last 10% SR Conditioning Cycle, L-S19

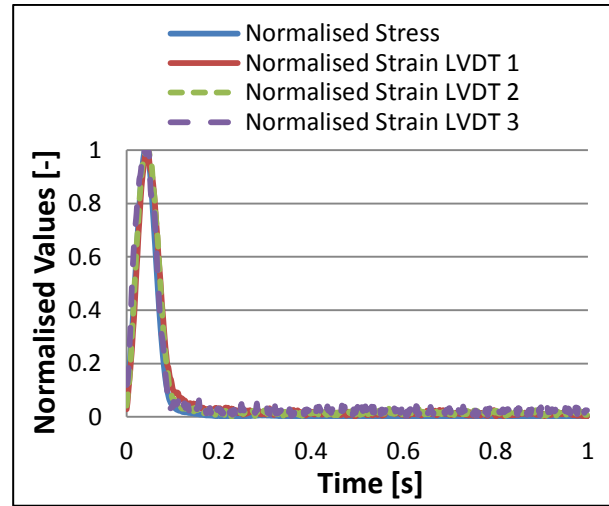


Figure F- 15: Last 10% SR 200 kPa Load Cycle, L-S19

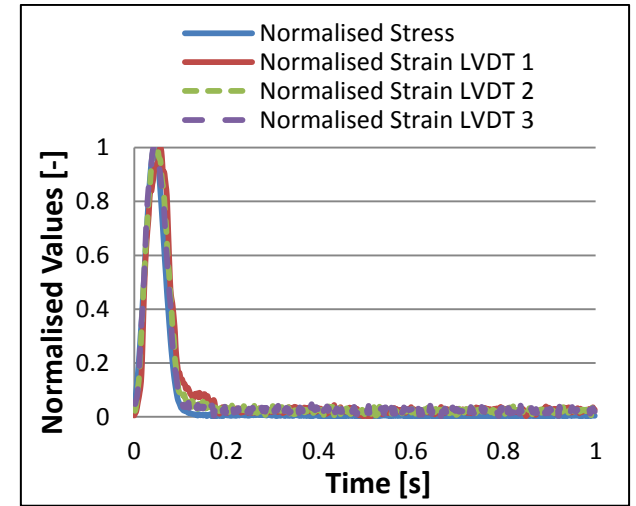


Figure F- 17: Last 10% SR 25 kPa Load Cycle, L-S19

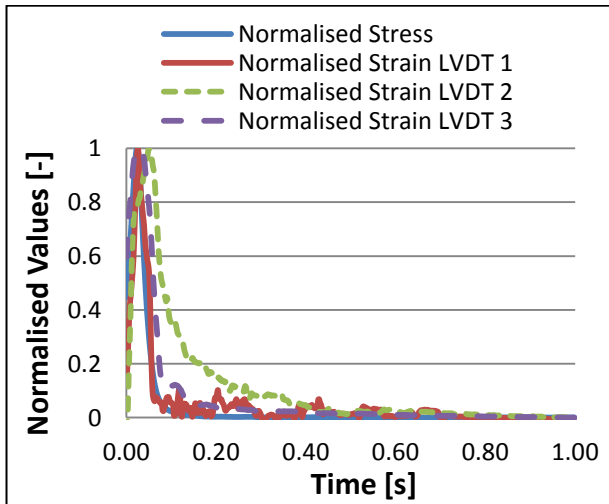


Figure F- 14: Last 55% SR Conditioning Cycle, L-S19

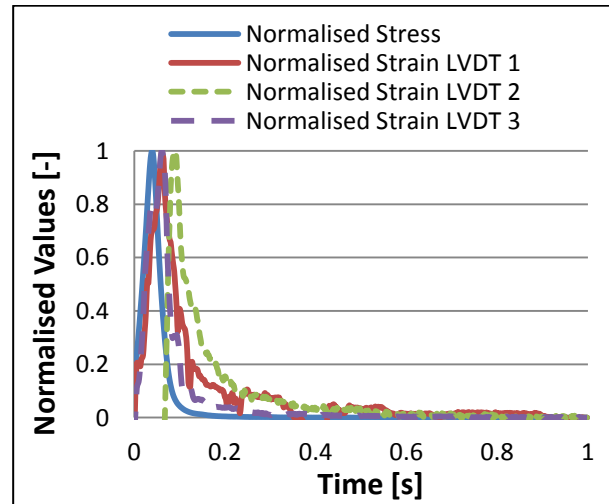


Figure F- 16: Last 55% SR 200 kPa Load Cycle, L-S19

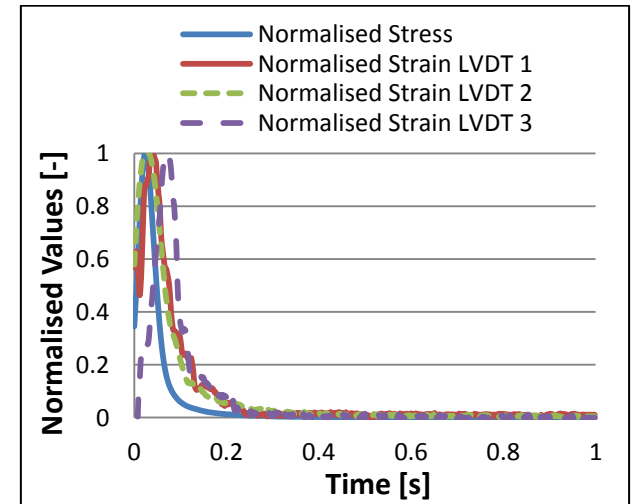


Figure F- 18: Last 55% SR 25 kPa Load Cycle, L-S19

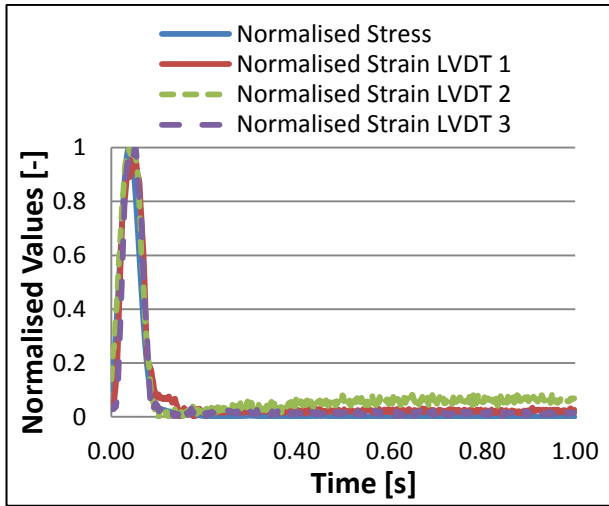


Figure F- 19: Last 10% SR Conditioning Cycle, L-G19C

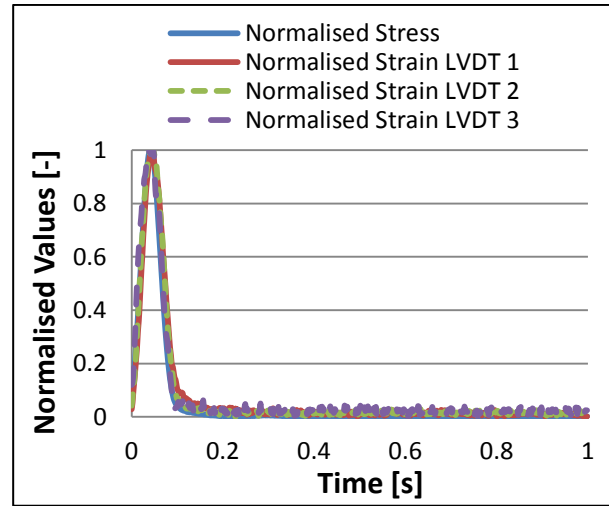


Figure F- 21: Last 10% SR 200 kPa Load Cycle, L-G19C

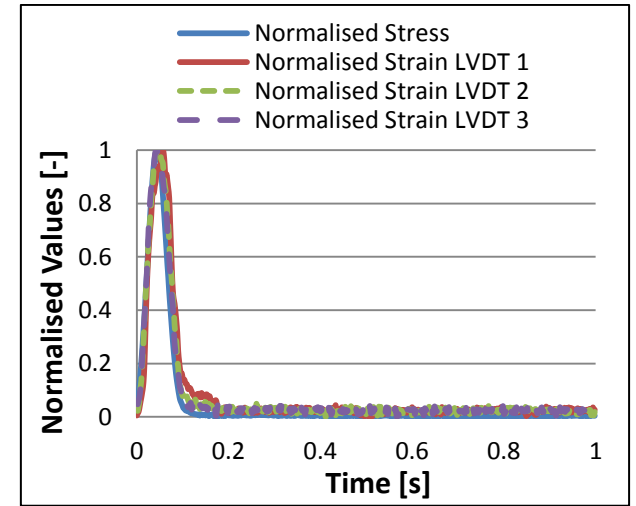


Figure F- 23: Last 10% SR 25 kPa Load Cycle, L-G19C

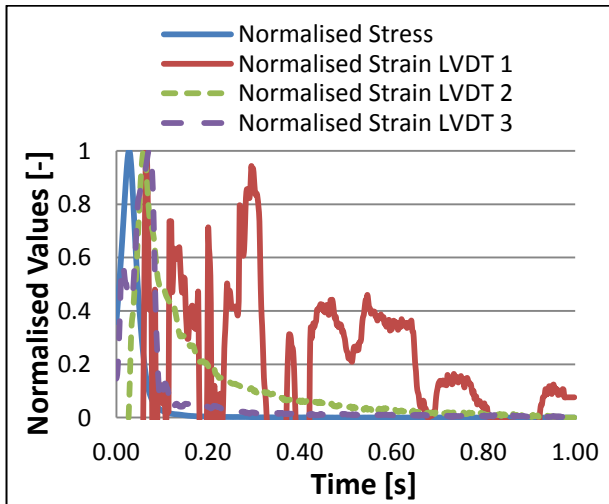


Figure F- 20: Last 55% SR Conditioning Cycle, L-G19C

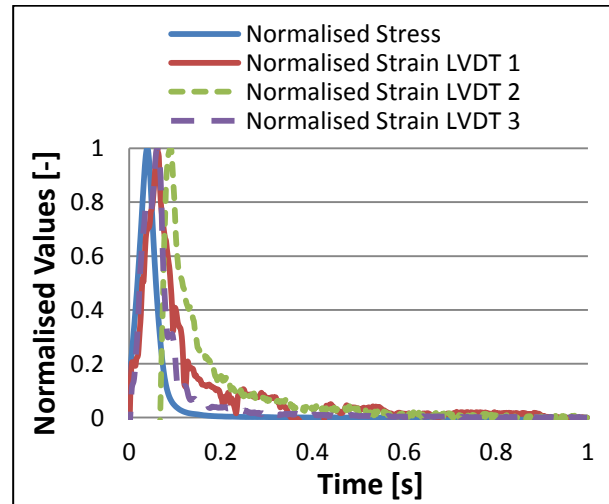


Figure F- 22: Last 55% SR 200 kPa Load Cycle, L-G19C

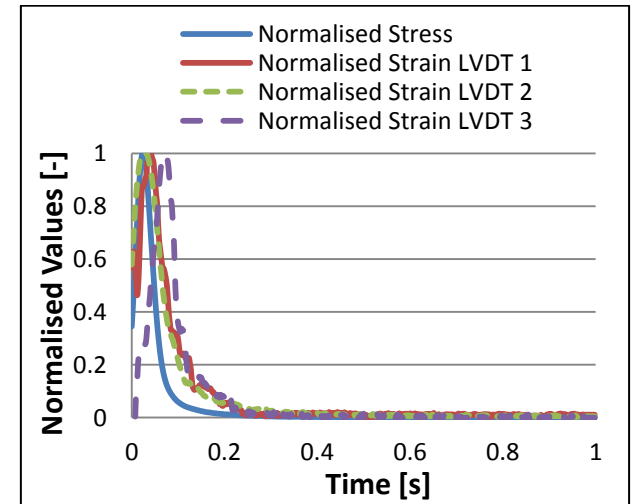


Figure F- 24: Last 55% SR 25 kPa Load Cycle, L-G19C

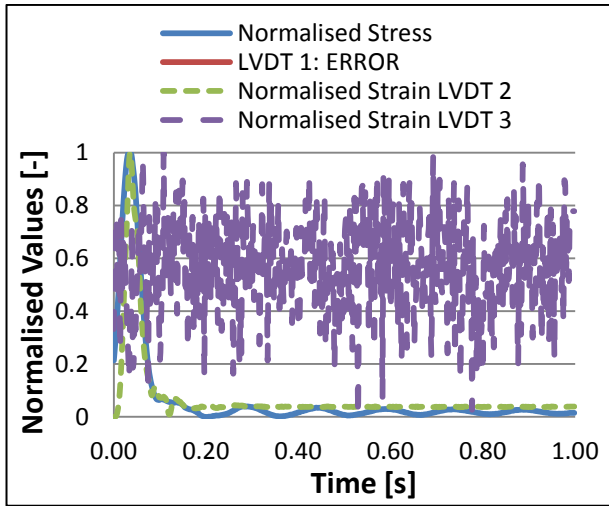


Figure F- 25: Last 10% SR Conditioning Cycle, L-Full

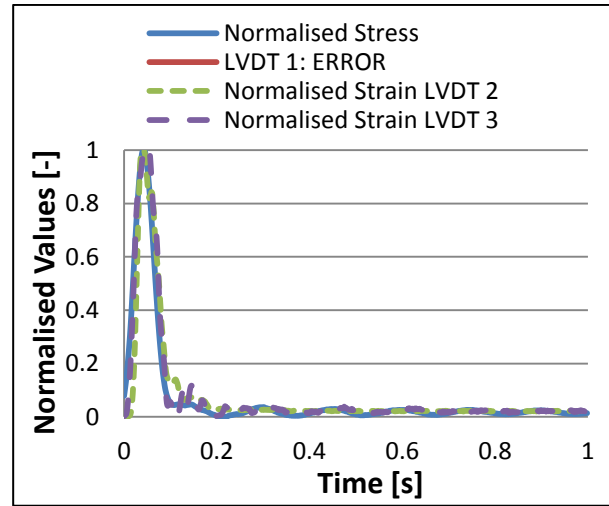


Figure F- 27: Last 10% SR 200 kPa Load Cycle, L- Full

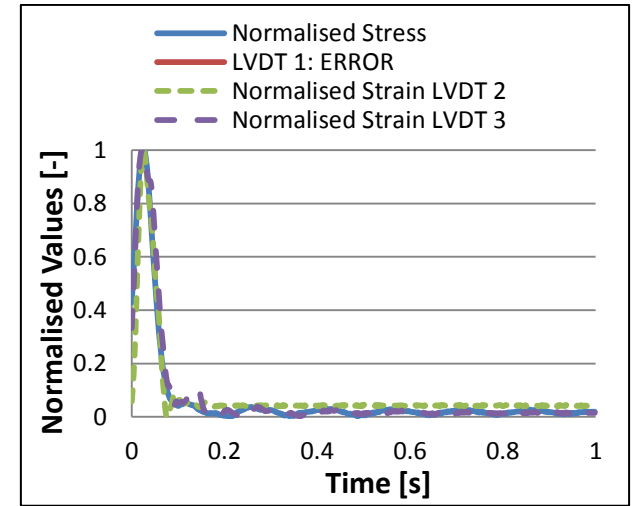


Figure F- 29: Last 10% SR 25 kPa Load Cycle, L- Full

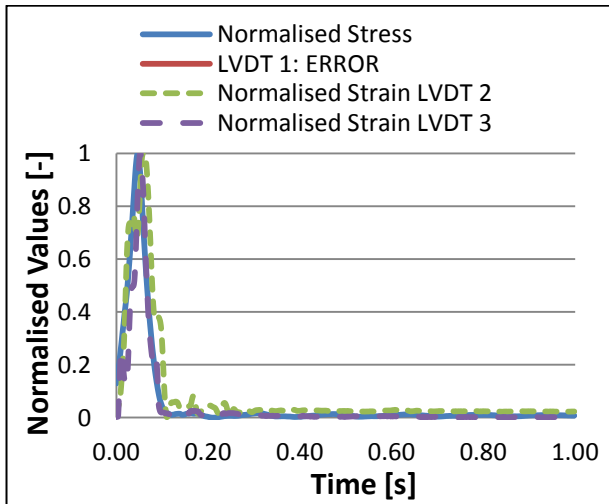


Figure F- 26: Last 55% SR Conditioning Cycle, L- Full

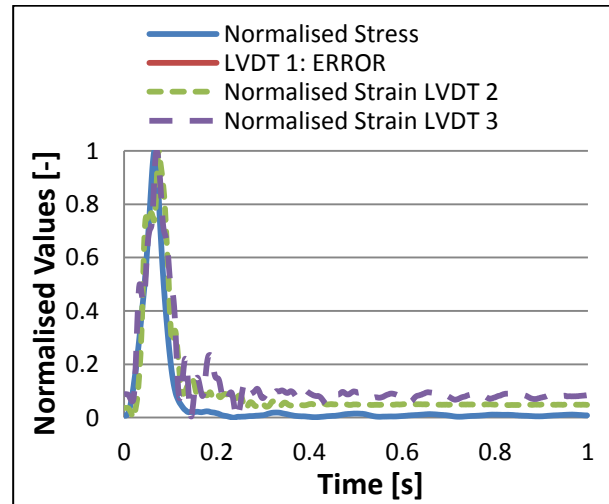


Figure F- 28: Last 55% SR 200 kPa Load Cycle, L- Full

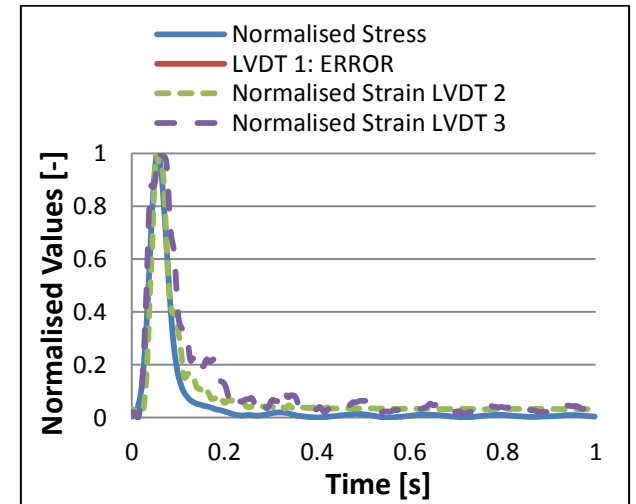


Figure F- 30: Last 55% SR 25 kPa Load Cycle, L- Full

Appendix G:

0.05 – 0.95 Loading Rate

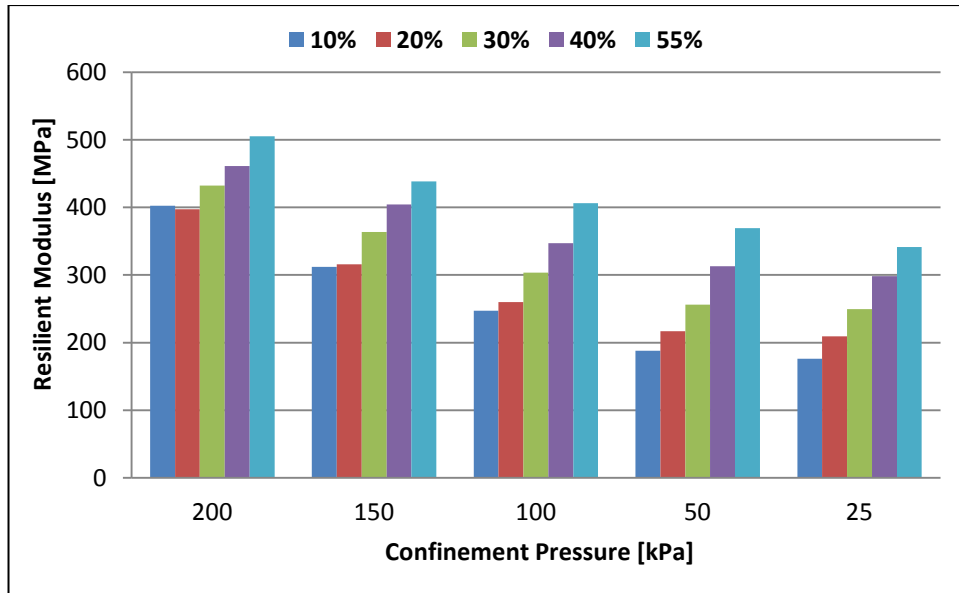


Figure G- 1: Small-size S19 Resilient Modulus Results, Rapid Loading

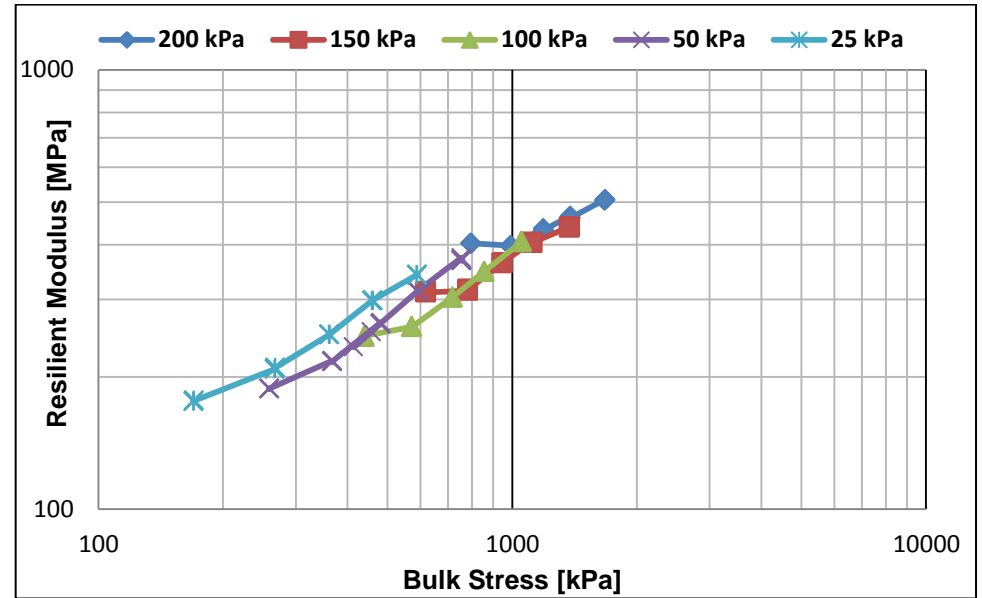


Figure G- 2: Resilient Modulus vs Bulk Stress, Small-size S19, Rapid Loading

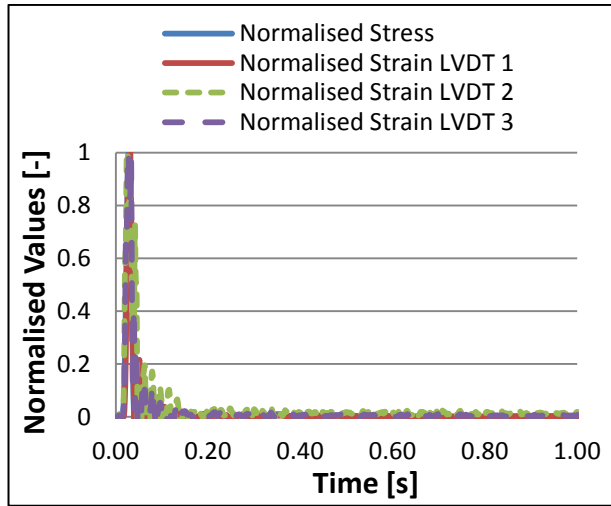


Figure G- 3: Last Rapid 10% SR Conditioning Cycle, S-S19

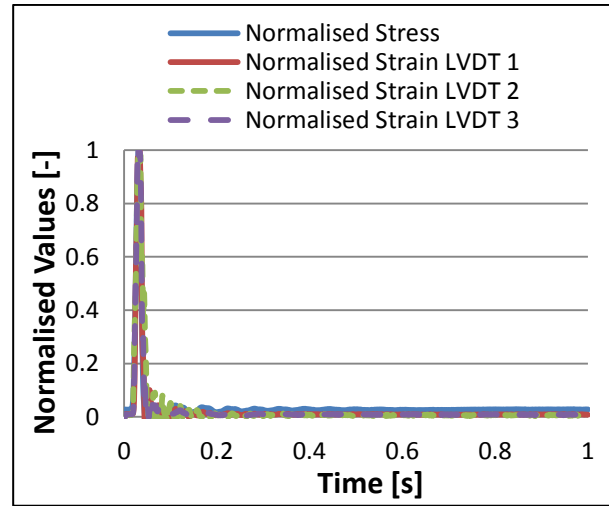


Figure G- 5: Last Rapid 10% SR 200 kPa Load Cycle, S-S19

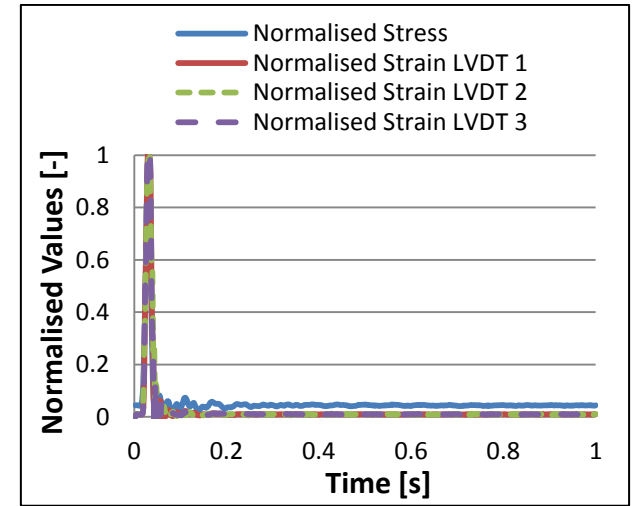


Figure G- 7: Last Rapid 10% SR 25 kPa Load Cycle, S-S19

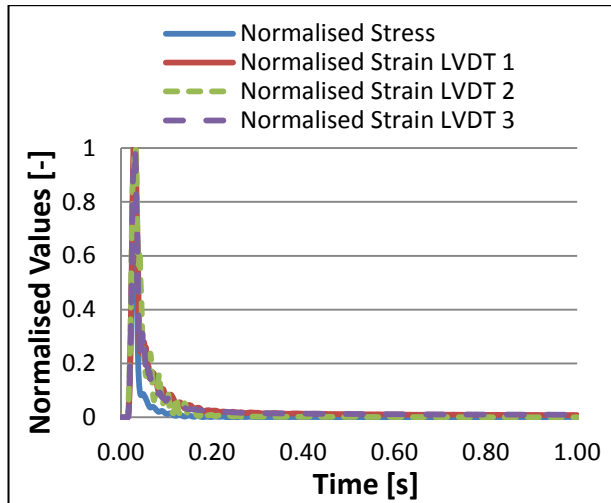


Figure G- 4: Last Rapid 55% SR Conditioning Cycle, S-S19

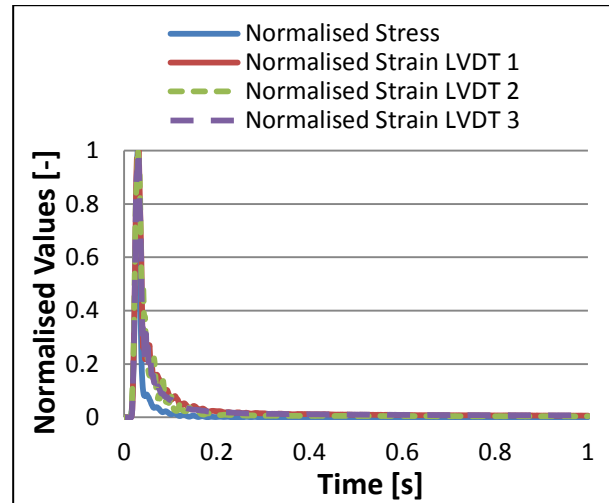


Figure G- 6: Last Rapid 55% SR 200 kPa Load Cycle, S-S19

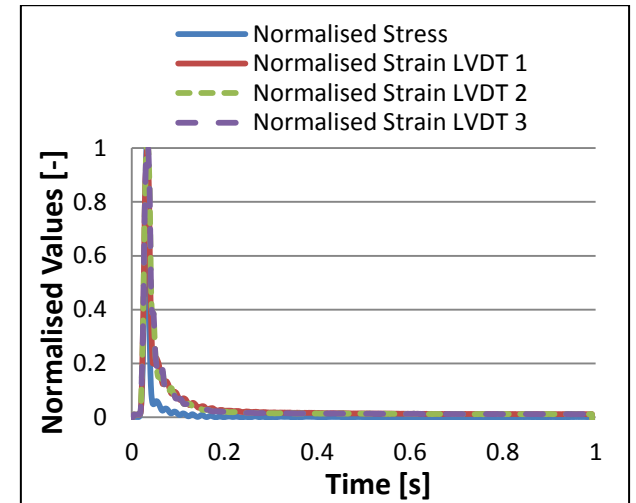


Figure G- 8: Last Rapid 55% SR 25 kPa Load Cycle, S-S19

Appendix H:

Comparison of Models and Influence of Deviator Stress Ratio

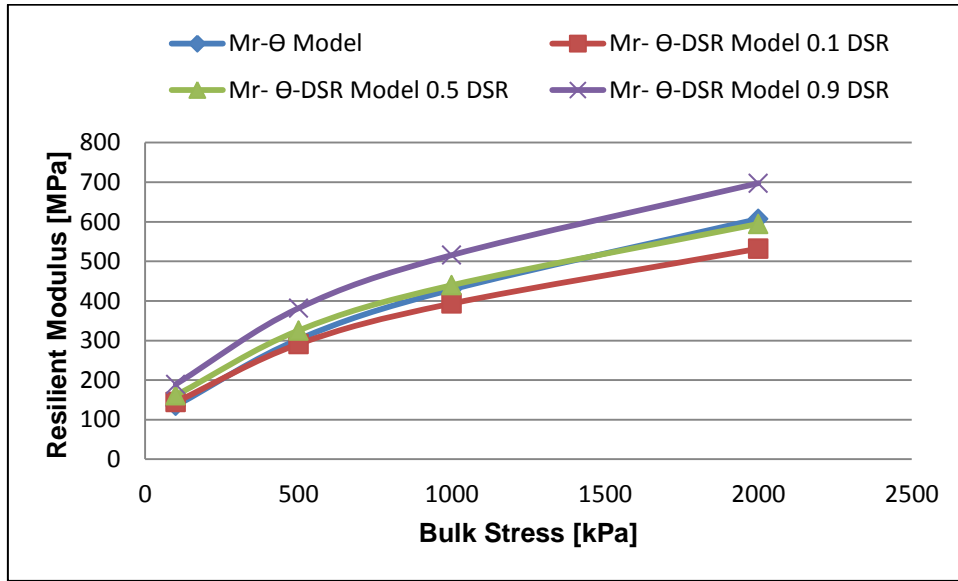


Figure H- 1: Comparison of Models at $SR_d = 10, 50$ and 90% for Small-size S19

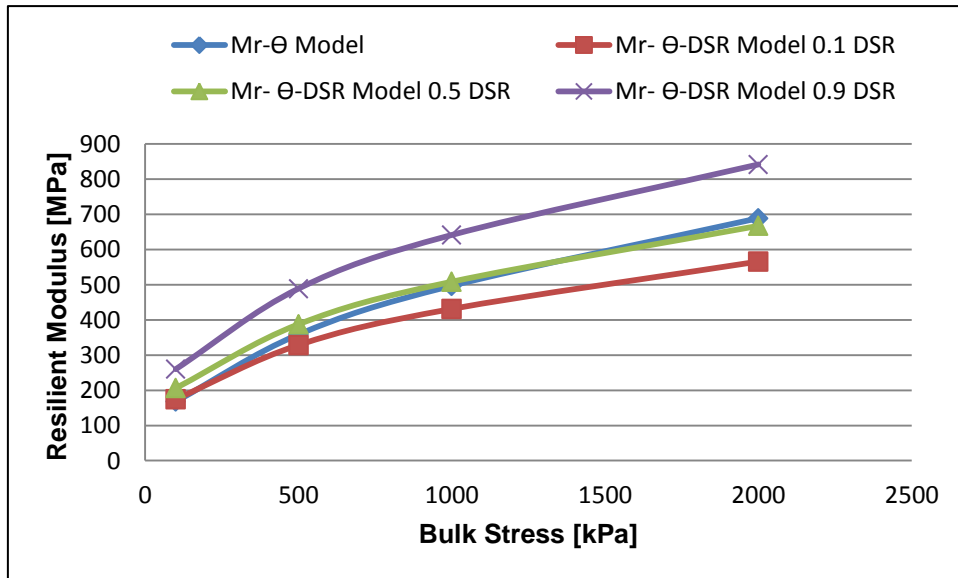


Figure H- 2: Comparison of Models at $SR_d = 10, 50$ and 90% for Small-size G19C

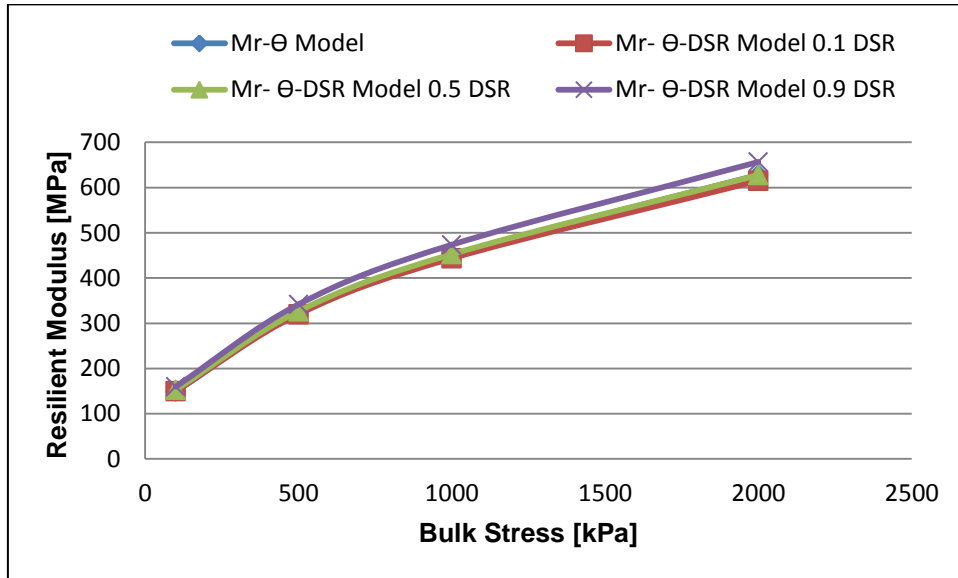


Figure H- 3: Comparison of Models at $SR_d = 10, 50$ and 90% for Large-size S19

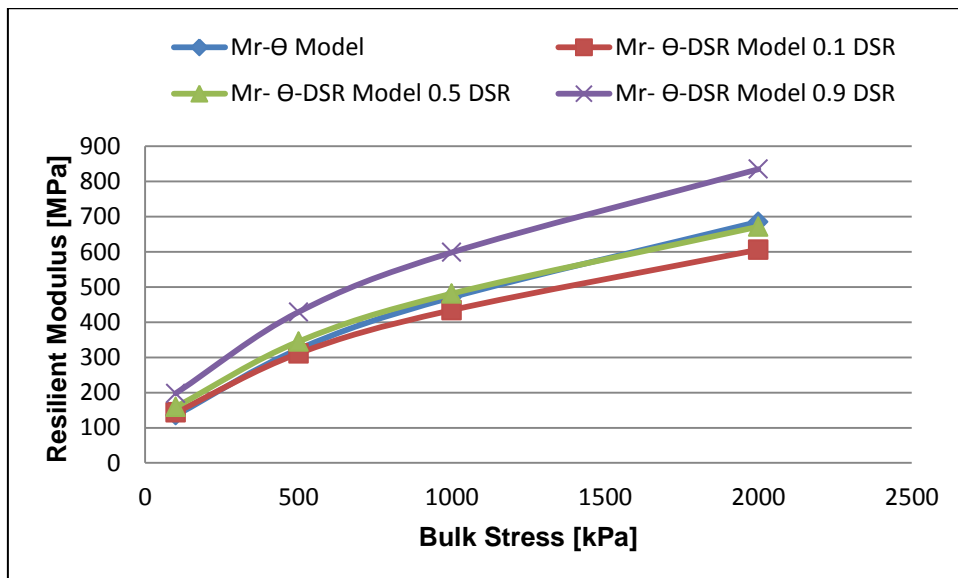


Figure H- 4: Comparison of Models at $SR_d = 10, 50$ and 90% for Large-size G19C

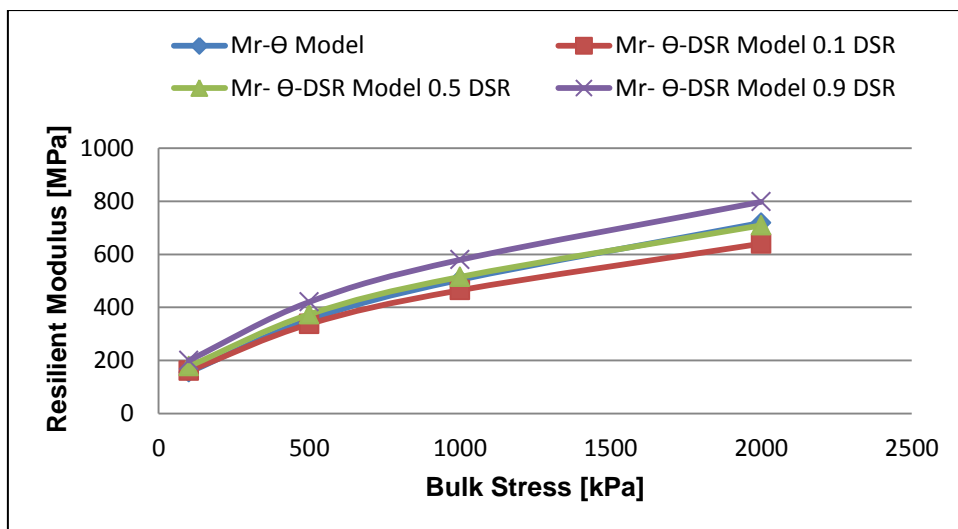


Figure H- 5: Comparison of Models at $SR_d = 10, 50$ and 90% for Large-size Full

Appendix I:

Influence of Increased Density on Resilient Modulus during Dynamic Testing

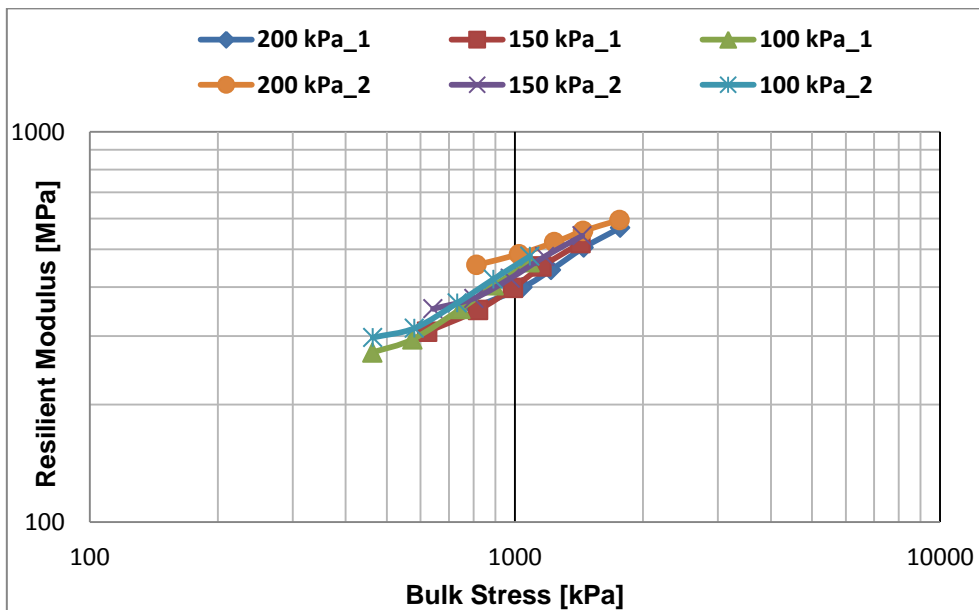


Figure I- 1: Increase in Resilient Modulus of *L-S19* Specimen after Initial Dynamic Loading

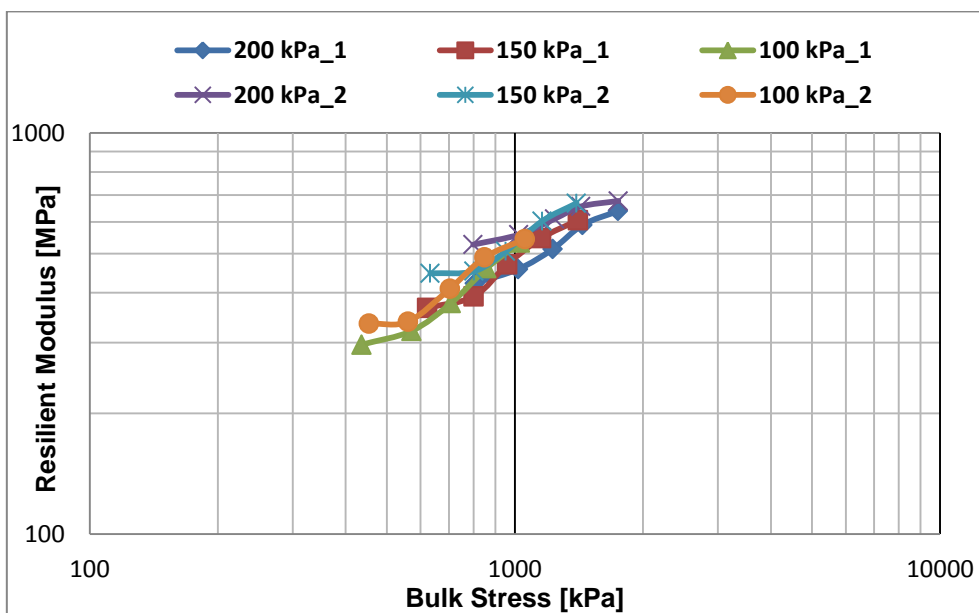


Figure I- 2: Increase in Resilient Modulus of *L-G19C* Specimen after Initial Dynamic Loading

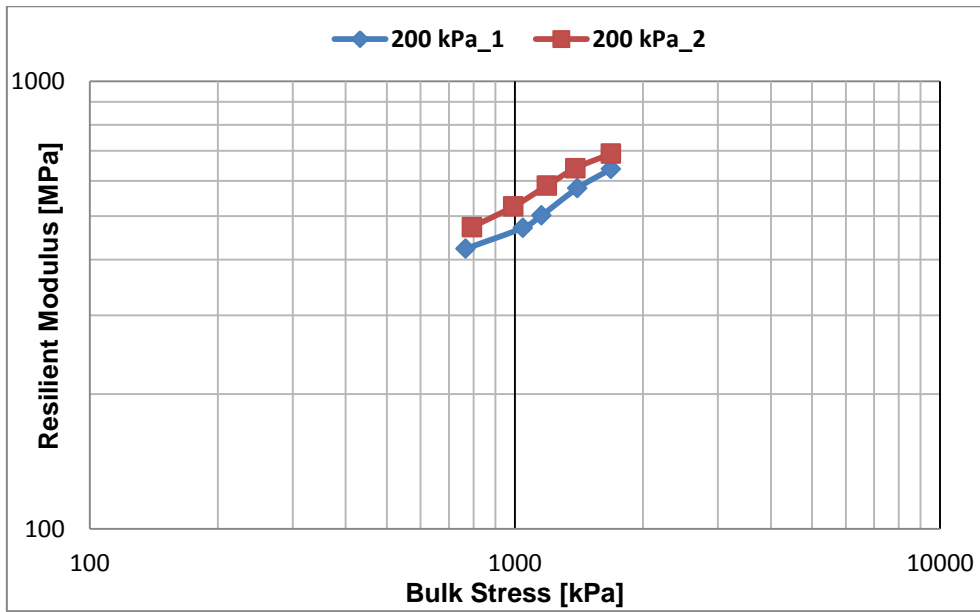


Figure I- 3: Increase in Resilient Modulus of *L-Full* Specimen after Initial Dynamic Loading

Appendix J:

Iterative Design Calculations of Resilient Modulus

Table J- 1: Iterative Design Calculations of M_r for Small-size S19 Specimens

Iteration	Layer	BISAR 3 Input M_r [Mpa]	Values from BISAR 3			Θ [kPa]	k1 [MPa]	k2 [-]	M_r [Mpa]	Mr Deviation from Previous
			61 [kPa]	62 [kPa]	63 [kPa]					
1	1	400.0	799.4	474.1	474.1	1747.6	13.40	0.50	560.2	40%
	2	400.0	725.5	236.7	236.7	1198.9			464.0	16%
	3	400.0	572.9	190.4	190.4	953.7			413.8	3%
2	1	560.2	797.5	504.2	504.3	1806.0			569.5	2%
	2	464.0	712.4	220.1	220.1	1152.6			454.9	-2%
	3	413.8	557.5	179.9	179.9	917.3			405.8	-2%
3	1	569.5	797.5	504.5	504.5	1806.5			569.5	0%
	2	454.9	712.2	218.2	218.3	1148.7			454.2	0%
	3	405.8	557.7	180.2	180.2	918.1			406.0	0%

Table J- 2: Iterative Design Calculations of M_r for Small-size G19C Specimens

Iteration	Layer	BISAR 3 Input M_r [Mpa]	Values from BISAR 3			Θ [kPa]	k1 [MPa]	k2 [-]	M_r [Mpa]	Mr Deviation from Previous
			61 [kPa]	62 [kPa]	63 [kPa]					
1	1	400.0	799.4	474.1	474.1	1747.6	19.17	0.47	640.6	60%
	2	400.0	725.5	236.7	236.7	1198.9			536.6	34%
	3	400.0	572.9	190.4	190.4	953.7			481.9	20%
2	1	640.6	796.6	520.1	520.1	1836.8			655.7	2%
	2	536.6	707.0	223.6	223.6	1154.2			527.1	-2%
	3	481.9	547.3	170.3	170.3	887.9			466.0	-3%
3	1	655.7	796.5	521.5	521.5	1839.5			656.2	0%
	2	527.1	706.1	219.5	219.5	1145.1			525.1	0%
	3	466.0	547.2	170.9	170.9	889.0			466.2	0%

Table J- 3: Iterative Design Calculations of M_r for Large-size S19 Specimens

Iteration	Layer	BISAR 3 Input M_r [Mpa]	Values from BISAR 3			Θ [kPa]	k1 [MPa]	k2 [-]	M_r [Mpa]	Mr Deviation from Previous
			61 [kPa]	62 [kPa]	63 [kPa]					
1	1	400.0	799.4	474.1	474.1	1747.6	16.42	0.48	591.2	48%
	2	400.0	725.5	236.7	236.7	1198.9			493.4	23%
	3	400.0	572.9	190.4	190.4	953.7			442.1	11%
2	1	591.2	797.2	510.5	510.5	1818.2			602.6	2%
	2	493.4	710.4	221.9	222.0	1154.3			484.5	-2%
	3	442.1	553.4	176.1	176.1	905.6			431.2	-2%
3	1	602.6	797.1	511.3	511.3	1819.7			602.8	0%
	2	484.5	709.8	219.1	219.1	1148.0			483.2	0%
	3	431.2	553.4	176.5	176.5	906.4			431.4	0%

Table J- 4: Iterative Design Calculations of M_r for Large-size G19C Specimens

Iteration	Layer	BISAR 3 Input M_r [Mpa]	Values from BISAR 3			Θ [kPa]	k1 [MPa]	k2 [-]	M_r [Mpa]	Mr Deviation from Previous
			61 [kPa]	62 [kPa]	63 [kPa]					
1	1	400.0	799.4	474.1	474.1	1747.6	11.13	0.54	627.2	57%
	2	400.0	725.5	236.7	236.7	1198.9			511.7	28%
	3	400.0	572.9	190.4	190.4	953.7			452.2	13%
2	1	627.2	796.7	516.9	516.9	1830.5			643.1	3%
	2	511.7	707.7	219.7	219.7	1147.1			499.7	-2%
	3	452.2	549.9	173.4	173.4	896.7			437.4	-3%
3	1	643.1	796.6	518.0	518.0	1832.6			643.5	0%
	2	499.7	706.9	215.9	215.9	1138.7			497.7	0%
	3	437.4	549.9	173.9	173.9	897.7			437.7	0%

Table J- 5: Iterative Design Calculations of M_r for Large-size Full Specimens

Iteration	Layer	BISAR 3 Input M_r [Mpa]	Values from BISAR 3			Θ [kPa]	k1 [MPa]	k2 [-]	M_r [Mpa]	Mr Deviation from Previous
			61 [kPa]	62 [kPa]	63 [kPa]					
1	1	400.0	799.4	474.1	474.1	1747.6	14.62	0.51	658.6	65%
	2	400.0	725.5	236.7	236.7	1198.9			543.4	36%
	3	400.0	572.9	190.4	190.4	953.7			483.6	21%
2	1	658.56	796.4	522.9	522.9	1842.2			676.5	3%
	2	543.41	705.8	222.1	222.1	1150.0			532.0	-2%
	3	483.56	545.9	169.2	169.2	884.3			465.3	-4%
3	1	676.50	796.2	524.6	524.6	1845.4			677.1	0%
	2	531.99	704.6	217.2	217.2	1139.0			529.4	0%
	3	465.28	545.7	169.9	169.9	885.5			465.6	0%